



Michigan Technological University
Create the Future Digital Commons @ Michigan Tech

Dissertations, Master's Theses and Master's
Reports - Open

Dissertations, Master's Theses and Master's
Reports

2014

MODEL UPDATING AND STRUCTURAL HEALTH MONITORING OF HORIZONTAL AXIS WIND TURBINES VIA ADVANCED SPINNING FINITE ELEMENTS AND STOCHASTIC SUBSPACE IDENTIFICATION METHODS

Antonio Velazquez Hernandez
Michigan Technological University

Follow this and additional works at: <https://digitalcommons.mtu.edu/etds>



Part of the [Civil Engineering Commons](#), and the [Mechanical Engineering Commons](#)

Copyright 2014 Antonio Velazquez Hernandez

Recommended Citation

Velazquez Hernandez, Antonio, "MODEL UPDATING AND STRUCTURAL HEALTH MONITORING OF HORIZONTAL AXIS WIND TURBINES VIA ADVANCED SPINNING FINITE ELEMENTS AND STOCHASTIC SUBSPACE IDENTIFICATION METHODS", Dissertation, Michigan Technological University, 2014.
<https://digitalcommons.mtu.edu/etds/886>

Follow this and additional works at: <https://digitalcommons.mtu.edu/etds>



Part of the [Civil Engineering Commons](#), and the [Mechanical Engineering Commons](#)

MODEL UPDATING AND STRUCTURAL HEALTH MONITORING OF
HORIZONTAL AXIS WIND TURBINES VIA ADVANCED SPINNING FINITE
ELEMENTS AND STOCHASTIC SUBSPACE IDENTIFICATION METHODS

By

Antonio Velazquez Hernandez

A DISSERTATION

Submitted in partial fulfillment of the requirements for the degree of

DOCTOR OF PHILOSOPHY

In Civil Engineering

MICHIGAN TECHNOLOGICAL UNIVERSITY

2014

© 2014 Antonio Velazquez Hernandez

This dissertation has been approved in partial fulfillment of the requirements for the
Degree of DOCTOR OF PHILOSOPHY in Civil Engineering

Civil and Environmental Engineering Department

Dissertation Advisor: *Dr. R. Andrew Swartz*

Committee Member: *Dr. William M. Bulleit*

Committee Member: *Dr. Yue Li*

Committee Member: *Dr. Bo Chen*

Department Chair: *Dr. David Hand*

To my son Bruno, my daughter Dana, my wife Erika, my mother Eva and my father Raul.

Table of Contents

List of Figures and Tables	viii
Acknowledgements	xvii
Abstract.....	xviii
Chapter 1. Introduction.....	1
1.1 Presentation.....	1
1.2 Methodological Framework.....	4
1.3 Organization.....	7
1.4 Justification	9
1.5 Objectives	11
1.5.1 General Objective	11
1.5.2 Particular Objectives	12
Chapter 2. Literature Review	13
2.1 Preliminary Study.....	13
Chapter 3. Aeroelastic Analysis	21
3.1 Introduction.....	22
3.2 Vibration Equations.....	24
3.3 Along-Wind Response	27
3.4 Across-Wind Response (Vickery's Method).....	29
3.5 Across-Wind Response (Rumman's Method)	32
3.6 Finite Element Prototype	32
3.7 Results	35
3.8 Conclusions.....	44
Chapter 4. Spinning Finite Element	47
4.1 Introduction.....	48

4.2 Spinning Finite Element	51
4.2.1 Coordinate System	51
4.2.2 Lagrange Equations	55
4.2.3 Steady State Equations	57
4.3 Vibration Equations.....	60
4.3.1 Equation of Motion.....	60
4.3.2 Eigenvalue Problem	61
4.4 Aeroelastic Analysis.....	63
4.4.1 Harmonic Wind Load	63
4.4.2 Distributed Stationary Random Wind Load.....	65
4.4.3 Spectral Response	69
4.5 Numerical Example	72
4.6 Conclusions.....	88

Chapter 5. Spinning Finite Element with Damped Gyroscopic Effects and Axial-Flexural-Torsional Coupling.....91

5.1 Introduction.....	91
5.2 Spinning Finite Element	96
5.2.1 Kinematic Description	97
5.2.2 Shape Functions.....	104
5.3 Lagrangian Equation.....	106
5.3.1 Kinetic Energy	109
5.3.2 Strain Energy	110
5.3.3 Non-Conservative Work	110
5.4 Equation of Motion	111
5.5 Eigenrealization	113
5.6 Numerical Example.....	117
5.7 Prototype.....	118
5.8 Results	120
5.9 Discussion.....	131

5.10 Conclusions.....	135
Chapter 6. Output-Only Cyclo-Stationary Linear-Parameter Time-Varying Stochastic Subspace Identification Method.....	137
6.1 Introduction.....	138
6.2 Numerical Model	141
6.2.1 Subspace Realization	141
6.2.2 Stochastic Subspace	143
6.2.3 Cyclo-Stationary Stochastic Subspace.....	149
6.2.4 Prediction and Residual States	155
6.2.5 Innovation Model.....	158
6.2.6 Kalman Filter.....	161
6.2.7 Stationary State Covariance	163
6.2.8 Stochastic Cyclo-Stationary System Markovs	165
6.2.9 Noise Identification.....	166
6.2.10 Iterative System Identification Algorithm.....	167
6.3 Numerical Example.....	172
6.3.1 Prototype	172
6.3.2 Results.....	173
6.4 Conclusions.....	193
Chapter 7. Model Updating via Adaptive Simulated Annealing	195
7.1 Introduction.....	195
7.2 Eigensystem Realization Algorithm (ERA)	198
7.3 Stochastic Subspace Identification (SSI).....	200
7.4 Spinning Finite Element (SFE).....	201
7.5 Complex-Conjugate Modal Assurance Criterion (MAC)	204
7.6 Adaptive Simulated Annealing (ASA).....	206
7.7 Numerical Simulation.....	210
7.8 Results	211

7.9 Discussion.....	219
7.10 Conclusions.....	220
 Chapter 8. Final Remarks	223
8.1 Future Work.....	223
8.2 Summary.....	223
8.3 Conclusions.....	225
 References	227
 Appendix A	249

List of Figures and Tables

Chapter 1. Introduction

Figure 1.1(a) Global scope of the Thesis Project including tower and rotor blades interaction	3
Figure 1.1(b). Scope of the Thesis Project for rotor blades	4
Table 1.2. Methodological framework of the Thesis project	6
Figure 1.2. Conceptual pyramid of the Thesis project	7
Figure 1.3. Incumbency of the Thesis project	8

Chapter 3. Aeroelastic Analysis

Figure 3.1. Wind turbine specimen for modal-base response.....	34
Table 3.1. Geometry Properties of the 65kW Wind Turbine.....	34
Figure 3.2. First three normalized modes of vibration experimentally calibrated using AMM technique corresponding to (a) 1.7Hz, (b) 13.5Hz, (c) 33.5Hz, (d) all three modes	35
Table 3.2. Some of the along-wind and across-wind statistic parameters for random realizations of wind induced vibrations	37
Figure 3.3(a). First set of random variable distributed used in the Monte Carlo simulation (3000 realizations)	38
Figure 3.3(b). Second set of random variable distributed used in the Monte Carlo simulation (3000 realizations)	38
Figure 3.4. Reynolds number vs Strouhal number (3000 realizations) combining across-wind and along-wind analysis, for the first three modes of vibration	39
Figure 3.5(a). Critical height construction in the across-wind direction for the first three dominant modes. Formulation of $F(z)$ for the induction of the critical height z_{ei}	39
Figure 3.5(b). Critical height construction in the across-wind direction for the first three dominant modes. Formulation of the aero-elastic damping at critical elevation z_{ei}	40
Figure 3.6. Along-wind cross-correlation coefficient (narrow-band cross-correlation) for three dominant frequencies; (b) Wind profile (boundary layer) evaluated at critical elevation z_{ei} . Describes wind velocities $U_{icr}(z)$ and $U_{10}(z_{ei})$	40
Figure 3.7. Profiles for number-of-peaks controls: (a) largest-peak-displacement factor K_x , (b)	

largest-peak-acceleration $K_{\ddot{x}}$, (c) expected number-of-peaks per-unit-time factor $\nu_{\ddot{x}}$, and (d) expected number-of-peaks per-unit-time-factor $\nu_{\ddot{x}}$	41
Figure 3.8. For the first three dominant modes: (a) Vortex-shedding-load in-the-wake spectral-density-function due to across-wind aerodynamics. Aero-elastic effects are not assessed, only structural damping affects the motion. (b) Lift-coefficient spectral density function acting on the wake of the structure at rest.....	41
Figure 3.9. Modal combined spectral density function of the along-wind fluctuating deflection, for three sample heights above grade.....	42
Figure 3.10. (a) Aero-elastic (gust) correction factor for the computation of fluctuating peak deflections, expressed in the frequency domain. (b) Structural (modal combined) acceleration response profile for three independent random realizations	42
Figure 3.11(a). Dynamic structural response of the wind tower for one random realization employing across-wind Rumman's method	43
Figure 3.11(b). Dynamic structural response of the wind tower for one random realization employing across-wind Vickery's method.....	43
Figure 3.11(c). Dynamic structural response of the wind tower for one random realization employing along-wind of distributed stationary wind load.....	44

Chapter 4. Spinning Finite Element

Figure 4.1. Orthogonal coordinate systems that govern the spinning motion of a wind turbine blade element.....	53
Figure 4.2. Cosine directories that constitute the base transformation matrix \mathbf{R} from spinning $x_s y_s z_s$ to local xyz coordinate systems	55
Figure 4.3. Global XYZ and spinning $x_s y_s z_s$ orthogonal coordinate systems that govern the spinning motion of a simplified HAWT wind turbine blade, where local xyz coincides with spinning $x_s y_s z_s$ reference frames.....	55
Figure 4.4. Tapered-swept gradient variation properties at the inboard and outboard ends of a spinning finite element.....	57
Figure 4.5. Degrees of freedom defined for a spinning finite element.....	57
Figure 4.6. Distributed periodic pressure applied to the SPE in the along-wind direction.....	64
Figure 4.7. Coherence (spatial correlation) function distribution for the auto-power and cross-	

power spectrum computation along the global X (horizontal) and Z (vertical) axes	67
Figure 4.8. Spectral energy distribution for a node at a set height Z, and a set rotation angle θ . (a) Modified rotationally-sampled spectrum, (b) original Kaimal spectrum	69
Table 4.1. Properties of the wind turbine prototype	73
Table 4.2. Aeroelastic random variables with Gaussian distributions	73
Figure 4.9(a). Structural dynamic response in local coordinate system xyz . Mode shapes	74
Figure 4.9(b). Structural dynamic response in local coordinate system xyz . Spinning rate velocity vs natural frequency, for the twelve blade spinning finite element modes	75
Figure 4.10. Normally distributed random-source parameters corresponding to damping (Rayleigh) matrix coefficients, terrain surface roughness length, Strouhal number, and drag coefficient from 3000 random realizations	79
Figure 4.11. Wind-induced velocity calibration by linking Reynolds number and Strouhal number for the first three harmonic tower frequencies: (a) Mild wind ($U_{cr} = 12\text{MPH}$); Heavy storm ($U_{cr} = 113\text{MPH}$); Extreme conditions ($U_{cr} = 194\text{MPH}$)	80
Figure 4.12. Critical wind velocity profiles (boundary layer) for (a) wind tower; and (b) wind blade at instantaneous rotation angle $\theta = 90^\circ$ evaluated for the first three fundamental tower frequencies	80
Figure 4.13. Critical wind velocity computation by random realizations adopting Extreme Value Type I (Gumbel) distribution	81
Figure 4.14(a). Monin number for the first three tower frequencies	81
Figure 4.14(b). Along-wind cross-correlation coefficients for the first three tower frequencies	82
Figure 4.15. Rotationally sampled spectra for the first three tower resonant , computed at two different locations: hub elevation (Z_I) and tip of the blade (Z_5)	82
Figure 4.16. Total spectral density of blade deflections in the along-wind direction for three wind field intensities: (a) mild wind; (b) heavy storm; and (c) extreme event	83
Figure 4.17. Modal combined number-of-peaks-per-unit-time ((a),(b)) and largest-peak factors ((c),(d)) computed for the second tower dominant frequency. Evaluated for fluctuating blade deflection ((a),(c)) and fluctuating blade acceleration ((b),(d)), respectively	84
Figure 4.18. Modal combined mean square value of the fluctuating along-wind (a) deflection; and (b) acceleration of blade element computed for the first three tower dominant frequencies ..	85
Figure 4.19. Along-wind peak response of blade element computed for the first three tower dominant frequencies. Evaluated for (a) fluctuating deflection and (bs) fluctuating acceleration, (c) peak shear (modal combined), and (d) peak moment (modal combined)	86

Figure 4.20. Along-wind peak response of blade element computed for the first three tower dominant frequencies, calculated for three rotation angles $n_t = 0$, and evaluated for (a) modal combined fluctuating deflection; (b) modal combined fluctuating acceleration; (c) peak shear (modal combined); and (d) peak moment (modal combined)	87
Figure 4.21. Example demand PDFs for (a) peak shear force; and (b) bending moment from 3000 random realizations with shear and moment nominal capacity (member strength) PDFs modeled using normal distributions in compliance with EN-50308	88

Chapter 5. Spinning Finite Element with Damped Gyroscopic Effects and Axial-Flexural-Torsional Coupling

Figure 5.1. Precession mode of a wind turbine blade with tapered-swept variation.....	93
Figure 5.2. Local xyz , spinning $x_s y_s z_s$, and inertial XYZ orthogonal coordinate systems governing the rotating motion of a wind turbine blade	98
Figure 5.3. Total displacements u , v and w traced on the middle line (center of gravity) of a blade element, before and after deflection.....	99
Figure 5.4. Relative displacements of a tapered-swept cross section that simultaneously presents rotations around three orthogonal axes to simulate geometric curving of the blade element.....	100
Figure 5.5. Angular (swept) displacements around three orthogonal axes on the middle line of the deflected cross-section. (a) Schematic, (b) swept around x_s axis (angle of incidence, twist angle or relative pitch angle), (c) swept around z_s axis (relative cone angle).....	101
Figure 5.6. Direction cosines that conform the base transformation matrix \mathbf{R} from spinning $x_s y_s z_s$ to local xyz coordinate system	102
Figure 5.7. Degrees of freedom of the Spinning Finite Element in three orthogonal directions, expressed for both ends inboard and outboard	106
Figure 5.8. Tapered-swept gradient variations of mechanical properties at the inboard and outboard ends of a Spinning Finite Element	108
Figure 5.9. Damped-Gyroscopic Eigenrealization Flow Diagram. Adopted from Zheng	116
Figure 5.10(a). Numerical example of a hypothetical wind turbine blade. (a) Load combinations applied at the free degrees of freedom of the outboard end	119
Figure 5.10(b). Numerical example of a hypothetical wind turbine blade. (b) Tapered-swept combination matrix of the hypothetical specimen with four different taper and four different sweep degrees; (c) Cross section at inboard and outboard ends	119

Figure 5.11. Structural response time histories (u = displacement, v = velocity, a = acceleration) for a fully coupled rotor blade with $n_t = 0$, $\Omega = 150$ rev/min, and $\zeta = 0.0001$ for: (a) blast wind load, (b) sinusoidal wind load, (c) chirp wind load	124
Figure 5.12. Structural response time histories (u = displacement, v = velocity, a = acceleration) of four dominant modes of a rotor blade with $n_t = 1$, $\zeta = 0.1$, $\Omega = 150$ rev/min and a chirp wind load applied. (a) 0% coupling, (b) 50% coupling, and (c) 100% coupling	124
Figure 5.13. Single-sided amplitude spectrum of flap deflection for different coupling ratios due to a sinusoidal wind load, $\Omega = 150$ rev/min, $\zeta = 0.0001$. (a) $n_t = 0$, (b) $n_t = 1$, (c) $n_t = 2$, (d) $n_t = 3$	125
Figure 5.14. Damping ratio versus peak base shear on lag mode (strong axis) for different coupling ratios. Chirp wind load, $\Omega = 150$ rev/min, (a) $n_t = 0$, (b) $n_t = 1$, (c) $n_t = 2$, (d) $n_t = 3$..	125
Figure 5.15. Phase and time histories of a fully coupled rotor blade in flap-bending rotation ϕ_x , under an harmonic excitation $F = F_0 \sin(2\pi nt)$, $F_0 = 0.5$, $n = 1$. (a) $n_t = 2$ (parabolic), (b) $n_t = 1$ (linear), and (c) $n_t = 0$ (constant)	126
Figure 5.16. Phase and time histories of a fully coupled rotor blade in torsional rotation (twist) θ_x , under an harmonic excitation $F = F_0 \sin(2\pi nt)$, $F_0 = 0.5$, $n = 1$. (a) $n_t = 2$ (parabolic), (b) $n_t = 1$ (linear), and (c) $n_t = 0$ (constant)	126
Figure 5.17. (a) Flap-mode phase distributions for different swept angles θ_x and ψ_x subjected to a chirp wind load, $\zeta = 0.0001$, $n_t = 0$. (a) $\Omega = 0$ rev/min, uncoupled; (b) $\Omega = 50$ rev/min, uncoupled; (c) $\Omega = 0$ rev/min, fully coupled; (d) $\Omega = 50$ rev/min, fully coupled	127
Figure 5.18. (a) Flap-mode phase distributions for different swept angles θ_x and ψ_x subjected to a chirp wind load, $\zeta = 0.0001$, $n_t = 1$. (a) $\Omega = 0$ rev/min, uncoupled; (b) $\Omega = 50$ rev/min, uncoupled; (c) $\Omega = 0$ rev/min, fully coupled; (d) $\Omega = 50$ rev/min, fully coupled	128
Figure 5.19. (a) Flap-mode phase distributions for different swept angles θ_x and ψ_x subjected to a chirp wind load, $\zeta = 0.0001$, $n_t = 2$. (a) $\Omega = 0$ rev/min, uncoupled; (b) $\Omega = 50$ rev/min, uncoupled; (c) $\Omega = 0$ rev/min, fully coupled; (d) $\Omega = 50$ rev/min, fully coupled	129
Figure 5.20. Frequency envelopes for different spinning velocities and different coupling ratios. First three dominant frequencies for a wind blast load applied; $\zeta = 0.0001$. (a) $n_t = 0$, (b) $n_t = 1$, (c) $n_t = 2$, (d) $n_t = 3$	130
Figure 5.21. Compass diagram progression of the a complex conjugate eigenvector associated with flap bending mode, drawn for eight different coupling intensities: (a) 25%, (b) 30%, (c)	

35%, (d) 40%, (e) 45%, (f) 50%, (g) 55%, (h) 60%. $n_t = 3$, $\zeta = 0.0001$, $\Omega = 150$ rev/min 130

Chapter 6. Output-Only Cyclo-Stationary Linear-Parameter Time-Varying Stochastic Subspace Identification Method

Figure 6.1. Rotating beam element under stochastic subspace identification using output signals only, and governed by a cyclo-stationary time-varying motion $\Omega(t)$	149
Figure 6.2. Block diagram of a cyclo-stationary stochastic subspace system with time-varying linear parameters \mathbf{A}_{pc} , \mathbf{A}_{ps} , \mathbf{C}_{pc} , \mathbf{C}_{ps} . Symbol Δ stands for delay	152
Figure 6.3. Kalman filter block diagram of a cyclo-stationary stochastic subspace system with time-varying linear parameters \mathbf{A}_{pc} , \mathbf{A}_{ps} , \mathbf{C}_{pc} , \mathbf{C}_{ps} . Symbol Δ stands for delay	156
Figure 6.4. Output-Only Cyclo-Stationary Linear-Parameter Time-Varying Stochastic Subspace Identification (CS-SSI-LPTV) algorithm.....	169
Table 6.1. Structural Dynamic Properties from Eigensystem Realization Theory	173
Figure 6.5. Chain-like spinning finite element model governed by a cyclo-stationary time-varying spinning velocity $\Omega(t)$. A preliminary set of six random out-of-plane loads (inputs) were imprinted on each node to excite the modal harmonics of the structure	175
Figure 6.6. (a) Typical set of outputs $y_i(t)$ (input data time histories for CS-SSI-LPTV model) adopting velocity signals (m/sec) of the spinning finite element (SFE) model running at constant spinning velocity $\Omega = 10$ RPM. (b) Corresponding spectral density functions	178
Table 6.2. Distribution of the Hankel matrix Singular-Value-Decomposition (SVD) values employed to define the order of the system n via CS-SSI-LPTV identification method	179
Table 6.3(a). Stability curves for distinct orders of the system n and for different structural damping ratios and three distinct spinning-velocity profiles, by means of the CS-SSI-LPTV identification algorithm.....	180
Table 6.3(b). Stability curves for distinct orders of the system n and for different structural damping ratios and three distinct spinning-velocity profiles, by means of the CS-SSI-LPTV identification algorithm.....	181
Table 6.4. Distributions of the auto-covariance matrix \mathbf{Q} of the input noise \mathbf{w}_k , for different structural damping ratios ζ and for three different spinning velocity time histories $\Omega(t)$	182
Table 6.5. Correlation distributions of the state covariance matrix Σ for different structural damping ratios ζ and for three different spinning velocity time histories $\Omega(t)$	183

Table 6.6. Distributions of the auto-covariance matrix \mathbf{R} of the output noise \mathbf{v}_k , for different structural damping ratios ζ and for three different spinning velocity time histories $\Omega(t)$	184
Table 6.7. Distributions of the cross-covariance matrix \mathbf{S} of the input/output noise pair \mathbf{w}_k and \mathbf{v}_k , for different structural damping ratios ζ and for three different spinning velocity time histories $\Omega(t)$	185
Table 6.8. Recursive $n_{it} = 100$ iterations of the state-covariance inverse matrix $\bar{\mathbf{\Omega}} = \mathbf{\Sigma}^{-1}$ aimed to reach stationary conditions of the covariance matrices, for different structural damping ratios ζ and for four different spinning velocity time histories $\Omega(t)$	186
Table 6.9. Spectral density functions $\Phi(z)$ of output signals \mathbf{y}_k for different structural damping ratios ζ and for four different spinning velocity time histories $\Omega(t)$	187
Table 6.10(a). Comparison of the identified first three dominant modes of the system computed for different structural damping ratios ζ and different spinning-velocity time histories $\Omega(t)$. CS-SSI-LPTV identification algorithm is benchmarked with the exact solutions from SFE.....	188
Table 6.10(b). Comparison of the identified first three dominant modes of the system computed for different structural damping ratios ζ and different spinning-velocity time histories $\Omega(t)$. CS-SSI-LPTV identification algorithm is benchmarked with the exact solutions from SFE.....	189
Table 6.11. Comparison of the identified dominant frequencies of the system computed for different structural damping ratios ζ and different spinning-velocity time histories $\Omega(t)$. CS-SSI-LPTV identification algorithm is benchmarked with a standard procedure (non cyclo-stationary) of Stochastic ID, and with the exact solutions from SFE.....	190
Table 6.12. Comparison of the identified CS-SSI-LPTV damping ratios versus SFE structural damping ratios ζ at different spinning-velocity time histories $\Omega(t)$	191
Figure 6.7(a)(b) Measured vs prediction of the output signal of the sixth node y_6 for different spinning velocity profiles $\Omega(t)$. For each cluster (a) null or (b) constant spinning velocity, simulations with five damping ratios are computed, from top to bottom, $\zeta = 0.0001$, $\zeta = 0.001$, $\zeta = 0.01$, $\zeta = 0.1$ and $\zeta = 0.5$	192
Figure 6.7(c)(d). Measured vs prediction of the output signal of the sixth node y_6 for different spinning velocity profiles $\Omega(t)$. For each cluster (c) linear or (d) smooth random spinning velocity, simulations with five damping ratios are computed, from top to bottom, $\zeta = 0.0001$, $\zeta = 0.001$, $\zeta = 0.01$, $\zeta = 0.1$ and $\zeta = 0.5$	192
Figure 6.8. Computational time versus cyclo-stationary transition-matrix coefficient s , for four distinct orders of the system n , via CS-SSI-LPTV algorithm. (a) $\alpha = 10$, (b) $\alpha = 30$ and (c) $\alpha =$	

Chapter 7. Model Updating via Adaptive Simulated Annealing

Figure 7.1. Scope of the Adaptive Simulated Annealing engine for SFE model updating via CS-SSI-LPTV 202

Figure 7.2. Adaptive Simulated Annealing (ASA) flowchart..... 209

Figure 7.3. Overview of wind turbine BWC XL.1(a) power generator, (b) blade airfoil cross section SH3045 profile type, (c) sensors deployment and instrumentation 211

Figure 7.4. Progression of Modal Assurance Criterion (MAC) for (left to right) initial $T_s = 1$, $1/3T_s$, $2/3T_s$, and T_s obtained through the ASA engine using CS-SSI-LPTV algorithm and SFE model, applied to four different cases: (a) $\Omega = 0$ RPM (final $T_s = 0.0015$), (b) $\Omega = 50$ RPM (final $T_s = 0.0181$), (c) $\Omega = 150$ RPM (final $T_s = 0.0037$), (d) $\Omega = 300$ RPM (final $T_s = 0.0196$) 213

Figure 7.5. (a) Spinning velocity Ω vs frequencies f_i^{SFE} of the updated model. (b) Energy absorption probability for different spinning velocities Ω produced by neighborhood-phase realizations of the updating model. The energy absorption is smaller - therefore convergence faster - for higher speeds 214

Figure 7.6. Update progression of three dominant SFE model frequencies obtained with the ASA engine using CS-SSI-LPTV algorithm, applied to four different cases: (a) $\Omega = 0$ RPM (final $T_s = 0.0015$), (b) $\Omega = 50$ RPM (final $T_s = 0.0181$), (c) $\Omega = 150$ RPM (final $T_s = 0.0037$), (d) $\Omega = 300$ RPM (final $T_s = 0.0196$) 214

Table 7.1. Comparison of exact and final predictions of target geometric/inertial parameters obtained with the ASA engine using CS-SSI-LPTV algorithm and SFE model, by means of MAC complex-conjugate mode shapes applied to four different cases: (a) $\Omega = 0$ RPM (final $T_s = 0.0015$), (b) $\Omega = 50$ RPM (final $T_s = 0.0181$), (c) $\Omega = 150$ RPM (final $T_s = 0.0037$), (d) $\Omega = 300$ RPM (final $T_s = 0.0196$) 215

Figure 7.7. Statistical distribution of target geometric/inertial parameters obtained with the ASA engine using CS-SSI-LPTV algorithm and SFE model, by means of MAC complex-conjugate mode shapes applied to four different cases: (a) $\Omega = 0$ RPM (final $T_s = 0.0015$), (b) $\Omega = 50$ RPM (final $T_s = 0.0181$), (c) $\Omega = 150$ RPM (final $T_s = 0.0037$), (d) $\Omega = 300$ RPM (final $T_s = 0.0196$) 216

Figure 7.8. Measured (CS-SSI-LPTV) vs predicted (SFE) complex mode shapes at minimum energy absorption obtained with the ASA engine by means of MAC complex-conjugate mode shapes applied to four different cases: (a) $\Omega = 0$ RPM (final $T_s = 0.0015$), (b) $\Omega = 50$ RPM (final $T_s = 0.0181$), (c) $\Omega = 150$ RPM (final $T_s = 0.0037$), (d) $\Omega = 300$ RPM (final $T_s = 0.0196$)..... 217

Figure 7.9. Transformation from complex-numbers to physical counterparts of the first four dominant modes shapes for (a) CS-SSI-LPTV and (b) SFE. (c) Update progression of two dominant SFE physical modes. $\Omega = 0$ RPM (final $T_s = 0.0015$)..... 218

Figure 7.10. Progression of energy acceptance probability and its corresponding energy error obtained with the ASA engine using CS-SSI-LPTV algorithm and SFE, applied to four different cases: (a) $\Omega = 0$ RPM (final $T_s = 0.0015$), (b) $\Omega = 50$ RPM (final $T_s = 0.0181$), (c) $\Omega = 150$ RPM (final $T_s = 0.0037$), (d) $\Omega = 300$ RPM (final $T_s = 0.0196$)..... 219

Acknowledgements

Special appreciation and recognition to my mentor and guide Dr. Andrew R. Swartz for his exceptional dedication, support, patience and friendship. My acknowledge to National Council for Science and Technology Mexico (CONACYT), National Science Foundation (NSF), and Michigan Technological University (MTU) for their financial support. Special thanks to Dr. Kenneth Loh and Dr. Valeria La Saponara, from University of California at Davis, for their friendship, guidance, help and support.

Abstract

Wind energy has been one of the most growing sectors of the nation's renewable energy portfolio for the past decade, and the same tendency is being projected for the upcoming years given the aggressive governmental policies for the reduction of fossil fuel dependency. Great technological expectation and outstanding commercial penetration has shown the so called Horizontal Axis Wind Turbines (HAWT) technologies. Given its great acceptance, size evolution of wind turbines over time has increased exponentially. However, safety and economical concerns have emerged as a result of the newly design tendencies for massive scale wind turbine structures presenting high slenderness ratios and complex shapes, typically located in remote areas (e.g. offshore wind farms). In this regard, safety operation requires not only having first-hand information regarding actual structural dynamic conditions under aerodynamic action, but also a deep understanding of the environmental factors in which these multibody rotating structures operate. Given the cyclo-stochastic patterns of the wind loading exerting pressure on a HAWT, a probabilistic framework is appropriate to characterize the risk of failure in terms of resistance and serviceability conditions, at any given time. Furthermore, sources of uncertainty such as material imperfections, buffeting and flutter, aeroelastic damping, gyroscopic effects, turbulence, among others, have pleaded for the use of a more sophisticated mathematical framework that could properly handle all these sources of indetermination. The attainable modeling complexity that arises as a result of these characterizations demands a data-driven experimental validation methodology to calibrate and corroborate the model. For this aim, System Identification (SI) techniques offer a spectrum of well-established numerical methods appropriated for stationary, deterministic, and data-driven numerical schemes, capable of predicting actual dynamic states (eigenrealizations) of traditional time-invariant dynamic systems. As a consequence, it is proposed a modified data-driven SI metric based on the so called Subspace Realization Theory, now adapted for stochastic non-stationary and time-varying systems, as is the case of HAWT's complex aerodynamics. Simultaneously, this investigation explores the characterization of the turbine loading and response envelopes

for critical failure modes of the structural components the wind turbine is made of. In the long run, both aerodynamic framework (theoretical model) and system identification (experimental model) will be merged in a numerical engine formulated as a search algorithm for model updating, also known as Adaptive Simulated Annealing (ASA) process. This iterative engine is based on a set of function minimizations computed by a metric called Modal Assurance Criterion (MAC). In summary, the Thesis is composed of four major parts: (1) development of an analytical aerodynamic framework that predicts interacted wind-structure stochastic loads on wind turbine components; (2) development of a novel tapered-swept-curved Spinning Finite Element (SFE) that includes damped-gyroscopic effects and axial-flexural-torsional coupling; (3) a novel data-driven structural health monitoring (SHM) algorithm via stochastic subspace identification methods; and (4) a numerical search (optimization) engine based on ASA and MAC capable of updating the SFE aerodynamic model.

Chapter 1. Introduction

1.1 Presentation

As of today, wind energy is one of the most growing sectors of the nation's renewable energy portfolio; the same tendency has been observed for the past decade and is expected to grow in the same rate for the upcoming years. To this effect, safety and economical concerns have emerged as a result of the newly design tendencies for massive scale wind turbine structures exhibiting high slenderness ratios and complex shapes, typically located in remote areas (i.e. offshore wind farms). Safety operation requires not only information regarding structural dynamic conditions under the aerodynamic action, but also a deep understanding of the environmental factors and mechanics in which these multi-body rotating structures operate. To this end, Horizontal Axis Wind Turbines (HAWT) have emerged as the alternative technology of choice in the wind energy industry because of their high energy production rate, manufacturing convenience, mechanistic design, and strong adaptability under different climates and geographies. Given the stochastic cyclo-stationary patterns of the wind loading acting on such devices, a probabilistic framework is appropriate to characterize the risk of failure, under both resistance and serviceability conditions, at any given time. Furthermore, sources of uncertainty such as material imperfections, variations in the rotating speed, aeroelastic damping, tower shadow effects, damped-gyroscopic phenomenon, turbulence, wake effects (vortex-shedding), flutter, buffeting, among others, have pleaded for the use of a more sophisticated mathematical framework that could properly handle all these sources of indetermination. Given the attainable modeling complexity that arises as a result of these characterizations, a need for a data-driven experimental validation methodology turns out to be imperative in order to validate the model. This solution is expected suitable for representing both cyclo- and non-cyclo- stationary structural aerodynamics. The ultimate goal: a holistic methodology capable of updating wind demand loads and geometrical/inertial properties of HAWTs using: (1) Structural Health Monitoring (SHM) techniques, (2) advanced Spinning Finite Elements (SFE), and (3) advanced search algorithms for model updating and characterization.

From this perspective, the so-called System Identification (SI) techniques offer a spectrum of well established numerical methods appropriated for stationary and deterministic numerical methods, capable of carrying out successful eigenrealizations of traditional time-invariant dynamic systems. In this line of thinking, it is proposed a modified data-driven SI technique based on the so-called Subspace Realization Theory, now adapted for stochastic non-stationary and time-varying aerodynamic systems. In order to achieve higher accuracy and predictability of real physical loads, stresses and strains, as well as gaining portability, computational stability and ease of use, the present investigation explores the detailed characterization of turbine loading and response envelopes for critical failure modes of both tower and rotor blade subsystems. To carry out this ordeal, it is proposed a novel spinning finite element (SFE) method general enough to encompass tapered-swept cross-section variations of blade elements by means of Lagrangian, Saint-Venant and Euler theories, all combined in a matrix-driven mathematical framework devoted for damped-gyroscopic effects. To this matter, a special consideration is taxed to the so-called yaw (Coriolis) effects, typically considered as the critical phenomena that dictate the time-varying structural aerodynamics of the integrated tower-nacelle-blades body system. Interaction of tower and rotor blades is also addressed as a multi-body problem and is studied in the along-wind spectral analysis. In this respect, the point of intersection between the aerodynamic framework (theoretical model) and the experimental identification (numerical model) may be a numerical search algorithm for model updating known as Adaptive Simulated Annealing (ASA) method. This iterative engine is based on a set of function minimizations that are dictated by correspondent rules also known as Modal Assurance Criterion (MAC), such a way it can be computed the internal energy of the system in order to convey the state of the physical structural system with the proposed model. Figure 1.1(a) illustrates the global scope of the Thesis project including tower and rotor blades substructures interaction, whereas Figure 1.1(b) schematizes the identified scope covering the analysis and thorough characterization of wind turbine blades subsystems in particular. Thus, next section will lead to the definition of the methodological and meta-methodological frameworks required for the development of the Thesis project.

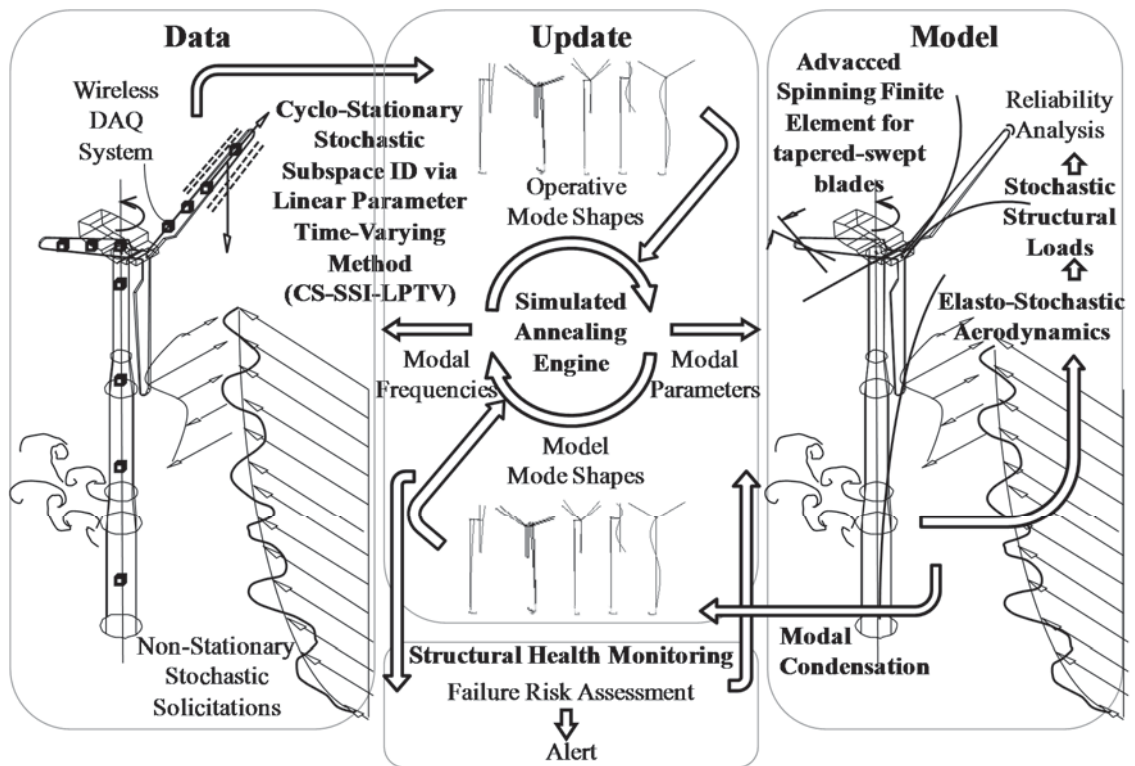


Figure 1.1(a) Global scope of the Thesis Project including tower and rotor blades interaction.

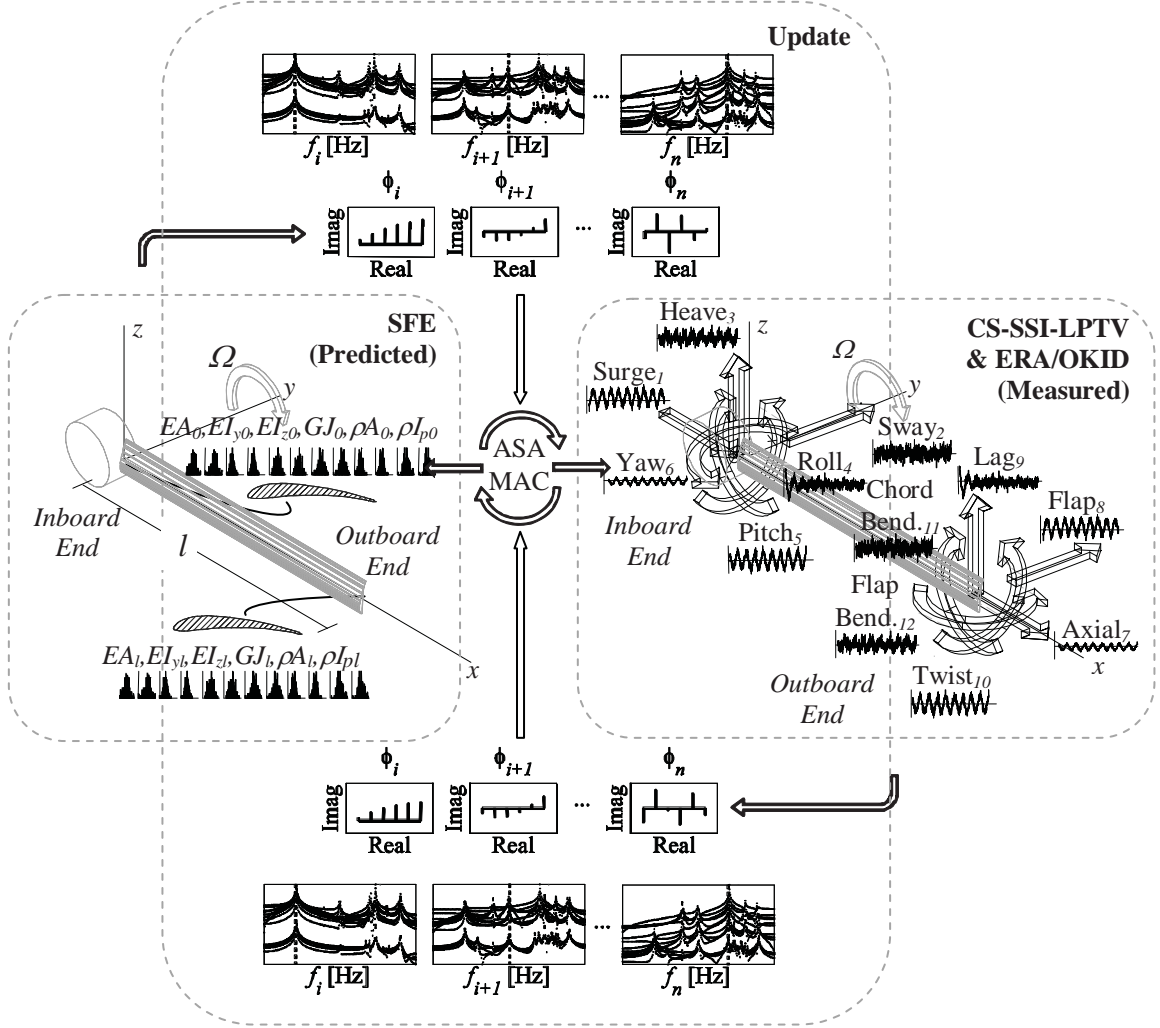


Figure 1.1(b). Scope of the Thesis Project for rotor blades.

1.2 Methodological Framework

Table 1.2 summarizes the completion of the methodological framework of the Thesis by compartmentalizing key answers to resolve the what, which, and how of each of the objectives to convey. Some of the systemic methodologies employed for this project can be understood as a set of ordered techniques and plays that offer new procedures and protocols to provide significant advantages in the characterization, modeling and prediction of the structural dynamics of HAWT blade systems. The Thesis manuscript is dissected into four major cores:

Introductory Framework. Here is justified the relevance of the theme chosen by the exposure of the objectives on the one hand, and the explanation of the structure of the thesis manuscript on the other.

Capitulation. Splitting into five major blocks that will cover all the steps to carry out the analysis, assumptions, derivations, mathematical theory, examples, reach, stretch and accomplishments of the Thesis.

Conclusions. Finds the relevant factors identified throughout the investigation. Books key points and draw comments about the possible implications that will have the new methodologies proposed at the present time and in the future. Examines conceptual limitations, strengths, weaknesses, and opportunities of research that could be taken up, recaptured and leveraged in a later time.

References. Lists references series, educational material, magazines, articles, websites, and others employed in this investigation.

Figure 1.3 schematizes the conceptual pyramid that comprises the branches of study and main fields involved in the present investigation. It is a five-level hierarchy that visualizes the extensional domains of every key concept in the research field of study. Here, axiomatic categories become definable by the induced common intensions of their immediate subcategories. This pyramid is known as extensional-diaeretic where undefined categories at the base are set to be independent fields of study. The various modes of induction explain the eventuality of concurrency theories about the same instances, merging from bottom to top. The following section provides a brief overview of the discussion topics that will be made along the five core chapters that make up the body of the thesis document.

Table 1.2. Methodological framework of the Thesis project.

Objective (What?)	Methodology (Which?)	Technique (How?)	Tools (With What?)	Goals (For What?)
• A general aerodynamic framework for rotor-blades	<ul style="list-style-type: none"> • Statistical analysis • Structural reliability • Assumed Modes method • Structural aerodynamics • Fragility curves • Along-wind response • Total fluctuating response: background and resonant contributions 	<ul style="list-style-type: none"> • Monte-Carlo simulation • Random processes • Spectral density and autocovariance, cross-covariance, co-spectrum, quadrature spectrum and coherence • Peak-values probability distribution of normal random signal • Distributed-stationary random-loads spectral analysis 	<ul style="list-style-type: none"> • <u>MatLab scripts**</u> • <u>Object-oriented programming**</u> • Matrix methods recipes • Numerical methods recipes 	<ul style="list-style-type: none"> • <u>A generalized spectral stochastic-aerodynamic method, in the frequency domain, that computes demand envelopes for tapered-swept-curved blades**</u>
• A general aerodynamic framework for wind towers	<ul style="list-style-type: none"> • Statistical analysis • Structural reliability • Assumed Modes method • Fragility curves • Across-wind response • Along-wind response 	<ul style="list-style-type: none"> • Monte-Carlo simulation • Random processes • Spectral density and autocovariance, cross-covariance, co-spectrum, quadrature spectrum and coherence • Peak-values probability distribution of normal random signal • Rumman's procedure • Vickery and coworkers procedures 	<ul style="list-style-type: none"> • <u>MatLab scripts**</u> • <u>Object-oriented programming**</u> • Matrix methods recipes • Numerical methods recipes 	<ul style="list-style-type: none"> • <u>A generalized spectral stochastic-aerodynamic method, in the frequency domain, that computes demand envelopes for tapered wind towers**</u>
• A sophisticated FEM that characterizes spinning structures with complex geometry	<ul style="list-style-type: none"> • Meirovitch method for gyroscopic linear systems • Arnold method • Schur decomposition • Hamiltonian systems • Newtonian algorithm • Lagrangian equations • Super-convergent shape functions 	<ul style="list-style-type: none"> • Assumed modes method • B-orthogonal and Schur decomposition numerical techniques • <u>Complex-number eigen-frequencies analysis**</u> • <u>Matrix-driven equations of motion for skew-symmetric systems with n-degree tapered-swept profiles**</u> • Hermitian shape functions 	<ul style="list-style-type: none"> • <u>MatLab scripts**</u> • ANSYS FE model • Numerical method recipes • Mathematica solver 	<ul style="list-style-type: none"> • <u>A spinning FEM for n-degree tapered-swept profiles with damped-gyroscopic, centrifugal effects and axial-flexural-torsional coupling**</u>
• A suitable SI algorithm for embedded programming dedicated to HAWT's Structural Health Monitoring	<ul style="list-style-type: none"> • Stationary and non-stationary methods • Non-parametric frequency-domain methodologies • Parametric time-domain methodologies • Eigensystem Realization Algorithm (ERA) • Observer/Kalman filter identification • Frequency-domain state-space SI 	<ul style="list-style-type: none"> • <u>Correlation methods, spectral estimation and ergodicity, predictor models, identifiability, convergence and consistency, informativity vs. Persistence of excitation**</u> • <u>Recursive methods**</u> • Kalman filter, observer/controller identification • <u>Cyclo-stationary indirect identification techniques**</u> 	<ul style="list-style-type: none"> • MatLab** • <u>Object-oriented programming**</u> • Matrix methods recipes • Numerical methods recipes • <u>Pseudocode**</u> • C, C++ compilers 	<ul style="list-style-type: none"> • <u>A stochastic subspace non-stationary time-varying SI algorithm for embedded programming**</u>
• A Simulated Annealing (SA) engine for HAWTs model updating using SHM	<ul style="list-style-type: none"> • SA method • Annealing schedule techniques • MAC method • Acceptance probabilities • Cooling schedule • Barrier avoidance 	<ul style="list-style-type: none"> • <u>Iterative algorithms implementation**</u> • <u>Optimization algorithms implementation**</u> • Search algorithms • <u>Linear and object-oriented programming**</u> 	<ul style="list-style-type: none"> • MatLab scripts • C, C++ compilers • <u>Visual Studio scripts**</u> • Numerical methods recipes • <u>Pseudocode**</u> 	<ul style="list-style-type: none"> • <u>A MAC based Simulated Annealing (SA) engine via stochastic subspace ID-LPTV method**</u>

** Original contributions to the research field.

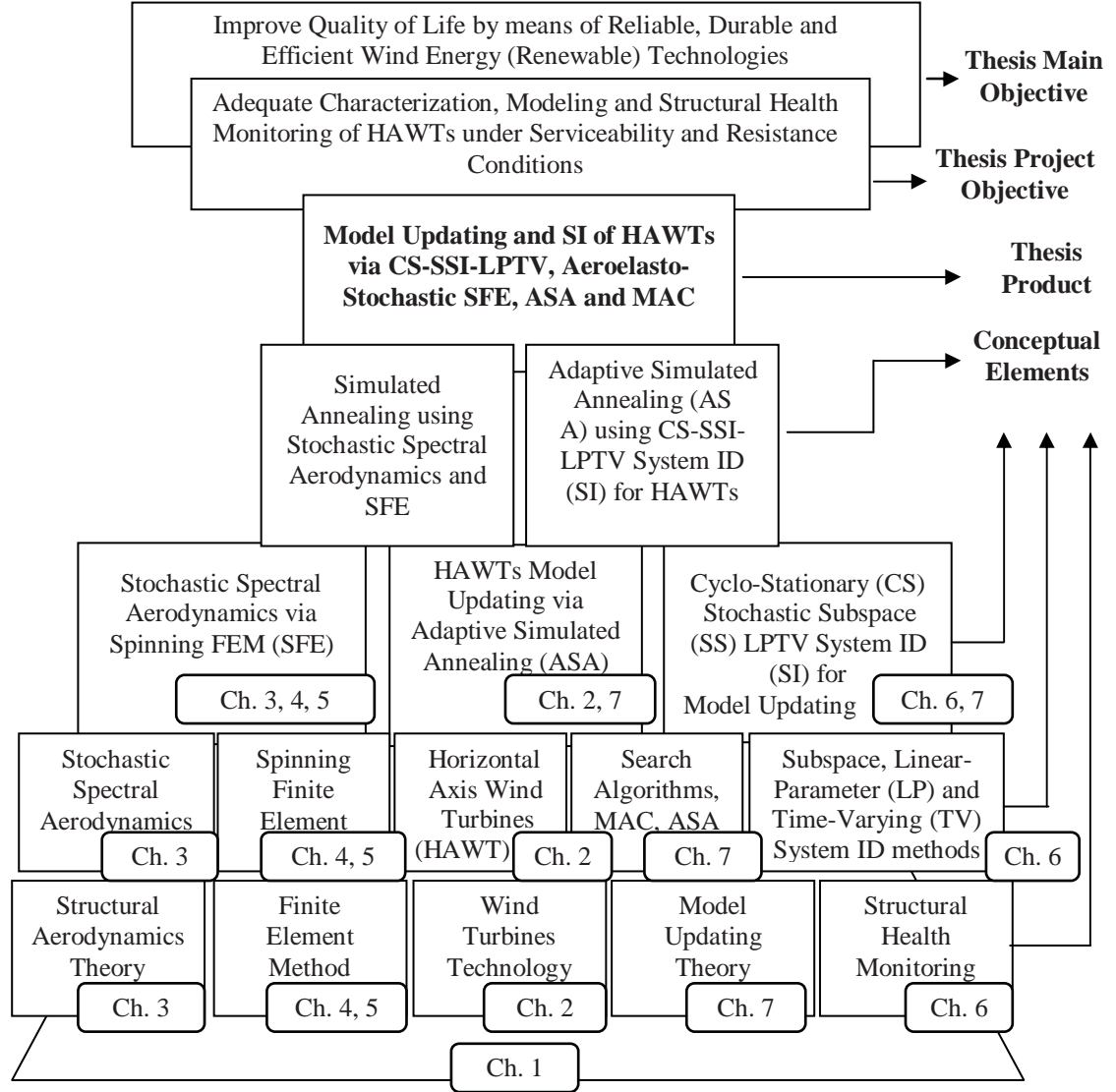


Figure 1.2. Conceptual pyramid of the Thesis project.

1.3 Organization

The document is composed of seven chapters that comprehensively review each of the steps to consolidate a numerical engine for model updating and system identification of horizontal-axis wind turbines (HAWTs) via cyclo-stationary stochastic subspace identification with linear-parameter time-varying methods (CS-SSI-LPTV), aeroelasto-stochastic analysis, damped-gyroscopic tapered-swept spinning finite elements (SFE) with axial-torsional-flexural coupling, and finally, adaptive simulated annealing (ASA) and modal assurance criterion (MAC). As delineated in Figure 1.3, Chapter 1 summarizes the

introduction of the Thesis project, justification, general and particular objectives and general overview of the Thesis document. Chapter 2 discusses generalities of the related theory and set the pillar elements that comprises it, as well as the wingspan, extent and limitations of the implicated mathematical framework. Chapter 3 deals with issues regarding tower and rotor blades sub-structuring, characterization principles and along-wind aeroelastic phenomena. This chapter tailors awareness of the practical – holistic – range of action and incidence of the eventual model updating engine, as seen as the final product of the Thesis endeavor. Chapter 4 discusses in detail the incursion of the concept of Spinning Finite Element, validated via stochastic spectral aeroelasticity. Chapter 5 deepens into a more sophisticated SFE theory, now embodying tapered-swept variations with damped-gyroscopic phenomenon and axial-flexural-torsional coupling, all combined. Chapter 6 proposes a novel cyclo-stationary stochastic subspace identification method using linear parameter time-varying methods, and establishes a practical algorithm with general rules for System Identification of rotating machinery. Chapter 7 encompasses the inclusion of a model updating method based on the principles of Boltzmann machines and optimization engines. It is based solely on experimental information and independent of the primary analytical model adopted for the rotor-blade system. Finally, Chapter 8 draws general conclusions and future work (see Figure 1.4).

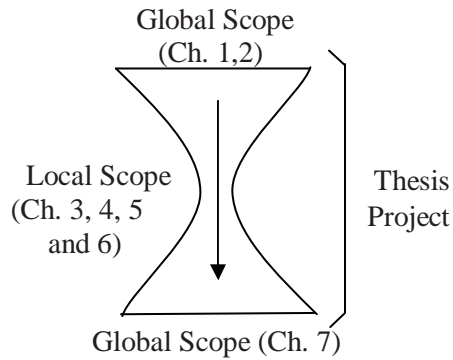


Figure 1.3. Incumbency of the Thesis project.

1.4 Justification

Wind energy technologies are an area of research which is maturing very fast in recent years due to the concern of long term global energy consumption. With advances in wind turbine technology accompanied by government decisions that are in favor of ‘green’ or renewable power, wind turbines are an increasingly viable economic choice to conventional fossil-fuelled power generation [Yang 2008]. Significant advances are being made in the areas of aerodynamic blade design, electrical generator design and variable speed transmissions. As a result, nonlinear effects are on demand at each subcomponent and, consequently, model dynamics and system model increase in order. Even with the existence of advance techniques for system identification and control, it is prohibitive to use complex and higher order models when simpler are available. Current research lines are focused on the modeling and identification of dynamic systems for controller design, state estimation, diagnosis and fault detection [Bonger 1991][Novak 1994]. Numerical models of existing wind turbine structures can be used for various reasons: (a) evaluating innovative designs, (b) evaluating the effect of loads in a current structure, (c) evaluating the effect of modifications on a current structure, (d) others. However, differences between the behavior of numerical models and real structures are common, particularly when dealing with spinning machinery. For example, Zhang [Zhang *et al.* 2001] reported 17.4% of difference in natural frequencies between the FEM and measurements of the Kap Shui Mun Bridge. Brownjohn and others [Brownjohn *et al.* 2003] had differences in up to 23% in the dynamic characteristics of the Pioneer Bridge in Western Singapur. Model Updating is typically performed to adjust a numeric model, so that it mimics reality. At the same time, System Identification (SI) techniques are used as a black box models that focus on input/output relationships, no physical significance on the model parameters are observed and is mainly oriented to applications for structural control and structural health monitoring. Originally developed by Juang and Pappa [Juang and Pappa 1985] the method was primitively created to obtain a realization of the system, generally effective for lightly damped structures where natural frequencies and mode shapes can be extracted from the realization. This method was particularly developed for impulse response functions [Juang 1994]. In counterpart, model updating is employed to use finite

element models (or models with physical meaning), focusing on the physical characteristics of the model, and used for retrofit studies/damage identification and others. To this aim, the goal of model updating deterministic methods, that include least squares and genetic algorithms, is to minimize an objective function that measures differences between the numerical model and the experimental structure system [Chiu-Tsong 1998]. On the other hand, probabilistic methods are built based on the Bayes inference [Mares *et al.* 2006] which intends to determine the probability of the structural parameters given a set of measurements and a particular model, where prior knowledge is available. Bayes's inference is used to estimate a PDF of a specific event based on observations where the posterior probability distribution contains all the information available after the data have been acquired. Bayes's inference involves a pre-known burden of information that forces codependency between the trace of the initial model and the experimental data, whereas deterministic models clearly delimitate independence between the measured data and the projected model. Model updating ponders the degree of uncertainty from assumptions in the data, identification process and model type, and it causes the calibrated model to become uncertain as well. In this respect, there are two sources of uncertainty: (1) aleatory, that corresponds to sole variability of the signals and, (b) epistemic, that is caused by uncertainty of an unknown process or mechanism present in the dynamic system. Epistemic uncertainty can be reduced by providing clues to improve prior PDFs by means of identifying areas of high probability, and then recalculate posterior PDFs as a result. In its core, the goal of model updating is to identify several possible solutions but physically different according to a pool of choices. Modeling to Generate Alternatives (MGA) methodologies [Chang *et al.* 1982] use the power of computers to reduce the number of possible solutions to a manageable size, leaving the final decision of selecting the most appropriate model to the analyst. In contrast, search algorithms such as Adaptive Simulated Annealing and Genetic Algorithms are both probabilistic based methods capable of finding a global minimum amongst many local minima for a given objective function [Levin and Lieven 1997]. For this aim, dynamic Finite Elements (FE) models are widely used to predict the geometrical/inertial properties of structures. However, results attained to FE modeling

often differ from the experimental data obtained from a vibration test. As mentioned before, this divergence may be caused by a number of reasons going from errors in the experimental data to model inaccuracies. In general, experimental measurements are assumed to be a better source of representation of how the structure actually behaves rather than the initial prediction of the FE model. Different updating methods have been tested based on whether they work in frequency or modal domains [Imregun and Visser 1991]. Some methods adjust the mass and stiffness matrices directly (direct methods) and some others make parametric modifications to the model (indirect methods). Indirect methods are proven to be the most physically meaningful, and typically make use of an objective function that quantifies the difference between the experimental and analytical data [Friswell and Mottershead 1995]. Attempts are then to find a set of parameters that minimizes the objective function by converting the model updating in a constrained optimization problem. Previous model updating work using simulated annealing has concentrated in small problems with very few parametric values with successful results [Nelder and Mead 1965]. However, although the simulated annealing is, in general, the most suitable method it tends to fail for large number of parametric values. It also produces disappointing results when is applied to cumbersome problems, generating wild oscillations about the correct parameter marks. This is due mainly to the accuracy and sophistication of the finite element model and represents a fundamental problem that many model updating algorithms encounter. Consequently, the development of a refined spinning finite element model and an adequate data-driven cyclo-stationary system identification method that could both appraise, to a good approximation, the structural dynamics of complex rotating machinery is mandatory to ensure accurate predictions of the model updating process of Horizontal Axis Wind Turbines (HAWTs). That said, it is now a convenient time to define the objectives of the Thesis project below.

1.5 Objectives

1.5.1 General Objective

Analyze, design, construct and implement a numerical model updating engine and a system identification scheme for Horizontal Axis Wind Turbines (HAWTs), based on the

development of advanced Spinning Finite Elements (SFE) and a cyclo-stationary stochastic subspace identification method with linear time-varying parameters (CS-SSI-LPTV), validated via aeroelasto-stochastic spectral analysis and random vibrations.

1.5.2 Particular Objectives

- Entrust a generalized spectral stochasto-aerodynamic method, in the frequency domain, that computes demand envelopes for tapered wind towers, as part of a preliminary work of study.
- Develop a general, yet specialized 3D Spinning Finite Element for n -degree tapered-swept-curved profiles with damped-gyroscopic and axial-flexural-torsional coupling, including centrifugal effects.
- Propose a stable and reliable numerical solution for the open mathematical problem of damped-gyroscopic and non-classical damping complex-conjugate eigenrealization.
- Entrust a generalized rotationally-sampled spectral stochasto-aerodynamic method, in the frequency domain, that computes demand envelopes for tapered-swept-curved blades, as part of the validation scheme of the theory developed.
- Develop a novel stochastic subspace, linear-parameter, time-varying system identification algorithm, applied for both stationary and non-stationary signals, in order to obtain representative eigen-properties of the rotor-blade system, based solely on experimental data.
- Develop a portable, yet efficient iterative numerical machine for model updating based on Adaptive Simulated Annealing (AS) and complex-conjugate Modal Assurance Criterion (MAC).

Once the objectives and scope of the Thesis project has been established, it is proper time now to enter formally into the discussion of the state of the art of the current status and research advances in model updating, finite element and system identification techniques for HAWTs. Chapter 2 will serve as a preamble to relieve compelling and relevant issues to further advance in the core Chapters of the Thesis.

Chapter 2. Literature Review

2.1 Preliminary Study

The analysis of wind turbines is well-established with several texts on the subject [Gasch and Tvele 2002][Burton *et al.* 2001][Manwell *et al.* 2002]. Full-aero-elastic dynamic modeling is used nowadays to design and analyze wind turbines [Molenaar 2003]. Modeling of wind turbine dynamics implies a complicated interaction of rotor/wake aerodynamics, atmospheric boundary-layer fluid dynamics, and structural dynamics [Hansen 2008][Buhl 2005][Det Norske Veritas 2001]. Outer contour of blade profiles are designed to be strong and stiff enough, made with materials like glass-fiber-reinforced polymers (GRPs), carbon fiber reinforced plastics (CFRPs), steel, aluminum, and wood [Griffin and Ashwill 2003]. Other studies [Hodges *et al.* 1996][Hodges 2003] model non-isotropic properties, including non-linear behavior critical for stability analysis. Two analytical frameworks are the backbone of actual wind turbine codes [Manwell *et al.* 2002]: (1) Momentum theory and (2) Blade element theory. Computational fluid dynamics on wind turbines has been performed by many authors, of which work done by Sorenson and Michelsen [Sorenson and Michelsen 2002], and Duque [Duque *et al.* 1999] are notable. Internal box like beam structure can be modeled with simple beam theory to compute stresses and deflection of the blade [Timoshenko and Gere 1972][Craig 1981]. Wilson, Lissaman and others [Wilson and Lissaman 1974][Wilson *et al.* 1976][Wilson *et al.* 1999] developed in the past computerized codes for this theory. National Renewable Energy Laboratory (NREL) has developed tools for wind turbine analysis [Hansen 2005][Anon 2005][Jonkman 2005][Laino 2005a][Wilson *et al.* 1996]. Simulated wind environments can be built with TurbSim (full-field three dimensional turbulence) [Kelley and Jonkman 2006] and IECWind (gust type simulations) [Laino 2005b] applications. Interfacing tools to assist MSC/AdamsTM platform have been developed for multi-body dynamic simulation [Wright and Elliott 1992]. Aero-elastic studies characterizing lumped-parameter representation of rotor blades with tower coupling have been performed to compute aerodynamic forces solving dynamic equations of motion [Murtagh *et al.* 2005][Jen *et al.* 1995][Murtagh *et al.* 2004][Chen *et al.* 2009]. Other efforts include Lobitz [Lobitz *et al.* 1996] that

incorporates flap/twist coupling into the rotor with off-axis fiber orientation, reducing aerodynamic loading by twisting the tip toward the feather [Liebst 1986][Zuteck 2002][Larwood and Zuteck 2006]. Baumgart [Baumgart 2002] developed a mathematical model for blades consisting of small rotations to account for blade lateral deflections, rotation of the chord, warping, extension and tilt. Lateral vibration is preferred as the dominant dynamic mode, including centrifugally tension effects with tapered beam profiles [Banerjee 2000][Naguleswaran 1994][Chung and Yoo 2002]. Bend-twist coupling effects have been barely studied in the past. Fedorov [Fedorov *et al.* 2010] employed finite element models that performed well for flap-wise bending, but poorly in torsion. More studies are required in this matter. Efforts have been made to characterize sweep-blade profiles instead of straight shapes with constant cross-section [*ibid.* Liebst 1986][*ibid.* Larwood and Zuteck 2006], with the aim to delay the onset of drag divergence. Jonkman and others [Jonkman 2003][Buhl 2005] have been working in models that generate mode shapes for straight, rotating, pitched and tapered blades. Derivation of equations of motion can be performed using Kane's method [Kane and Levinson 1985]. Blade response can be computed through a linear summation of lower bending modes (superposition) [Rao 2005][*ibid.* Jonkman 2003]. Limitations on the FAST three bending modes: first flap, first edge, and second flap coupled through built-in twist, can be achieved using sophisticated spinning finite elements developed in the past [Leung and Fung 1988][*ibid.* Chung and Yoo 2002], or by Modes program [*ibid.* Buhl 2005]. Analysis in the elastic and post-elastic regimes have been carried out by Das [Das *et al.* 2009] solving the governing equations by variational principles [Swaminathan and Rao 1977]. The present project will intend to expand Leung general mathematical model for tapered-sweep beams, then couple wind tower by substructure synthesis approach [Scheble and Strizzolo 1998]. The blade system will be treated as a multi-body dynamic entity allowing the free vibration characteristics using discrete parameter approach [Murtagh *et al.* 2004]. Free vibration properties of blade will include flap, edge and torsion modes [Yokoyama 1988][Khulief and Bazoune 1992][Lee and Kuo 1993]. Blades will be excited by a rotationally sampled wind turbulence spectra using mode acceleration method [Madsen 1984]. This latter will account for six major DOF's

originated from the translational (surge, sway, and heave) and rotational (roll, pitch, and yaw) motions of the support platform of the blades (inboard end) with respect to the inertia frame [Yoo and Shin 1998]. The remaining six DOF's at the outboard (radial out) end will produce the commented flap and edge modes in two orthogonal directions, as well as torsion action [Bazoune *et al.* 1999]. Analysis will include post-elastic dynamic behavior of rotating tapered blades [Pohit *et al.* 1999]. This mathematical framework will use standard linear finite elements of tapered properties with six degrees of freedom (DOF) at each node [Kosmatka 1986], with special attention in bend-twist effects and characterization [Dimitrov 2008]. As a result, the resultant base shear will be imparted into the top of the tower. To do that, a rotationally sampled stationary wind loading will be applied [*ibid.* Murtagh *et al.* 2005] on the structure, including composite materials [Bechly and Clausen 1995][*ibid.* Pohit *et al.* 1999], in order to characterize in full the combined fluid-structure interaction and aerodynamics [Ahlstrom 2005][Hansen *et al.* 2006][Oye 1996]. At the same time, tower fluid-structure interaction will incorporate along-wind effects (distributed stationary random loads) [Simiu and Scanlan 1996] and across-wind effects (Rumman's method and Vickery's method) [Rumman 1970][Vickery and Clark 1972]. The tower/nacelle will be then coupled with rotating blades by combining their equations of motion and solving compatibility conditions in the frequency domain at the top. Finally, probabilistic fragility analysis is derived on the tower/nacelle/blade system to determine the reliability of the system as a whole [Velazquez and Swartz 2011]. All forms of wind turbines are designed to extract power from a moving air stream. The blades have an airfoil cross-section and extract wind by a lift force caused by a pressure difference between blade sides. For maximum efficiency, the blades often incorporate twist and taper. LM Glasfiber in Denmark is the largest independent blade manufacturer with a product range that consists of standard blades in lengths from 13.4 to 61.5 meters for turbines from 250 kW to 5 MW.

Wood has a natural composite structure of low density, good strength and fatigue resistance. The drawbacks are the sensitivity to moisture and the processing costs. There are, however, techniques that overcome these problems. Most larger wind turbine blades

are made out of Glass Fiber Reinforced Plastics (GRP), e.g. glass fibre reinforced polyester or epoxy. According to [*ibid.* Kosmatka 1986], is a weight advantage of up to 30 % achieved when using epoxy compared to the cheaper polyester resin. Carbon Fiber Reinforced Plastic (CFRP) blades are used in some applications. It has been assumed that this material system was strictly for aerospace applications and too expensive for wind turbines. However, by using effective production techniques, some manufacturers produce cost effective wind turbine blades. The advantage with carbon fiber is the high specific strength. Since the beginning of the modern wind power era, the preferred designs for wind turbines have been with either two or three blades. Many early prototypes have two blades, e.g. Nasudden (Sweden), but the three-bladed concept has been the most frequently used during recent years. Basic aerodynamic principles determine that there is an optimal installed blade area for a given rotational speed. A turbine for wind farm applications generally has a tip speed of 60–70 m/s. With these tip speeds a three-bladed rotor is 2–3% more efficient than a two-bladed rotor. It is even possible to use a single bladed rotor if a counterbalance is mounted. The efficiency loss is about 6% compared with the two-bladed rotor construction. Although fewer blades give lower blade costs, there are penalties. The single-bladed rotor requires a counterbalance and is therefore not lighter than a two-bladed design. The two-bladed rotor must accept very high cyclic loading if a rigid hub system is employed. However, the loading can be reduced by using a teetered hub [*ibid.* Chen *et al.* 2009]. The teeter system allows the rotor blades to rock as a pair to make it possible for the rotor to tilt backwards and forwards a few degrees away from the main plane during rotation. The three-bladed rotor is dynamically simpler and a little more aerodynamically efficient. Three-bladed designs have also been preferred since they are considered to look more aesthetic in the landscape. In counterpart, the two-bladed rotors offer potential reductions in both fabrication and maintenance costs [*ibid.* Anon. 2005].

Generally speaking, most wind turbine blades where adaptations of airfoils developed for aircraft have not been optimized for wind turbine uses. In recent years, developments of improved airfoil sections for wind turbines have been an ongoing effort. The

prevailing tendency among blade manufacturers is to use NACA 63 sections as a main layout with several modifications in order to improve performance for special applications and wind field conditions. To gain efficiency, the blade is both tapered and twisted. The taper, twist and airfoil characteristic should all be combined in order to give the best possible energy capture for the rotor speed and site conditions. A number of technologies known from aircraft industry are being adapted for use in wind turbine applications. A problem when dealing with wind turbine blades is that even at relatively low wind speed, the innermost part of some blades begin to stall. Normally stall-controlled wind turbine blades are supposed to control power at 14–15 m/s when the outer part of the blade begins to stall. If the innermost part of the blade is stalling, say at around 8–9 m/s, the efficiency will decline. In practice, however, it is not possible to design a thick profile that does not suffer from premature stall, but vortex generators may improve the dynamic behavior. The company LM Glasfiber claims that improvements of up to 4–6% of the annual production can be obtained using vortex generators.

From a modeling viewpoint, properties as weight, mass and stiffness distributions are of great importance for the dynamic behavior of the wind turbine. The spar is the most important structural part for structural analysis and acts like a main beam. The blade can therefore be treated as a beam structure and classical beam element theory can be used. A correct description of the coupling between the blades and the hub, especially in pitch regulated turbines, where the stiffness of the pitching system will influence the overall dynamics and control system, is also of major importance. The most common types of towers are the lattice and tubular types constructed from steel or concrete. For small wind turbines, the tower may be supported by guy wires. Tower substructures can be designed in two ways, soft or stiff. A stiff tower has a natural frequency which lies above the blade passing frequency. Soft towers are lighter and cheaper but have to withstand more movement and will suffer higher stress levels. Most modern wind turbines have conical towers made of steel. The tubular shape allows access from inside the tower to climb up to the nacelle, which is preferred in bad weather conditions. The towers are manufactured in sections of 20–30 meters with flanges at both ends. Sections are then transported to the

foundation for the final assembly. The tower is coupled to both the foundation and the bedplate. Depending on the type of foundation, the coupling can be treated as elastic or not. In a soft connection the foundation will affect the dynamics of the super-structure and must be treated as a part of the wind turbine. A yaw mechanism is used in the connection between tower and bedplate. The connection will affect the dynamics of the complete wind turbine. From a modeling standpoint of view, the tower's mass and stiffness distribution must be known in advance. A correct matching of the tower's eigenfrequencies to the other components is crucial for a successful wind turbine design. The hub connects the turbine blades to the main shaft. Blades are bolted to the hub flanges by threaded bushes that are glued into the blade root. The flange bolt holes can be elongated, in order to enable the blade tip angle to be adjusted. The hub type can be either rigid or teetered, and complicated hub shapes make it convenient to use cast iron. The hub must also be highly resistant to metal fatigue, which is difficult to achieve in a welded construction. The nacelle contains the key components of the wind turbine, including the gearbox and the electrical generator. The bedplate is generally made of steel and, in modern wind turbines, service personnel may enter the nacelle from the tower substructure. There are four different drive train configurations: (a) long shaft with separate bearings; gearbox supported by the shaft with torque restraints; (b) rear bearing integrated in the gearbox, gearbox mounted on the bedplate; (c) rotor bearings completely integrated in the gearbox; (d) rotor bearings on a stationary hollow axle; power transmission by a torque shaft. In principle, it is necessary to align the rotor axis with the wind in order to extract as much energy from the wind as possible. Most horizontal axis wind turbines use forced yawing. An electrical or hydraulic system is used to align the machine with the wind. The yaw drive reacts on signals from, e.g. a wind vane on top of the nacelle. Almost all manufacturers of upwind machines brake the yaw mechanism whenever it is not used. In slender wind turbines however, like the Swedish Nordic 1000, the yaw mechanism is of importance for the dynamic behavior of the system. The yaw mechanism must fulfill the requirements of a soft and damped connection between the nacelle and the tower. A hydraulic system is used to give the right characteristics whether the mechanism is yawing or not. This specific system is not furnished with any

mechanical brakes. In some wind situations, the turbine will rotate in the same direction for a long time. The cables that transport current from the generator down the tower will then be twisted. By using a device that counts the number of twists the cable can be twisted back.

Most aeroelastic codes used in practical design work assume small blade deflections and application of wind loads on the undeflected structure. However, with the design of lighter and more flexible wind turbines, these assumptions may not longer be valid. The present investigation has had the objective to improve current modeling possibilities by including effects of geometrical nonlinearities primarily introduced by large blade deflections. Comparable FE commercial software employed for wind turbines modeling includes popular platforms such as ABAQUS, ANSYS and SOLVIA.

FE modeling of wind turbines requires special considerations due to both large displacements and rotations. The use of constraint equations that defines one or several DOFs as function of one or several other DOFs is one of the key features for wind turbine modeling within the FEM theory. As for example, in ANSYS user-defined constraint equations are given through user subroutines. This constraint can be linear or nonlinear, i.e., it can be dependent on time or previous deformations. Constraint equations are typically used to specify the connection between rotor shaft and bedplate. Another example is modeling of a possible pitch system. Constraints could then be set to, e.g. tie all DOFs except the rotational DOF in the pitching point (pitch bearing). All constraint equations must be specified on the deformed geometry to allow for large displacement analysis. The constrained nodes must therefore be specified in local coordinate systems. The general method in ANSYS is to implement user-defined local coordinate systems through subroutines. This allows transformation of degrees of freedom at an individual node from global directions to a local direction through an orthogonal transformation. The transformations could then be updated by the user in each increment. User-defined systems are also used to specify springs and dashpots in local systems. Simulating wind turbine response in time, using FEM, is computationally intensive. Time simulations are

therefore generally made using beam elements to reduce DOFs. There are several blade element types available. The most common types are based on the Euler-Bernoulli or the Timoshenko beam theories, [*ibid.* Chen *et al.* 2009]. The Timoshenko element, class C0, takes into account shear deformation and rotary inertia but uses low order shape functions, which basically mean discontinuous first derivatives. The Euler-Bernoulli element belongs to the class C1 which means continuous first derivatives between blade elements. The Euler-Bernoulli theory does not include rotary inertia in the formulation of the kinetic energy, as it is implicitly contained in the translation terms. The only rotary inertia neglected is the rotational inertia of the cross-section which always remains low for a slender beam. Modeling wind turbine blades with shell elements is computationally prohibitive and ofte is used the so-called Domain Decomposition (DDM) method. This disassembly technique makes it possible to split up the problem into domains and solve the system in parallel. The Euler-Bernoulli beam was chosen because of the slender nature of the structure, which reproduces shear effects as small. Following Chapter 3 is disputed some basics of aeroelastic analysis performed for both combined HAWT tower and rotor blade subsystems, where discussion on resistance and optimization issues takes place and serves to pave the foundations of the development of a comprehensive Spinning Finite Element.

Chapter 3. Aeroelastic Analysis

The study of efficiency and safety for wind turbine structures under variable operating conditions is increasingly important for wind turbine design. Optimum aerodynamic performance of a wind turbine demands that serviceability effects and ultimate strength loads remain under safety design limits. From the perspective of wind turbine efficiency, variations in wind speed causes bluffing effects and vortex shedding that lead to vibration intensities in the longitudinal and transversal direction that can negatively impact aerodynamic performance of the turbine. From the perspective of wind turbine safety, variations in loading may lead to transient internal loads that threaten the safety of the structure. Inertial effects and asynchronous delays on rotational-force transmission may generate similar hazards. Monitoring and controlling displacement limits and load demands at critical tower locations can improve the efficiency of wind power generation, not to mention the structural performance of the turbine from both a strength and serviceability point of view. In this study, a probabilistic monitoring approach is developed to measure the response of the combined tower/nacelle/blade system to stochastic loading, estimate peak demand, and compare that demand to building code-derived estimates of structural resistance. Risk assessment is performed for the effects of along and across-wind forces in a framework of quantitative risk analysis with the goal of developing a near real-time estimate of structural risk that may be used to monitor safety and serviceability of the structure as well as regulate the aggressiveness of the controller that commands the blade angle of attack. To accomplish this goal, a numerical simulation of the aerodynamic performance of a wind turbine (including blades, the nacelle and the tower) is analyzed to study the interaction between the structural system and incoming flow. A model based on distributed-stationary random wind load profile for the combined along-wind and across-wind responses is implemented in Matlab to simulate full aero-elastic dynamic analysis to simulate tower with nacelle, hub, rotor and tower substructures. Self-weight, rotational, and axial effects of the blades, as well as lateral resistance of substructure elements are incorporated in the finite element model, including vortex-shedding effects on the wake zone. Reliability on the numerical solution

is inspected on the tower structure by comparing the numerical solution with established experimental-analytical procedures.

3.1 Introduction

To address global sustainable energy concerns, considerable interest has been paid to renewable energy sources including wind. Wind turbines structures have become a popular platform for generation of energy due to concerns regarding potential shortages of traditional fossil-fuel sources along with social and economic pressures caused by their use. These concerns have forced the energy production industry to start looking to alternative solutions and approaches for energy generation [Lanzafame and Messina 2007]. To sustain the movement toward adoption of sustainable wind energy, increased safety and efficiency of wind turbine structures are critical issues to be addressed. Wind-induced response analyses and aerodynamic performance play important roles in both safety and efficiency of wind turbines [Larsen 2006][Stathopoulos and Baniotopoulos 2007]. Aero-elastic loading of such structures commonly provoke highly complex effects, such as the coupled across-wind/along-wind response, aero-elastic torsion, lock-in, and buffeting phenomenon that can be difficult to characterize and reproduce in analytical fashion [Dyrbye and Hansen 1997][Shinozuka 1998][IEC 61400-12 1998].

Wind loads are often highly unpredictable and may differ radically from those measured and assumed during the design phase. At the same time, structurally pressures to control costs force designers to adopt efficient tower designs and eliminate overly-conservative designs [Simiu *et al.* 1981]. As a consequence, slender structures that are more wind-sensitive from the point of view of serviceability, strength, and safety are becoming more common and may present more risk than older structural systems. An accurate loading evaluation algorithm that can estimate in-situ loading from dynamic response data can aid in design and performance assessment of these designs. However, such an algorithm requires a precise mathematical model of the turbine components and substructures. Slenderness ratios of wind turbines promote significant flexibility of the characterized dynamic multi-body system [Clough and Penzien 1975]. Operating

characteristics of wind turbines are determined by the dynamic performance of the tower and blades combined. In modeling such systems, Lavassas [Lavassas and Nikplaidis 2003] has used 5028 four-node shell elements to analyze the dynamic response of a tower; output results has proved analytical that is closely related to mesh density, while Naguleswaran [Naguleswaran 1994] has developed simplified rotating blades to cantilever beam to characterize dynamic phenomenon. Murtagh *et al.* [Murtagh *et al.* 2005] have modeled the wind turbine blades as a multi-degree-of-freedom entities, formulating the model as a centrifugal stiffening due to rotation and blade gravity loadings. Chen *et al.* [Chen *et al.* 2009] employed a dynamic FEM to calculate the wind-induced response of the blades and tower combined. These effects need to be accounted for if the loading is to be estimated from the dynamic response of the tower.

In addition, the aero-elastic loadings and coupling effects alter the structural resistance and serviceability of the system through non-linear effects including vortex shedding, buffeting and flutter [Tamara *et al.* 1996]. Monitoring of these wind-induced vibration effects using Monte Carlo stochastic simulations can help to characterize in a better way loading demands and resistance behavior, particularly the evaluation of the randomly treated equivalent static forces known as gust factors, employed for determining the maximum response [Chen and Jang 2008]. Semi-experimental methods may be used for across-wind to calculate estimates of the peak response (deflection, base shear and overturning moment) in that direction, particularly focused on the contribution of high frequency content [Vickery and Basu 1983]. Several procedures for estimating this across-wind response phenomenon exist in the literature today. The most widely used are the procedures developed by Rumman [Rumman 1970] and Vickery [Vickery and Clark 1972] employed to characterize the design of steel stacks and tall slender structures. Special considerations for taper-cross sections are derived properly in a mathematical framework for stationary-distributed random wind loads in the along-wind orientation, as well as analytical generation of gradient variations in the tower external diameter, with the aim of a realistic representation of the tower profile. Both procedures will be used to construct a model for across-wind peak-load estimation, and will be coupled with the

along-wind dynamic analysis to account for torsion effects in the coherence functions. Both fluid-structure interaction effects are estimated by using a self-developed Matlab® computer program that evaluates the structural response to time-dependent forces (distributed stationary random-wind loads). The program is conditioned to reproduce random realizations of the lift and drag coefficients, wind velocity, tower surface roughness, surface roughness length, Strouhal number, structural damping, aeroelastic damping, among others. A simplified reliability performance assessment is computed to generate probability distribution curves.

In summary, the present paper is focused on the classical problem of dynamic along-wind response from one side [Simiu and Lozier 1979], Rumman's and Vickery's procedure for across-wind response, to the other [*ibid.* Rumman 1970] [*ibid.* Vickery and Clark 1972]. A comparison of the stochastic loading estimated from across-wind and along-wind coupled effects from one side, and nacelle/rotor/blade/tower substructure coupled systems from the other, to the stochastic resistance of the structure. This outline may establish the basis of the development of a real-time estimate of the probability of exceedance of the defined design serviceability failure state of the structure. Such information can provide valuable insights for future maintenance and operation of turbines.

3.2 Vibration Equations

The dynamic equations of motion that represent MDOF's system for aero-elastic wind induced vibration are [Chopra 2007]:

$$\mathbf{M}_n \ddot{\mathbf{u}}_n(t) + \mathbf{C}_n \dot{\mathbf{u}}_n(t) + \mathbf{K}_n \mathbf{u}_n(t) = \mathbf{Q}_n(t) \quad (3.1)$$

where \mathbf{C}_n is the normalized damping matrix, $\mathbf{u}_n(t)$, $\dot{\mathbf{u}}_n(t)$ and $\ddot{\mathbf{u}}_n(t)$ are the time-dependent displacement, velocity and acceleration vectors respectively, in modal coordinates, and $\mathbf{Q}_n(t)$ is the normalized time varying wind load vector applied to the

tower height (dismissing, at present, the wind load effects on the blades). When a bluff body is immersed within wind flow, the body will experience pressures distributed over its surface. These pressures result in a net force on the body, the along-wind component due to drag force and the across-wind component due to lift force [Simiu and Scanlan 1996]. Bearing these loadings in mind, Equation (3.1) may be re-expressed as a linear system where the generalized coordinates $\xi(t)$ satisfy the uncoupled equations of the form:

$$\ddot{\xi}_i(t) + 2\varsigma_i\omega_i\dot{\xi}_i(t) + \omega_i^2\xi_i(t) = \frac{Q_i(t)}{M_i} \quad i = 1, 2, \dots, n \quad (3.2)$$

where ς_i , ω_i , and M_i are the damping ratio, modal frequency (rad/sec), and generalized mass in the i th mode, for n total number of modes. Here [Meirovitch 1986]:

$$f_i = \sqrt{\frac{k_i}{m_i}}; \quad \omega_i = 2\pi f_i; \quad \varsigma_i = \frac{c_i}{2\sqrt{k_i m_i}} \quad (3.3)$$

$$M_i = \int_0^h x_i^2(z) m(z) dz$$

(3.4)

where $x_i(z)$ is the i th normal mode of the wind turbine, and $m(z)$ the distributed unit mass along the pole, h is the total height of the wind tower, f_i is the i th natural frequency (Hz) and z is the actual vertical position of the studied tower cross-section. The generalized force may be expressed as:

$$Q_i(t) = \int_{i=0}^h p(z, t) x_i(z) dz \quad (3.5)$$

The function $p(z, t)$ is the pressure distribution applied on in the along-wind direction as a function of both height and time. By definition:

$$p(z, t) = F(t)\delta(z - z_1) \quad (3.6)$$

where $\delta(z - z_1)$ is the unit impulse function acting at time $t = 0$, defined by:

$$\left. \begin{aligned} \delta(t) &= 0 \quad \text{for } t \neq 0 \\ \lim_{\Delta t \rightarrow 0} \int_0^{\Delta t} \delta(t) dt &= 1 \end{aligned} \right\} \quad (3.7)$$

and $F(t)$ is a concentrated force acting at a point of coordinate z_1 , therefore:

$$\begin{aligned} Q_i(t) &= \lim_{\Delta_z \rightarrow 0} \int_{z_1}^{z_1 + \Delta_z} p(z, t) x_i(z) dz \\ Q_i(z_1, t) &= x_i(z_1) F(t) \end{aligned} \quad (3.8)$$

The response to a harmonic load of the form $F(t) = F_0 \cos(2\pi ft)$ acting on the structure at coordinate z_1 , where f is the frequency in Hz, will be:

$$Q_i(z_1, t) = F_0 x_i(z_1) \cos(2\pi ft) \quad (3.9)$$

It can be verified that [Hurty and Rubinstein 1996]:

$$\xi_i(z_1, f, t) = F_0 x_i(z_1) H_i(f) \cos[2\pi ft - \phi_i(f)] \quad (3.10)$$

Here, the admittance function is defined as:

$$H_i(f) = \frac{1}{4\pi^2 f_i^2 M_i \{ [1 - (f/f_i)^2]^2 + 4\zeta_i^2 (f/f_i)^2 \}^{1/2}} \quad (3.11)$$

and the phase is given by:

$$\phi_i(f) = \tan^{-1} \frac{2\zeta_i(f/f_i)}{1-(f/f_i)^2} \quad (3.12)$$

Hence, the response of the wind tower at location z , accounting for all modal contributions, becomes:

$$x(z, z_1, f, t) = F_0 \sum_{i=1}^n x_i(z) x_i(z_1) H_i(f) \cos[2\pi f t - \phi_i(f)] \quad (3.13)$$

3.3 Along-Wind Response

Expanding Equation (3.9) for the case of a distributed stationary random load where an infinite number of forces $F_i(t)$ of wind in nature act on the exposed surface A of the structure. The spectral density function of the along-wind fluctuating deflection for mode i is given by [Newland 1996]:

$$S_{ix}(z, f) = \frac{\rho^2}{16\pi^2} \frac{x_i^2(z) C_D^2}{f_i^4 M_i^2 \{ [1 - (f/f_i)^2]^2 + 4\zeta_i^2 (f/f_i)^2 \}} + \int_0^h \int_0^h \int_0^{D(z)} \int_0^{D(x)} x_i(z_1) x_i(z_2) U(z_1) U(z_2) S_u^{1/2}(z_1) S_u^{1/2}(z_2) \cdot \text{Coh}(y_1, y_2, z_1, z_2, f) dy_2 dy_1 dz_2 dz_1 \quad (3.14)$$

where ρ is the air density, C_D is the drag coefficient, $U(z)$ is the wind velocity profile acting on the longitudinal direction. Recommended values of C_D for towers with tapered cross-sections are presented in [Basu 1983] $S_u(z)$ is the design spectral density of the longitudinal velocity fluctuations:

$$S_u(z, f) = \frac{200u_*^2 f_{mn}}{f(1 + 50f_{mn})^{5/3}} \quad (3.15)$$

where u_* is the shear velocity

$$u_* = \frac{U(z)}{2.5 \ln(z/z_0)} \quad (3.16)$$

and f_{mn} is the Monin or similarity coordinate given by:

$$f_{mn} = \frac{f z}{U(z)} \quad (3.17)$$

The term z_0 represents the surface roughness length for a given surface type. The across-wind cross-correlation coefficient is defined as:

$$\text{Coh}(y_1, y_2, z_1, z_2, f) = \exp \left\{ - \frac{f [C_z^2 (z_1 - z_2)^2 + C_y^2 (y_1 - y_2)^2]^{1/2}}{\frac{1}{2} [U(z_1) + U(z_2)]} \right\} \quad (3.18)$$

The pairs (y_1, z_1) and (y_2, z_2) are coordinates of points M_1 and M_2 where the line M_1, M_2 is assumed to be perpendicular to the direction of the mean wind. $C_y = 16$ and $C_z = 10$ are the exponential decay coefficients for horizontal and vertical separation, respectively. The mean square value of the fluctuating along-wind deflection for mode i is declared as:

$$\sigma_{ix}^2(z) = \int_0^\infty S_{ix}(z, f) df \quad (3.19)$$

Finally, the largest modal peak expected value occurring in the time interval T is:

$$x_{ipk}(z) = K_{ix}(z) \sigma_{ix}(z) \quad (3.20)$$

where,

$$K_{ix}(z) = [2 \ln(\nu_{ix}(z)T)]^{1/2} + \frac{0.557}{[2 \ln(\nu_{ix}(z)T)]^{1/2}} \quad (3.21)$$

is the largest-peak-displacement factor that accounts for the probability that in the time interval T there will be no peaks equal or larger to $x_{pk}(z)$. At the same time:

$$\nu_{ix}(z) = \left[\frac{\int_0^\infty f^2 S_{ix}(z, f) df}{\int_0^\infty S_{ix}(z, f) df} \right]^{1/2} \quad (3.22)$$

is the number-of-peaks per unit of time factor. Shear and moment functions $S_{ixpk}(z)$ and $M_{ixpk}(z)$, for the along-wind direction, may finally be obtained as follows:

$$S_{ixpk}(z) = (2\pi f_i)^2 \int_z^h m(z_1) x_{ipk}(z_1) dz_1 \quad (3.23)$$

$$M_{ixpk}(z) = (2\pi f_i)^2 \int_z^h m(z_1) x_{ipk}(z_1) (z_1 - z) dz_1 \quad (3.24)$$

3.4 Across-Wind Response (Vickery's Method)

The assessment of the across-wind response requires the computation of the height z_{ei} for each mode at which the longitudinal wind velocity $U(z=z_{ei})$ generates vortex shedding with frequencies equal to the natural frequencies of the structure; scenario that is in compliance with $U(z_{ei}) = U_i(z_{ei}) = U_{icr}(z_{ei})$ for modal shape i . It has to be met the following conditions:

$$U_i(z_{ei}) = \frac{1}{S_{tr}} f_i D(z_{ei}); \quad \Re e_i = 67,000 U_i(z_{ei}) D(z_{ei}) \quad (3.25)$$

where S_{tr} is the Strouhal number [Basu and Vickery 1983], $D(z_{ei})$ is the taper-diameter function evaluated at height z_{ei} , and $\Re e_i$ is the Reynolds number necessary to generate critical conditions in mode i . The root-mean-square (RMS) of the modal generalized coordinate for tapered-like wind towers is given by [*ibid.* Vickery and Clark 1972];

$$\overline{\xi_i^2}^{1/2}(z_{ei}) = \overline{\xi_{nom,i}^2}^{1/2}(z_{ei}) \left(\frac{\varsigma_i}{\varsigma_i + \varsigma_{ai}(z_{ei})} \right)^{1/2} \quad (3.26)$$

Here, the nominal RMS of the generalized coordinate is integrated as follows:

$$\overline{\xi_{nom,i}^2}^{1/2}(z_{ei}) \approx \frac{0.016 \overline{C_{Li}^2}^{1/2} L_i^{1/2} \rho D^4(z_{ei}) x_i(z_{ei})}{\varsigma_i^{1/2} S_{tr}^2 M_i \beta^{1/2}(z_{ei})} \quad (3.27)$$

where,

$$\beta(z_{ei}) \approx \frac{0.1 D(z_{ei})}{z_{ei}} - \left. \frac{dD(z)}{dz} \right|_{z=z_{ei}} \quad (3.28)$$

and $\overline{C_{Li}^2}^{1/2}$ stands for the modal RMS of the lift coefficient. Recommended values of this quantity are given in [Simiu *et al.* 1981]. Modal span-wise correlation parameter $L_i = 2.5$ if $\Re e_i < 2 \times 10^5$ and $L_i = 1.0$ if $\Re e_i \geq 2 \times 10^5$. Modal aero-elastic damping $\varsigma_{ai}(z_{ei})$ is given by:

$$\varsigma_{ai}(z_{ei}) = -\frac{\rho D_0^2}{M_i} \int_0^h K_{a0} \left(\frac{U_i(z; z_{ei})}{U_{icr}(z_{ei})} \right) \left[\frac{D(z)}{D_0} \right]^2 x_i^2(z) dz \quad (3.29)$$

Here, D_0 is the outside diameter at the base, and $K_{a0}(z, z_{ei})$ is an aero-elastic damping parameter that depends on the wind velocity profile [Braam and van Dam 1998]. By definition:

$$\frac{U(z; z_{ei})}{U_{cr}(z_{ei})} = \frac{\ln(z/z_0)}{\ln(z_{ei}/z_0)} \quad (3.30)$$

In practice, is required to calculate first hand a critical function $F_{cr}(z_{ei})$ to obtain z_{ei} properly, as follows:

$$F_i(z_{ei}) = \frac{D^4(z_{ei})x_i(z_{ei})}{\{\beta(z_{ei})[\zeta_i + \zeta_{ai}(z_{ei})]\}^{1/2}} \quad (3.31)$$

The fluctuating mean square value of deflection in the across-wind direction y , for mode i , is computed as:

$$\sigma_{yi}(z) = \xi_i^{2/2}(z_{ei})x_i(z) \quad (3.32)$$

The expected modal deflection becomes:

$$y_{ipk}(z) = g_{yi}\sigma_{yi}(z) \quad (3.33)$$

The term g_{yi} is the gust factor and is treated similar as Equation (3.21) but evaluated for one hour duration:

$$g_{yi} = [2\ln(3600f_i)]^{1/2} + \frac{0.557}{[2\ln(3600f_i)]^{1/2}} \quad (3.34)$$

Finally, shear and moment function $S_{iypk}(z)$ and $M_{iypk}(z)$, for the across-wind direction, are computed similar to Equation (3.23) and Equation (3.24):

$$S_{iypk}(z) = (2\pi f_i)^2 \int_z^h m(z_1) y_{ipk}(z_1) dz_1 \quad (3.35)$$

$$M_{iypk}(z) = (2\pi f_i)^2 \int_z^h m(z_1) y_{ipk}(z_1) (z_1 - z) dz_1 \quad (3.36)$$

3.5 Across-Wind Response (Rumman's Method)

A detailed presentation for Rumman's method previously applied by the authors may be found in [Berman and Fi 1971]. This is an intuitive method that appears to characterize properly the wind induced vibrations phenomenon in practice. Peak deflection on the across-wind direction is defined as:

$$y_{ipk}(z) = \frac{\rho}{16\pi^2} \frac{C_L}{\zeta_i} \frac{D^2(h)}{M_i S_{tr}^2} x_i(z) \int_0^h D(z) x_i(z) dz \quad (3.37)$$

Restrictions in the variation of the aero-elastic ratio C_L/ζ_i must be defined in advance [ibid. Rumman 1970]. Peak shear and moments are obtained directly from Equation (3.35) and Equation (3.36).

$$S_{ipk}(z=0) = \omega_i^2 \int_0^h m(z) Y_i(z) dz \quad (3.38)$$

$$M_{ipk}(z=0) = \omega_i^2 \int_0^h m(z) Y_i(z) (z) dz \quad (3.39)$$

3.6 Finite Element Prototype

The steel tower under scrutiny schematized in Figure 3.1 is a model prototype of a Nordtank 65KW re-engineered from the so called 55KW model group [Prowell and Veletzios 2010]. A finite model of the actual specimen Nordtank 65kW was implemented

in ANSYS 11.0 and calibrated for base excitation implementing synthesized ground-motion accelerations. The original modeled turbine was manufactured in Denmark; properties for the model come from a previous experimental study [*ibid.* Prowell and Veletzos 2010]. The Nordtank 65 consists of nacelle, bedplate, rotor and 3 blades fixed pitch made of fiberglass reinforced polyester ($E_b = 79.497 \times 10^9 \text{ N/m}^2$); swept area up to 214 m^2 . The blades are assumed to be prismatic cantilever beams 7.9 m rotor diameter. A rectangular hollow cross-section that is connected to the hub is modeled with flexural motion in the transverse direction only, as studied in [*ibid.* Murtagh *et al.* 2005]. Two axial phenomena are embedded in the model: (1) centrifugal stiffening and (2) blade gravity or self-weight effects. Experimental calibration of natural frequencies and mode shapes were made using Assumed Modes Method (AMM) and Modal Assurance Criterion (MAC). Experimental data was processed to infer natural frequencies, mode shapes, and equivalent viscous damping. Eigensystem Realization Analysis (ERA) was adopted to endure the dynamic characteristics of the wind tower. A clear illustration of those mentioned methodologies as adopted for turbine load monitoring is presented with more detail in [Velazquez and Swartz 2011]. Wind tower is made of hot dip-galvanized tubular steel with 0.2in thickness ($E_t = 199.947 \times 10^9 \text{ N/m}^2$). The damping ratio of the structure for the dominant mode is estimated to be 1%. Rotational hinges at two key point locations were constructed in the model. Geometric properties of the wind turbine are enlisted in Table 3.1.

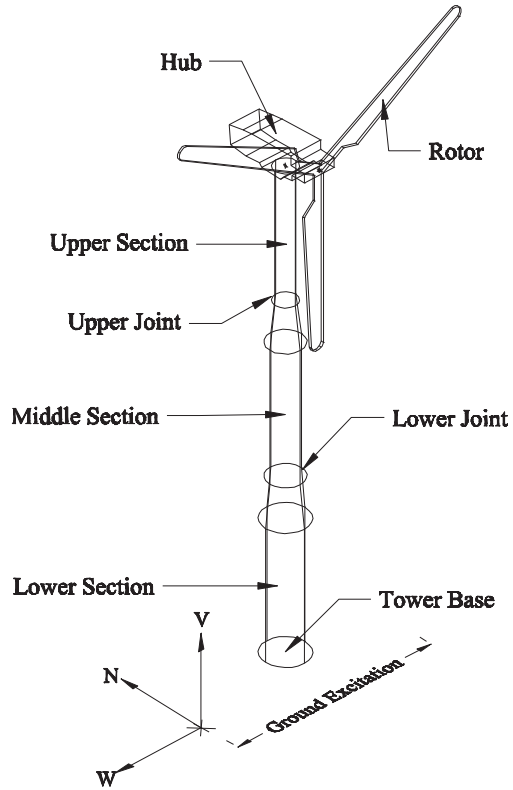


Figure 3.1. Wind turbine specimen for modal-base response.

Table 3.1. Geometry Properties of the 65kW Wind Turbine [8]

Geometry	Value
Rotor diameter	628 in
Tower height	864 in
Tower wall thickness	0.20 in
Rotor hub height	888 in
Tower mass	14 kips
Nacelle mass	5 kips
Rotor mass (with hub)	4 kips

3.7 Results

Shedding forces are of central importance for slender tapered structures. Figure 3.2 plots normalized modal shapes experimentally calibrated and verified using MAC, ERA and AMM methods as determined in [ibid. Velazquez and Swartz 2011][Zimmerman *et al.* 2008]. Table 3.2 depicts the means and variances assigned to random quantities to formulate random realizations. Similarly, Figure 3.3 depicts the distributions of the random variables used in the Monte Carlo simulation to illustrate the major sources of uncertainty. Figure 3.4 depicts the relation between S_{tr} and $\Re e$, illustrating the relationship between the structural frequency f_i and the vortex shedding frequency f acting in the wake. Figure 3.5 depicts the critical function $F(z_{ei})$ for an example set of three modes with critical probability of across-wind harmonic motion. The absolute maximum is taken as the reference point to establish z_{ei} , and subsequently, the establishment of the aero-dynamic damping $\varsigma_{ai}(z_{ei})$. Figure 3.6(a) frames the variation of the along-wind cross-correlation coefficient in the frequency domain. This parameter is pointing out that, in this direction, the correlation increases for low across-wind loading and tend to decrease when across-wind response gain more relevance.

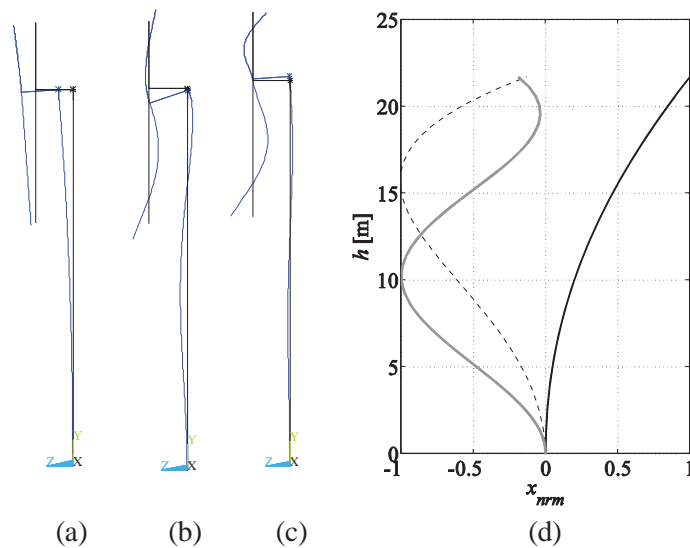


Figure 3.2. First three normalized modes of vibration experimentally calibrated using AMM technique corresponding to (a) 1.7Hz, (b) 13.5Hz, (c) 33.5Hz, (d) all three modes.

Similarly, Figure 3.6(b) depicts three wind-velocity profiles required to match critical harmonic conditions in the wake for the three dominant modes. It is seen that $U_2(z_{ei}) = 100$ m/s is necessary for the second mode to vibrate in critical scenario, whereas only $U_1(z_{ei}) = 10$ m/s needed to generate significant vibrations in the fundamental mode. Figure 3.7 shows four control factors for the number-of-peaks occurrences that may be regarded as rare events and are treated as Poisson type. It may also be viewed as the probability that, given the interval T (Equation (3.21)), the ratio $K_x(z)$ of the largest peak to the RMS of the deflection is less than a pre-established threshold. Similar quantities are thrown out for the calculation of peak accelerations. These parameters are in close relation with the horizontal and vertical correlation acquainted in the $\text{Coh}(y_1, y_2, z_1, z_2, f)$ term. Coupling and torsion effects are accounted for using this process.

Calculations of the auto-correlation and cross-correlation terms are presented next. Figure 3.8 depicts the normalized spectral density function for the lift coefficient and the spectral density function of the induced lateral force $L_1(z, t)$, assuming that the structure is at rest under the action of the vortex shedding in the wake. As it is shown, the primary (natural) frequency dominates the dynamic prediction overall. Figure 3.9 plots the overall power spectral density functions of fluctuating deflection for three heights along the tower showing spectral energy distribution changes with height. Coupled effect between across-wind and along-wind is contemplated throughout the mechanical admittance function. The wind-induced vibrations have a greater impact in the third upper section for lower frequencies, and lower impact at lower altitudes. High-frequency content demands more stress in this latter area. The second and third modes are more closely related in lower sections of the tower. Figure 3.10 sketches the variation performance of gust factor. The factor for the first mode is in good agreement with that in the literature [*ibid.* Chien and Jang 2008]. For detailed derivations of the actual mode shape, the gust factor error increase in 1% or 3%, making the effect of moderate deviations from a straight line mode shape (higher frequencies) insignificant. Figure 3.11 summarizes the benchmark of the

two methodologies in the across-wind direction compared with the resultant along-wind solicitations.

Table 3.2. Some of the along-wind and across-wind statistic parameters for random realizations of wind induced vibrations.

Property	μ	σ
$U(z_{ei})=U_{1cr}(z_{ei})$	10 m/s	3.7 m/s
$\bar{C}_L^{2^{1/2}}$	0.295	0.04
C_D	0.8	0.11
ς_i	0.006	0.0011
z_0 (low grass, steppe)	2.5 cm	0.0039 cm
k/D	5.05×10^{-4}	1.3×10^{-4}
S_{tr}	0.32	0.037

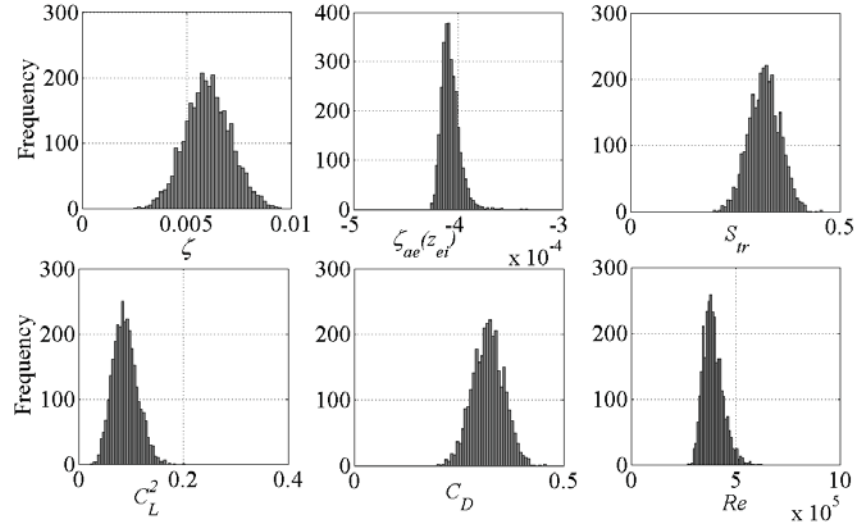


Figure 3.3(a). First set of random variable distributed used in the Monte Carlo simulation (3000 realizations).

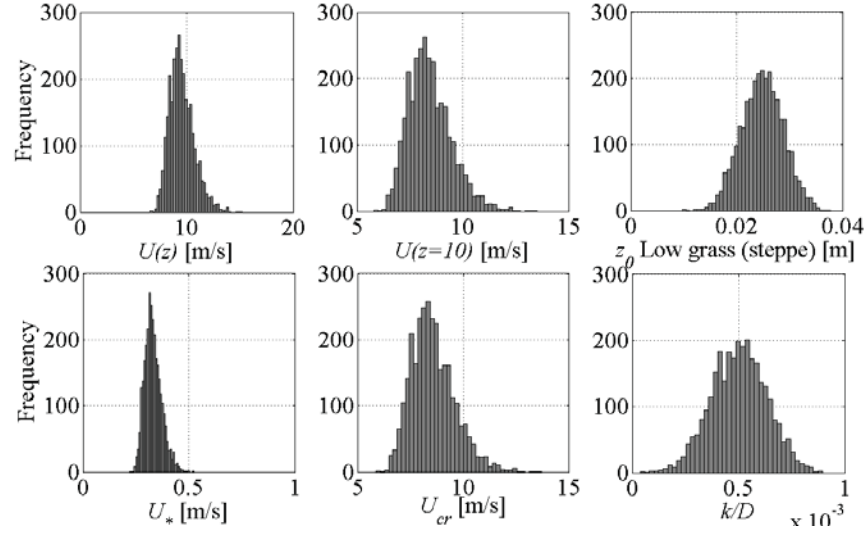


Figure 3.3(b). Second set of random variable distributed used in the Monte Carlo simulation (3000 realizations).

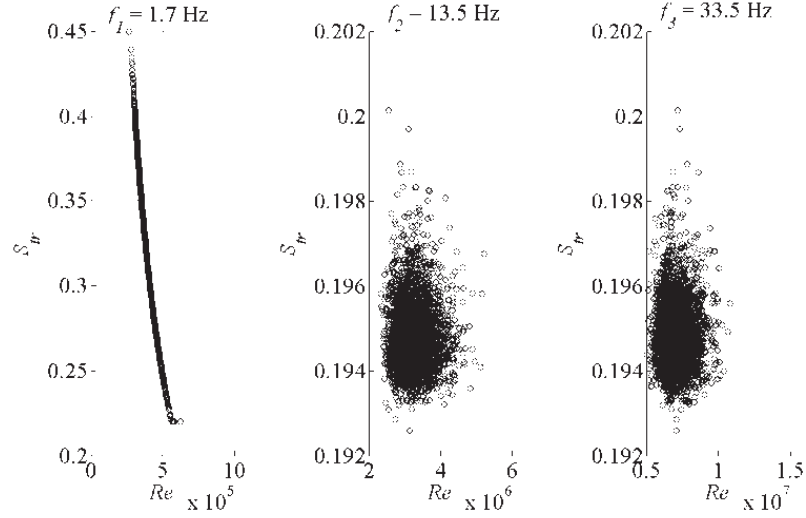


Figure 3.4. Reynolds number vs Strouhal number (3000 realizations) combining across-wind and along-wind analysis, for the first three modes of vibration.

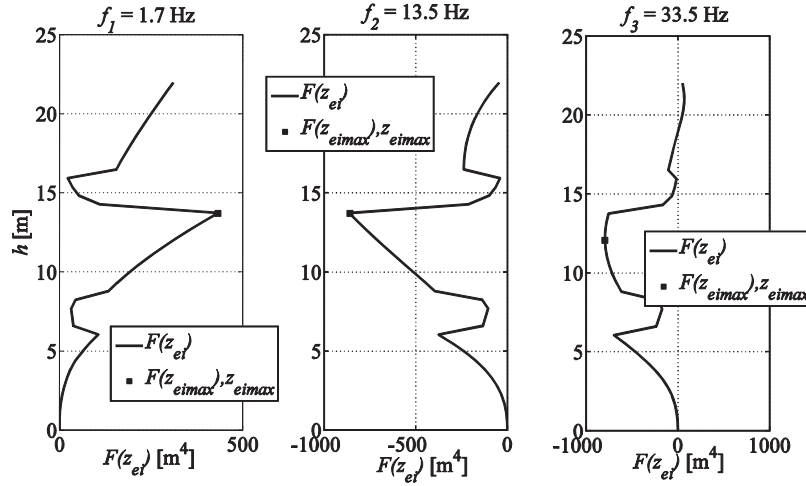


Figure 3.5(a). Critical height construction in the across-wind direction for the first three dominant modes. Formulation of $F(z)$ for the induction of the critical height z_{ei} .

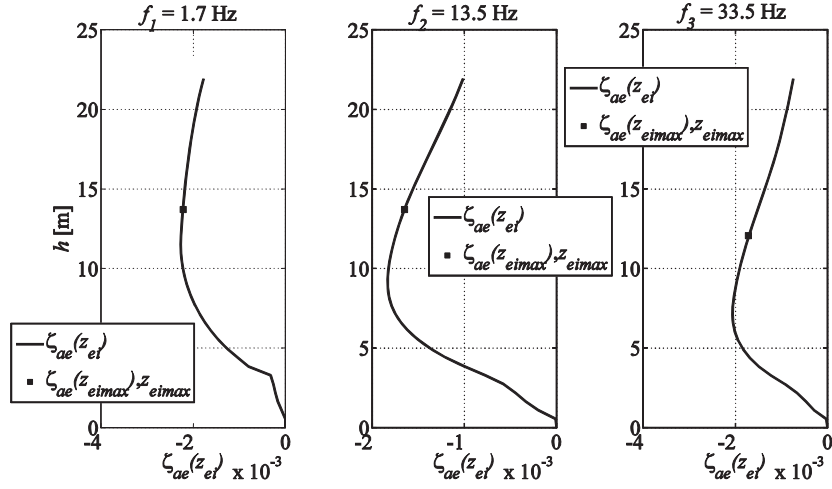


Figure 3.5(b). Critical height construction in the across-wind direction for the first three dominant modes. Formulation of the aero-elastic damping at critical elevation z_{ei} .

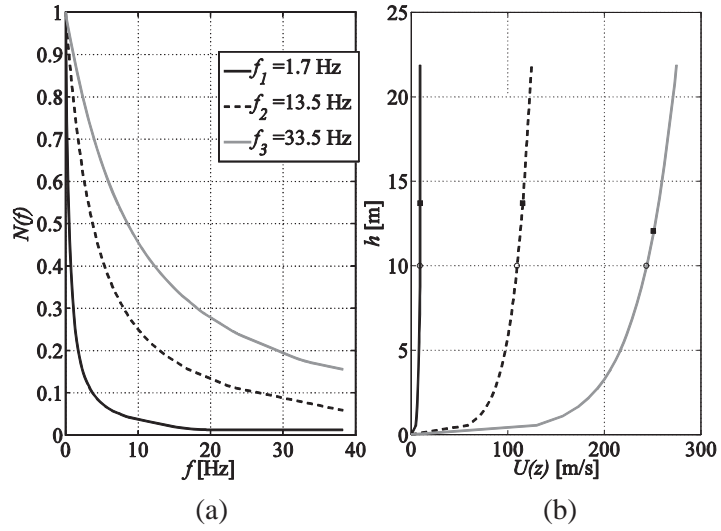


Figure 3.6. Along-wind cross-correlation coefficient (narrow-band cross-correlation) for three dominant frequencies; (b) Wind profile (boundary layer) evaluated at critical elevation z_{ei} .

Describes wind velocities $U_{icr}(z)$ and $U_{10}(z_{ei})$.

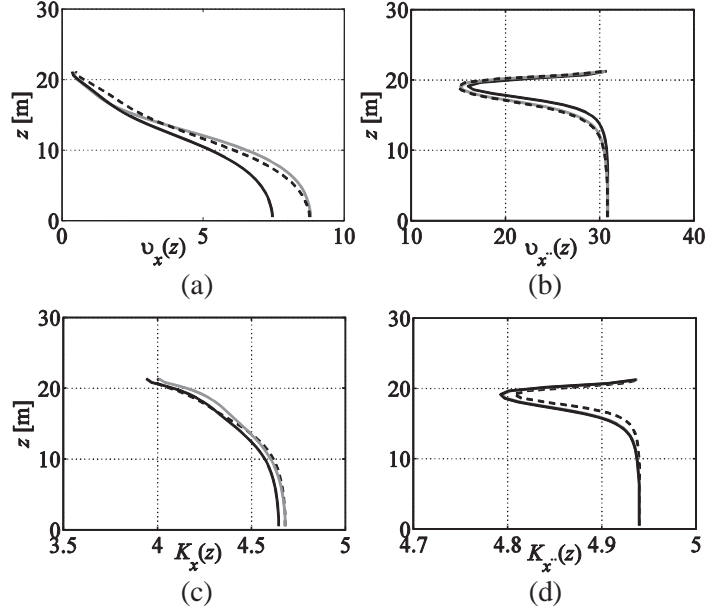


Figure 3.7. Profiles for number-of-peaks controls: (a) largest-peak-displacement factor K_x , (b) largest-peak-acceleration K_x , (c) expected number-of-peaks per-unit-time factor ν_x , and (d) expected number-of-peaks per-unit-time-factor ν_x .

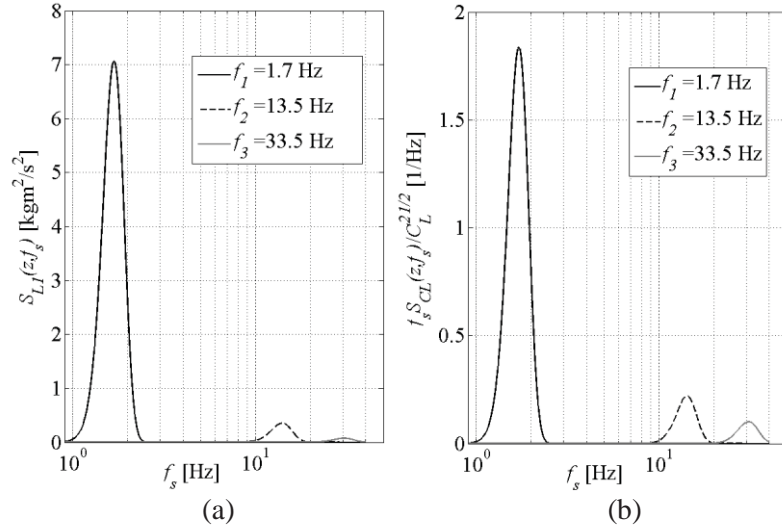


Figure 3.8. For the first three dominant modes: (a) Vortex-shedding-load in-the-wake spectral-density-function due to across-wind aerodynamics. Aero-elastic effects are not assessed, only structural damping affects the motion. (b) Lift-coefficient spectral density function acting on the wake of the structure at rest.

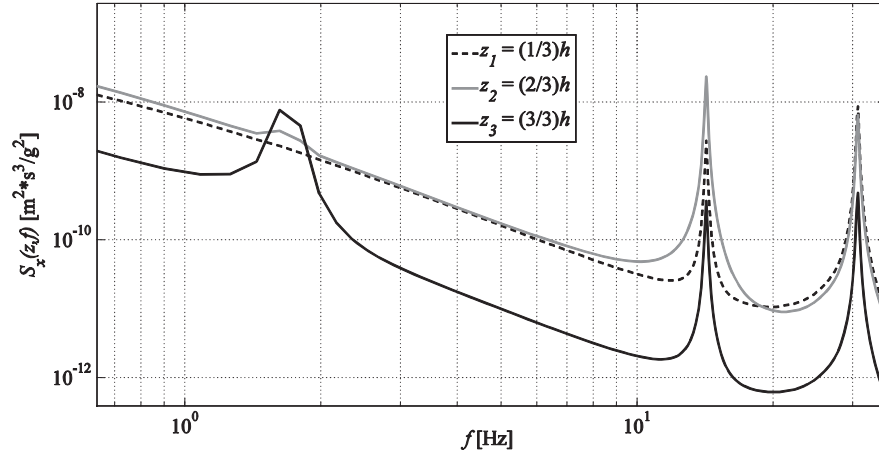


Figure 3.9. Modal combined spectral density function of the along-wind fluctuating deflection, for three sample heights above grade.

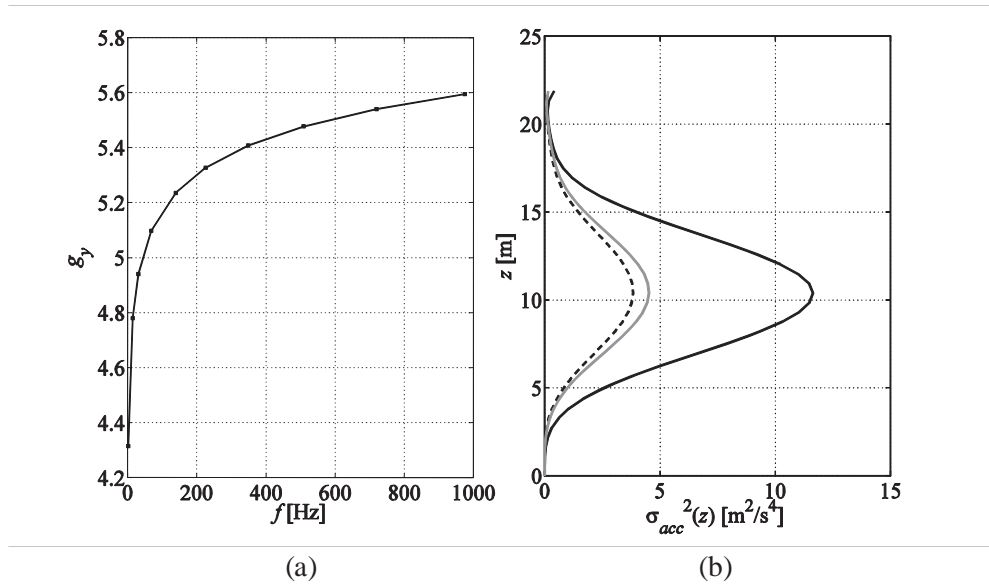


Figure 3.10. (a) Aero-elastic (gust) correction factor for the computation of fluctuating peak deflections, expressed in the frequency domain. (b) Structural (modal combined) acceleration response profile for three independent random realizations.

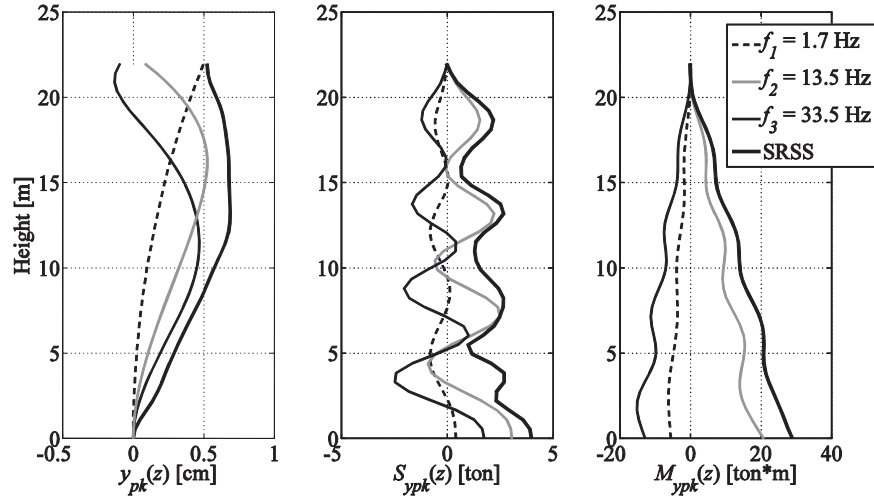


Figure 3.11(a). Dynamic structural response of the wind tower for one random realization employing across-wind Rumman's method.

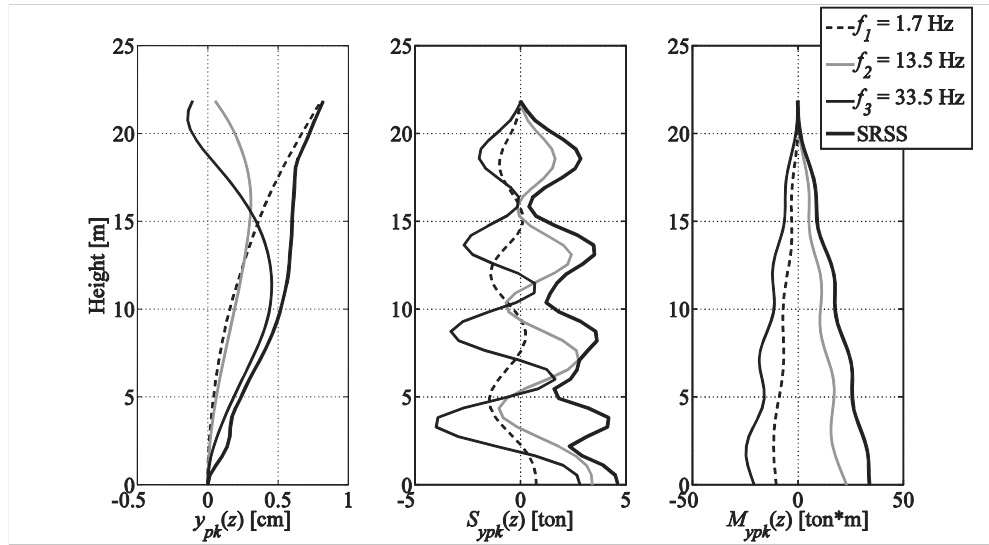


Figure 3.11(b). Dynamic structural response of the wind tower for one random realization employing across-wind Vickery's method.

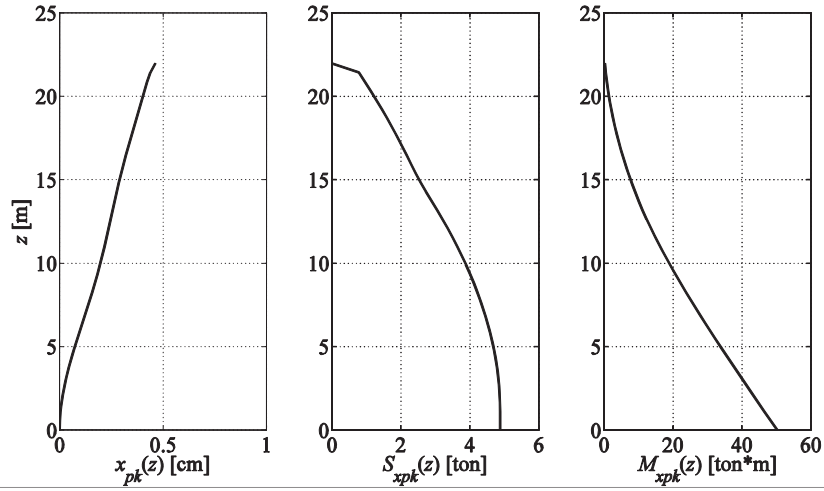


Figure 3.11(c). Dynamic structural response of the wind tower for one random realization employing along-wind of distributed stationary wind load.

3.8 Conclusions

Given appropriate selection of the aerodynamic parameters based on the turbulence field at an specific site, the predictive stochastic model presented here provide more accurate estimates of the across-wind response of wind towers. However, exclusion of the blade/nacelle/rotor/tower substructure interaction can considerably underestimate the response at the top of the tower and must be included in future formulations. Analytical results indicate that, due to vortex shedding, there are larger cross-wind than along-wind effects when critical shedding conditions are established for the second and third mode; along-wind response dominates otherwise. It is important to note that the flow around the wind tower corresponds a little below to the trans-critical Reynolds-number region. The response predicted by the two methods is in agreement with less than 15% of maximum difference as shown Figure 3.11. A relevant insight is that the maximum response due to excitement of the fundamental mode occurs when the shedding frequency at about 2/3 of the tower height is equal to the natural frequency. This observation was observed previously in [*ibid.* Velazquez and Swartz 2011] and is confirmed now with this improved methodology. For typical tapered steel structures drag loads in the longitudinal direction are dominant for high wind velocity profiles. Vortex excitation of the second

mode is more dominant for the third upper and middle sections compared to the fundamental mode, whereas the most severe acceleration intensities are primarily observed in the mid-span. When considering the vertical and horizontal correlation of the integration points (y_1, z_1) (y_2, z_2) , and the outline of the wind turbine system, the fluctuating wind velocity can be properly simulated by power spectrum analysis. The total response at the top of the tower has shown that the maximum displacement increases considerably as compared to the case where the mass is only modeled for the hub and nacelle. This contribution should be considered in the wind turbine design.

Finally, the wind-induced aerodynamic effects studied here outline behavioral trends more than realistic response parameters capable of being used in design. Future work will focus on utilizing dynamic sensor data to establish the wind speed distributions that can then be used to estimate loading demand statistics that can be compared to structural resistance. Fused with an automated damage detection system, this system can form the basis of a real-time probability-based risk assessment tool to aid in management and operation of wind turbine structures and their power plants. Now, it is appropriate time to introduce Chapter 4 that will thoroughly discuss the basics of a matrix-based Spinning Finite Element (SFE) method, combined with aero-elasto-stochastic analysis performed in the along-wind direction, and with the incursion of random vibration theory principles, in order to assess and validate the extent of the SFE towards the dynamic response of HAWT rotor blades subsystems.

Chapter 4. Spinning Finite Element

Wind energy has experienced considerable growth compared to other sectors of the nation's renewable energy portfolio during the past decade with similar trends expected for the near future; however safety and economical concerns have emerged due to new megawatt designs that utilize extremely large-scale wind turbine structures. Safe and economical operation requires not only information regarding structural dynamic conditions under dynamic action, but also the environmental loading factors in which these slender, multi-body structures operate. Given the stochastic nature of the loading on the turbine structures, a probabilistic framework is appropriate to characterize the risk that loads pose to the structure at a given time. Furthermore, sources of uncertainty such as aeroelastic damping, material imperfections, soil-structure interaction, among others, suggest for the use of a more sophisticated mathematical framework that can properly characterize uncertainty. This study explores the characterization of the turbine loading and response envelopes for critical failure modes for complex turbine blade geometries (tapered, twisted, and swept) through use of spinning finite elements (SPE) fused with traditional aeroelastic interaction theory. A framework is presented to develop an analytical estimation of the loading environment (including loading effects) based on rotationally sampled spectral densities via full 3-dimensional SPE implementation. To illustrate this approach, along-wind complex behaviors such as wind shear gradients, tower shadow effects, centrifugal stiffening, and gyroscopic effects are investigated as applied to the SPE model. The proposed solution includes methods that are based on modal decomposition of the blade elements and random vibration theory. Finally, to illustrate the framework's potential for risk-assessment, estimated demand statistics (generated by Monte Carlo method) are compared to code-based resistance curves that determine a probabilistic estimate of the risk of blade failure given a stochastic loading environment.

4.1 Introduction

The wind energy industry has grown in technical and economical importance over the past few decades. Installed power generation capacity from wind turbines has increased exponentially since the early 90's, particularly in China, the United States, and the European Union. Global cumulative installed wind capacity has grown from 6,100 MW in 1996 to 238,351 MW by 2011 [EWEA 2012]. This growth has not come without technical challenges. Rotor diameters and tower heights have increased over this time, from approximately 15m in 1985, to 160m by 2011. Furthermore, wind turbines are increasingly built in remote sites that are difficult to access and monitor. To insure proper and safe performance of a wind turbine it is necessary to establish a monitoring scheme to protect its operational components, comply with safety requirements, ensure quality and quantity of power supply, and guarantee productivity [Gardner *et al.* 2003][BWEA 2005].

In this respect, structural health monitoring (SHM) techniques can play an important role for the characterization of the risk posed to the turbine structures due to wind loading demands and dynamic performance of these multi-body systems (tall slender towers and large rotor blades). Such a practice will require stochastic models that are accurate, but sufficiently low-order to be useful in an autonomous SHM framework. Such models must be able to accurately represent complex turbine blade geometries, but also replicate the statistics of the coupled fluid/structure interaction including load effects unique to wind turbine structures (*e.g.*, tower-blade rotational motion harmonics).

The development of aeroelastic models for wind turbine blades, with the inclusion of rotationally-sampled wind-induced response analysis, has attracted interest in the structural design practice of the HAWT wind turbines. Some authors [Baumgart 2002] [Naguleswaran 1994] have modeled the rotating blades as simplified cantilever beams to analyze their linear aerodynamic response. Some studies concerning the blade-tower coupling effect were carried out by Murtagh *et al.* [Murtagh 2005] where a combined time-frequency domain analysis was utilized using a rotationally-sampled spectrum.

Similarly, Chen *et al.* [Chen *et al.* 2009] treated the mean wind velocity of the rotating blades according to natural wind shear effects using harmony superposition method. Experimental studies were made by Lee *et al.* [Lee 2001] demonstrating the complexity of the dynamic analysis process. In general, these studies have made use of standard beam-type finite elements for the along-wind aerodynamic analysis, but results constantly have shown that there is a need to improve the prediction of the complexity of load distributions, strain fields, coupled deflections, centrifugal stiffening, and nonlinear dynamic effects (such as gyroscopic phenomena) for blade elements with complex gradient geometry. These limitations in the current analytical methodologies, especially for the case of wind turbines with large diameters and complex geometries, demonstrate the need for sophisticated modal dynamic techniques, in this case, those based on spinning finite elements (SPEs) [Wittrick and Williams 1982].

Due to its great flexibility and large slenderness ratio, a wind turbine can be treated as a flexibly dynamic multi-body system in continuous rotating motion [Lanzafame and Messina 2007]. Dynamic analysis of spinning structures has been studied in multiple engineering disciplines including applications aerospace, automotive, and wind energy. The approaches used include SPEs, which have the ability to properly characterize blade elements with complex geometry such as tapered, swept, and twisted shape configurations; but also the potential to adequately model centrifugal, gyroscopic, and rotational-stiffening forces [Leung and Fung 1988]. The spinning finite element can also be employed to reproduce shadow (tower) effects and address model scale problems. Previous efforts have been made to study the vibration of SPEs around an axis of rotation in these various disciplines. Nelson [Nelson 1985] studied vibrations of a finite element on a shaft with a rotating disk. Bauer [Bauer 1980] established the dynamics of similar structures now revolving on the axis of rotation. Wittrick and Williams [*ibid.* Wittick and Williams 1982] employed the discrete and distributed mass methods to determine the spinning dynamics of straight bars. Christensen and Lee [Christensen and Lee, 1986] developed a nonlinear finite element formulation for spinning structures with no restraints, resulting in partial differential equations with variable coefficients, which in

turn, are difficult to solve and translate in numerical algorithms. Leung [*ibid.* Leung and Fung 1988] has presented an integrated and robust method for determining mode shapes of rotating, tapered, curved, and twisted beams.

Some advantages observed for the use of SPEs are: (1) reduced number of elements necessary to model turbine blades; (2) they can simulate, with good precision, the continuum of cross sections for complex geometry all along the blade element; (3) they account for the variation and distribution of centrifugal forces at different dynamic stages; (4) they handle coordinate mapping from global to local in continually spinning frame of reference; and (5) they adequately represent the so-called damped gyroscopic phenomena as a measure of aerodynamic instability. To realize these advantages, one of the main challenges of combining the aeroelasticity and SPE approaches is the derivation of the (skew-symmetric) gyroscopic damping matrix inside the velocity dependent term of the rotationally dynamic equation of motion. Gyroscopic (Coriolis) effects produced as a consequence of a rotating blade system produce the unintended effect of perturbing the natural expected vibration of a self-rotating structure, which in turn is expected to produce a deviated modal response from that of the classical theory for non-rotating structures [Wilkinson 1965]. The combination of damping and gyroscopic effects cause the dynamic system to fall in the complex numbers domain, rendering the modal solution to the eigenvalue problem to be non-trivial. To overcome this issue, the Arnoldi iterative method [Zheng *et al.* 1997] has been adopted to orthogonally decouple the damped gyroscopic structural system. This method is a numerical approach that makes use of the Schur decomposition to solve the complex-numbered eigenvalue problem. In addition, a Rayleigh-Ritz updated methodology for wind turbine blades was presented by Jonkman [Jonkman 2003] as part of an investigation into unsteady aerodynamics to assess blade response to wind-inflows (in terms of aerodynamic forces and out-of-plane bending moments), and is also incorporated into this study to find mode shapes.

The principle contribution of this paper is a framework for fusion of spinning finite elements with stochastic aeroelasticity methods via rotationally sampled spectrum

formulated for wind turbine blades of complex mass and geometry distribution (including tapered-swept-twisted blade profiles). The proposed analytical framework provides structural designers with greater freedom to model complex blade geometries and still include the rotationally-stochastic dynamic effects of the entire loading environment in the along-wind direction. This novel scheme is intended to serve as a low-order model basis for future performance monitoring and structural health monitoring (SHM) applications, but may also be of interest to turbine blade designers as well. A complete derivation for variable-gradient cross-section spinning finite element is presented in the following section. Section 4.3 depicts its inclusion in the equation of motion for an operational wind turbine blade. Section 4.4 incorporates traditional aeroelastic theory with the element with Section 4.5 providing a numerical example of the approach for a realistic turbine blade via the Monte Carlo method with some observations made about the behavior of various possible models made using this framework. Conclusions and comments regarding future work follow. The various terms of the matrices that make up the rotationally dynamic equation of motion are presented in the Appendix A.

4.2 Spinning Finite Element

Spinning finite elements are adapted for modeling of turbine blades in order to properly account for the rotational effects that the blade undergoes. The principle benefit to this approach is the inherent mapping between global and time-varying local coordinate systems that these elements possess. The fact that these elements can be utilized in a spectral element, random vibrations framework is another major advantage in potential SHM applications where computationally inexpensive, low-order models are desirable.

4.2.1 Coordinate System

Modeling wind turbine blade behavior under realistic conditions is difficult; one approach is to utilize skeletal beam elements in a continuously rotating framework. In such an approach, the equations of motion are established according to Lagrangian equations and expanded for the case of dynamic objects in continuous spinning motion.

This rotational movement tends to create deviation from classical structural dynamics theory derived for non-spinning structures. At the same time, second-order phenomena, such as the so-called gyroscopic or Coriolis effect, emerges from the free rotation and wind inflow alignment of the rotor components. These peculiar characteristics of the spinning elements are not considered in traditional finite elements, and must be properly addressed, especially when considering structures with large rotational inertial masses.

For this purpose, Leung and Fung [*ibid.* Leung and Fung 1988] derived a skeletal spinning finite element defined by beam members with constant cross-section embedded in a rotationally sampled field. An expanded derivation for cantilever beams with tapered-swept variation was induced by Rao [Rao 2005] and Larwood [Larwood 2009] and has been expanded for n_t tapered-swept variation degree in this study (see Figure 4.1) for the case of nonlinear shape-variation distributions. In this approach, one must consider three coordinate systems: (1) xyz acting as the local principal axes, (2) $x_s y_s z_s$ in association with the rotational motion of the blade such that y_s coincides with the spinning axis, and (3) a global static XYZ that governs both tower and blades substructures is located on top of the mast (hub location), having the spinning y_s axis coincident with the global Y axis.

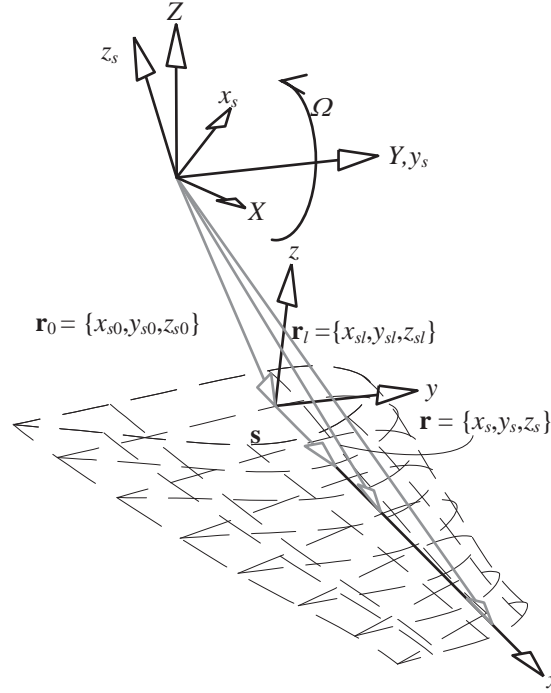


Figure 4.1. Orthogonal coordinate systems that govern the spinning motion of a wind turbine blade element.

Any point along the blade is defined by $\mathbf{r} = \mathbf{r}_0 + \xi(\mathbf{r}_l - \mathbf{r}_0)$, for $0 \leq \xi \leq 1$, where \mathbf{r} , \mathbf{r}_0 and \mathbf{r}_l are the position vectors controlled by the spinning coordinate system $x_s y_s z_s$. The spinning matrix is defined by:

$$\mathbf{\Omega} = \Omega \begin{bmatrix} 0 & 0 & 1 \\ 0 & 0 & 0 \\ -1 & 0 & 0 \end{bmatrix} \quad (4.1)$$

where Ω is the spinning constant speed with respect to the global-inertial coordinate system XYZ. It can be seen that

$$\begin{aligned} \mathbf{r} &= \{x_s, y_s, z_s\}^T \\ \mathbf{v} &= \dot{\mathbf{r}} + \mathbf{\Omega} \mathbf{r} \\ \mathbf{a} &= \ddot{\mathbf{r}} + 2\mathbf{\Omega} \dot{\mathbf{r}} + \mathbf{\Omega} \mathbf{\Omega} \mathbf{r} \end{aligned} \quad (4.2)$$

where \mathbf{r} , \mathbf{v} and \mathbf{a} are the position, velocity and acceleration absolute vectors, respectively. Superscripts \cdot and $\ddot{}$ mean first and second differentiation with respect to time. If \mathbf{u} and \mathbf{u}_s are displacement vectors in local xyz and spinning $x_s y_s z_s$ coordinate systems respectively, then the displacements $\mathbf{u} = \{u, v, w\}^T$, $\mathbf{u}_s = \{u_s, v_s, w_s\}^T$ with transformation: $\mathbf{u}_s = \mathbf{R}^T \mathbf{u}$, where u , v and w are local beam displacements; u_s , v_s and w_s are those thought as spinning beam displacements. The matrix \mathbf{R} is a base transformation matrix from local to spinning coordinate systems defined as (see Figure 4.2):

$$\mathbf{R} = \begin{bmatrix} \alpha_{11} & \alpha_{12} & \alpha_{13} \\ \alpha_{21} & \alpha_{22} & \alpha_{23} \\ \alpha_{31} & \alpha_{32} & \alpha_{33} \end{bmatrix} \quad (4.3)$$

For a typical horizontal wind turbine (HAWT) system the blade elements can be considered to be approximately in alignment with the spinning reference point when just one element is employed to characterize dynamic behavior. It is important to note that, for tapered-swept configuration, gyroscopic and centrifugal effects are primarily controlled by the expanding parameters contained in \mathbf{R} and \mathbf{r}_0 both exogenous in nature, so the HAWT simplification presented here is without any loss in generality. Consequently, $\mathbf{u}_s = \mathbf{u}$, $\mathbf{r}_0 = \{x_{s0}, y_{s0}, z_{s0}\} = \{0, 0, 0\}$, and $\mathbf{R} = \mathbf{I}$ where \mathbf{I} is the identity matrix (see Figure 4.3). When the element is deformed the position and velocity vectors will be given by $\mathbf{r}_u = \mathbf{r} + \mathbf{u}$ and $\dot{\mathbf{r}}_u = \dot{\mathbf{u}}$.

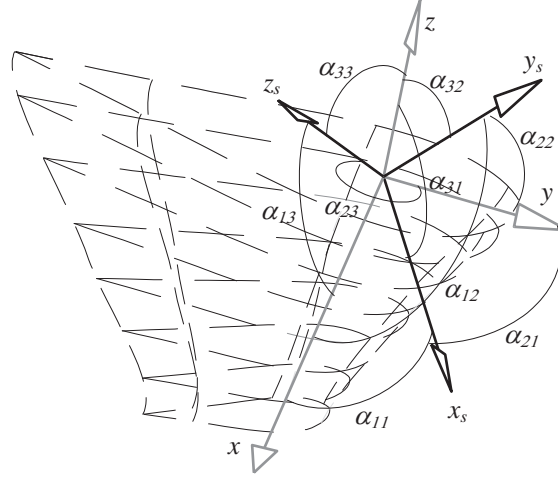


Figure 4.2. Cosine directories that constitute the base transformation matrix \mathbf{R} from spinning $x_s y_s z_s$ to local xyz coordinate systems.

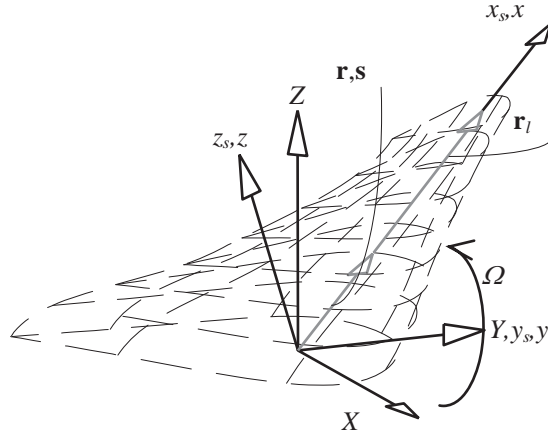


Figure 4.3. Global XYZ and spinning $x_s y_s z_s$ orthogonal coordinate systems that govern the spinning motion of a simplified HAWT wind turbine blade, where local xyz coincides with spinning $x_s y_s z_s$ reference frames.

4.2.2 Lagrangian Equations

General expression for Lagrange equations is given by:

$$\frac{d}{dt} \left(\frac{\partial T}{\partial \dot{\mathbf{u}}} \right) - \frac{\partial T}{\partial \mathbf{u}} + \frac{\partial U}{\partial \mathbf{u}} = \mathbf{F} \quad (4.4)$$

where T and U are the kinetic and strain energies respectively, and \mathbf{F} is defined as the generalized force vector. Expanding the energy terms and incorporating gradient variations of the cross-section and material distributions of n_t degrees at every point along the beam yields:

$$\begin{aligned}
T &= \frac{1}{2} \int \rho A(s) \mathbf{v}^T \mathbf{v} ds \\
U &= \frac{1}{2} \int EA(s) \left(\frac{\partial u}{\partial s} \right)^2 ds + \\
&\quad \frac{1}{2} \int EI_z(s) \left(\frac{\partial^2 v}{\partial s^2} \right)^2 ds + \frac{1}{2} \int EI_y(s) \left(\frac{\partial^2 w}{\partial s^2} \right)^2 ds + \\
&\quad \frac{1}{2} \int F_c(s) \left(\frac{\partial v}{\partial s} \right)^2 ds + \frac{1}{2} \int F_c(s) \left(\frac{\partial w}{\partial s} \right)^2 ds
\end{aligned} \tag{4.5}$$

where $\rho A(s)$, $EA(s)$, $A(s)$, $EI_y(s)$, $EI_z(s)$ and $F_c(s)$ are the tapered-swept variations of mass density, elastic modulus, cross-section area, moments of inertia around y and z , and generalized axial (centrifugal) force, respectively (presuming an equivalent, uniform modulus of elasticity is used). The integration variable s sweeping along the blade is depicted in Figure 4.4 and is controlled by the local system xyz . For tapered cross sections [ibid. Larwood 2009], now expanding for decreasing non-linear gradient variations across the span of the blade:

$$\begin{aligned}
\Gamma(s) &= \Gamma_0 \sqrt[n_t]{1 + \left(\sqrt[n_t]{\Gamma_l / \Gamma_0} - 1 \right) \frac{s}{l}}, \quad n_t = 1, 2, 3, \dots \\
\Gamma_0 &= EA_0, EI_{y0}, EI_{z0}, GJ_0, \rho A_0, \rho I_{p0} \\
\Gamma_l &= EA_l, EI_{yl}, EI_{zl}, GJ_l, \rho A_l, \rho I_{pl}
\end{aligned} \tag{4.6}$$

where the zero subscript represents the property at the inboard node, l subscript term stands for the property at the outboard node, and n_t is the degree of the function order. In Equation (4.6) $\Gamma(s)$ recapitulates the inertia and stiffness terms. It is either one of the studied parameters of the cross-section/material properties at location s ($0 \leq s \leq l$), l is

the length of the blade, and (Γ_o, Γ_l) are gradient variation pairs of those mentioned properties at the inboard and outboard end points, respectively. Similarly, polar moments of inertia of mass ρI_{p0} and ρI_{pl} , and polar moments of inertia of area GJ_0 and GJ_l , are defined at those locations. At the same time, Figure 4.5 illustrates the six degrees of freedom asserted for the inboard end (nearer the rotor hub location), and the complementary six degrees of freedom for the outboard end.

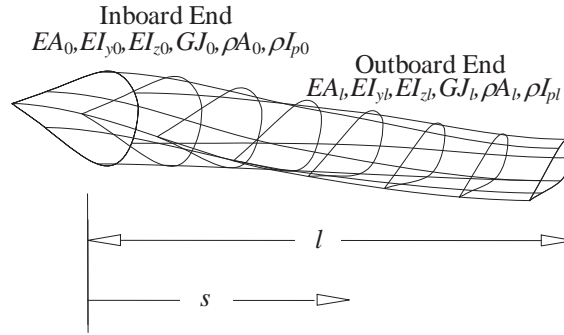


Figure 4.4. Tapered-swept gradient variation properties at the inboard and outboard ends of a spinning finite element.

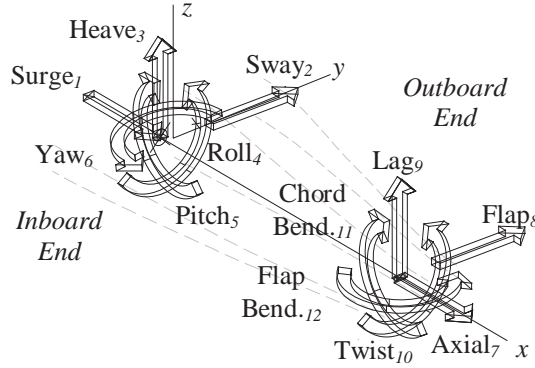


Figure 4.5. Degrees of freedom defined for a spinning finite element.

4.2.3 Steady State Equations

Expanding Equation (4.3) for absolute velocity yields:

$$\begin{aligned}
\mathbf{v} &= \dot{\mathbf{u}} + \boldsymbol{\Omega}(\mathbf{r} + \mathbf{u}) \\
\mathbf{v}^T \mathbf{v} &= \dot{\mathbf{u}}^T \dot{\mathbf{u}} + \\
&\quad \mathbf{u}^T \boldsymbol{\Omega}^T \boldsymbol{\Omega} \mathbf{u} + \mathbf{r}^T \boldsymbol{\Omega}^T \boldsymbol{\Omega} \mathbf{r} + \\
&\quad 2\dot{\mathbf{u}}^T \boldsymbol{\Omega} \mathbf{r} + 2\dot{\mathbf{u}}^T \boldsymbol{\Omega} \mathbf{u} + 2\mathbf{r}^T \boldsymbol{\Omega}^T \boldsymbol{\Omega} \mathbf{u}
\end{aligned} \tag{4.7}$$

Furthermore, expanding Equation (4.6) by use of Equation (4.3) in order to fully develop the kinetic energy T along the blade element, and adapting integration terms for tapered-swept variations (expressed in local coordinate system) [*ibid.* Leung and Fung 1988] yields:

$$\begin{aligned}
\mathbf{M}_B &= \int_0^l \rho A(s) \mathbf{m} ds \\
\mathbf{K}_{\Omega B} &= \int_0^l \rho A(s) \mathbf{k}_{\Omega} ds \\
\mathbf{G}_B &= \int_0^l \rho A(s) \mathbf{g} ds
\end{aligned} \tag{4.8}$$

$$\begin{aligned}
\mathbf{m} &= \begin{bmatrix} \mathbf{N}_1^T \mathbf{N}_1 & & \\ & \mathbf{N}_2^T \mathbf{N}_2 & \\ & & \mathbf{N}_3^T \mathbf{N}_3 \end{bmatrix} \\
\mathbf{g} &= \begin{bmatrix} & & \mathbf{N}_1^T \mathbf{N}_3 \\ & \mathbf{0} & \\ -\mathbf{N}_1^T \mathbf{N}_3 & & \end{bmatrix} \\
\mathbf{k}_{\Omega} &= \Omega^2 \begin{bmatrix} \mathbf{N}_1^T \mathbf{N}_1 & & \\ & 0 & \\ & & \mathbf{N}_3^T \mathbf{N}_3 \end{bmatrix} \\
\mathbf{N} &= \begin{bmatrix} \mathbf{N}_1 & & \\ & \mathbf{N}_2 & \\ & & \mathbf{N}_3 \end{bmatrix}
\end{aligned} \tag{4.9}$$

Similarly, the corresponding expansion of the strain energy term U , in local coordinates, is given by,

$$\mathbf{K}_{eB} = \begin{bmatrix} EA(s)\mathbf{K}_{e1} & & \\ & EI_z(s)\mathbf{K}_{e2} & \\ & & EI_y(s)\mathbf{K}_{e3} \end{bmatrix} \quad (4.10)$$

$$\mathbf{K}_{cB} = \begin{bmatrix} \mathbf{0} & & \\ & \mathbf{K}_{c1} & \\ & & \mathbf{K}_{c2} \end{bmatrix}$$

$$\mathbf{K}_{e1} = \int_0^l \mathbf{N}_1'^T \mathbf{N}_1' ds$$

$$\mathbf{K}_{e2} = \int_0^l \mathbf{N}_2''^T \mathbf{N}_2'' ds$$

$$\mathbf{K}_{e3} = \int_0^l \mathbf{N}_3''^T \mathbf{N}_3'' ds \quad (4.11)$$

$$\mathbf{K}_{c1} = \int_0^l F_c(s) \mathbf{N}_2'^T \mathbf{N}_2' ds$$

$$\mathbf{K}_{c2} = \int_0^l F_c(s) \mathbf{N}_3'^T \mathbf{N}_3' ds$$

where the prime notation denotes differentiation with respect to s . Alongside the energy terms, the centrifugal force acting all along the blade element is sensitive to the spinning velocity and to the presence of a tapered-swept blade configuration. It is assumed here that the change in geometry is gradual. For nonlinear variations within the cross-section (without losing generality in the derivation) the centrifugal force per unit length is defined as $\tau_c(s) = -\rho A(s) \mathbf{s}^T \boldsymbol{\Omega} \boldsymbol{\Omega} \mathbf{r}$, Alternatively, $\tau_c(s) = A(s) \Omega^2 (a + bs)$, where $\mathbf{r} = \mathbf{r}_0 + s\mathbf{s}$, $\mathbf{r}_0 = \{x_{s0}, y_{s0}, z_{s0}\}^T$ and $\mathbf{s} = \{\alpha_{11}, \alpha_{12}, \alpha_{13}\}^T$; the latter being the unit vector projected in the local x axis, as depicted in Figure 4.1. Similarly, $a = \alpha_{11}x_{s0} + \alpha_{13}z_{s0}$, $b = \alpha_{11}^2 + \alpha_{13}^2$, and the force per unit length $\rho A(s) = \rho A(s)$, according to Equation (4.6), taking $(\rho A_0, \rho A_l)$ pair instead. Therefore, the centrifugal nonlinear force function is given by:

$$F_c(s) = F_{c0} - \int_0^s \tau_c(x) dx; \quad F_{c0} = \int_0^l \tau_c(x) dx \quad (4.12)$$

For HAWT approximation $a = 0$, $b = 1$, $\mathbf{s} = \{1, 0, 0\}^T$ and $\mathbf{r}_g = \{0, 0, 0\}^T$. Finally, the shape functions of the tapered-swept spinning finite element can be adopted directly from

Leung [*ibid.* Leung and Fung 1988]:

$$\begin{aligned}
\mathbf{N}_1 &= [1 - \xi, \xi] \\
\mathbf{N}_2 &= [1 - 3\xi^2 + 2\xi^3, \xi(\xi^2 - 2\xi + 1)l, 3\xi^2 - 2\xi^3, \xi^3 - \xi^2l] \\
\mathbf{N}_3 &= [1 - 3\xi^2 + 2\xi^3, -\xi(\xi^2 - 2\xi + 1)l, 3\xi^2 - 2\xi^3, -(\xi^3 - \xi^2)l]
\end{aligned} \tag{4.13}$$

for all $\xi = s/l$.

4.3 Vibration Equations

Once the properties of the spinning finite element are determined, the equations governing the vibrational motion of the blade can be derived from the equation of motion.

4.3.1 Equation of Motion

From the expanded energy terms defined in Equation (4.4) and Equation (4.5), the free-vibration dynamic linear system that governs the motion of the blade spinning finite element at any instant is given by:

$$\mathbf{M}_B \ddot{\mathbf{q}}(t) + [2\mathbf{G}_B + \mathbf{C}_B] \dot{\mathbf{q}}(t) + [\mathbf{K}_{eB} + \mathbf{K}_{cB} - \mathbf{K}_{\Omega B}] \mathbf{q}(t) = \mathbf{0} \tag{4.14}$$

where \mathbf{M}_B and \mathbf{K}_{eB} are the traditional mass and elastic stiffness matrices for beam elements, \mathbf{G}_B is the skew-symmetric gyroscopic matrix, \mathbf{C}_B is a classical (Rayleigh) damping matrix. \mathbf{C}_B is assumed to be proportional to the mass and stiffness matrices and to be independent of the Lagrange derived equations; it is inserted in the linear system as such in order to decouple the complex mode that the gyroscopic system produces, but also to preserve completeness on the generality equations of the damped gyroscopic dynamic system. The damping matrix is thusly defined as a superposition of mass-proportional damping and stiffness-proportional damping $\mathbf{C}_B = a_0 \mathbf{M}_B + a_1 \mathbf{K}_B$, where a_0

and a_1 are unknown proportional coefficients with units of sec^{-1} and sec , respectively [Meirovitch 1986]. $\mathbf{K}_{\Omega B}$ is the stabilizing stiffness spinning matrix and \mathbf{K}_{cB} is the destabilizing centrifugal stiffness matrix, $\mathbf{q}(t)$ is the global nodal displacement vector (inboard and outboard ends) when the oscillation occurs about the steady state, as a function of time. In Equation (4.14) the prime notation indicates differentiation with respect to time t . The general solution of the dynamic equation system for nonlinear second-degree-order tapered-swept blades is too long to show here and is presented in the Appendix A. The system modeled by Equation (4.14) is loaded by forces acting in the along-wind direction, that will produce wind-induced vibrations, bearing on the blade projected area [*ibid.* Leung and Fung 1988], namely:

$$\mathbf{M}_B \ddot{\mathbf{q}}(t) + [2\mathbf{G}_B + \mathbf{C}_B] \dot{\mathbf{q}}(t) + [\mathbf{K}_{eB} + \mathbf{K}_{cB} - \mathbf{K}_{\Omega B}] \mathbf{q}(t) = \mathbf{F}_B(t) \quad (4.15)$$

where the along-wind load vector $\mathbf{F}_B(t)$ is a function of time and is applied to the exposed area (or active surface) with which the wind mass is initially in contact. The blade system can be treated as a bluff body immersed within a rotationally sampled wind flow [Murtagh *et al.* 2004] experiencing periodic pressures distributed over its surface.

4.3.2 Eigenvalue Problem

Equation (4.15) is prohibitively difficult to solve directly with typical modal-based methods due to skew-symmetry of the gyroscopic matrix. It is noted that the gyroscopic terms are much smaller than the damped natural frequency of each mode (assumed the system is lightly damped), and the mode shapes are real valued for any instance (in general, they approximate normal modes), where the imaginary part of each mode shape vector becomes negligible. This mathematical fact can be interpreted as the blade deflections parallel to the axis of rotation (x_s, z_s) tending to be large compared to the perpendicular deflections (y_s) [Meirovitch 1980]. For such a case, the Arnoldi iterative method [Horn and Johnson 1985] can be adopted to solve for the generalized eigenvalue problem that is computed using complex numbers, thus the coupling between the

gyroscopic and damping matrices becomes evident [*ibid.* Zheng *et al.* 1997]. The final goal is to obtain an eigen-realization solution acquired by employing only real numbers to get mode shapes. To accomplish this goal, the Schur decomposition has been adopted to solve for the uncoupled matrix problem [*ibid.* Horn and Johnson 1985]. Defining $\mathbf{K}_B = \mathbf{K}_{eB} + \mathbf{K}_{cB} - \mathbf{K}_{\Omega B}$ as the equivalent stiffness matrix and expressing the combined equation in state-space form yields:

$$\begin{aligned} \mathbf{A}\dot{\mathbf{y}}(t) + \mathbf{B}\mathbf{y}(t) &= \mathbf{Q}_B(t) \\ \mathbf{A} &= \begin{bmatrix} [\mathbf{G}_B + \mathbf{C}_B] & \mathbf{M}_B \\ -\mathbf{M}_B & \mathbf{0} \end{bmatrix}; \quad \mathbf{y}(t) = \begin{Bmatrix} \mathbf{q}(t) \\ \dot{\mathbf{q}}(t) \end{Bmatrix} \\ \mathbf{B} &= \begin{bmatrix} \mathbf{K}_B & \mathbf{0} \\ \mathbf{0} & \mathbf{M}_B \end{bmatrix}; \quad \mathbf{Q}_B(t) = \begin{Bmatrix} \mathbf{F}_B(t) \\ \mathbf{0} \end{Bmatrix} \end{aligned} \quad (4.16)$$

The state matrix \mathbf{A} is non-symmetric, so it is reduced to Hassenberg form and a B-orthogonal matrix $\boldsymbol{\varphi}_k = [\varphi_1, \varphi_1, \dots, \varphi_k]$ is found such that:

$$\begin{aligned} \boldsymbol{\varphi}_k^T \mathbf{B} \boldsymbol{\varphi}_k &= \mathbf{I}_k \\ \boldsymbol{\varphi}_k^T \mathbf{A} \boldsymbol{\varphi}_k &= \mathbf{H}_k \end{aligned} \quad (4.17)$$

$$\mathbf{H}_k = \begin{bmatrix} h_{11} & h_{12} & \dots & h_{1k} \\ \beta_2 & h_{22} & \dots & h_{2k} \\ & \ddots & \ddots & \\ & & \beta_k & h_{kk} \end{bmatrix} \quad (4.18)$$

$$\beta_{k+1} \boldsymbol{\varphi}_{k+1} = \mathbf{B}^{-1} \mathbf{A} \boldsymbol{\varphi}_k - \sum_{i=1}^k h_{ik} \boldsymbol{\varphi}_i \quad (4.19)$$

where \mathbf{I}_k is the identity matrix, k is the number of steps required for the Arnoldi reduction process, and β_{k+1} and h_{ik} are the direct outcome of a Schmit orthogonalization process applied on Equation (4.18). Matrix \mathbf{H}_k is the upper triangular Hessenberg form of \mathbf{A} to be decoupled in sets of block pairs, discarding to eliminate any complex-numbers. As a result of this formulation, the Schur theorem stipulates that matrix \mathbf{H}_{2n} can be

transformed in an upper quasi-triangular matrix \mathbf{R} and an orthogonal transformation \mathbf{U}_s by a real similarity matrix operation that takes the form $\mathbf{H}_{2n}\mathbf{U}_s = \mathbf{U}_s\mathbf{R}_s$, where $n = 12$, the total number of blade modes considered in the analysis (see Figure 4.5). Wilkinson [*ibid.* Wilkinson 1965] presents the derivation uncoupled non-symmetric system (Equation 4.18) by means of \mathbf{U}_s and \mathbf{R}_s to extract c_i , the uncoupled damping coefficient of mode i , and ω_i , the circular frequency (rad/sec) of that orthogonal mode. This technique is employed in this study to extract damping coefficients to be used in the aeroelastic analysis described in the following section.

4.4 Aeroelastic Analysis

This paper presents the integration of spinning finite element theory with aeroelastic analysis in the using a random vibration approach. Simplifications made in the prior section to mitigate the numerical effect of complex mode shapes resulting from the gyroscopic damping matrix limit the present study to along-wind direction effects only, at this time [Soong and Grigoriu 1992]. Across-wind and complex-frequency analyses will not be considered within the scope of the present study.

4.4.1 Harmonic Wind Load

The system represented by Equation (4.15) may be re-expressed as an independent linear system where the generalized coordinates $\xi(t)$, defined in local coordinate system xyz , form a particular solution of the canonical differential equation:

$$\ddot{\xi}_i(t) + 2\zeta_i\omega_i\dot{\xi}_i(t) + \omega_i^2\xi_i(t) = \frac{F_{Bi}(t)}{m_{ni}}, \quad i = 1, 2, \dots, n \quad (4.20)$$

where m_{ni} is the generalized mass of the i th mode, for n total number of blade modes considered in the analysis [Hansen 2008], yielding:

$$\varsigma_i = \frac{c_i}{2\sqrt{k_i m_i}}, \quad m_{ni} = \int_0^l \varphi_i(x)^2 m(x) dx, \quad f_i = \frac{\omega_i}{2\pi} \quad (4.21)$$

where $\varphi_i(x)$ is the B-orthogonal i th normal mode of the wind turbine, and $m(x)$ is the distributed mass along the blade element, both governed by the local coordinate system, xyz ; l is the total length, and f_i is the i th natural frequency (Hz). Coefficients k_i and m_i come directly from the B-orthonormalization of matrix \mathbf{B} containing the symmetric mass matrix \mathbf{M}_b and the symmetric equivalent stiffness matrix \mathbf{K}_b . The generalized force in the i th mode is expressed as $F_{Bi}(t) = \int_{i=0}^l p(x,t) \varphi_i(x) dx$, where $p(x,t)$ is a periodic, homogeneously distributed wind pressure applied in the along-wind direction, depending mainly on the blade instantaneous rotation and the rotor spinning velocity Ω , as a function of both the blade length and time. By definition, $p(x,t) = F(t) \delta(x - x_F)$, where $\delta(x - x_F)$ is the unit impulse function acting at time $t = 0$ (see Figure 4.6), defined $\delta(t) = 0$ for $t \neq 0$ and $\lim_{\Delta t \rightarrow 0} \int_0^{\Delta t} \delta(t) dt = 1$. The force $F(t)$ is a concentrated force acting at a point, x_F , measured from the inboard end of the element in the local reference system, xyz . Therefore, $F_{Bi}(t) = \lim_{\Delta x \rightarrow 0} \int_{x_F}^{x_F + \Delta x} p(x,t) \varphi_i(x) dx$ or, expressed in an alternative fashion and given an punctual impulse force at x_F , $F_{Bi}(x_F, t) = \varphi_i(x_F) F(t)$.

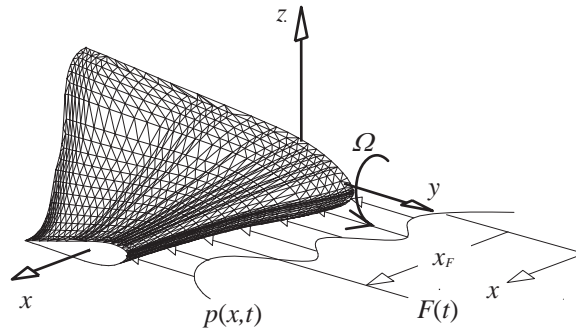


Figure 4.6. Distributed periodic pressure applied to the SPE in the along-wind direction.

The response to a punctual harmonic load, of the form $F(t) = F_0 \cos(2\pi f t)$, acting on the blade element at coordinate x_F , given a frequency f , will be

$F_{Bi}(x_F, t) = F_0 \phi_i(x_F) \cos(2\pi f t)$. It can be verified that the modal coordinate in the i th mode for the steady-state solution is given by [Simiu and Scanlan 2007]:

$$\xi_i(x_F, f, t) = F_0 \phi_i(x_F) H_i(f) \cos\{2\pi f t - \phi_i(f)\} \quad (4.22)$$

Here, the admittance function is defined as:

$$H_i(f) = \frac{1}{4\pi^2 f_i^2 m_{ni} \sqrt{\left[1 - \left(\frac{f}{f_i}\right)^2\right]^2 + 4\zeta_i^2 \left(\frac{f}{f_i}\right)^2}} \quad (4.23)$$

and the corresponding phase is given by:

$$\phi_i(f) = \tan^{-1} \frac{2\zeta_i \left(\frac{f}{f_i}\right)}{1 - \left(\frac{f}{f_i}\right)^2} \quad (4.24)$$

Hence, the response of the wind turbine blade at any position x , given a harmonic load acting at location x_F , accounting for all modal contributions, will be:

$$u(x, x_F, f, t) = F_0 \sum_{i=1}^n \phi_i(x) \phi_i(x_F) H_i(f) \cos\{2\pi f t - \phi_i(f)\} \quad (4.25)$$

4.4.2 Distributed Stationary Random Wind Load

It is necessary to model the effect of a general random along-wind loading function, not just impulse or harmonic loads. Expanding Equation (4.20) for the case of a distributed stationary random load where an infinite number of wind forces, $F_{Bi}(X_i, Z_i, t)$, act on the contact surface $A(Z)$ of the blade element, here using the global coordinate system, XYZ

(see Figure 4.7). Horizontal pressures in orthogonal directions must be accounted for to simulate the multi-directional effects of the wind [Shinozuka 1971] via a spatial correlation function relating the points on the active surface of the blade [Di Paola and Zingales 2008][Ambrosini *et al.* 2002]. The wind power spectral density matrix, expressed in global coordinates XYZ , is defined as:

$$\mathbf{S}_{uuR} = \begin{bmatrix} S_{uR(1,1)} & & & & & \\ \vdots & \ddots & & & & \\ S_{uR(j,1)} & \cdots & S_{uR(j,j)} & & \text{sym} & \\ \vdots & & \vdots & \ddots & & \\ S_{uR(k,1)} & \cdots & S_{uR(k,j)} & \cdots & S_{uR(k,k)} & \\ \vdots & & \vdots & & \vdots & \ddots \\ S_{uR(n_z,1)} & \cdots & S_{uR(n_z,j)} & \cdots & S_{uR(n_z,k)} & \cdots & S_{uR(n_z,n_z)} \end{bmatrix} \quad (4.26)$$

$$S_{uR(j,k)} = \sqrt{S_{uR}(Z_j, f) \cdot S_{uR}(Z_k, f)} \text{Coh}(X_j, X_k, Z_j, Z_k, f) \quad (4.27)$$

where $S_{uR(j,j)}$ is the auto-power spectrum at discrete contact point j , and $S_{uR(j,k)}$ the cross-power spectrum of the fluctuating wind between discrete points j and k as defined in Figure 4.7.

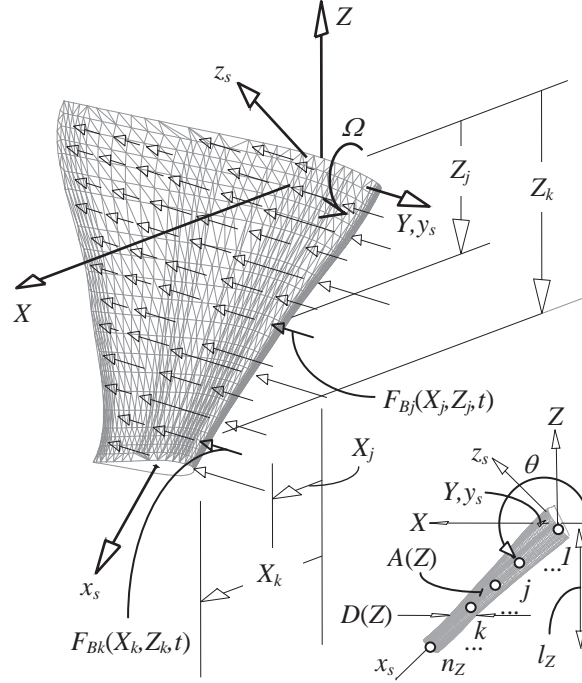


Figure 4.7. Coherence (spatial correlation) function distribution for the auto-power and cross-power spectrum computation along the global X (horizontal) and Z (vertical) axes.

Simultaneously, $S_{uR}(Z, f)$ is the design rotationally-sampled spectral density of the longitudinal velocity fluctuations. The term $\text{Coh}(X_j, X_k, Z_j, Z_k, f)$ is the across-wind cross-correlation coefficient defined by:

$$\text{Coh}(X_j, X_k, Z_j, Z_k, f) = \exp \left\{ - \frac{f \{ C_z^2 (Z_j - Z_k)^2 + C_y^2 (X_j - X_k)^2 \}^{1/2}}{\frac{1}{2} \{ U(Z_j) + U(Z_k) \}} \right\} \quad (4.28)$$

Pairs (X_j, Z_j) and (X_k, Z_k) are coordinates of points n_j and n_k where the line defined by n_j - n_k is assumed to be perpendicular to the direction of the mean wind. For practical purposes $C_y = 16$ and $C_z = 10$ are the exponential decay coefficients used for global horizontal and global vertical separation, respectively. The present study adopts the well known Kaimal spectrum [Kaimal *et. al.* 1972] for the along-wind field at vertical position Z :

$$S_u(Z, f) = \frac{200u_*^2 c}{f(1 + 50c)^{5/3}} \quad (4.29)$$

where $u_* = U(Z)/(2.5 \ln(Z/Z_0))$ is the shear velocity and $c = fz/U(Z)$ is the Monin or similarity coordinate. The term Z_0 represents the surface roughness length for a given surface or terrain surrounding the wind turbine structure. The term $U(Z)$ is the total wind velocity envelope (mean wind plus fluctuating) acting at elevation Z in the longitudinal (along-wind) direction. The assessment of $U(Z)$ is in agreement with the primary harmonic frequencies f_{Ti} of the tower and thusly requires some knowledge of D_T as the tapered cross-section diameter of the wind tower projected in the along-wind direction, evaluated at its maximum height (rotor and hub elevation). At this location, the longitudinal wind velocity $U(Z=0)$ generates vortex shedding with frequencies equal to the natural frequencies of the tower substructure, the critical velocity $U_{cr} = U(Z=0)$ for a given tower mode shape i_T [Basu 1983] and must meet the following conditions:

$$\begin{aligned} U(Z=0) &= \frac{1}{S_{tr}} f_{Ti} D_T \\ \Re e &= 67,000 U(Z=0) D_T \end{aligned} \quad (4.30)$$

where S_{tr} is the Strouhal number, and $\Re e$ is the Reynolds number necessary to generate such critical harmonic conditions on the fundamental tower mode i_T . Once U_{cr} is properly evaluated, it is possible to determine the associated wind velocity envelope for the blade elements according to their instantaneous angle of rotation, θ . Simultaneously, Murtagh [*ibid.* Murtagh *et al.* 2005] proposed a rotationally-sampled spectrum $S_{uR}(Z, f)$ that is defined using 70% of the original Kaimal spectrum variance (by area under the curve), proportionally increased at each node. The aim of this characterization is to capture the rotating effects, such as the periodicity of blade spinning and how this spinning motion affects the disturbance of the stationary wind field in the along-wind direction within the turbulent flow. The goal is to better represent the intensity and redistribution of the turbulent energy content in the spinning dynamic system. A modified rotationally-

sampled spectrum is proposed in this investigation where $S_u(Z, f)$ is obtained for each node in particular at its current height. The original 70% of the variance remains intact whereas the remaining 30% is distributed among three normal (Gaussian) peaks, corresponding to a three-rotor-blade arrangement revolving at a constant spinning velocity, Ω . By identifying frequencies within the spectrum at 1Ω , 2Ω and 3Ω , with proportional reduction factors of 18% for the first, 9% for the second, and 3% for the third maximum peaks respectively (Figure 4.8), it is possible to construct the modified rotationally-sampled spectrum $S_{uR}(Z, f)$ to be used in Equation (4.27). This approach captures the tendency of the spectrum peaks to be more pronounced towards the tip of the blade.

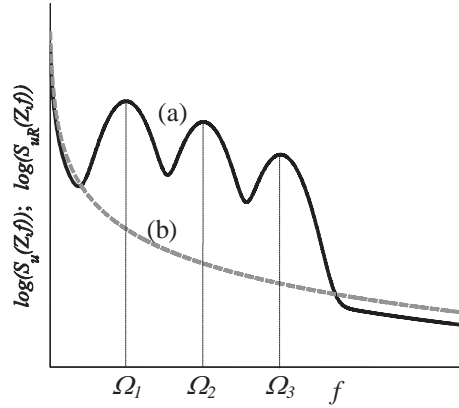


Figure 4.8. Spectral energy distribution for a node at a set height Z , and a set rotation angle θ . (a) Modified rotationally-sampled spectrum, (b) original Kaimal spectrum.

4.4.3 Spectral Response

The analysis proposed in this study uses a random vibrations approach to model the response of the turbine blades to random aeroelastic loadings. The spectral density function of the along-wind fluctuating deflection for mode i is given by [Simiu and Scanlan 2007]:

$$S_{ix}(Z, f) = \frac{\rho^2}{16\pi^2} \frac{\phi_i^2(Z) \frac{1}{2} C_D^2(Z) (1 + N(f))}{f_i^4 m_{ni}^2 \left\{ \left[1 - \left(\frac{f}{f_i} \right)^2 \right]^2 + 4\zeta_i^2 \left(\frac{f}{f_i} \right)^2 \right\}}.$$

$$\int_0^{l_z} \int_0^{l_z} \int_0^{D(Z)} \int_0^{D(Z)} \phi_i(Z_j) \phi_i(Z_k) U(Z_j) U(Z_k) S_{uR(j,k)} dX_j dX_k dZ_j dZ_k \quad (4.31)$$

where ρ is the air density, $C_D(Z)$ is the drag coefficient applied to the cross-section located at global height Z , and $D(Z)$ is the projected depth function of the cross-section at that elevation (see Figure 4.7). Similarly, $N(f)$ is the along-wind cross-correlation coefficient defined as:

$$N(f) = \frac{1}{\zeta} - \frac{1}{2\zeta^2} (1 - e^{-2\zeta})$$

$$\zeta = \frac{77}{5} \frac{f D_{\min}}{U(\frac{2}{3} l_z)}; \quad D_{\min} = \min \{D(Z)\} \quad (4.32)$$

Magnitude l_z can be obtained by projecting the blade length l in the vertical (global) axis Z , given a rotation angle θ for the beam with respect to the horizontal axis (see Figure 4.7). In this line of thinking, the corresponding integrated (modal combined) spectral density function may be computed by superposition of modes $S_x(Z, f) = \sum_{i=1}^n S_{ix}(Z, f)$. The mean square value of the fluctuating along-wind deflection is obtained, for arbitrary mode i , as the integral of the spectral density $\sigma_{ix}^2(Z) = \int_0^\infty S_{ix}(Z, f) df$ and, in the case of the mean square value of the fluctuating acceleration, $\sigma_{ix}^2(Z) = 16\pi^4 \int_0^\infty f^4 S_{ix}(Z, f) df$ also for blade mode i . Finally, the largest peak modal expected value of critical indicators of fluctuation behavior (deflection and acceleration) occurring in a predefined time interval, T , can be computed as $x_{ipk}(Z) = K_{ix}(Z) \sigma_{ix}(Z)$ and $\ddot{x}_{ipk}(Z) = K_{ix}(Z) \sigma_{ix}(Z)$, respectively, where:

$$K_{ix}(Z) = [2\ln(\nu_{ix}(Z)T)]^{1/2} + \frac{0.557}{[2\ln(\nu_{ix}(Z)T)]^{1/2}} \quad (4.33)$$

$$K_{i\ddot{x}}(Z) = [2\ln(\nu_{i\ddot{x}}(Z)T)]^{1/2} + \frac{0.557}{[2\ln(\nu_{i\ddot{x}}(Z)T)]^{1/2}} \quad (4.34)$$

are the largest-peak displacement (Equation (4.33)) and largest-peak acceleration (Equation (4.34)) factors that account for the probability that, in the time interval T , there will be no peaks equal or larger to $x_{ipk}(Z)$ or $\ddot{x}_{ipk}(Z)$, respectively. Simultaneously:

$$\nu_{ix}(Z) = \left[\frac{\int_0^\infty f^2 S_{ix}(Z, f) df}{\int_0^\infty S_{ix}(Z, f) df} \right]^{1/2} \quad (4.35)$$

$$\nu_{i\ddot{x}}(Z) = \left[\frac{\int_0^\infty f^6 S_{i\ddot{x}}(Z, f) df}{\int_0^\infty f^4 S_{i\ddot{x}}(Z, f) df} \right]^{1/2} \quad (4.36)$$

are the corresponding number-of-peaks-per-unit-time factors. Shear and moment functions $S_{ixpk}(x)$ and $M_{ixpk}(x)$, expressed in local coordinates, xyz , can be obtained by projecting all modal peak displacement responses back from the global XYZ to the local xyz reference based on the current instantaneous rotation angle θ :

$$S_{ixpk}(x) = (2\pi f_i)^2 \int_x^l m(x_1) x_{ipk}(x_1) dx_1 \quad (4.37)$$

$$M_{ixpk}(x) = (2\pi f_i)^2 \int_x^l m(x_1) x_{ipk}(x_1) (x_1 - x) dx_1 \quad (4.38)$$

Finally, total displacements, shears, and moments can be computed directly by linear superposition of all n modes incorporated in the model. It is important to underline that the quantities used from Equation (4.26) to Equation (4.36) are formulated in global coordinates XYZ . At the same time, those parameters are fundamentally dependent on the instantaneous rotation θ , given a time t . Also, the integration variable Z runs along the

vertical (raised) direction, whereas the X term is sweeping the horizontal (laying) direction. Rotation angle θ is positive in the counter-clockwise direction. Accordingly, the blade reaches its maximum height at $\theta = 90^\circ$ and its minimum at $\theta = 270^\circ$.

4.5 Numerical Example

A numerical example is provided in this section to demonstrate the capabilities of the proposed framework. Because the framework relies on aeroelasticity, its output is stochastic; therefore a large number of stochastic input parameters are used for the provided example using the Monte Carlo method to illustrate the full capabilities of the approach. To accomplish this goal, a full state-space analysis as a linear summation of the lower bending modes and centrifugal forces has been derived for an aeroelastic analysis via SPE by computing 3000 stochastic realizations for a generic HAWT model. Three fundamental modes were considered for a tower model consisting of a nacelle, bedplate, and shaft. The wind tower is modeled as a hot dip-galvanized tubular steel with 0.51cm thickness ($E_t = 200$ GPa). The rotor system consists of three blades with fixed pitch, made of fiberglass reinforced polyester ($E_b = 80$ GPa); swept area up to 214 m^2 . The blades are assumed to be tapered-swept cantilever beams 7.92 m rotor diameter. The specimen has been reconstructed as a modified version of a Tjaereborg type blade [*ibid.* Hansen 2008]. To illustrate the effect of the blade geometry on the modeled response, three geometries are considered: $n_t = 0$ (constant), $n_t = 1$ (linear), and $n_t = 2$ (parabolic) gradient variation. The material properties modeled at the inboard end are: $\rho_0 = 2600 \text{ kg/m}^3$, $E_0 = 72 \text{ N/m}^2$, $\nu_0 = 0.33$; and at the outboard end are: $\rho_l = 2600 \text{ kg/m}^3$, $E_l = 72 \text{ N/m}^2$, $\nu_l = 0.33$; air density $\rho_{air} = 1.25 \text{ kg/m}^3$. Geometric properties for the inboard end are: the projected depth normal to the along-wind direction is $d_0 = 1 \text{ m}$, the area of exposure is $A_0 = 0.038 \text{ m}^2$, the orthogonal inertias are $I_{y0} = 0.0009 \text{ m}^4$ and $I_{z0} = 0.00484 \text{ m}^4$, the polar moment of inertia is $J_0 = 9.125 \times 10^{-4} \text{ m}^4$, and the mass moment of inertia is $I_{p0} = 0.1 \text{ kg} \cdot \text{m}^2$. For the case of the outboard end geometric properties can be approximated as: $d_l = 0.01 \text{ m}$, $A_l = 0.01 A_0 \text{ m}^2$, $I_{yl} = 0.01 I_{y0} \text{ m}^4$, $I_{zl} = 0.01 I_{z0} \text{ m}^4$, $J_l = 0.01 J_0 \text{ m}^4$, and $I_{pl} = 0.01 I_{p0} \text{ kg} \cdot \text{m}^2$. The length of blade specimen is $l = 15 \text{ m}$ and yaw

eccentricity is $Y_0 = 0.609$ m. The number of discrete points to be considered in the local longitudinal axis, x is $n_x = 40$ per blade element. The total number of active tower modes used is $n_T = 3$. General geometric properties of the wind turbine are given in Table 4.1.

Table 4.1. Properties of the wind turbine prototype.

Geometry	Value
Rotor diameter	15.95m
Tower height	21.94 in
Rotor hub height	22.55 in
Nacelle mass	2.27 ton
Rotor mass (with hub)	1.81 ton

Table 4.2 shows the Gaussian random variables used as inputs to the Monte Carlo method calculations as sources of uncertainty of the aerodynamic model from which the spectral analysis of wind-induced vibration loads were derived (wind velocity is given elsewhere and is non-Gaussian). The statistical parameters for the aeroelastic damping ς_i are restrained by the stability operational limits of the rotor blade system, whereas the terrain roughness length Z_0 is defined for plain terrain in low grass or steppe configurations.

Table 4.2. Aeroelastic random variables with Gaussian distributions.

Property	μ	σ
C_D	0.8	0.11
ς_i	0.006	0.0011
a_0	0.8	0.05
a_I	0.002	0.0005
Z_0 (low grass, steppe)	2.5 cm	0.0039 cm

Figure 4.9(a) depicts the coupled structural modal response of the rotor blades whereas Figure 4.9(b) shows the variations in the blade natural frequencies for different spinning rates. The torsion mode is computed as independent (uncoupled) amongst the eleven remaining mode shapes. Unitary normalization is applied with special attention paid to the four dominant modes (yaw, pitch, flap and lag). Yaw and pitch frequency modes increase linearly from the static position, whereas for larger spinning velocities (*e.g.*, $\Omega \approx 11$ rad/sec) axial, flap, lag and twist modes produce incremental changes at higher spinning rates. Thus, it is important to note that heave and sway modes become unpredictable at high velocities.

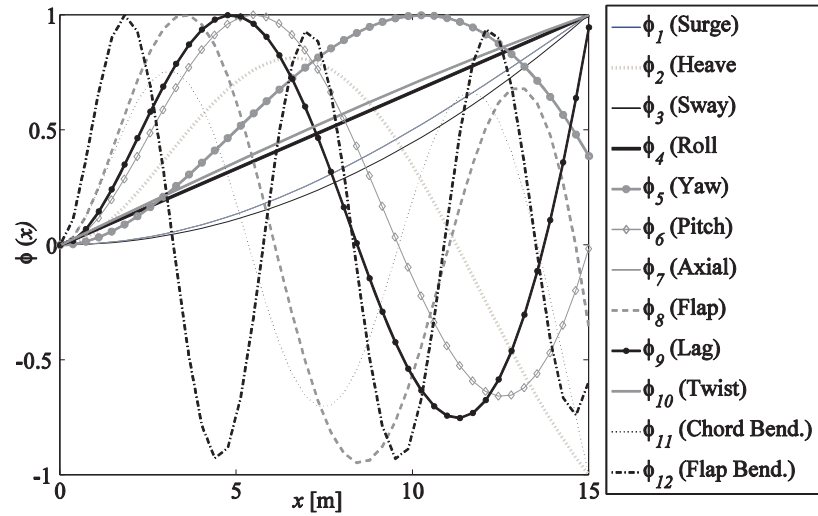


Figure 4.9(a). Structural dynamic response in local coordinate system xyz . Mode shapes.

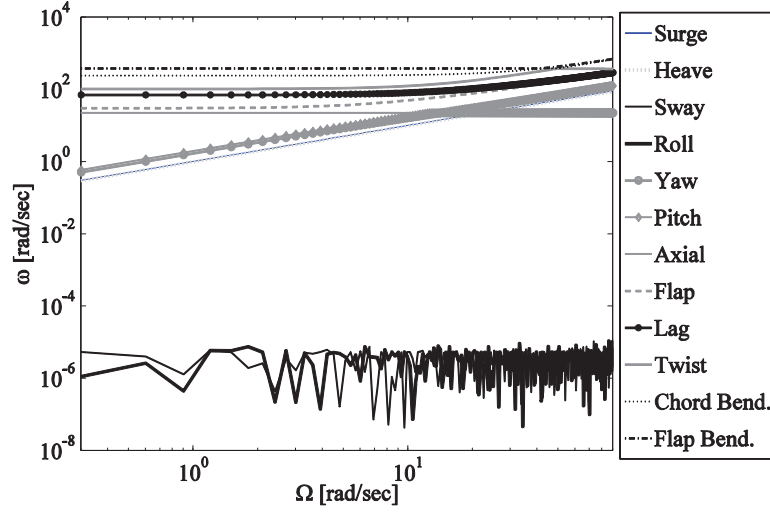


Figure 4.9(b). Structural dynamic response in local coordinate system xyz . Spinning rate velocity vs natural frequency, for the twelve blade spinning finite element modes.

Figure 4.10 presents the normalized-distributed random parameters due to the damping matrix coefficients, achieved for the 3000 realizations. The five sources of stochastic behavior described are constituted as Gaussian-normal with standard deviations commonly observed in the field. Strouhal number is based on Reynolds number intensities of the order $1 \times 10^4 \leq Re \leq 1 \times 10^7$. Figure 4.11 shows correlations of Reynolds number vs Strouhal number derived from these inputs, and for three different wind field intensities: mild wind events selected to excite the first resonant frequency of a generic tower design, heavy storm events designed to excite the second tower resonant frequency, and somewhat improbable extreme wind events designed to excite the third tower resonant frequency (for illustrative purposes). The Strouhal number term is restricted as defined in the wind design code limits for low Reynolds numbers (mild wind). For all cases shown in Figure 4.11 the vortex shedding frequencies are examined that match the critical wind velocity U_{cr} that may occur at the top of the tower. Simultaneously, Figure 4.12 depicts critical wind velocity profiles for both tower and blade substructures for the same three wind scenarios. It is important to note that the critical wind speed is reached at the rotor hub (nacelle) height and is extended as much as the blade length permits. Also, the boundary layer profile applied to the blade elements varies depending on the instantaneous rotation angle of the element (*e.g.*, Figure 4.12 is

depicting a blade with 90° punctual angle).

Figure 4.13 shows the random distribution of the critical wind velocity for extreme values Type I (Gumbel) computed on top of the wind tower (hub elevation), as being a major non-Gaussian contributor to the randomness of the model. It is observed that there is more variation for stronger wind fields and the along-wind velocity U should match U_{cr} for every Monte Carlo realization. Figure 4.14(a) depicts the Monin number or Similarity Coordinate, c , found using the model, which is correlated with the roughness length Z_0 and tends to be asymptotic for higher wind-inflow frequencies independent of blade geometry. This result demonstrates that the distribution of the along-wind spectral density function tends to be less pronounced at lower heights, and better distributed at higher ones, given a fixed frequency. The along-wind cross-correlation coefficient, $N(f)$, depicted in Figure 4.14(b), is plotted across the frequency spectra for two distinctive taper-swept degrees: $n_t = 0$ (constant variation) and $n_t = 2$ (parabolic variation). For this particular case, it can be demonstrated from the model that a geometry reduction of 90% at the tip of the blade implies an amplification of the spectral fluctuating deflection of as much as two times the intensity originally computed for $n_t = 0$. This result agrees with established theory that predicts that the ends of the blades are most critical for flexural displacements and that the narrowing of the exposed area in this region will lead to a reduction of the stresses recorded in those locations. Here it is evident that higher values of $N(f)$ imply a reduction of load demands (50% or more) in the stress intensity for $n_t = 0$ compared to $n_t = 2$ demonstrating the importance of the accurate modeling and the need to be able to consider higher-order cross-sectional variations. Furthermore, this load reduction effect becomes more evident at higher wind intensities, meaning that proper modeling of tapered-swept profiles is of particular importance to achieve accurate results. Figure 4.15 plots the along-wind, rotationally sampled spectrum for three wind intensities at different locations along the blade and for two tapered-swept degree variations, corresponding to one particular configuration at a 90° rotation angle. It can be seen that the nodal points of the blade experience slightly different wind load intensities with small or null variations between the $n_t = 0$ and $n_t = 2$ models, as expected. The rotationally

sampled projections trace three “humps” with pronounced scatter at higher wind speeds associated with the spinning velocity and these shift right or left depending on the actual spinning velocity Ω , assumed to be constant for each realization.

Figure 4.16 depicts the total spectral density (response) of blade deflections. It is noted that the fundamental frequency of the blade element is dominant, being the maximum peak within the spectrum, pulling the closest rotationally sampled “hump” up as the harmonic motion begins to be excited. This effect vanishes as the wind field intensity becomes large. Simultaneously, when the tapered-swept degree is $n_t = 2$ the lower peaks happen to be at approximately $\frac{3}{4}$ of distance from the blade root. The strain registered in this area decreases substantially compared to the constant cross-section scenario ($n_t = 0$), and is independent of the wind-field intensity as it is shown in Figure 4.16. For $n_t = 0$ two frequencies permute the peak displacements at frequencies $f = 10\text{Hz}$ or lower, whereas for $n_t = 2$ only one peak is exhibited and it exceeds the previous case in magnitude. At the same time, Figure 4.17 outlines the modal-combined number-of-peaks-per-unit-time coefficient $K_x(Z)$, and the largest-peak factor $K_{\dot{x}}(Z)$ for three different tapered-swept variations and wind field intensities. As was observed in Figure 4.16, lower peaks occur at approximately $\frac{3}{4} l_z$, and the number of peaks computed for $n_t = 2$ decrease in magnitude with respect to $n_t = 0$ and $n_t = 1$, but is not the case for $n_t = 1$ versus $n_t = 0$. This result indicates that the probability of exceeding expected peak load decreases at higher tapered-swept variations when wind field intensities are high. Figure 4.18 shows the modal combined mean square value of the fluctuating deflections and accelerations for the same cases studied above. The same pattern is observed for the structural response along the blade element, presuming a “resting” zone at the $\frac{3}{4} l_z$ point where deflections and accelerations are reduced 25% or more for parabolic geometric variations. It is interesting to note that displacements and accelerations hit their maximums at $1/3 l_z$ and l_z for $n_t = 2$, corresponding to the second and first natural frequencies, respectively. For $n_t = 0$, peaks generated by the second mode are shifted towards the mid span. A similar illustration is obtained for the along-wind peak responses (*e.g.*, peak displacement, peak acceleration, peak shear, and peak moment), delineated in Figure 4.19 for different

variations of both tapered-swept order and angular rotation $\theta = 90^\circ$. As expected, shears and moments are reduced by at least 50% along the outer two-thirds of the blade element where aerodynamic loading is critical. The previously identified relief zone, postulated at approximately $\frac{3}{4} l_z$, helps to accommodate the complex aerodynamic loadings that occur at $\frac{1}{2} l_z$ [Johansen *et al.* 2009]. This effect is not evident for the constant cross section model, $n_t = 0$, where loading is partially offset to this more critical region at $x = \frac{1}{2} l_z$. Differences are less critical at $x = 0 l_z$ (the hub location) where complex load paths and complex surface stability can be modeled whether blade geometry is improved or not. Corresponding curves are plotted in Figure 4.20 for along-wind peak responses at different rotational angles, (*i.e.*, $\theta = 0^\circ$, $\theta = 90^\circ$ and $\theta = 270^\circ$). It can be seen that for different tapered-swept coefficients, n_t , differences in stress distribution occur mostly around areas of peak magnitudes and. For example, at $\theta = 270^\circ$, the blade element produces its maximum perturbation when the highest wind scenario occurs, and its minimum when a mild wind occurs meaning that the horizontal position (*e.g.*, $\theta = 180^\circ$ or $\theta = 270^\circ$) becomes either the most risky or the more safe position for the blade depending on the intensity of the wind gust the structure is resisting at some given time.

Finally, Figure 4.21 provides a means to visualize potential failure regions by comparing the capacity probability density function (PDF) to the demand PDF for peak shear forces and peak bending moments (at the base of the rotor blades) generated by the Monte Carlo method using for 3000 random realizations. The loading capacity at the base (material strength) is modeled in this example as a normal distribution, taking EN-50308 as a standard norm to produce the PDF [CEN EN-50308 2004]. Here, the theoretical high wind demand curve overlaps the capacity (resistance) curve over a small percentage at its highest level. This overlapping region may be used to represent the probability of failure for the turbine under a given set of operating conditions.

It has been shown from Figure 4.16 to Figure 4.21 that blades with tapered-swept profiles tend toward lower flap-bending loads compared to those with baseline straight cross-sections requiring tapered-swept models to represent their vibrational behavior

accurately. Similarly, it is observed that energy dissipation increases with higher n_t degrees of tapered-swept variations. Under those conditions, the load demand tend to be, in general, lower for flap and chord bending modes. For the case of tapered cross-sections, the slender shape of the blade limits the influence of the extreme wind loading and wind-induced vibrations. This effect is achieved by minimizing the exposed area, but also by allowing for increased rotational speed. Numerical results from this study applied for different rotational angles show that every time a rotor blade passes through the tower shade at its lowest position, the rotor tends to push less against the tower substructure. In principle, this result shows that the blade model can amplify or dampen the tower harmonic oscillations when the rotational speed of the rotor blades matches the natural frequency of the tower, matching expectation.

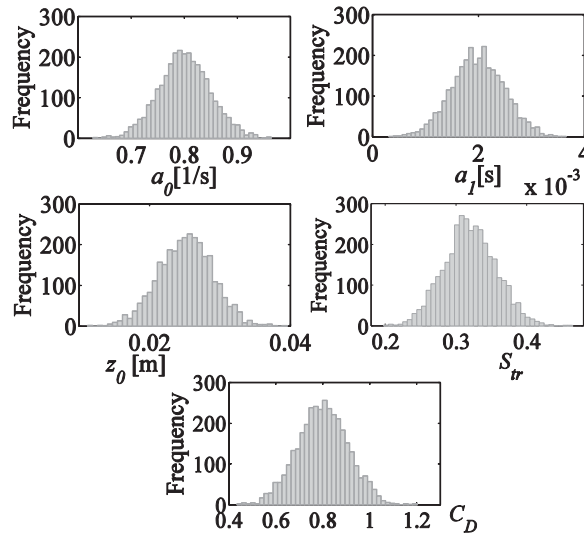


Figure 4.10. Normally distributed random-source parameters corresponding to damping (Rayleigh) matrix coefficients, terrain surface roughness length, Strouhal number, and drag coefficient from 3000 random realizations.

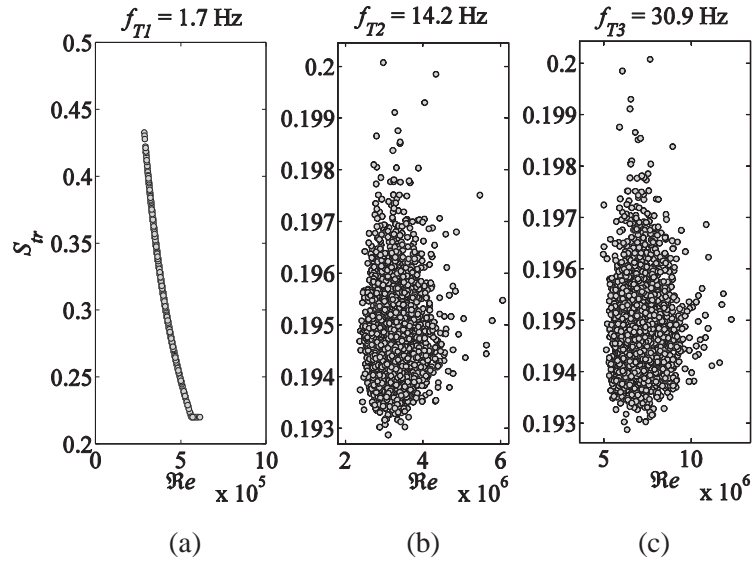


Figure 4.11. Wind-induced velocity calibration by linking Reynolds number and Strouhal number for the first three harmonic tower frequencies: (a) Mild wind ($U_{cr} = 12\text{MPH}$); Heavy storm ($U_{cr} = 113\text{MPH}$); Extreme conditions ($U_{cr} = 194\text{MPH}$).

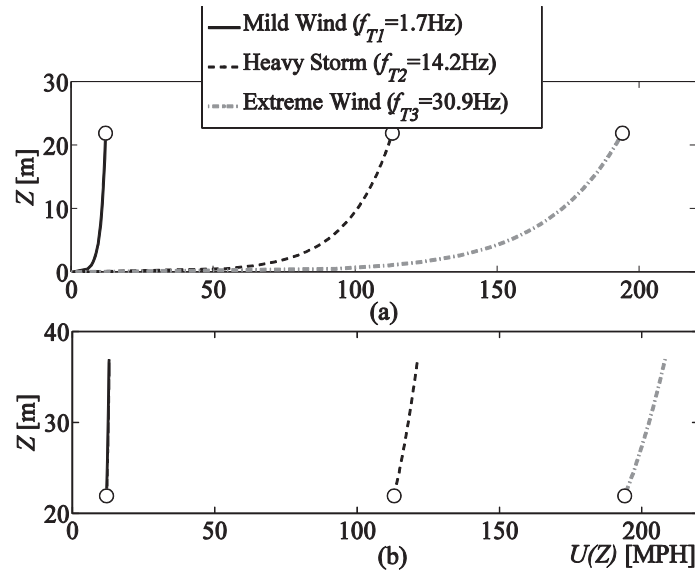


Figure 4.12. Critical wind velocity profiles (boundary layer) for (a) wind tower; and (b) wind blade at instantaneous rotation angle $\theta = 90^\circ$ evaluated for the first three fundamental tower frequencies.

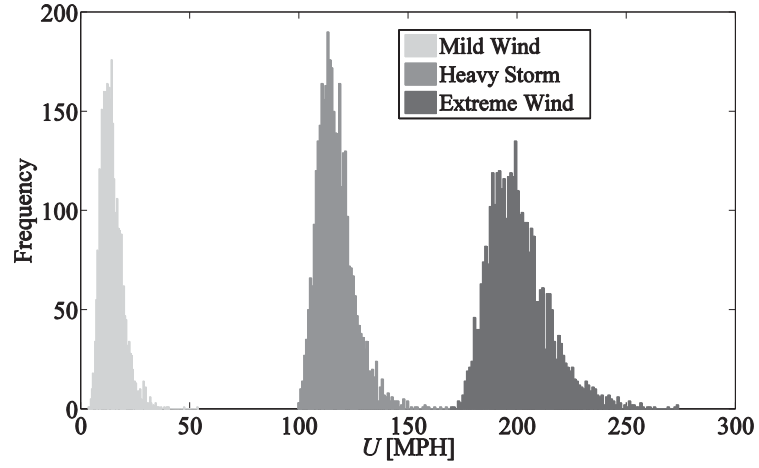


Figure 4.13. Critical wind velocity computation by random realizations adopting Extreme Value Type I (Gumbel) distribution.

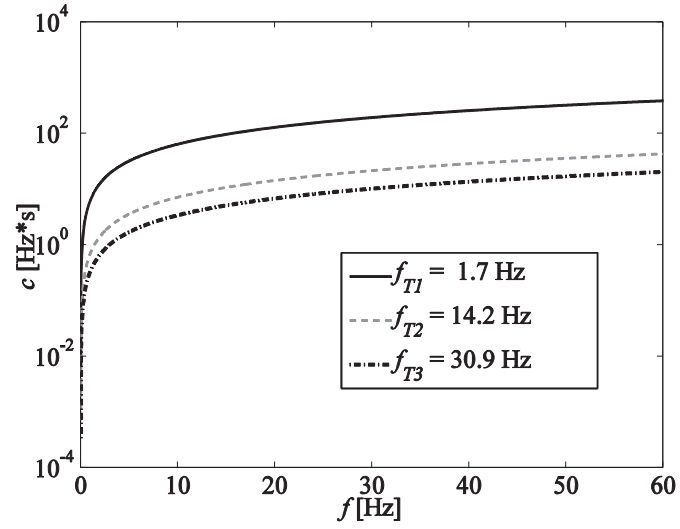


Figure 4.14(a). Monin number for the first three tower frequencies.

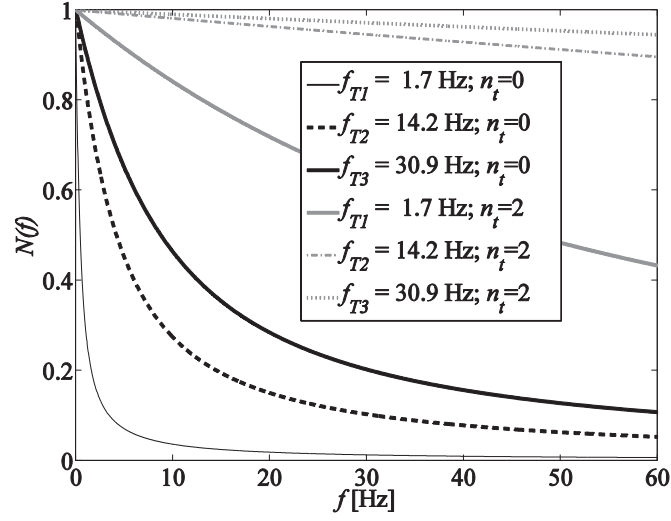


Figure 4.14(b). Along-wind cross-correlation coefficients for the first three tower frequencies.

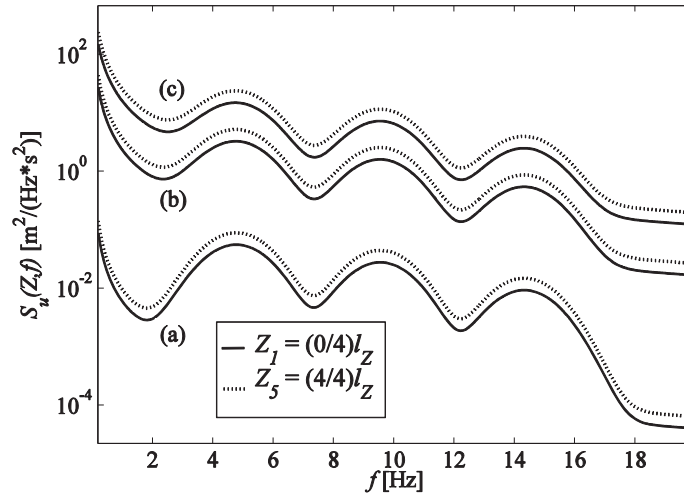


Figure 4.15. Rotationally sampled spectra for the first three tower resonant , computed at two different locations: hub elevation (Z_1) and tip of the blade (Z_5).

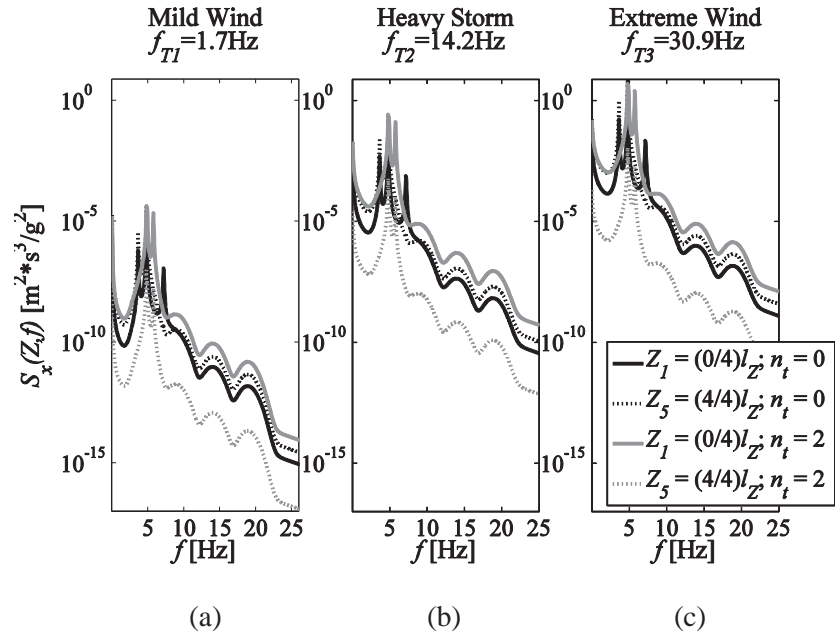


Figure 4.16. Total spectral density of blade deflections in the along-wind direction for three wind field intensities: (a) mild wind; (b) heavy storm; and (c) extreme event.

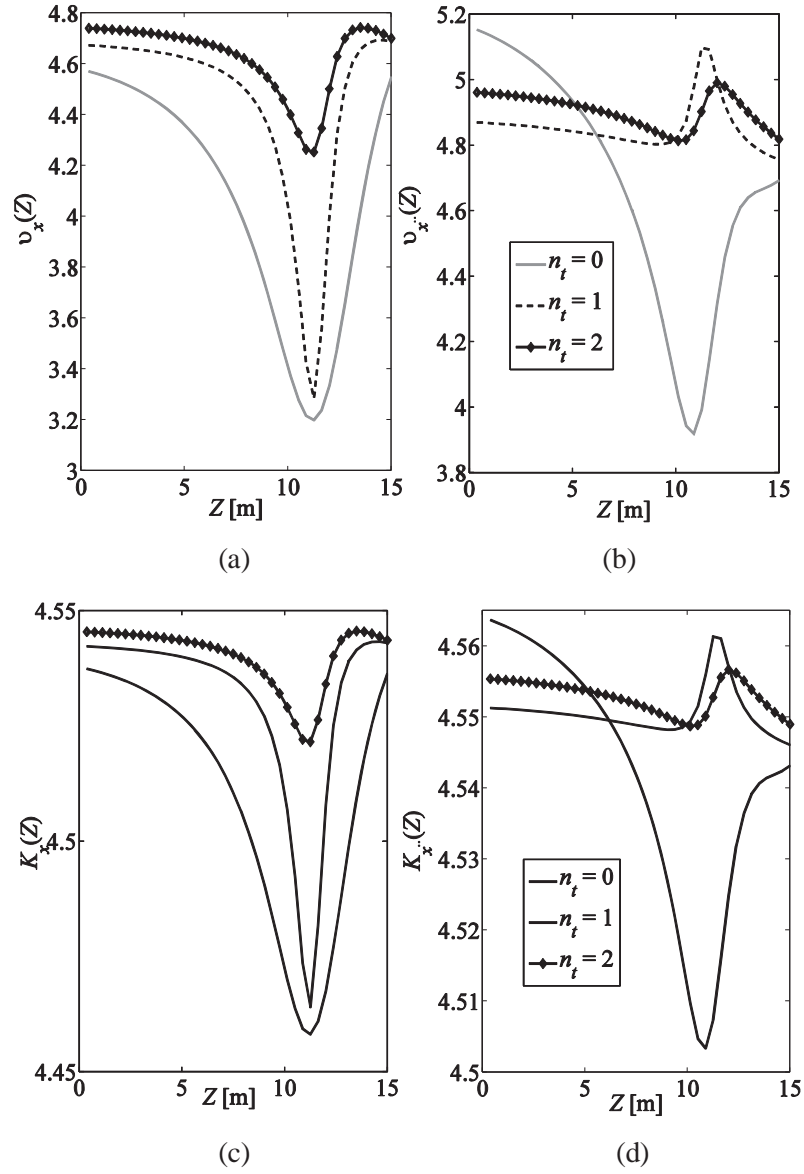


Figure 4.17. Modal combined number-of-peaks-per-unit-time ((a),(b)) and largest-peak factors ((c),(d)) computed for the second tower dominant frequency. Evaluated for fluctuating blade deflection ((a),(c)) and fluctuating blade acceleration ((b),(d)), respectively.

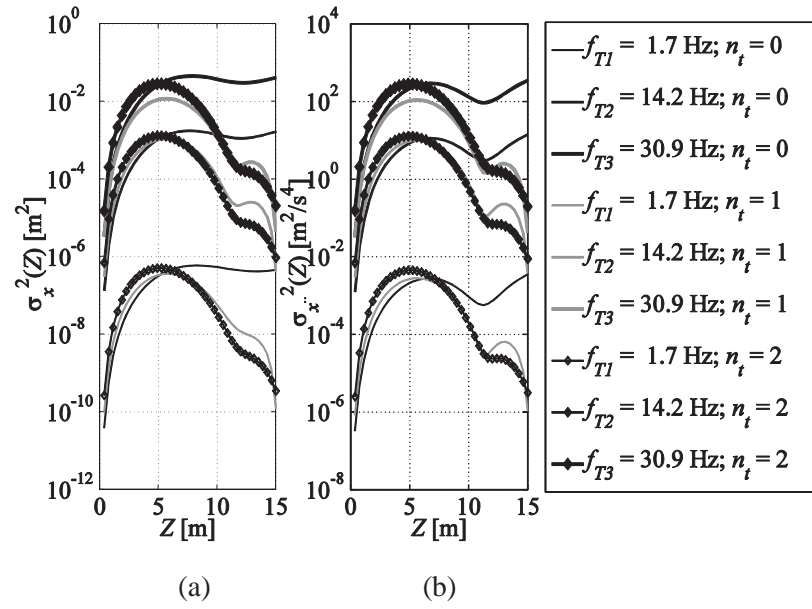


Figure 4.18. Modal combined mean square value of the fluctuating along-wind (a) deflection; and (b) acceleration of blade element computed for the first three tower dominant frequencies.

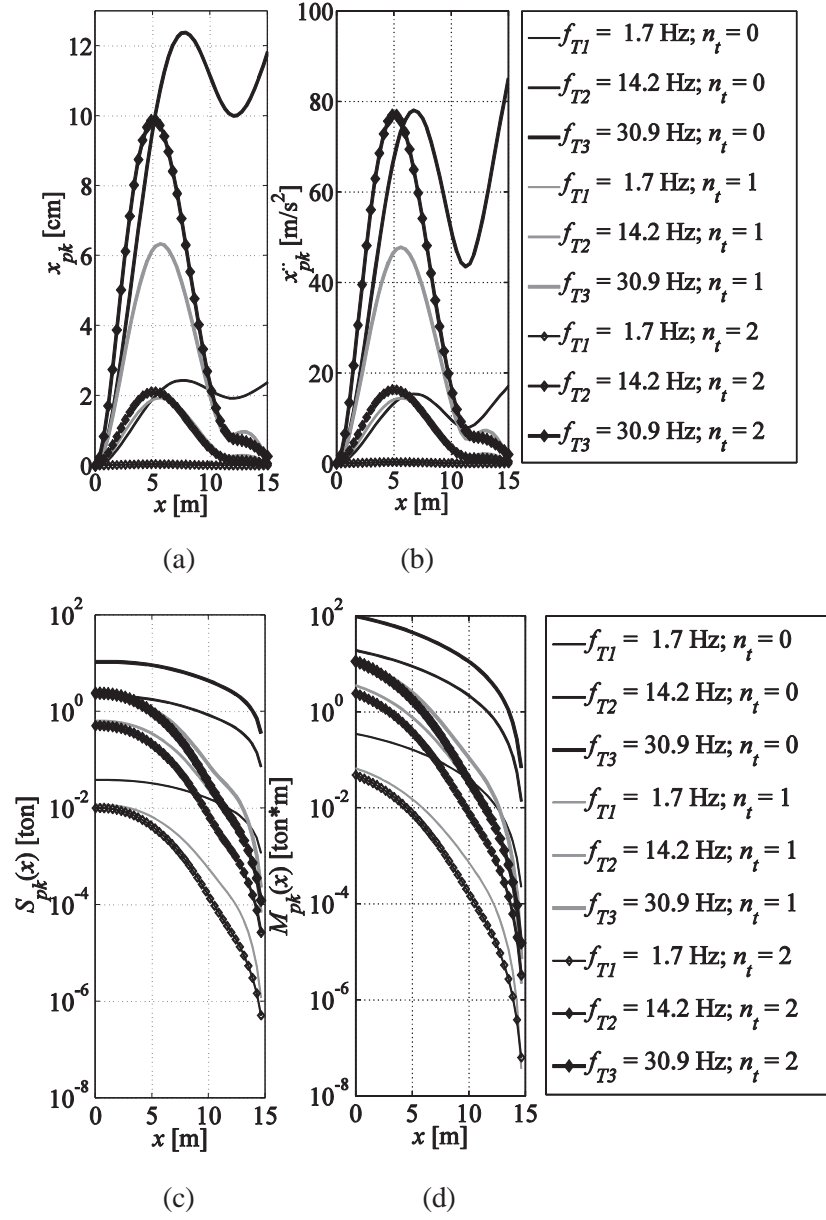


Figure 4.19. Along-wind peak response of blade element computed for the first three tower dominant frequencies. Evaluated for (a) fluctuating deflection and (bs) fluctuating acceleration, (c) peak shear (modal combined), and (d) peak moment (modal combined).

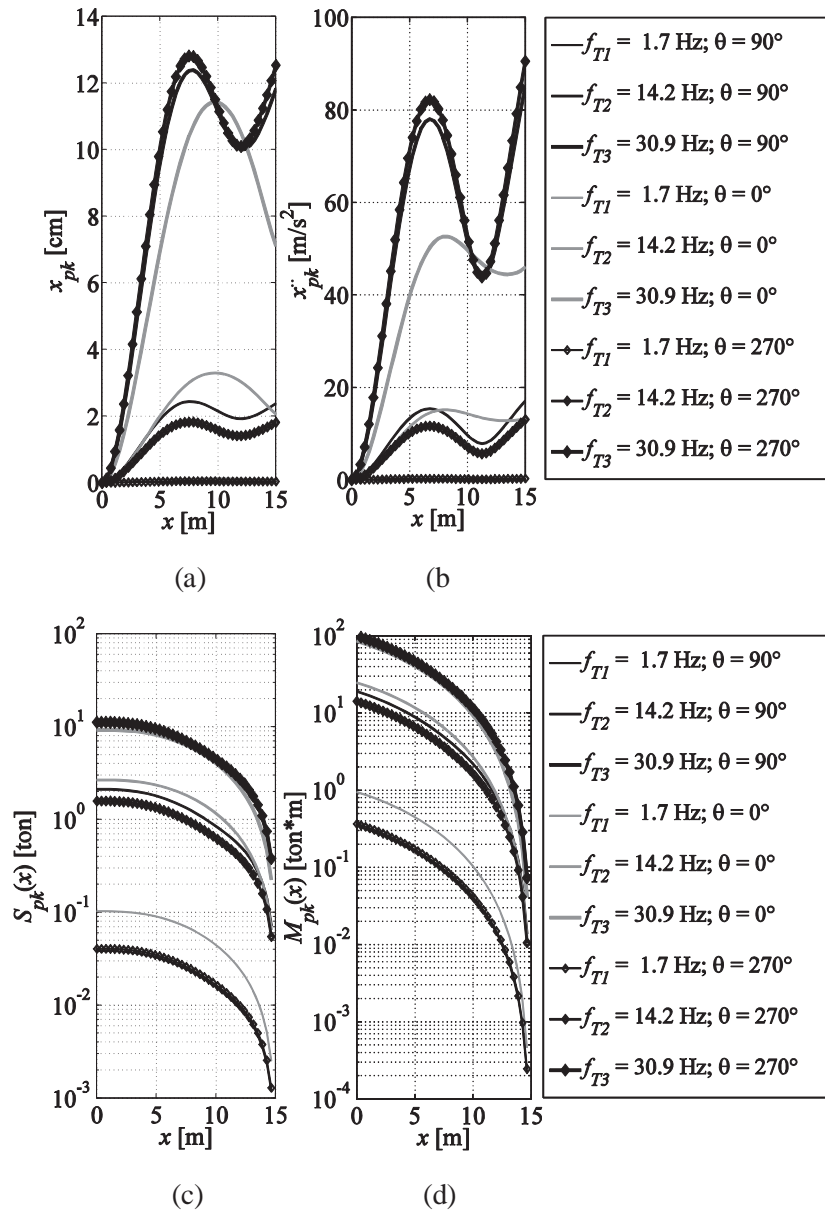
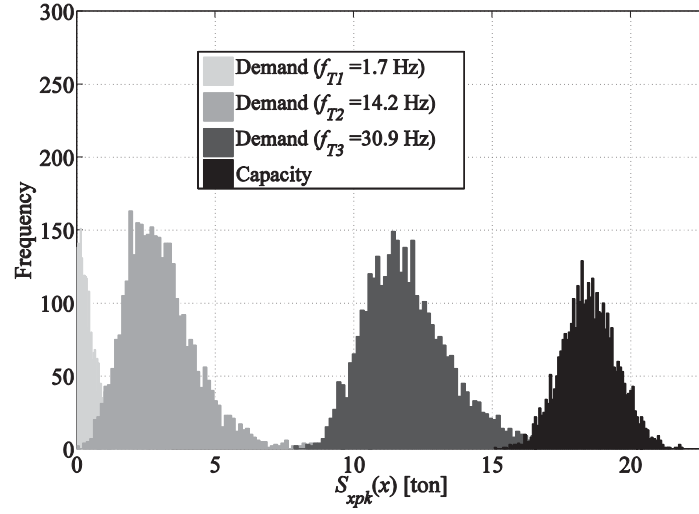
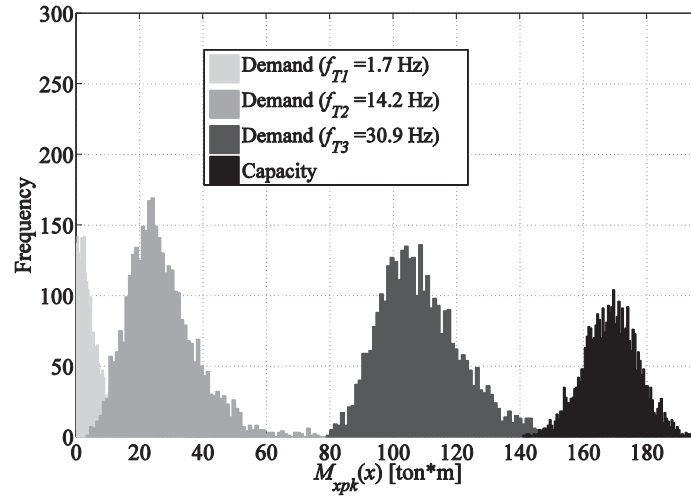


Figure 4.20. Along-wind peak response of blade element computed for the first three tower dominant frequencies, calculated for three rotation angles $n_i = 0$, and evaluated for (a) modal combined fluctuating deflection; (b) modal combined fluctuating acceleration; (c) peak shear (modal combined); and (d) peak moment (modal combined).



(a)



(b)

Figure 4.21. Example demand PDFs for (a) peak shear force; and (b) bending moment from 3000 random realizations with shear and moment nominal capacity (member strength) PDFs modeled using normal distributions in compliance with EN-50308.

4.6 Conclusions

In this study analytical probabilistic-aerodynamic results from a simulated full-scale wind turbine have been derived using a novel framework that integrates aeroelastic theory with spinning finite element analysis. Calibrated fundamental frequencies and mode shapes associated with each of the twelve inscribed degrees of freedom allotted to

the SPEs have been derived for complex blade geometries with torsion being treated as an uncoupled mode at this time. A theoretical framework of full n -degree tapered-swept variational characterization has been established with special attention paid to developing a numerically stable solution of the Lagrangian equations for parabolic tapered-swept cross sections to illustrate the usefulness of the method. Applicability to turbines with narrow and long blades has been demonstrated and show good agreement with previously established results.

While additional computational effort is required to derive the properties of high-order SPEs, once derived, they may be used in simulations with no additional computational cost. The benefits of using more accurate high-degree tapered-swept variations to model tapered-swept blades include more accurate modeling of energy dissipation effects, peak stresses, deflections, complex aerodynamic load paths, key fatigue loading parameters, and overall performance improvement. Better models of these behaviors may lead to more efficient (less conservative) designs in the future.

The framework presented here is intended to provide a means to model stochastic load/structure interactions (including flutter and buffeting) in complex turbine structures using relatively low-order models that may be suitable for use in automated monitoring applications including load estimation, performance evaluation, and structural health monitoring. However, the framework also provides an efficient platform to study the effects of important sources of uncertainty during the design phase, including lift coefficient, aeroelastic damping, material imperfections, soil-structure interaction, modeling assumptions, power transmission torque, nacelle weight, nacelle eccentricity, pitch controls, and others. Additional future work is recommended to study these effects using this new framework and also to integrate across-wind dynamics and tower coupling effects into the framework as well. In addition, torsion coupling and gyroscopic effects must be incorporated into the present aeroelastic framework by obtaining precise values of damping coefficients, frequencies and mode shapes with special attention paid to the undamped instability that is produced as a result of the gyroscopic motion. Integration of

torsional coupling and gyroscopic damping presents significant numerical challenges not encountered in the current framework and is the focus of ongoing work. It is time now to present Chapter 5 that introduces the guidelines and minuteness of an improved and more sophisticated tapered-swept spinning finite element that includes damped-gyroscopic effects combined with axial-flexural-torsional coupling. This effort eventually will pay off in a more reliable characterization of the tensor stresses involved in the mechanical behavior of rotating HAWT blades systems.

Chapter 5. Spinning Finite Element with Damped Gyroscopic Effects and Axial-Flexural-Torsional Coupling

Due to their aeroelastic behavior, tapered-swept blades offer the potential to optimize energy capture and decrease fatigue loads in horizontal-axis wind turbines (HAWT's). Nevertheless, modeling special complex geometries requires great computational effort necessitating tradeoffs between faster computation times and numerical accuracy. In this study, a condensed Spinning Finite Element (SFE) method approach is presented to alleviate this issue by means of modeling wind-turbine rotor blades using tapered-swept cross-sectional variations of arbitrary order via Lagrangian equations. Axial-flexural-torsional coupling is achieved for axial deformation, torsion, in-plane bending, and out-of-plane bending using a super-convergent element approach. Special attention is paid to damped yaw effects, expressed within the skew-symmetric damped gyroscopic matrix. The proposed framework is expected to be particularly useful to characterize models with complex-shape cross-sections at low computation cost. Dynamics of the model is achieved through modal analysis performed with complex-conjugate eigenvectors. By means of mass, damped gyroscopic, and stiffness (axial-flexural-torsional coupling) matrices condensation, a numerical example is carried out with different tapered and swept variation intensities over a practical range of spinning velocities in order to verify the suitability and convenience of the mathematical model. The paper concludes with some recommendations, and insights for practical design and optimization.

5.1 Introduction

Wind energy technologies have gathered substantial interest over the last decade. Wind technology applications are projected to represent at least 20% of the total energy production mix by 2025, and worldwide energy policies now promote the development of wind turbines and related technologies [DLR & EREC 2010]. In recent years, the commercial applications of horizontal-axis wind turbines (HAWTs) with high-rate power expectations have forced the design practice to maximize for size and slenderness in

order to optimize power generation [Lazaridis 2005]. Therefore, tower and rotor blades substructures have been subjected to both increasing wind-induced stresses and reduced factors of safety in design. The increase in the effective flow velocity from the root to the tip of the blade requires the shape to be tapered, twisted and pitched in order to achieve the optimum reduction in flow velocity over the entire length of the blade. Profiles with complex geometry, such as tapered-swept rotor beams with nonlinear mass and geometry variations have been promoted to alleviate combined dynamic strains, but also to delay the appearance of drag divergence within the rotor blades as well as substantially reducing hub loads [Lanzafame and Messina 2007]. As an example, Ashwill [Ashwill 2010] successfully designed, fabricated, tested and evaluated a sweep-twist adaptive blade that achieved 5-8% greater energy capture without higher operating loads on the turbine. Other investigations Bottasso *et al.* [Bottasso *et al.* 2011] have focused on the design of wind turbines with bend-twist coupling by exploiting the orthotropic properties of composite materials, then optimizing for minimum weight while satisfying design constraints such as maximum fatigue loads, maximum tip deflection and placement of natural frequencies, all for the same performance in annual energy production.

These extreme design conditions typically led the structure to alternate in a risk zone of induced stresses where second-order effects take place. Such effects can reflect wind-induced vibrations and wind-induced loading that threaten the integrity of the structure under both normal operational (serviceability) and harsh (extreme wind) conditions. The difficulties for modeling this phenomenon accurately arise when these second-order effects interfere with and distort the expected strain and loading field along the rotor blade [Malatkar 2003], typically designed for optimal energy capture. Examples of the consequences of these loadings are the torsion coupling and damped-gyroscopic responses. Those effects typically manifest themselves as nonlinear phenomena, and because of their impact in determining fatigue loads as well as limit states, they have warranted intensive attention over the past years. In this regard, the most serious effects include the yaw dynamics on free-yaw wind turbines as well as yaw loads on controlled-yaw rotors. A free-yaw rotor typically produces stresses caused by the weight of the

blades and directly induces dynamic moment pairs (commonly referred to as inertial torque). Fatigue loads, due to the exhaustion of the fabrication material, typically govern the maximum allowable strain field imposed on the structure. This yaw-related phenomenon has been identified as a real threat for the safety of the wind turbine. Yaw-motion effects are the second largest cause of structural failures in California's windmill farms [Lynette 1988]. The out-of-plane dynamic pair produced by the yaw-torque is also known as Coriolis moment or gyroscopic effect [Lalanne and Ferraris 1998]. These coupled effects, combined with the in-plane rotation movement, function as a longitudinal lever that depends on the actual spinning velocity Ω , but also on the mass distribution of the combined wind turbine gearbox, nacelle and rotor blades. It is expected that, after obtaining the dynamic properties of the wind turbine, the computed natural frequencies and modes of vibration will exhibit nonlinear variations as Ω increases. The resulting harmonics are called precession modes [Manwell and McGowan 2009], and occur when the mass or center of inertia of each cross section of the blade element describes out-of-plane orbits around the rotational trace that connect them; in other words, is the out-of-plane expansive inertia generated by the pitch projection in conjunction with the tapered-swept variation of the blade element (see Figure 5.1).

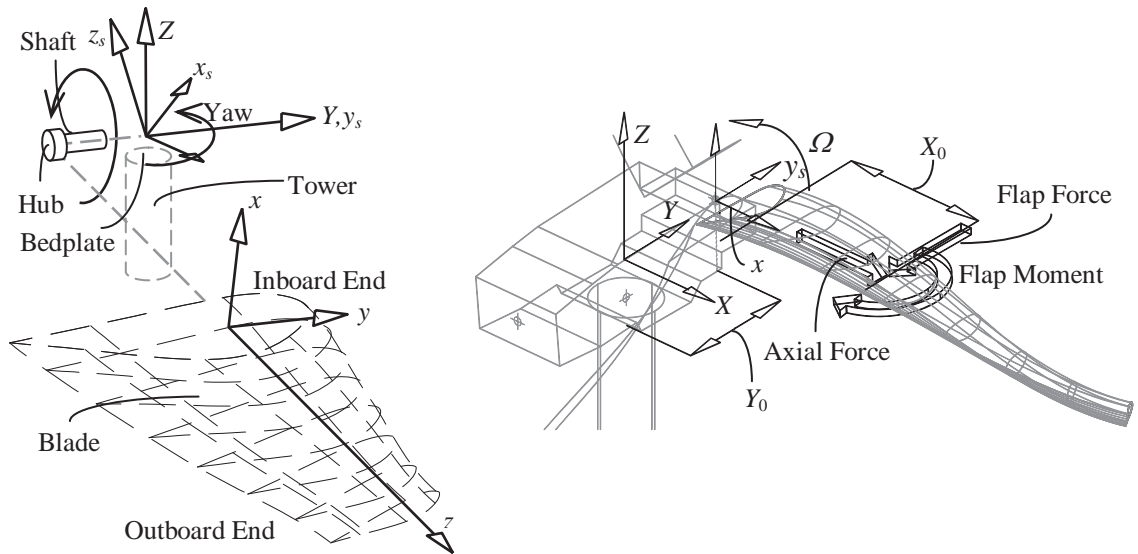


Figure 5.1. Precession mode of a wind turbine blade with tapered-swept variation.

This orbit is composed of two superimposed motions: (1) blade rotating around hub center (in-plane motion), (2) rotating shaft flexing around its non-deflected position (out-of-plane motion). Therefore, the rotor will be tracing in forward whirl mode or in backward whirl mode, depending on the actual orbit direction defined by the direction of the yaw motion. Those cyclic moments depend on the yaw rate and can easily exceed the allowable aerodynamic moments. Gyroscopic effects can be correctly determined by understanding the yaw motion behavior in conjunction with teetering motion around the tower bedplate. Rotational vibrations coming from the governing modes can produce this tremor around the wind tower longitudinal axis. In fact, the structural response is commonly treated as a superposition of the dominating lower bending modes at the inboard end: first flap (heave), first edge (yaw), and second flap (pitch). Those are correlated to some extent with the corresponding delayed degrees of freedom at the outboard end: third flap (lag), second edge (flap bending), and fourth flap (chord bending) [Griffin 2002]. Whatever the dominant mode is, torsion mode is typically treated as an uncoupled mode, but the fact of the matter is that bending and torsion vibrations are tightly coupled [Ozgumus and Kaya 2007]. Due to this coupling, there are always some secondary rotations present in the system that can produce severe errors in the measurement of the gyroscopic output. The gyroscopic output increases independently of how small or large the secondary rotation is. This increased gyroscopic output is called cross-axis error, and can be mistakenly interpreted as a natural feature of the gyroscopic output itself [Bhadbhade *et al.* 2008]. To tackle this problem, Weaver *et al.* [Weave *et al.* 1990] constructed a theory of coupled flexural/torsional vibration explicitly suited for thin-walled beams. Similarly, Oguamanam [Oguamanam 2003] studied a free flexural/torsional vibration of an Euler-Bernoulli beam with a rigid mass at the tip. Ganguli and Chopra [Ganguli and Chopra 1997] focused their attention on Optimization Analysis based on frequency constraints specific for the Helicopter Engineering community. This work consolidated an optimization scheme for mass distribution, blade stiffness (flap, lag, torsion), and blade geometry (sweep, anhedral and planform taper). Another study [Salarieh and Ghorashi 2006] considered the effects of shear deformation and rotary inertia, under free-vibration conditions, of a Timoshenko

beam with a rigid mass on the tip. Some studies suggest that plane instabilities occur when periodic motions dominate the non-linear vibrations of a cantilever beam [Lewandowski 1994]. Some authors have demonstrated the ability of the p -version finite element method to characterize these non-linear dynamics [MacEwen 2001]. However, few studies have treated this phenomenon using tapered-swept cross-section variations along the blade and the increased complexity that arises from the inclusion of axial-flexural-torsional coupling into the mathematical framework. This study intends to provide a theoretical framework, based on Spinning Finite Elements (SFE) adapted to tapered-swept blade profiles, to characterize basic rules of axial-torsion and flexion-torsion coupling. This correlation is modulated by superconvergent and Hermite cubic shape function descriptors that model the loading transmission from one end of the blade to the other.

Given the scope, limitations and complexities of the present investigation, aerodynamic analysis, such as wind-structure interaction, turbulence modeling, flutter and buffeting analysis, gust effects, wind spectral analysis, aerodynamic damping, wake effects, vortex shedding patterns and others related to wind engineering and aerodynamics will not be subject of this work. In this regard, no load shares are affiliated with or representative of wind aerodynamics or wind solicitations. Predefined modal testing loads with convenient frequency range (i.e. chirp, sinusoidal, impulse (blast)) have been applied to successfully excite the blade fundamental modes of vibration. The numerical example is pointed only to gain some knowledge, usefulness, convenience and computational advantages of the mathematical model. In summary, the main contribution of the present study is the proposition of a new matrix-based mathematical model for characterizing the structural (mechanical) response of n_t order tapered-swept wind turbine blades with the inclusion of both damped-gyroscopic effects and axial-flexural-torsional coupling. The combined triad of (1) tapered-swept characterization, (2) gyroscopic effects and (3) coupling modes is, in its core, the new contribution of this investigation. The numerical example given here serves only as an inducement to gain sensitivity of the model, acquire some insights of the limitations and capabilities of the methodology presented, and advance its

interpretation from a more physical (practical) perspective.

5.2 Spinning Finite Element

For this study blade elements are modeled as skeletal beam structures in rotational motion by means of a p -version spinning finite element method. Mass, damped gyroscopic, and stiffness matrices are derived using the principles of d'Alembert and Lagrangian equations. Leung [Leung and Fung 1988] has advanced towards a more accurate mathematical framework by proposing a closed-form solution method that obtains eigenvalues and eigenvectors of rotating beams with constant cross-section. A spinning finite element is defined explicitly for the gyroscopic or Coriolis effect. Equations of motion are derived using Lagrangian equations controlled by the spinning motion that creates deviation from that of classical theory for non-spinning structures. Leung [*ibid.* Leung and Fung 1988] derived a skeletal spinning finite element conformed by straight beam members. An expanded derivation for tapered-swept beam cross sections has been induced by Larwood [Larwood 2009] and is expanded in the present study for swept variations along the blade. Given the complexity of the mathematical scheme proposed, the incorporation of anisotropic models to characterize composite materials will be discarded in the analysis. For the present study, beams with non-uniform cross section, non-uniform thickness, elastic, homogeneous, and isotropic materials are considered only.

The proposed SFE takes on the concepts of small deformations. When the deformation of the wind turbine blade is small and the change in volume is almost negligible (i.e. less than 2% of the length of the blade), it is possible to approximate the deformation as linear. The scope and limitations of the proposed SFE oscillate in this range of operability only and is not valid for large blade deformations. At the same time, it is well known that the polar moment of inertia cannot be utilized to analyze any non-circular cross-section shaft for large deformations. According to Saint-Venant's torsion theory, for any non circular cross-sections, plane cross-sections will not remain plane after any torsional

deformation and, therefore, warping phenomenon will occur. Computation of strain distributions based on the assumption of planarity will give misleading results for large deformations. Nevertheless, for small twisting deflections (i.e. less than 2% of the length of the blade) the planar cross-section assumption can be treated as a manageable linear approximation. It should be emphasized that this problem of torsion and warping must need to be resolved for torsion-free and warping free cantilever problems in order to predict to a high accuracy the stress and strain distributions. The approximation of planar sections remained plane after twist is in fact an overestimate. That's why this assumption should be treated with extreme caution given the fact that the true value of torsion stiffness is typically only 1% or 2% of the value computed from the polar moment of inertia.

5.2.1 Kinematic Description

Consider three orthogonal axes for a tapered-swept beam element in rotation motion (see Figure 5.2): (1) xyz acting as the local principal axes, (2) $x_s y_s z_s$ directly associated with the rotational motion of the blade such that y_s coincides with the spinning axis, and (3) a global static (reference) XYZ through which the blades inertia is measured. Spinning y_s -axis coincides with Y -axis and rolls on top of the wind tower (at hub location).

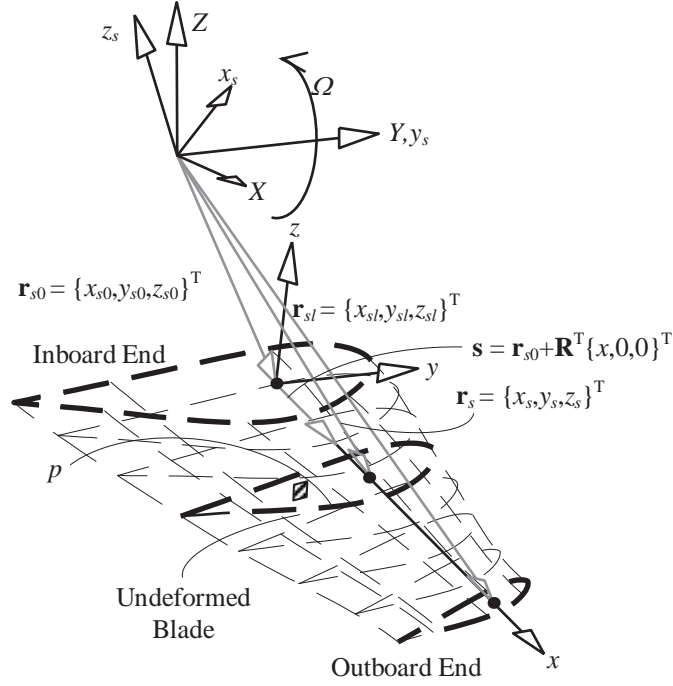


Figure 5.2. Local xyz , spinning $x_s y_s z_s$, and inertial XYZ orthogonal coordinate systems governing the rotating motion of a wind turbine blade.

Any point along the blade, from the local coordinate system point of view, is defined by $\mathbf{r}_s = \mathbf{r}_{s0} + \xi(\mathbf{r}_{sl} - \mathbf{r}_{s0})$, $0 \leq \xi \leq 1$, or $\mathbf{r}_s = \mathbf{r}_{s0} + s \mathbf{s}$, $0 \leq s \leq l$, l being the length of the blade [ibid. Leung and Fung 1988]. Here, \mathbf{r}_{s0} , \mathbf{r}_{sl} and \mathbf{r}_s are the position vectors along the blade controlled by the spinning coordinate system $x_s y_s z_s$, and $\mathbf{s} = \{1, 0, 0\}^T$ is the unit vector along the blade at the middle line longitudinal axis governed by the local reference. The spinning matrix is defined when the axis y_s is rotating:

$$\mathbf{\Omega} = \Omega(t) \begin{bmatrix} 0 & 0 & 1 \\ 0 & 0 & 0 \\ -1 & 0 & 0 \end{bmatrix} \quad (5.1)$$

$\Omega(t)$ is the spinning velocity with respect to the global-inertial co-ordinate system XYZ . Here, the spinning coordinate system $x_s y_s z_s$ does not necessarily rotate at constant speed

since the wind velocities acting on the blade exhibit constant variations in time, and even height. It is defined the relative (local) displacement components u , v and w of a tapered-swept cross section located at points x_s, y_s, z_s in the spinning coordinate system (see Figure 5.3), which are also velocity and space dependent.

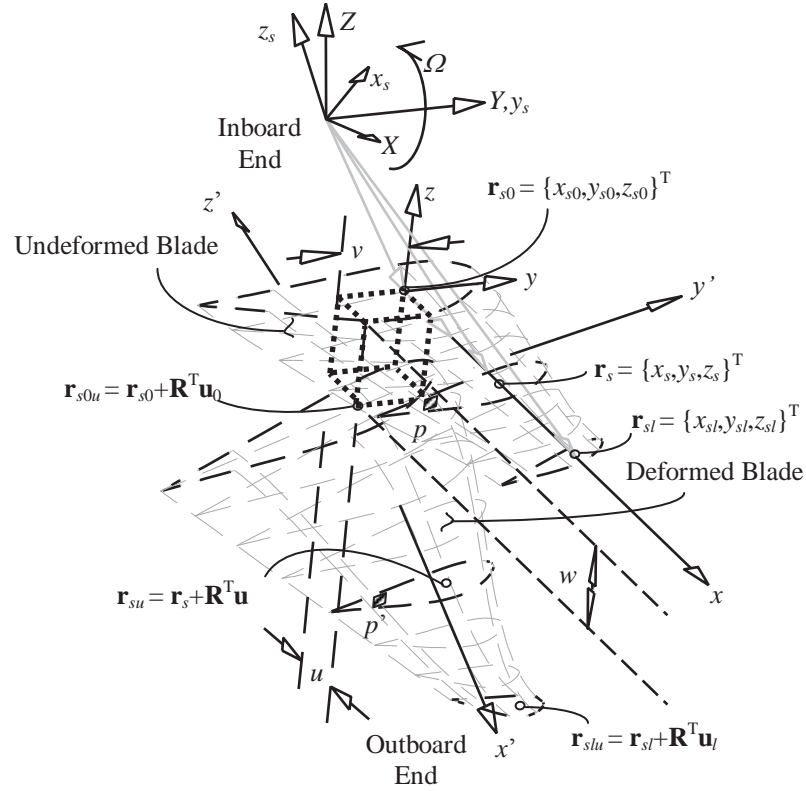


Figure 5.3. Total displacements u , v and w traced on the middle line (center of gravity) of a blade element, before and after deflection.

The longitudinal displacement u , transverse v and transverse w are traced along the axes x , y and z , respectively. According to Timoshenko theory for bending [Wang *et al.* 2000], Saint-Venant theory for torsion [Wempner and Talaslidis 2003], and excluding warping effects all expressed in local coordinates xyz (see Figure 5.4):

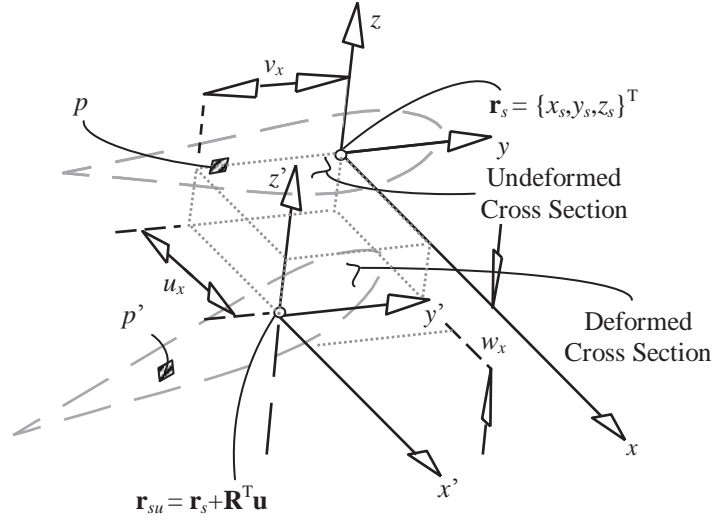


Figure 5.4. Relative displacements of a tapered-swept cross section that simultaneously presents rotations around three orthogonal axes to simulate geometric curving of the blade element.

$$\mathbf{u} = \mathbf{u}_0 + \mathbf{u}_r$$

$$\begin{Bmatrix} u(x, y, z, t) \\ v(x, y, z, t) \\ w(x, y, z, t) \end{Bmatrix} = \begin{Bmatrix} u_x(x, t) \\ v_x(x, t) \\ w_x(x, t) \end{Bmatrix} + \begin{Bmatrix} -y\psi_x(x, t) + z\phi_x(x, t) \\ y\cos(\theta_x(x, t)) - y - z\sin(\theta_x(x, t)) \\ y\sin(\theta_x(x, t)) + z\cos(\theta_x(x, t)) - z \end{Bmatrix} \quad (5.2)$$

where \mathbf{u}_0 is the local displacement vector with no rotations on the cross section, \mathbf{u}_r is the local rotation vector with no displacements of the cross section, u_x is the longitudinal displacement, v_x one transversal displacement, and w_x the other transversal displacement drawn from the middle line (center of gravity) of the studied cross section, θ_x is the rotation around x -axis, ϕ_x rotation around y -axis, and ψ_x rotation around z -axis (see Figure 5.5). Similarly, coordinates x , y and z are the local reference of a point p that belongs to the cross section before deformation. The rotation of this plane affects the absolute deflections of the ending axial, bending, and torsion shapes. The same point p' after deformation of the cross-section located at x units from the inboard end, and at any given time t , when displacements u_x , v_x, w_x and rotations θ_x, ϕ_x, ψ_x are applied, will exhibit coordinates $\{x + u(x, y, z, t), y + v(x, y, z, t), z + w(x, y, z, t)\}^T$ (expressed in local

coordinates xyz) [Stoykov and Ribeiro 2013]. Now, let \mathbf{u} and \mathbf{u}_s be the deflection vectors along the principal beam axes with reference to the local xyz and spinning $x_s y_s z_s$ coordinate systems, respectively.

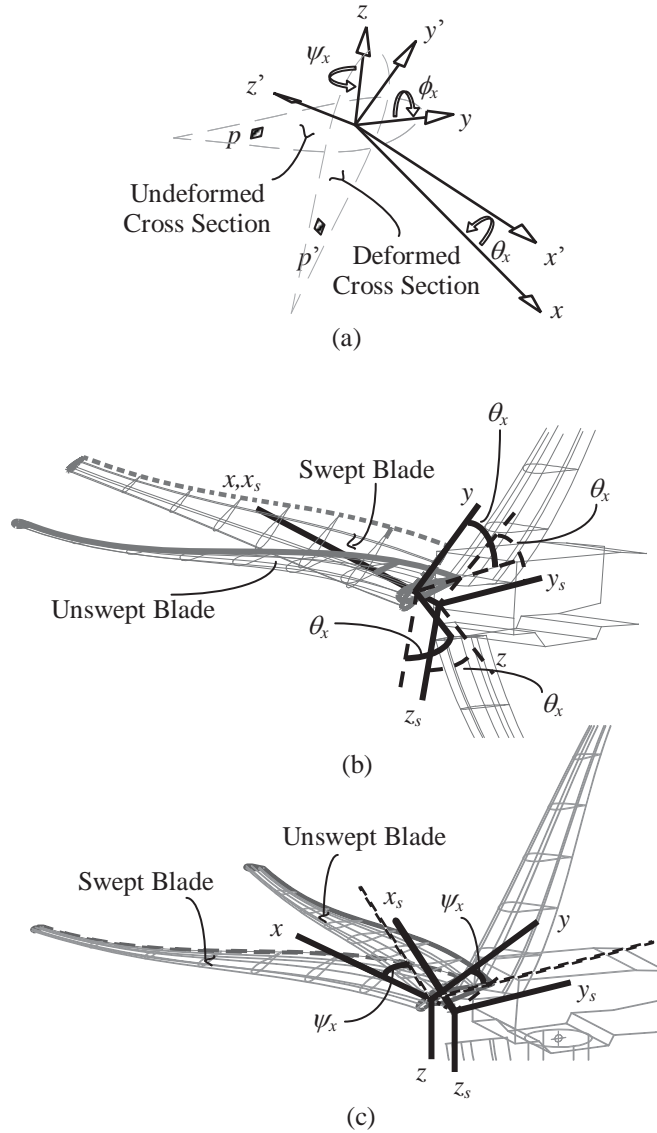


Figure 5.5. Angular (swept) displacements around three orthogonal axes on the middle line of the deflected cross-section. (a) Schematic, (b) swept around x_s axis (angle of incidence, twist angle or relative pitch angle), (c) swept around z_s axis (relative cone angle).

It is said that $\mathbf{u} = \{u(x, y, z, t), v(x, y, z, t), w(x, y, z, t)\}^T$ and the transformation basis $\mathbf{u}_s = \mathbf{R}^T \mathbf{u}$ and $\mathbf{u} = \mathbf{R} \mathbf{u}_s$ are valid across the blade length, where \mathbf{R} is the transformation matrix between the spinning $x_s y_s z_s$ and the local xyz coordinate systems (see Figure 5.6). By definition:

$$\mathbf{R} = \begin{bmatrix} \alpha_{11} & \alpha_{12} & \alpha_{13} \\ \alpha_{21} & \alpha_{22} & \alpha_{23} \\ \alpha_{31} & \alpha_{32} & \alpha_{33} \end{bmatrix} \quad (5.3)$$

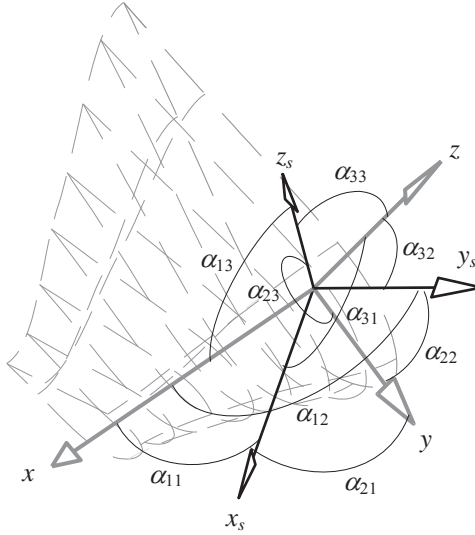


Figure 5.6. Direction cosines that conform the base transformation matrix \mathbf{R} from spinning $x_s y_s z_s$ to local xyz coordinate system.

For a given point $\mathbf{r}_s = \{x_s, y_s, z_s\}^T$, before deformation and between inboard and outboard ends, there exists a correspondent deflected point \mathbf{r}_{su} governed by the spinning coordinate system $x_s y_s z_s$ such that $\mathbf{r}_{su} = \mathbf{r}_s + \mathbf{u}_s$ or $\mathbf{r}_s + \mathbf{R}^T \mathbf{u}$. In other words:

$$\mathbf{r}_{su} = \begin{Bmatrix} x_s \\ y_s \\ z_s \end{Bmatrix} + \begin{bmatrix} \alpha_{11} & \alpha_{12} & \alpha_{13} \\ \alpha_{21} & \alpha_{22} & \alpha_{23} \\ \alpha_{31} & \alpha_{32} & \alpha_{33} \end{bmatrix} \begin{Bmatrix} u(x, y, z, t) \\ v(x, y, z, t) \\ w(x, y, z, t) \end{Bmatrix} \quad (5.4)$$

In order to compute the inertial forces (virtual work) of a general point p during rotation, it is necessary to determine the expression for the absolute velocity with respect to the inertial (fixed) coordinate system XYZ . Hence:

$$\mathbf{v}_s = \dot{\mathbf{r}}_{su} + \mathbf{\Omega} \mathbf{r}_{su} \quad (5.5)$$

$$\mathbf{v}_s = \mathbf{R}^T \dot{\mathbf{u}} + \mathbf{\Omega} \mathbf{r}_s + \mathbf{\Omega} \mathbf{R}^T \mathbf{u} \quad (5.6)$$

where $\dot{\mathbf{r}}_{su} = \dot{\mathbf{r}}_s + \dot{\mathbf{u}}_s = \mathbf{R}^T \dot{\mathbf{u}}$ given $\dot{\mathbf{r}}_s = \mathbf{0}$. Similarly:

$$\dot{\mathbf{u}} = \begin{Bmatrix} \dot{u}_x \\ \dot{v}_x \\ \dot{w}_x \end{Bmatrix} + \begin{Bmatrix} -y\dot{\psi}_x + z\dot{\phi}_x \\ -y\sin(\theta_x)\dot{\theta}_x - z\cos(\theta_x)\dot{\theta}_x \\ y\cos(\theta_x)\dot{\theta}_x - z\sin(\theta_x)\dot{\theta}_x \end{Bmatrix} \quad (5.7)$$

where superscript \cdot means differentiation with respect to time, whereas $\dot{u}_x, \dot{v}_x, \dot{w}_x, \theta_x, \dot{\theta}_x, \dot{\phi}_x$ and $\dot{\psi}_x$ are evaluated at the same cross-section of \mathbf{r}_s at a distance x along the middle line from the inboard end, at a given time t . The first vector term of Equation (5.7) is known as the relative velocity, whereas the second is the gyroscopic (Coriolis) velocity. Computing now the product $\mathbf{v}_s^T \mathbf{v}_s$ controlled by the spinning coordinate system:

$$\begin{aligned} \mathbf{v}_s^T \mathbf{v}_s = & \dot{\mathbf{u}}^T \mathbf{R} \mathbf{R}^T \dot{\mathbf{u}} + \mathbf{u}^T \mathbf{R} \mathbf{\Omega}^T \mathbf{\Omega} \mathbf{R}^T \mathbf{u} + \mathbf{r}_s^T \mathbf{\Omega}^T \mathbf{\Omega} \mathbf{r}_s + \\ & 2\dot{\mathbf{u}}^T \mathbf{R} \mathbf{\Omega} \mathbf{\Omega} + 2\dot{\mathbf{u}}^T \mathbf{R} \mathbf{\Omega} \mathbf{\Omega}^T \mathbf{u} + 2\mathbf{r}_s^T \mathbf{\Omega}^T \mathbf{\Omega} \mathbf{R}^T \mathbf{u} \end{aligned} \quad (5.8)$$

Noting that $\mathbf{R} \mathbf{R}^T = \mathbf{I}$ and $\mathbf{\Omega}^T \mathbf{\Omega} = \mathbf{\Omega}^2$ provided that:

$$\mathbf{\Omega}^2 = \mathbf{\Omega}^2(t) \begin{bmatrix} 1 & 0 & 0 \\ 0 & 0 & 0 \\ 0 & 0 & 1 \end{bmatrix} \quad (5.9)$$

For small displacements and small rotations the approximate identities $\sin \theta_x \approx \theta_x$, $\sin \phi_x \approx \phi_x$, $\sin \psi_x \approx \psi_x$, $\cos \theta_x \approx 1$, $\cos \phi_x \approx 1$ and $\cos \psi_x \approx 1$ are adopted. Local velocity vector will take the form [Stoykov and Ribeiro 2010]:

$$\dot{\mathbf{u}} \approx \begin{Bmatrix} \dot{u}_x - y\dot{\psi}_x + z\dot{\phi}_x \\ \dot{v}_x - y\theta_x\dot{\theta}_x - z\theta_x\dot{\theta}_x \\ \dot{w}_x + y\theta_x\dot{\theta}_x - z\theta_x\dot{\theta}_x \end{Bmatrix} \quad (5.10)$$

5.2.2 Shape Functions

For instance, local velocity vector can be expressed as $\dot{\mathbf{u}} = \dot{\mathbf{N}}_d \dot{\mathbf{d}}$, where:

$$\dot{\mathbf{N}}_d = \begin{bmatrix} 1 & 0 & 0 & 0 & z & -y \\ 0 & 1 & 0 & -y\theta_x - z & 0 & 0 \\ 0 & 0 & 1 & y - z\theta_x & 0 & 0 \end{bmatrix}; \quad \dot{\mathbf{d}} = \begin{Bmatrix} \dot{u}_x \\ \dot{v}_x \\ \dot{w}_x \\ \dot{\theta}_x \\ \dot{\phi}_x \\ \dot{\psi}_x \end{Bmatrix} \quad (5.11)$$

Geometric $\dot{\mathbf{N}}_d$ is the local-velocities shape matrix, and $\dot{\mathbf{d}}$ is the velocity vector along the neutral axis, as a function of time t and distance x , all governed by the local coordinate system. Similarly $\mathbf{u} = \mathbf{N}_d \mathbf{d}$ and,

$$\mathbf{N}_d = \begin{bmatrix} 1 & 0 & 0 & 0 & z & -y \\ 0 & 1 & 0 & z & 0 & 0 \\ 0 & 0 & 1 & y & 0 & 0 \end{bmatrix}; \quad \mathbf{d} = \{u_x, v_x, w_x, \theta_x, \phi_x, \psi_x\}^T \quad (5.12)$$

where \mathbf{N}_d is the local-displacements shape matrix, and \mathbf{d} is the displacement vector

along the neutral axis. The displacements of the blade neutral axis can be expressed in terms nodal coordinates, stating that $\mathbf{d} = \mathbf{N}\mathbf{q}$, $\dot{\mathbf{d}} = \mathbf{N}\dot{\mathbf{q}}$, $\mathbf{u} = \mathbf{N}_d\mathbf{N}\mathbf{q}$ and $\dot{\mathbf{u}} = \dot{\mathbf{N}}_d\mathbf{N}\dot{\mathbf{q}}$, where \mathbf{q} is the vector of generalized displacements and $\dot{\mathbf{q}}$ is the vector of generalized velocities. By definition $\mathbf{q} = \{\mathbf{q}_0, \mathbf{q}_l\}^T$ and $\dot{\mathbf{q}} = \{\dot{\mathbf{q}}_0, \dot{\mathbf{q}}_l\}^T$ where \mathbf{q}_0 are the generalized displacements at the inboard end $\mathbf{q}_0 = \{u_0, v_0, w_0, \theta_0, \phi_0, \psi_0\}^T$, and \mathbf{q}_l are the correspondent generalized displacements at the outboard end $\mathbf{q}_l = \{u_l, v_l, w_l, \theta_l, \phi_l, \psi_l\}^T$. Same logic for $\dot{\mathbf{q}}_0$ and $\dot{\mathbf{q}}_l$ where $\dot{\mathbf{q}}_0 = \{\dot{u}_0, \dot{v}_0, \dot{w}_0, \dot{\theta}_0, \dot{\phi}_0, \dot{\psi}_0\}^T$ and $\dot{\mathbf{q}}_l = \{\dot{u}_l, \dot{v}_l, \dot{w}_l, \dot{\theta}_l, \dot{\phi}_l, \dot{\psi}_l\}^T$, all controlled by the local coordinate system xyz . Similarly, \mathbf{N} is the matrix of shape functions with dimensions 12x12 defined as [Fonseca and Ribeiro 2006]:

$$\mathbf{N} = \begin{bmatrix} \mathbf{N}^u(\xi) \\ \mathbf{N}^v(\xi) \\ \mathbf{N}^w(\xi) \\ \mathbf{N}^\theta(\xi) \\ \mathbf{N}^\phi(\xi) \\ \mathbf{N}^\psi(\xi) \end{bmatrix} = \begin{bmatrix} g_1(\xi) & g_2(\xi) & \cdots & g_{12}(\xi) \\ f_1(\xi) & f_2(\xi) & \cdots & f_{12}(\xi) \\ f_1(\xi) & f_2(\xi) & \cdots & f_{12}(\xi) \\ g_1(\xi) & g_2(\xi) & \cdots & g_{12}(\xi) \\ g_1(\xi) & g_2(\xi) & \cdots & g_{12}(\xi) \\ g_1(\xi) & g_2(\xi) & \cdots & g_{12}(\xi) \end{bmatrix} \quad (5.13)$$

where \mathbf{N}^u , \mathbf{N}^v , \mathbf{N}^w , \mathbf{N}^θ , \mathbf{N}^ϕ and \mathbf{N}^ψ are the shape function vectors for longitudinal along x , transverse across y , transverse across z , torsion around x , rotation around y , and rotation around z , respectively. Previous shape functions are controlled by the local coordinate system xyz , where $\xi = s/l$ is a non-dimensional local coordinate term in synchrony with the integration variable s (see Figure 5.2). Shape functions must follow the global geometric boundary conditions to correctly account for stress and strain distributions; because the developed model is declared for just one finite element, only twelve shape functions are needed per vector, one for each degree of freedom the blade element consists of (see Figure 5.7). For this study the first two longitudinal and torsional shape functions are assumed to be linear functions. On the contrary, the first four transverse shape functions are presumed to be Hermite cube functions [Ribeiro and Petyt 1999]. In

general:

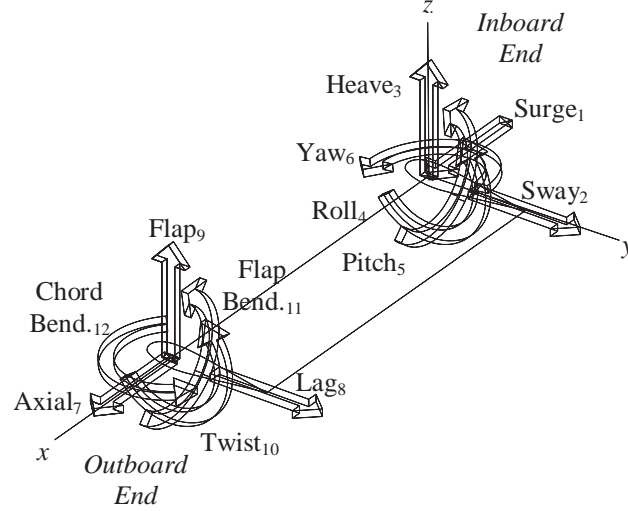


Figure 5.7. Degrees of freedom of the Spinning Finite Element in three orthogonal directions, expressed for both ends inboard and outboard.

$$\begin{aligned}
 g_{r-2}(\xi) &= \sum_{n=0}^{\text{int}(r/2)} \frac{(-1)^n (2r-2n-5)!!}{2^n n! (r-2n-1)!} \xi^{r-2n-1}, \quad r > 2 \\
 f_{r-4}(\xi) &= \sum_{n=0}^{\text{int}(r/2)} \frac{(-1)^n (2r-2n-7)!!}{2^n n! (r-2n-1)!} \xi^{r-2n-1}, \quad r > 4
 \end{aligned} \tag{5.14}$$

Another viable solution rather more sophisticated is presented by Chhabra and Ganguli [Chhabra and Ganguli 2010], who develop super-convergent functions that account for centrifugal stiffening effects, and are obtained from governing static homogeneous differential equations. Here, the modes that will control the stress distribution are axial deformation, in-plane bending, out-of-plane bending, and torsion.

5.3 Lagrangian Equation

The general expression for Lagrange equations is given by:

$$\frac{d}{dt} \left(\frac{\partial T}{\partial \dot{\mathbf{u}}} \right) - \frac{\partial T}{\partial \mathbf{u}} + \frac{\partial U}{\partial \mathbf{u}} + \frac{\partial W_{nc}}{\partial \mathbf{u}} - \frac{d}{dt} \frac{\partial W_{nc}}{\partial \dot{\mathbf{u}}} = \mathbf{F} \quad (5.15)$$

where T and U are the kinetic and strain energies, W_{nc} is the non-conservative work and \mathbf{F} is the generalized force vector corresponding to the absolute deflection \mathbf{u} . Kinetic energy T , strain energy U , and non-conservative work W_{nc} , can be defined as:

$$T = \frac{1}{2} \int_0^l \rho A(s) \mathbf{v}_s^T \mathbf{v}_s ds \quad (5.16)$$

$$U = \frac{1}{2} \int_0^l EA(s) \left(\frac{\partial u_x}{\partial s} \right)^2 ds + \frac{1}{2} \int_0^l EI_z(s) \left(\frac{\partial^2 v_x}{\partial s^2} \right)^2 ds + \frac{1}{2} \int_0^l EI_y(s) \left(\frac{\partial^2 w_x}{\partial s^2} \right)^2 ds + \frac{1}{2} \int_0^l GJ(s) \left(\frac{\partial \theta_x}{\partial s} \right)^2 ds + \frac{1}{2} \int_0^l F_c(s) \left(\frac{\partial v_x}{\partial s} \right)^2 ds + \frac{1}{2} \int_0^l F_c(s) \left(\frac{\partial w_x}{\partial s} \right)^2 ds \quad (5.17)$$

$$\delta W_{nc} = c_u \int_0^l \left(\frac{\partial u_x}{\partial t} \right) \delta u_x ds + c_v \int_0^l \left(\frac{\partial v_x}{\partial t} \right) \delta v_x ds + c_w \int_0^l \left(\frac{\partial w_x}{\partial t} \right) \delta w_x ds + c_\theta \int_0^l \left(\frac{\partial \theta_x}{\partial t} \right) \delta \theta_x ds + c_\phi \int_0^l \left(\frac{\partial \phi_x}{\partial t} \right) \delta \phi_x ds + c_\psi \int_0^l \left(\frac{\partial \psi_x}{\partial t} \right) \delta \psi_x ds \quad (5.18)$$

where $\rho A(s)$, $EA(s)$, $A(s)$, $EI_y(s)$, $EI_z(s)$, $GJ(s)$ and $F_c(s)$ are the tapered-swept variations of mass density, elastic modulus, cross-section area, moments of inertia around y , moment of inertia around z , polar moment of inertia around x , and generalized axial (centrifugal) force, respectively. As mentioned before, the material presumes an equivalent uniform modulus of elasticity for the characterized homogeneous-isotropic material. Simultaneously, c_u , c_v , c_w , c_θ , c_ϕ and c_ψ are damping coefficients for u_x , v_x , w_x , θ_x , ϕ_x , ψ_x , respectively. For convenience, both the strain energy U and the non-conservative work W_{nc} are expressed in local coordinates, and because the kinetic energy quantity is independent from the system of reference it can be conveniently denoted in terms of spinning coordinates $x_s y_s z_s$. By definition $\delta W_{nc} = \partial W_{nc} / \partial \mathbf{u} - d(\partial W_{nc} / \partial \dot{\mathbf{u}}) / dt$ where δ is the variation or the difference between two paths of the non-conservative work

for a given time t , can be conceived as a virtual change of configuration occurring at constant time, and consistent with the kinematic constraints of the system (otherwise arbitrary). In general, the operator δ follows the same rules as the derivatives but time is not included in the equation. The integration variable s sweeping along the blade is depicted in Figure 5.2. For tapered cross sections [*ibid.* Larwood 2009], now expanding for decreasing non-linear gradient variations across the span of the blade:

$$\begin{aligned} \Gamma(s) &= \Gamma_0, \quad n_t = 0 \\ \Gamma(s) &= \Gamma_0 \sqrt[n_t]{1 + \left(\sqrt[n_t]{\Gamma_l/\Gamma_0} - 1 \right) \frac{s}{l}}, \quad n_t = 1, 2, 3, \dots \end{aligned} \quad (5.19)$$

$$\left\{ \begin{matrix} \Gamma_0 \\ \Gamma_l \end{matrix} \right\} = \left\{ \begin{matrix} EA_0 \\ EA_l \end{matrix} \right\} = \left\{ \begin{matrix} EI_{y0} \\ EI_{yl} \end{matrix} \right\} = \left\{ \begin{matrix} EI_{z0} \\ EI_{zl} \end{matrix} \right\} = \left\{ \begin{matrix} GJ_0 \\ GJ_l \end{matrix} \right\} = \left\{ \begin{matrix} \rho A_0 \\ \rho A_l \end{matrix} \right\} = \left\{ \begin{matrix} \rho I_{p0} \\ \rho I_{pl} \end{matrix} \right\}$$

where the zero subscript represents the material/geometry property at the inboard node, the l subscript term stands for the property at the outboard node, and the integer value n_t stands for the tapered-swept order or function degree. The wildcard variable $\Gamma(s)$ can take pairs according to the property to be computed, and can be either one of the studied parameters of the cross-section/material properties at location s ($0 \leq s \leq l$). Similarly, polar moments of inertia of mass ρI_{p0} and ρI_{pl} , are defined at the same locations based on the gross (effective) section properties of the blade (Figure 5.8).

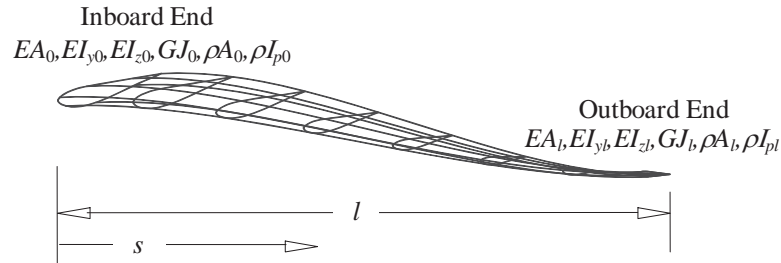


Figure 5.8. Tapered-swept gradient variations of mechanical properties at the inboard and outboard ends of a Spinning Finite Element.

5.3.1 Kinetic Energy

Expanding the product $\mathbf{v}_s^T \mathbf{v}_s$ towards the integration of Equation (5.16):

$$\begin{aligned} \mathbf{v}_s^T \mathbf{v}_s = & \dot{\mathbf{q}}^T \mathbf{N}^T \dot{\mathbf{N}}_d^T \mathbf{R} \mathbf{R}^T \dot{\mathbf{N}}_d \mathbf{N} \dot{\mathbf{q}} + \\ & \mathbf{q}^T \mathbf{N}^T \mathbf{N}_d^T \mathbf{R} \boldsymbol{\Omega}^T \boldsymbol{\Omega} \mathbf{R}^T \mathbf{N}_d \mathbf{N} \mathbf{q} + \\ & \mathbf{r}_s^T \boldsymbol{\Omega}^T \boldsymbol{\Omega} \mathbf{r}_s + 2 \dot{\mathbf{q}}^T \mathbf{N}^T \dot{\mathbf{N}}_d^T \mathbf{R} \boldsymbol{\Omega} \boldsymbol{\Omega}^T + \\ & 2 \dot{\mathbf{q}}^T \mathbf{N}^T \dot{\mathbf{N}}_d^T \mathbf{R} \boldsymbol{\Omega} \boldsymbol{\Omega}^T \mathbf{N}_d \mathbf{N} \mathbf{q} + \\ & 2 \mathbf{r}_s^T \boldsymbol{\Omega}^T \boldsymbol{\Omega} \mathbf{R}^T \mathbf{N}_d \mathbf{N} \mathbf{q} \end{aligned} \quad (5.20)$$

The first, second, third, fourth, fifth, and sixth terms of Equation (5.20) are associated with mass inertia, spinning stiffness, non-conservative kinetic energy, centrifugal force, gyroscopic effect, and spinning force, respectively. The contribution of the blade element to the total kinetic energy, calculated by traditional assembly method, is found to be:

$$T_B = \frac{1}{2} \dot{\mathbf{q}}^T \mathbf{M}_B \dot{\mathbf{q}} + \dot{\mathbf{q}}^T \mathbf{G}_B \mathbf{q} + \frac{1}{2} \mathbf{q}^T \mathbf{K}_{\Omega B} \mathbf{q} + \dot{\mathbf{q}}^T \mathbf{F}_{cB} + \mathbf{F}_{\Omega B}^T \mathbf{q} + T_0 \quad (5.21)$$

where,

$$\begin{aligned} \mathbf{M}_B = \int_0^l \rho A(s) \mathbf{m} ds; \quad \mathbf{G}_B = \int_0^l \rho A(s) \mathbf{g} ds; \quad \mathbf{K}_{\Omega B} = \int_0^l \rho A(s) \mathbf{k}_{\Omega} ds \\ \mathbf{F}_{cB} = \int_0^l \rho A(s) \mathbf{f}_c ds; \quad \mathbf{F}_{\Omega B} = \int_0^l \rho A(s) \mathbf{f}_{\Omega} ds; \quad T_0 = \int_0^l \rho A(s) t_0 ds \end{aligned} \quad (5.22)$$

$$\begin{aligned} \mathbf{m} &= \mathbf{N}^T \dot{\mathbf{N}}_d^T \dot{\mathbf{N}}_d \mathbf{N} \\ \mathbf{g} &= \mathbf{N}^T \dot{\mathbf{N}}_d^T \mathbf{R} \boldsymbol{\Omega} \boldsymbol{\Omega}^T \mathbf{N}_d \mathbf{N} \\ \mathbf{k}_{\Omega} &= \mathbf{N}^T \mathbf{N}_d^T \mathbf{R} \boldsymbol{\Omega}^T \boldsymbol{\Omega} \mathbf{R}^T \mathbf{N}_d \mathbf{N} \\ \mathbf{f}_c &= \mathbf{N}^T \dot{\mathbf{N}}_d^T \mathbf{R} \boldsymbol{\Omega} \boldsymbol{\Omega}^T \\ \mathbf{f}_{\Omega} &= \mathbf{r}_s^T \boldsymbol{\Omega}^T \boldsymbol{\Omega} \mathbf{R}^T \mathbf{N}_d \mathbf{N} \\ t_0 &= \mathbf{r}_s^T \boldsymbol{\Omega}^2 \mathbf{r}_s \end{aligned} \quad (5.23)$$

5.3.2 Strain Energy

Expressions for the strain energy necessitate derivation of the local displacement vector \mathbf{d} with respect of the integration variable s . Say $\partial \mathbf{d} / \partial s = \partial \mathbf{N}(s) \mathbf{q} / \partial s = \mathbf{N}' \mathbf{q}$ and $\partial^2 \mathbf{d} / \partial s^2 = \partial^2 \mathbf{N}(s) \mathbf{q} / \partial s^2 = \mathbf{N}'' \mathbf{q}$, where $\mathbf{N}' = [\mathbf{N}^{u'}, \mathbf{N}^{v'}, \mathbf{N}^{w'}, \mathbf{N}^{\theta'}, \mathbf{N}^{\phi'}, \mathbf{N}^{\psi'}]^T$ and $\mathbf{N}'' = [\mathbf{N}^{u''}, \mathbf{N}^{v''}, \mathbf{N}^{w''}, \mathbf{N}^{\theta''}, \mathbf{N}^{\phi''}, \mathbf{N}^{\psi''}]^T$. For stiffness purposes, there is no need for the displacement field $\mathbf{u} = \{u(x, y, z, t), v(x, y, z, t), w(x, y, z, t)\}$, but instead the displacements on the middle line \mathbf{d} in the local coordinate system xyz may be used. In principle:

$$\begin{aligned} \left(\frac{\partial u_x}{\partial s} \right)^2 &= \mathbf{N}^{u'}{}^T \mathbf{N}^{u'} \mathbf{q}; & \left(\frac{\partial^2 v_x}{\partial s^2} \right)^2 &= \mathbf{N}^{v''}{}^T \mathbf{N}^{v''} \mathbf{q} & \left(\frac{\partial^2 w_x}{\partial s^2} \right)^2 &= \mathbf{N}^{w''}{}^T \mathbf{N}^{w''} \mathbf{q} \\ \left(\frac{\partial \theta_x}{\partial s} \right)^2 &= \mathbf{N}^{\theta'}{}^T \mathbf{N}^{\theta'} \mathbf{q}; & \left(\frac{\partial v_x}{\partial s} \right)^2 &= \mathbf{N}^{v'}{}^T \mathbf{N}^{v'} \mathbf{q} & \left(\frac{\partial w_x}{\partial s} \right)^2 &= \mathbf{N}^{w'}{}^T \mathbf{N}^{w'} \mathbf{q} \end{aligned} \quad (5.24)$$

The contribution of the blade element to the total strain energy, calculated by commonly known assembly method, is found to be:

$$U_B = \frac{1}{2} \mathbf{q}^T (\mathbf{K}_{eB} + \mathbf{K}_{cB}) \mathbf{q} \quad (5.25)$$

where:

$$\begin{aligned} \mathbf{K}_{eB} &= [EA(s) \mathbf{k}_{e1} + EI_z(s) \mathbf{k}_{e2} + EI_y(s) \mathbf{k}_{e3} + GJ(s) \mathbf{k}_{e4}] \\ \mathbf{K}_{cB} &= [\mathbf{k}_{c1} + \mathbf{k}_{c2}] \end{aligned} \quad (5.26)$$

$$\begin{aligned} \mathbf{k}_{e1} &= \int_0^l \mathbf{N}^{u'}{}^T \mathbf{N}^{u'} ds; & \mathbf{k}_{e2} &= \int_0^l \mathbf{N}^{v''}{}^T \mathbf{N}^{v''} ds; & \mathbf{k}_{e3} &= \int_0^l \mathbf{N}^{w''}{}^T \mathbf{N}^{w''} ds \\ \mathbf{k}_{e4} &= \int_0^l \mathbf{N}^{\theta'}{}^T \mathbf{N}^{\theta'} ds; & \mathbf{k}_{c1} &= \int_0^l F(s) \mathbf{N}^{v'}{}^T \mathbf{N}^{v'} ds; & \mathbf{k}_{c2} &= \int_0^l F(s) \mathbf{N}^{w'}{}^T \mathbf{N}^{w'} ds \end{aligned} \quad (5.27)$$

5.3.3 Non-Conservative Work

The variation of the non-conservative work term can be integrated by means of the

nodal coordinates and shape functions by applying the expanding Hamilton principle to each of the damping coefficients of which this energy term is composed. For example, for the case of the energy dissipation of the deflection u_x it can be seen that $\partial u_x / \partial t = \partial \mathbf{N}^u \mathbf{q} / \partial t = \mathbf{N}^u \dot{\mathbf{q}}$, $d(\partial u_x / \partial \dot{\mathbf{q}}) / dt = 0$ and $\partial u_x / \partial \mathbf{q} = \partial \mathbf{N}^u \mathbf{q} / \partial \mathbf{q} = \mathbf{N}^u$; therefore:

$$c_u \int_0^l \frac{\partial u_x}{\partial t} \delta u_x ds = c_u \int_0^l \frac{\partial u_x}{\partial t} \left(\frac{\partial u_x}{\partial \mathbf{q}} - \frac{d}{dt} \frac{\partial u_x}{\partial \dot{\mathbf{q}}} \right) ds = c_u \int_0^l \mathbf{N}^u \dot{\mathbf{q}} \mathbf{N}^u ds \quad (5.28)$$

Proceeding similarly for the rest of the damped energy dissipation terms are:

$$\begin{aligned} \delta W_{nc} &= \mathbf{C}_B \dot{\mathbf{q}} \\ \mathbf{C}_B &= [c_u \mathbf{C}_u + c_v \mathbf{C}_v + c_w \mathbf{C}_w + c_\theta \mathbf{C}_\theta + c_\phi \mathbf{C}_\phi + c_\psi \mathbf{C}_\psi] \\ \mathbf{C}_u &= \int_0^l \mathbf{N}^{uT} \mathbf{N}^u ds; \quad \mathbf{C}_v = \int_0^l \mathbf{N}^{vT} \mathbf{N}^v ds; \quad \mathbf{C}_w = \int_0^l \mathbf{N}^{wT} \mathbf{N}^w ds \\ \mathbf{C}_\theta &= \int_0^l \mathbf{N}^{\theta T} \mathbf{N}^\theta ds; \quad \mathbf{C}_\phi = \int_0^l \mathbf{N}^{\phi T} \mathbf{N}^\phi ds; \quad \mathbf{C}_\psi = \int_0^l \mathbf{N}^{\psi T} \mathbf{N}^\psi ds \end{aligned} \quad (5.29)$$

$$(5.30)$$

5.4 Equation of Motion

Retaking Lagrangian expansion from Equation (5.15) it is possible to apply the nodal displacement vector \mathbf{q} in two parts $\mathbf{q} = \mathbf{q}_{ss} + \mathbf{q}_{ns}$, where \mathbf{q}_{ss} is the steady-state nodal displacement, and \mathbf{q}_{ns} is the non-steady nodal coordinate oscillating in the close proximity of \mathbf{q}_{ss} . For steady conditions only $\mathbf{q}_{ns} = \dot{\mathbf{q}}_{ns} = \dot{\mathbf{q}}_{ss} = \mathbf{q} = \mathbf{0}$, $\mathbf{q} = \mathbf{q}_{ss}$ and $\mathbf{F} = \mathbf{0}$. Now, from the expanded kinetic energy, strain energy, and non-conservative work, it can be said that:

$$\begin{aligned} T_B &= \frac{1}{2} \mathbf{q}_{ss}^T \mathbf{K}_{\Omega B} \mathbf{q}_{ss} + \mathbf{F}_{\Omega B}^T \mathbf{q}_{ss} + T_0 \\ U_B &= \frac{1}{2} \mathbf{q}_{ss}^T (\mathbf{K}_{eB} + \mathbf{K}_{cB}) \mathbf{q}_{ss} \\ \delta W_{nc} &= 0 \end{aligned} \quad (5.31)$$

Lagrange equation can be reformulated by pre-multiplying the absolute displacement vector \mathbf{u} in a steady-state fashion $\mathbf{u}_{ss} = \mathbf{N}_d \mathbf{N} \mathbf{q}_{ss}$; in other words:

$$\frac{d}{dt} \left(\frac{\partial T}{\partial \dot{\mathbf{q}}_{ss}} \right) - \frac{\partial T}{\partial \mathbf{q}_{ss}} + \frac{\partial U}{\partial \mathbf{q}_{ss}} + \frac{\partial W_{nc}}{\partial \mathbf{q}_{ss}} - \frac{d}{dt} \frac{\partial W_{nc}}{\partial \dot{\mathbf{q}}_{ss}} = \mathbf{F} \quad (5.32)$$

Expanding Equation (5.32) will result in the following:

$$[\mathbf{K}_{eB} + \mathbf{K}_{cB} - \mathbf{K}_{\Omega B}] \mathbf{q}_{ss} = \mathbf{F}_{\Omega B} \quad (5.33)$$

If small oscillation about the steady state is now considered where $\dot{\mathbf{q}} = \dot{\mathbf{q}}_{ns}$, the end result of the energy terms will be:

$$\begin{aligned} T_B &= \frac{1}{2} \dot{\mathbf{q}}_{ns}^T \mathbf{M}_B \dot{\mathbf{q}}_{ns} + \dot{\mathbf{q}}_{ns}^T \mathbf{G}_B \{\mathbf{q}_{ss} + \mathbf{q}_{ns}\} + \frac{1}{2} \{\mathbf{q}_{ss} + \mathbf{q}_{ns}\}^T \mathbf{K}_{\Omega B} \{\mathbf{q}_{ss} + \mathbf{q}_{ns}\} + \\ &\quad \dot{\mathbf{q}}_{ns}^T \mathbf{F}_{cB} + \mathbf{F}_{\Omega B}^T \{\mathbf{q}_{ss} + \mathbf{q}_{ns}\} \\ U_B &= \frac{1}{2} \{\mathbf{q}_{ss} + \mathbf{q}_{ns}\}^T (\mathbf{K}_{eB} + \mathbf{K}_{cB}) \{\mathbf{q}_{ss} + \mathbf{q}_{ns}\} \\ \delta W_{nc} &= \mathbf{i} \mathbf{C}_B \dot{\mathbf{q}}_{ns}; \quad \mathbf{i} = \{1, 2, \dots, 12\} \end{aligned} \quad (5.34)$$

Combining Equation (5.34) with Equation (5.33) and knowing in advance that the non-steady oscillation resets the Lagrange equation as follows:

$$\frac{d}{dt} \left(\frac{\partial T}{\partial \dot{\mathbf{q}}_{ns}} \right) - \frac{\partial T}{\partial \{\mathbf{q}_{ss} + \mathbf{q}_{ns}\}} + \frac{\partial U}{\partial \{\mathbf{q}_{ss} + \mathbf{q}_{ns}\}} + \frac{\partial W_{nc}}{\partial \{\mathbf{q}_{ss} + \mathbf{q}_{ns}\}} - \frac{d}{dt} \frac{\partial W_{nc}}{\partial \dot{\mathbf{q}}_{ns}} = \mathbf{F} \quad (5.35)$$

Finally, by expanding Equation (5.35) the governing equation of motion that controls the tapered-swept blade, including axial-flexural-torsional coupling, is given by:

$$\mathbf{M}_B \ddot{\mathbf{q}}_{ns} + [2\mathbf{G}_B + \mathbf{C}_B] \dot{\mathbf{q}}_{ns} + [\mathbf{K}_{eB} + \mathbf{K}_{cB} - \mathbf{K}_{\Omega B}] \mathbf{q}_{ns} = \mathbf{F} \quad (5.36)$$

The term \mathbf{M}_B is the integrated mass matrix, \mathbf{G}_B is the gyroscopic (Coriolis) matrix, \mathbf{C}_B the damping matrix, $[2\mathbf{G}_B + \mathbf{C}_B]$ is the combined damped gyroscopic matrix, \mathbf{K}_B is the stiffness matrices for non-rotating beam elements, \mathbf{K}_{cB} is the stabilizing centrifugal stiffness matrix, $\mathbf{K}_{\Omega B}$ is the destabilizing stiffness spinning matrix, and $[\mathbf{K}_{eB} + \mathbf{K}_{cB} - \mathbf{K}_{\Omega B}]$ is the integrated stiffness matrix, all defined in the spinning coordinate system $x_s y_s z_s$.

5.5 Eigenrealization

Modal analysis is arguably the most popular and efficient method for solving engineering dynamic problems. The concept of modal analysis, as introduced by Rayleigh (1877), was originated from the linear dynamics of undamped systems. The subject of study of this paper intends to embrace the original concept of orthogonality relationship not only over the mass and stiffness, but also over the gyroscopy, as part of the mathematical descriptors of the proposed spinning finite element. By definition, damping is an influence within or upon an oscillatory system that has the effect of reducing, restricting or preventing its oscillations. In physical systems, and for the case of free-yaw spinning structures, damping is produced by processes that dissipate the energy stored in the oscillation – structural vibration – on one hand, but also throughout the gyroscopic (Coriolis) motion, on the other. Real-life systems are however, not undamped, but possess some kind of energy dissipation mechanism not well understood as of today. In order to apply modal analysis of undamped spinning systems to their damped counterparts, it is common practice to assume proportional damping. The damping pattern in this study, however, is idealized coupled and non-classical, therefore non-proportional. This involves investing an extra effort to solve the resulting non-linear equations of motion. To this aim, dynamic analysis of Equation (5.36) is rather difficult to solve since it contains complex-number eigenvectors due to the skew-symmetric nature of the gyroscopic matrix [Meirovitch 1974][Wilkinson 1965]. The so-called Arnoldi iterative method [Horn and Johnson 1985] is employed in this analysis to solve the generalized eigenvalue problem (see Figure 5.9). Coupling between damping and

gyroscopic matrices are described as the main contributors of identified eigenvalue divergences [Zheng *et al.* 1997]. Consequently, the Schur theorem is applied to transform the equivalent state-space system of Equation (5.36) into its Hessenberg form by means of the so-called B-orthogonal matrix incursion. This is how, by applying Schur decomposition, both an upper quasi-triangular and an orthogonal transformation matrices are formed to solve for the now uncoupled dynamic system of equations. According to Zheng [*ibid.* Zheng *et al.* 1997], space integration of coupled/uncoupled super-convergent shape functions offer the possibility to acquire for damping energy quantifiers. For the case of axial-flexural-torsional coupling the damping is evidently not classical. Above this, the incursion of the gyroscopic (Coriolis effects) terms will impact in a much higher degree of complexity for damping quantification. Indeed, the skew-symmetric nature of the damped-gyroscopic matrix term of Equation (5.36) forces to write a 2nd order differential equation of motion as two sets of first order differential equations in order to converge for a practical solution. Consequently, there is a need to define the velocity and acceleration, as stated in Equation (5.5) to Equation (5.7), in order to solve the resultant governing equations commonly called *dynamics matrix*. Now, for any damped system – classically or non-classically damped – it must be assumed that the free-vibration response decays with time and it is expressed as a superposition of exponentially decayed sinusoidal displacement series. These series can be expressed in complex values that will induce complex mode shape vectors and complex modal coordinates. At this point in time, the response equation is a trial function composed by periodically decreased real and imaginary parts that can be interpreted as a set of complex modal coordinates. The real part of this latter equals $-\zeta\omega_n$ and the imaginary part equals $\omega_d = \omega_n(1-\zeta^2)^{1/2}$ for $\zeta \leq 1$. By solving the first order differential equations the problem now ends up dealing with a two complex-conjugate standard eigenvalue problem. The solution to one of these standard eigenvalue problems implies the solution of the other, which implies obtaining effective damping ratios. Recall that eigenvectors may be arbitrarily scaled, as for the undamped case, the eigenvectors can be more intuitively scaled so that the response is purely real or purely imaginary. It is important to underline

that the real modes arising from systems with zero or classical damping have nodes, which are stationary points at which the structure has zero displacement. In contrast, for a complex modal vector there is not always a point on the structure at which the modal displacement is zero at all times within a periodic cycle.

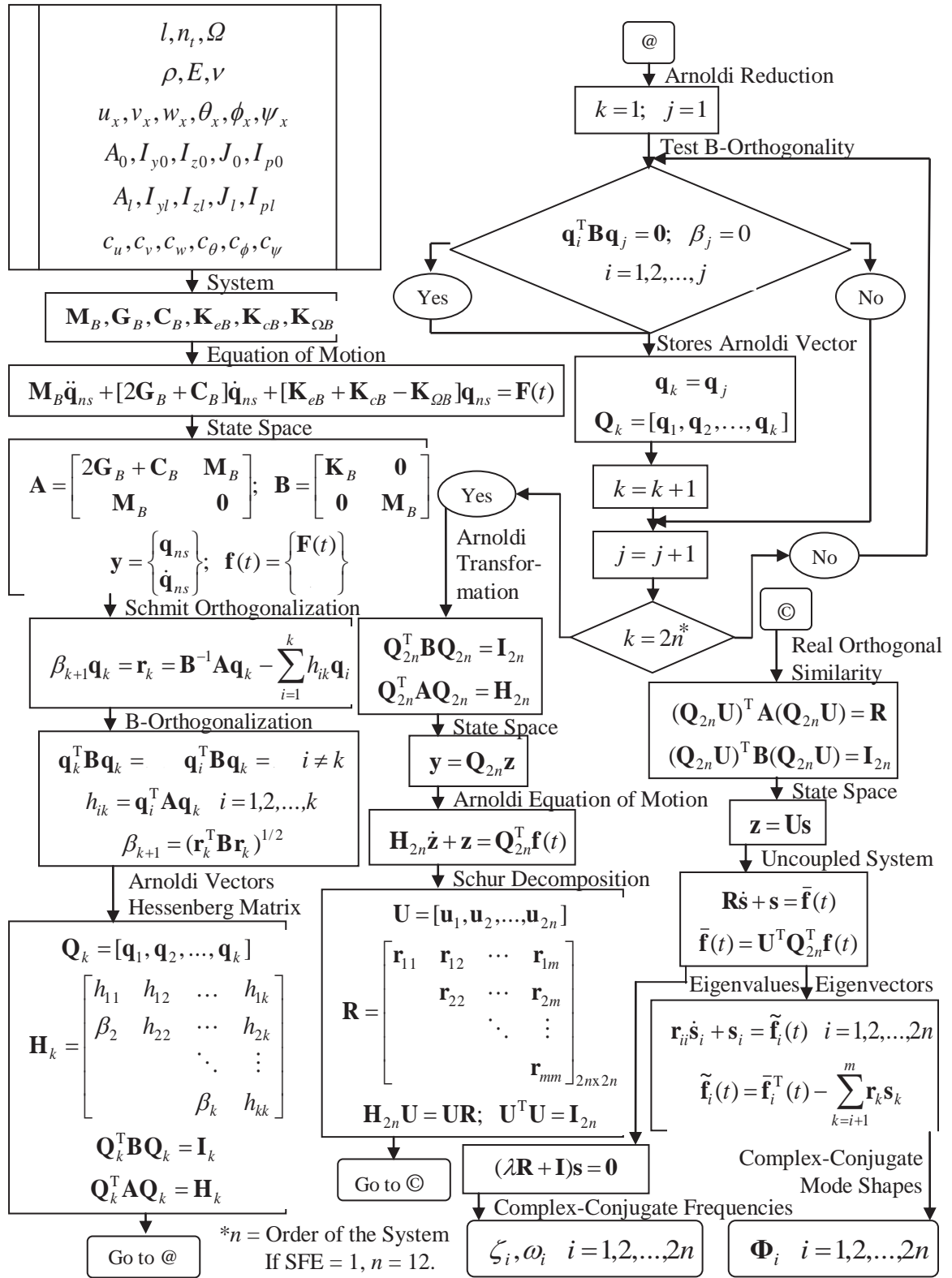


Figure 5.9. Damped-Gyroscopic Eigenrealization. Adapted from Zheng [Zheng et al. 1997].

This is why the use of classical damping methods (e.g. Rayleigh damping or Caughey damping) is prohibited and also the reason why the calculation of damping ratios are *per se* not self-evident. In the long run, natural frequencies ω_i , damping ratios ζ_i , as well as physical mode shapes Φ_i are finally obtained tailoring a time-domain analysis of an uncoupled system of equations representative of the original damped-gyroscopic system with axial-flexural-torsional coupling.

5.6 Numerical Example

A numerical example is provided in this section to demonstrate the capabilities of the proposed theoretical framework. To accomplish this goal, an impulse-type wind blast load, an harmonic force of order $F = F_0 \sin(2\pi nt)$, and a chirp load have been applied individually on each of the six DOFs at the outboard (free) end (see Figure 5.10(a)). All specimens are modeled via damped-gyroscopic SFE elements so that the variation response, axial-torsional-flexural coupling and structural mechanics can be identified. Standard numerical methods (*e.g.*, modified Newton method) for the solution of the uncoupled equations of motion have been implemented.

The concept of coupling percentage is introduced in the discussion only to gain some sensibility and awareness on the impact and transcendence of the modal coupling. This concept is defined within the computation of the dynamic matrices as the ratio of occurrence of coupling terms – or cells – within the equations of motion. As for example, 0% corresponds to the case of total uncoupling (zero value) of all spinning dynamic terms not associated with coupling inside (1) mass modes in \mathbf{M}_B , (2) damped-gyroscopic modes in \mathbf{G}_B and \mathbf{C}_B , (3) centrifugal stiffness modes in \mathbf{K}_{cB} , (4) spinning stiffness modes in $\mathbf{K}_{\Omega B}$, and (5) elastic stiffness modes in \mathbf{K}_{eB} . For example, super-convergent axial-deformation functions $g_1(\zeta)$ and $g_7(\zeta)$ will be the only terms different from zero in the first row of Equation (5.13). By contrast, a scenario with 100% coupling implies that all coherent (correlation) terms – or cells – of all dynamic matrices become different than zero and are exactly defined as the super-convergent shape functions depicted in Equation (5.14). In

other words, super-convergent functions $g_1(\zeta)$ to $g_{12}(\zeta)$ will be all different from zero in the first row of Equation (5.13). Conversely, a 50% coupling scenario means that only half of the coupling strength will be applied to all the correlated (coupled) terms except the uncoupled, that rule applies homogeneously to all dynamic model matrices. For this case, the super-convergent axial-deformation functions $g_1(\zeta)$ and $g_7(\zeta)$ will remain the same, whereas the remaining terms will be downsized to $0.5g_2(\zeta)$, $0.5g_3(\zeta)$, $0.5g_4(\zeta)$, $0.5g_5(\zeta)$, $0.5g_6(\zeta)$, $0.5g_8(\zeta)$, $0.5g_9(\zeta)$, $0.5g_{10}(\zeta)$, $0.5g_{11}(\zeta)$ and $0.5g_{12}(\zeta)$. It is important to underline here that the background of this concept does not have any physical interpretation as such, nor replaces the original coupling reciprocity of the model, but rather is a numerical artifice that serves to earn some knowledge, feeling and introspection of the impact of the axial-flexural-torsional coupling in the mathematical model proposed.

5.7 Prototype

A series of wind turbine blade geometries with different tapered-swept variations have been modeled to exemplify the characterization of the theoretical framework presented in this study (see Figure 5.10(b)). The blades are modeled after those of a realistic turbine device exhibiting a start-up wind speed of 3.1 m/s, cut-in wind speed 3.5-4.5 m/s and maximum design wind speed of 54 m/s. Rotor speed range is set from 0 to 350 rev/min. The hypothetical blade specimen is of length 1.25 m, and assumed 34 kg wind turbine mass.

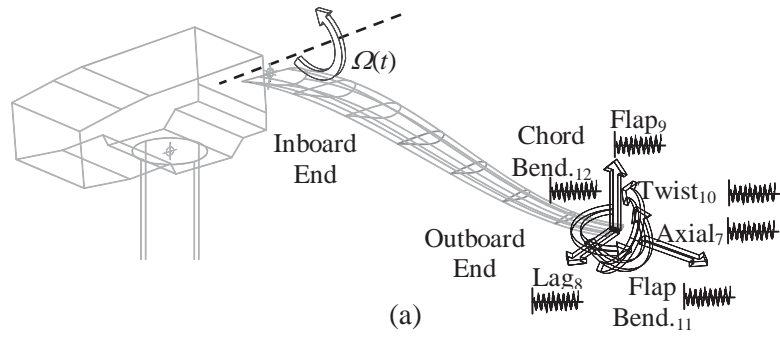
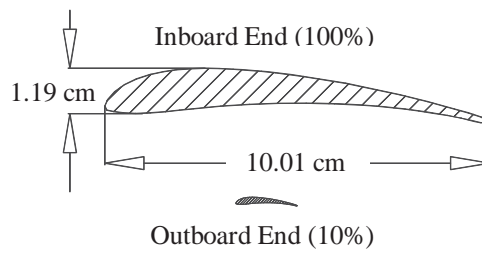


Figure 5.10(a). Numerical example of a hypothetical wind turbine blade. (a) Load combinations applied at the free degrees of freedom of the outboard end.

	$\theta_x = 0; \psi_x = 0$	$\theta_x \neq 0; \psi_x = 0$	$\theta_x = 0; \psi_x \neq 0$	$\theta_x \neq 0; \psi_x \neq 0$
$n_t = 0$				
$n_t = 1$				
$n_t = 2$				
$n_t = 3$				

(b)



(c)

Figure 5.10(b). Numerical example of a hypothetical wind turbine blade. (b) Tapered-swept combination matrix of the hypothetical specimen with four different taper and four different sweep degrees; (c) Cross section at inboard and outboard ends.

Blades are characterized after the commercial SH3045 airfoil profile with tapered-swept variation in geometry, in inertia or both. For elastic, homogeneous and isotropic material parameters ρ , E , ν_0 and G are fixed as constants, whereas in their own domain, geometric functions $A(s)$, $I_y(s)$, $I_z(s)$ and $J(s)$ are presumed to be decreasing gradient variables of order n_t . To illustrate the effect of such tapered gradients, three geometries are considered: $n_t = 0$ (constant), $n_t = 1$ (linear), and $n_t = 2$ (parabolic) variations. Material properties assigned all along and all across the blade specimen are: $\rho_0 = 1826.873$ kg/m³, $E_0 = 19305.319$ N/m², and $\nu_0 = 0.33$. Geometric properties for the inboard end are: $d_0 = 0.1$ m, area $A_0 = 6.392 \times 10^{-4}$ m², orthogonal inertias $I_{y0} = 5.453 \times 10^{-9}$ m⁴ and $I_{z0} = 3.637 \times 10^{-7}$ m⁴, polar moment of inertia $J_0 = 3.690 \times 10^{-7}$ m⁴, and mass moment of inertia $I_{p0} = 1.865 \times 10^{-5}$ kg*m². For simplicity purposes and bearing in mind that the example is only an academic exercise, all the geometric quantities at the outboard end are approximated as a proportion of the inboard end: $d_l = 0.1 d_0$, $A_l = 0.1 A_0$, $I_{yl} = 0.1 I_{y0}$, $I_{zl} = 0.1 I_{z0}$, $J_l = 0.1 J_0$, and $I_{pl} = 0.1 I_{p0}$. In other words, and rephrasing Equation (5.19), $EA_l = 0.1 EA_0$, $EI_{yl} = 0.1 EI_{y0}$, $EI_{zl} = 0.1 EI_{z0}$, $GJ_l = 0.1 GJ_0$, $\rho A_l = 0.1 \rho A_0$ and $\rho I_{pl} = 0.1 \rho I_{p0}$. Length of blade specimen is $l = 1.5$ m and yaw eccentricity is taken as $Y_0 = 0.1$ m. The effects of varying taper and sweep angles, as described in Figure 5.10(b), are investigated.

5.8 Results

Figure 5.11 depicts response time histories for a fully coupled rotor blade with $n_t = 0$, $\Omega = 150$ rev/min, and $\zeta = 0.0001$ for three different load combinations including blast, sinusoidal, and chirp wind loads. Overall, the numerical analysis required a cluster of simulations, in a trial and error basis, to be performed using different combinations of the damping coefficients $c_u, c_v, c_w, c_\theta, c_\phi, c_\psi$ in order to reach the desirable output damping ratios ζ_i . According to this set of numerical simulations carried out (i.e. Figure 5.11 and Figure 5.12), deflections due to axial, flexural and torsional modes were identified for different spinning velocities, damping ratios, geometrical/inertial tapered variations, load

combinations, mode coupling intensities and geometrical swept gradient projections. Persistent excitations for the axial-torsional mode were observed from numerical simulations; but most importantly, a pronounced flexural-torsional mode coupling was identified throughout the scope of the numerical analysis, as illustrated in Figure 5.11(a-c). Similar coupling association has been observed in previous experimental studies [Linscott *et al.* 1981]. Generally speaking, stronger acceleration content occurs for coupled systems rather than the uncoupled ones, as stated in [Hansen 2008]. Both lag and flap modes are dominant for the half coupling and full coupling cases, as presented in Figure 5.11 and Figure 5.12. Figure 5.13 shows the spectral density functions of the dominant flap mode using different flexural-torsional coupling mode intensities, where 0% is the uncoupled case scenario and 100% is a fully coupled rotor blade. It can be seen that the first three dominant frequencies exhibit an increasing shift to the right for higher tapered-swept order degrees. Similarly, high frequency content associated with heave, sway, and torsion coupling, is recognized for $n_t = 2$ and higher.

Figure 5.14 summarizes the relationship between damping ratio and base shear in the chord-wise direction (strong axis) for the same coupling cases described in Figure 5.13. It can be observed from Figure 5.13 that free yaw motion reduces the blade bending moments and base shears under most operating conditions. The effect of a decreasing tapered-swept parabolic gradient variation imposed on the blade specimen greatly influences the overall behavior and structural response. In fact, such trends are the result of a complex combination between the dynamic load type, its duration, its frequency content, the prevailing spinning velocity, the coupling intensity and finally, the tapered-swept order projected for both the mass and geometry distributions within the blade. Numerical results are thrown as they are casted by the algorithm and, in this line of thinking, a direct interpretation of the pattern presented in Figure 5.14(c) and Figure 5.14(d) for 50% coupling percentage is obviously not self-evident. Data suggest that the base shear is very sensible to the ratio between the damped-gyroscopic matrix $\mathbf{G}_B + \mathbf{C}_B$ and the integrated stiffness matrix $\mathbf{K}_B = \mathbf{K}_{cB} + \mathbf{K}_{\Omega B} + \mathbf{K}_{eB}$. When the overall stiffness tends to be large compared to the energy the blade is able to absorb or dissipate this kind of

peak jumps lay out. This pattern occurs when dealing with both high spinning velocities and high-frequency external loads (e.g. incremental chirp load) at the same time.

The stiffness distribution of the rotor blades plays an important role on the efficiency of the mass distribution, where flexible specimens (higher n_t) tend to lessen inertia loads towards the tip of the blade. Similar inertia patterns have been observed by [Johansen *et al.* 2009]. Correlation of the torsion (twist) mode with flap bending and lag bending corresponding modes is fairly strong and coherent for low and mid spinning velocities, as seen in Figure 5.15 and Figure 5.16. However, flexible elements present complex dynamics of the rotor vibrations given a combined pitch and relative cone angles (swept degrees). This phenomenon is better illustrated in Figure 5.15 and Figure 5.16 where phase time-histories are analyzed for flap bending and torsion modes under a harmonic sinusoidal excitation for three different tapered-swept variations. Overall coupling effects tend to be stronger on the flap-bending mode rather than the twist (rotation) mode. Similarly, Figure 5.17 to Figure 5.19 present flap-mode phase distributions for different swept angles θ_x and ψ_x (see Figure 5.5) and for three different tapered-swept orders. It can be observed from Figure 5.17 to Figure 5.19 that the cone angle (angle of incidence) plays an important role on the influence of yawing. The cone angle improves stability around the axis of yaw in the wind rotor. It was also identified that coupled pitch angle has a positive influence on yawing. In general terms, and through the observation of Figure 5.17 to Figure 5.19, high stresses in rotor blades with imprinted pitch angle occur at high wind loads. Similarly, specific blade mass per base turning moment ratio increases with a decreasing tapered-swept order, where $n_t = 0$ is the more disadvantageous case. It has been observed as well that a decrease in mass density by tapered variation ($n_t = 1, 2, 3$) of the cross section, relative to maximum peak deflections, implies a substantial reduction of the overall mechanical response without a significant impact on the principal flap-wise stiffness. A similar discussion was observed by Kooij [Kooij 2003]. Figure 5.20 illustrates the spinning action of the rotor blade versus the dominant frequencies of the dynamic model for different coupling-mode intensities.

Divergences tend to be more pronounced for uncoupled systems which can result in overestimation of the mechanical loads and structural responses for higher modes. By observing the performance of the sixteen specimens defined in Figure 5.10(b) it was concluded that the model presented in this study demonstrates the suitability of flexible rotor blades for high-speed rotors.

The effects of the gravitational and centrifugal force are observed to be severe with respect to the edge-wise and flap-wise bending moments of the rotor blade and can be predicted by analyzing the complex-conjugate modal content of the mode (Figure 5.21). Centrifugal and gravitational actions are greatly increased when an applied sinusoidal wind load equates a spinning velocity, resulting in a high amplification of the dominant mode, as has been observed for the acceleration signal in Figure 5.11(c) and Figure 5.12(c). Superimposed high-frequency signals coming from high-order modes such as heave, sway and roll occur in this scenario. Flap-wise bending is mostly dominant when impulse and chirp wind loads are applied in the rotating out-of-plane direction, but is relatively less serious than other harmonic effects, such as the centrifugal and yaw (gyroscopic) motions that are in agreement with observations made by Walker [Walker 1996]. Also, when high gyroscopic moments occur, the result is high bending moments around the rotor pitch axis. Flap-wise and edge-wise bending moments, combined with yaw motor bending moments, may affect overall blade stability for low damping ratios (*i.e.* displacement signal in Figure 5.11(c)). In general terms, bending moments are relatively large in relation to the section modulus in the innermost blade region, whereas coupling loads are minimal in the outermost blade zone (Figure 5.8). Stiffness distribution is critical to promote a proper loading distribution for both coupled and uncoupled mode cases (Figure 5.13(a-d)). Increased flexibility can be an asset for loading reduction but operative deflections must be limited to serviceability restrictions as pointed out by Cox *et al.* [Cox *et al.* 2004].

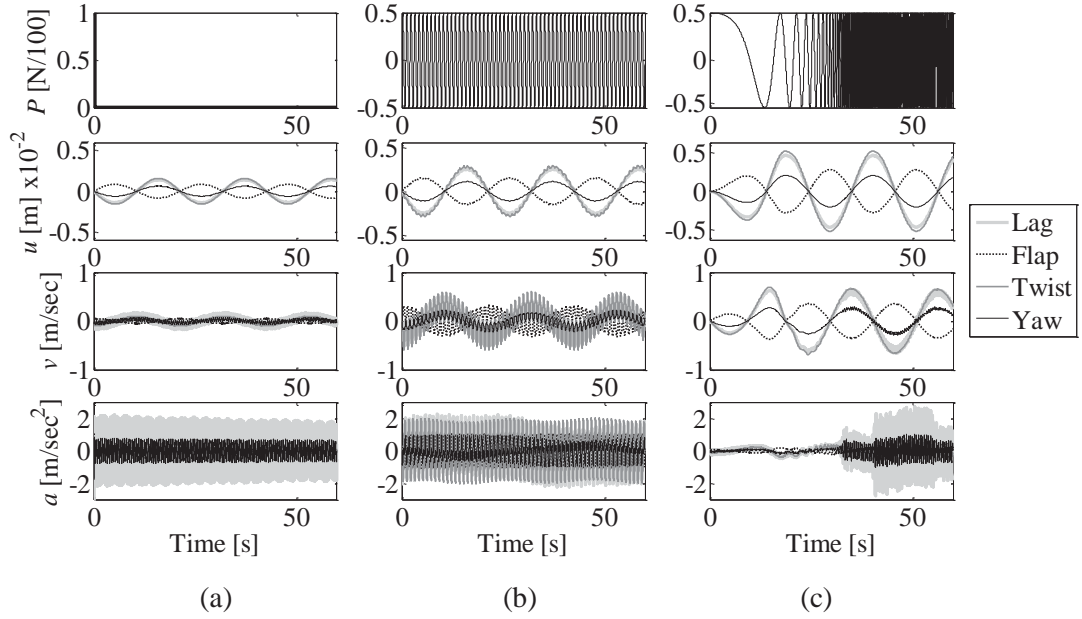


Figure 5.11. Structural response time histories (u = displacement, v = velocity, a = acceleration) for a fully coupled rotor blade with $n_t = 0$, $\Omega = 150$ rev/min, and $\zeta = 0.0001$ for: (a) blast wind load, (b) sinusoidal wind load, (c) chirp wind load.

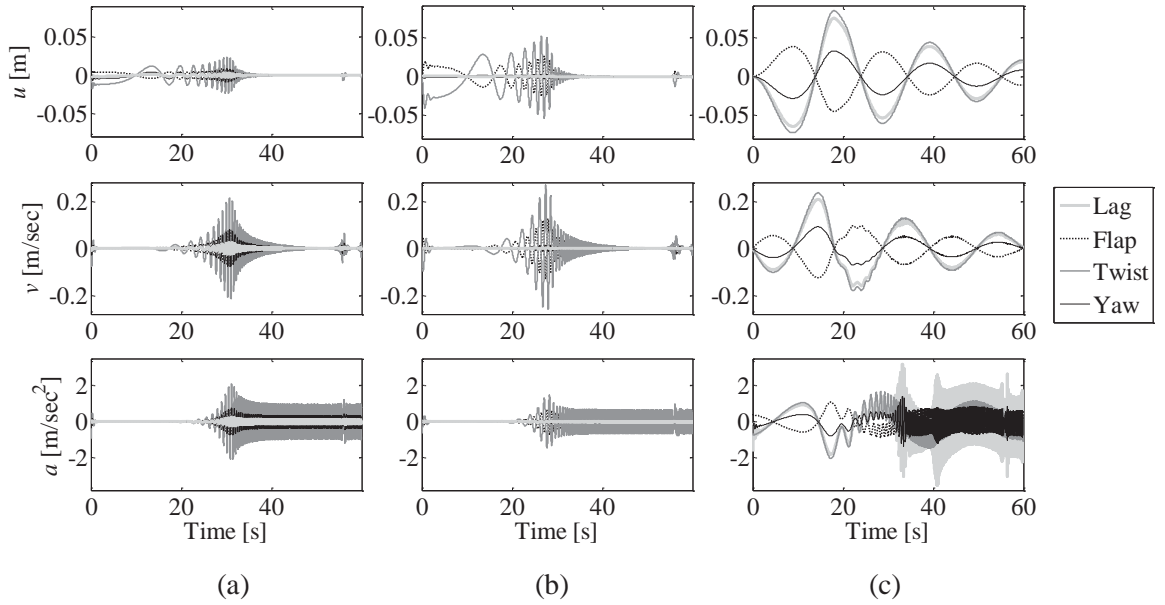


Figure 5.12. Structural response time histories (u = displacement, v = velocity, a = acceleration) of four dominant modes of a rotor blade with $n_t = 1$, $\zeta = 0.1$, $\Omega = 150$ rev/min and a chirp wind load applied. (a) 0% coupling, (b) 50% coupling, and (c) 100% coupling.

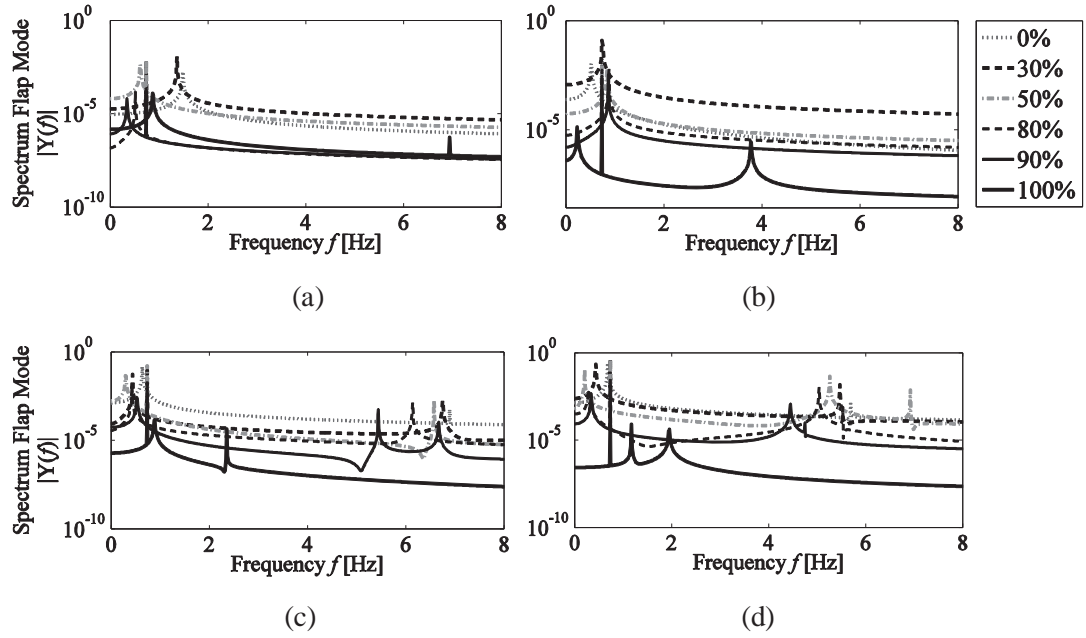


Figure 5.13. Single-sided amplitude spectrum of flap deflection for different coupling ratios due to a sinusoidal wind load, $\Omega = 150$ rev/min, $\zeta = 0.0001$. (a) $n_t = 0$, (b) $n_t = 1$, (c) $n_t = 2$, (d) $n_t = 3$.

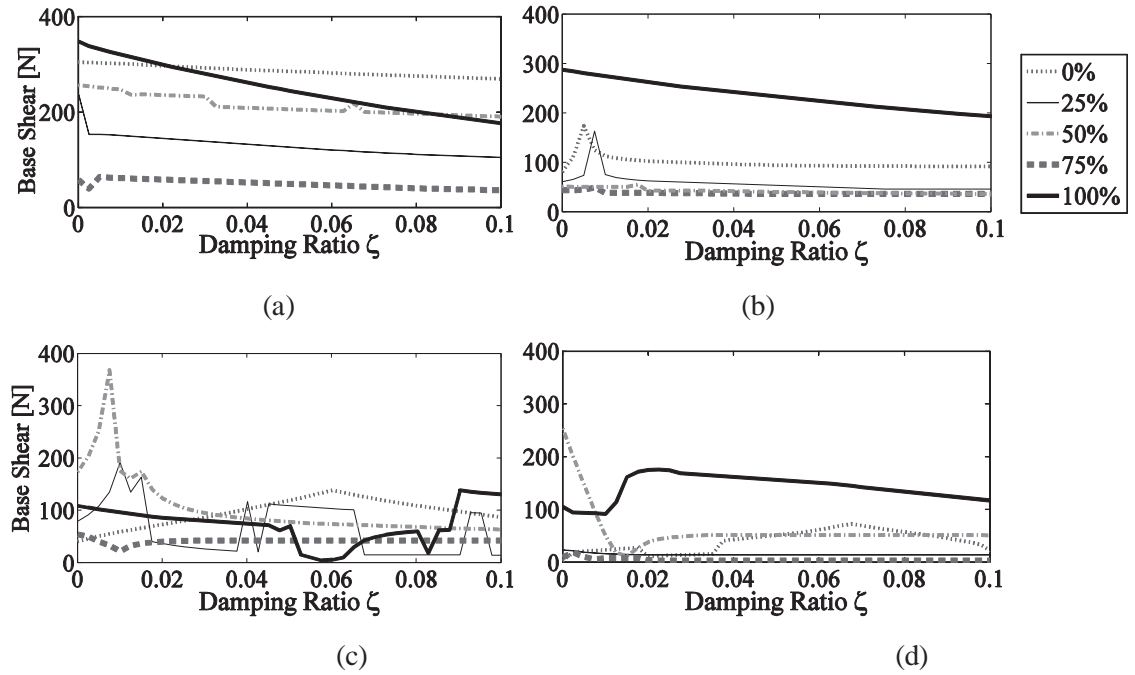


Figure 5.14. Damping ratio versus peak base shear on lag mode (strong axis) for different coupling ratios. Chirp wind load, $\Omega = 150$ rev/min, (a) $n_t = 0$, (b) $n_t = 1$, (c) $n_t = 2$, (d) $n_t = 3$.

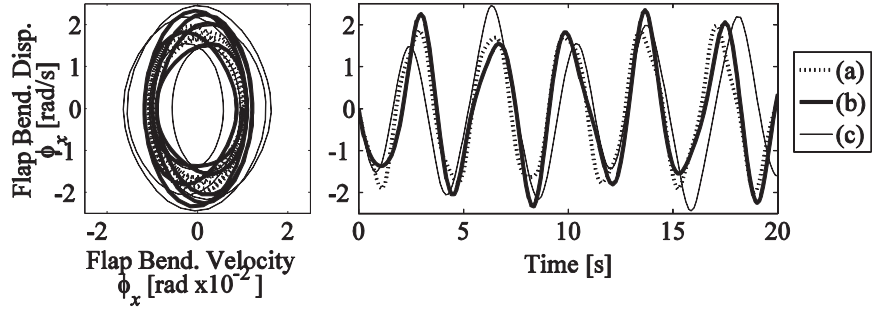


Figure 5.15. Phase and time histories of a fully coupled rotor blade in flap-bending rotation ϕ_x , under an harmonic excitation $F = F_0 \sin(2\pi nt)$, $F_0 = 0.5$, $n = 1$. (a) $n_t = 2$ (parabolic), (b) $n_t = 1$ (linear), and (c) $n_t = 0$ (constant).

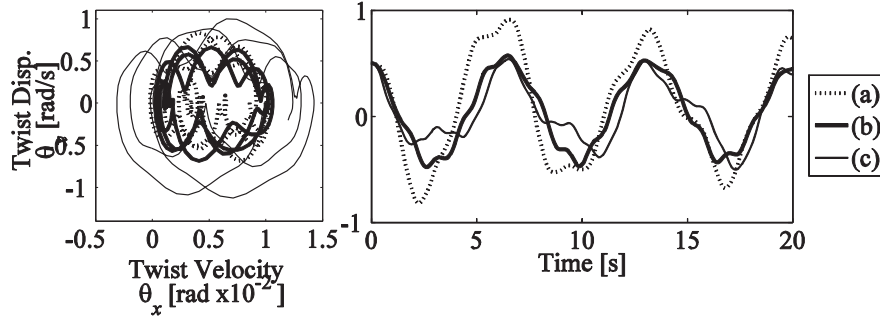


Figure 5.16. Phase and time histories of a fully coupled rotor blade in torsional rotation (twist) θ_x , under an harmonic excitation $F = F_0 \sin(2\pi nt)$, $F_0 = 0.5$, $n = 1$. (a) $n_t = 2$ (parabolic), (b) $n_t = 1$ (linear), and (c) $n_t = 0$ (constant).

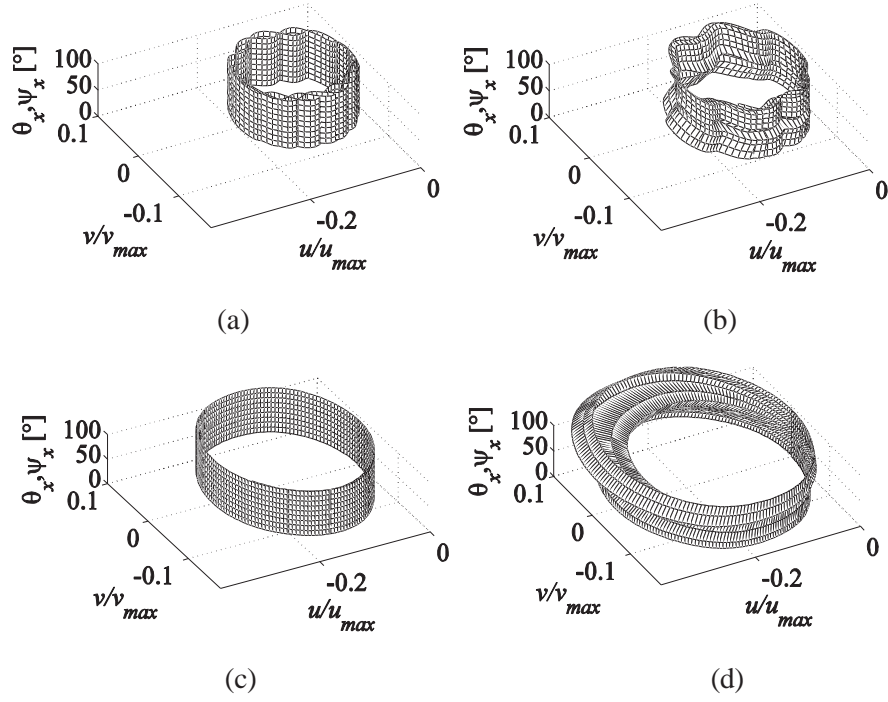


Figure 5.17. (a) Flap-mode phase distributions for different swept angles θ_x and ψ_x subjected to a chirp wind load, $\zeta = 0.0001$, $n_t = 0$. (a) $\Omega = 0$ rev/min, uncoupled; (b) $\Omega = 50$ rev/min, uncoupled; (c) $\Omega = 0$ rev/min, fully coupled; (d) $\Omega = 50$ rev/min, fully coupled.

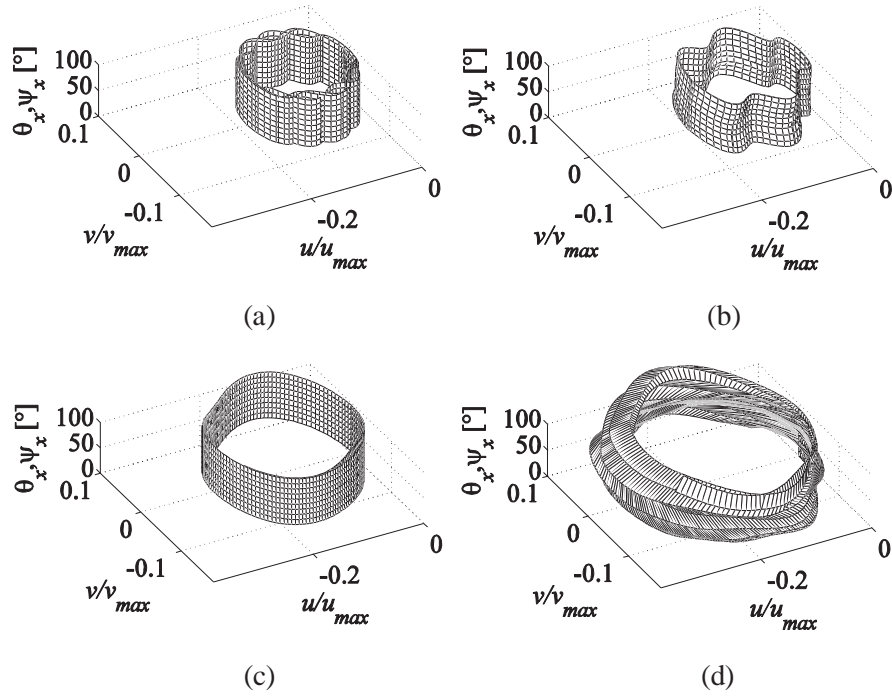


Figure 5.18. (a) Flap-mode phase distributions for different swept angles θ_x and ψ_x subjected to a chirp wind load, $\zeta = 0.0001$, $n_t = 1$. (a) $\Omega = 0$ rev/min, uncoupled; (b) $\Omega = 50$ rev/min, uncoupled; (c) $\Omega = 0$ rev/min, fully coupled; (d) $\Omega = 50$ rev/min, fully coupled.

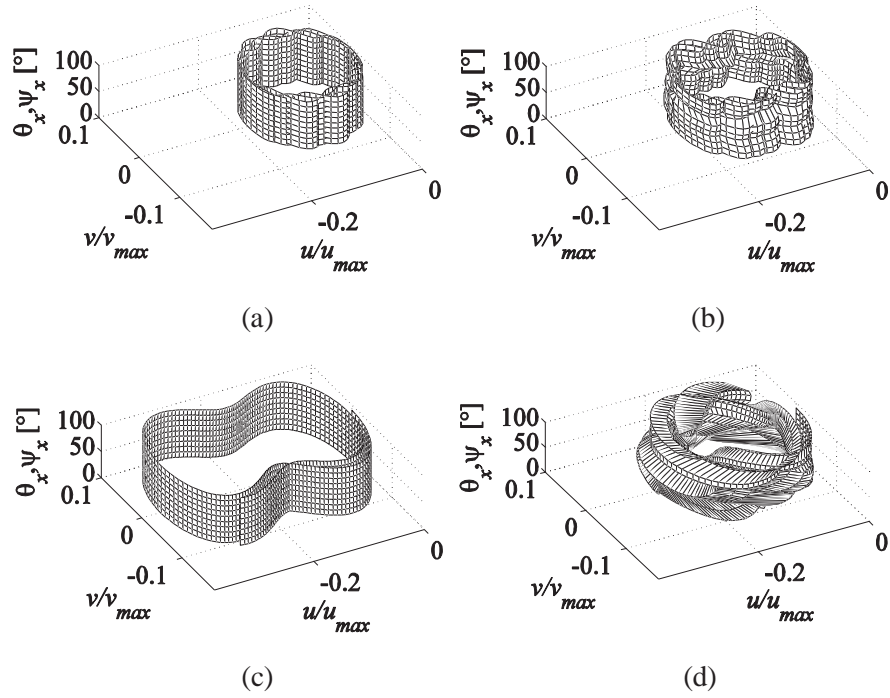


Figure 5.19. (a) Flap-mode phase distributions for different swept angles θ_x and ψ_x subjected to a chirp wind load, $\zeta = 0.0001$, $n_t = 2$. (a) $\Omega = 0$ rev/min, uncoupled; (b) $\Omega = 50$ rev/min, uncoupled; (c) $\Omega = 0$ rev/min, fully coupled; (d) $\Omega = 50$ rev/min, fully coupled.

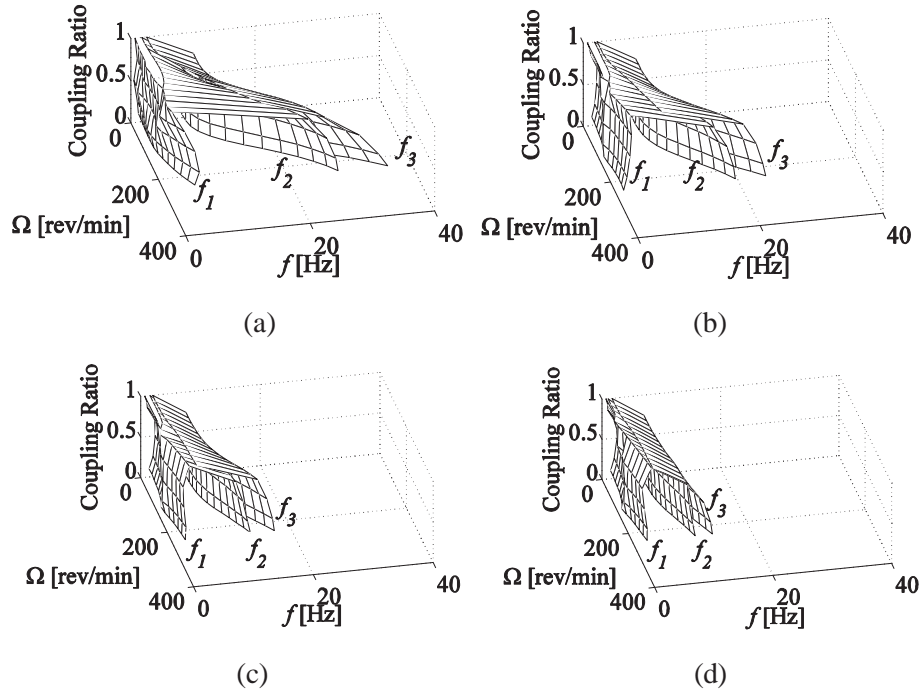


Figure 5.20. Frequency envelopes for different spinning velocities and different coupling ratios. First three dominant frequencies for a wind blast load applied; $\zeta = 0.0001$. (a) $n_t = 0$, (b) $n_t = 1$, (c) $n_t = 2$, (d) $n_t = 3$.

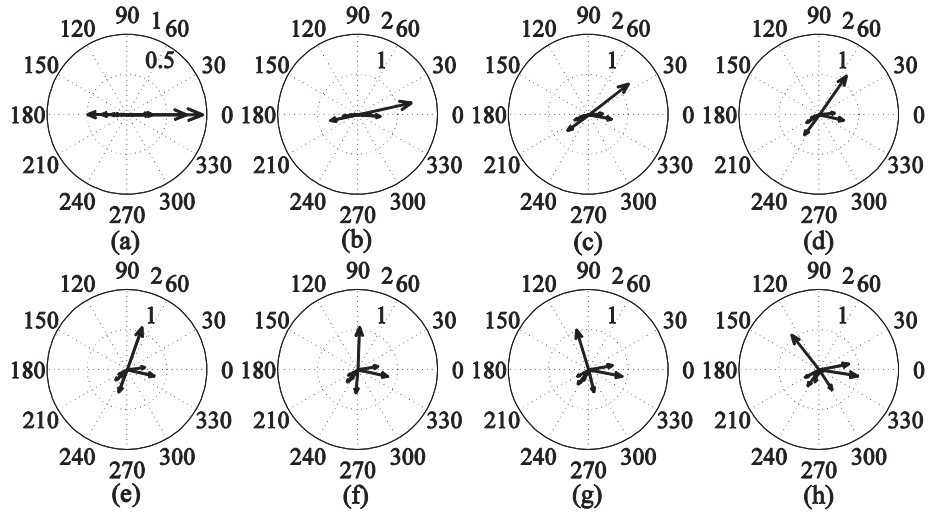


Figure 5.21. Compass diagram progression of the a complex conjugate eigenvector associated with flap bending mode, drawn for eight different coupling intensities: (a) 25%, (b) 30%, (c) 35%, (d) 40%, (e) 45%, (f) 50%, (g) 55%, (h) 60%. $n_t = 3$, $\zeta = 0.0001$, $\Omega = 150$ rev/min.

5.9 Discussion

Generally speaking, the emphasis of this numerical example is to gain a top level parametric view about complex materials and shape variations of wind turbine blades. The aim is to illuminate somehow the important structural interactions when the need requires an optimal – therefore complex – design on the blade specimens. As observed in Figure 5.14, structural mechanics is governing the so-called inboard zone of the specimen (where less power is produced but the greatest bending loads are sustained). At the same time, deflections rule on the outer 50% of the span as observed by Johansen [*ibid.* Johansen *et al.* 2009] and confirmed by the outcomes of the numerical simulation (see Figure 5.12). As observed in Figure 5.14, and just beyond the blade root area, which is typically projected in the industry as a circular cross-section, transition occurs from critical mechanical response to critical serviceability response at around 25% span. In this region, the load paths are complex and very sensitive to the assorted tapered-swept variation. Cox *et al.* [*ibid.* Cox *et al.* 2004] have observed that the surface area per unit length in this region is the greatest and subsequently tends to introduce concerns about buckling and local deformation effects. Hoogedoorn *et al.* [Hoogedoorn *et al.* 2010] studied the static aerodynamic response of two-dimensional (2D) wind turbine airfoil under varying wind conditions, and concluded that the static aero-elastic effects can improve the lift over drag ratio at off-the-range wind speed conditions. This tendency is identified by observing the phase plots of Figure 5.17 to Figure 5.19 drawn for high spinning velocities and coupling modes where the energy dispersion is simultaneously larger for two orthogonal – mutually exclusive – directions (i.e. Figure 5.17(b) or Figure 5.17(d)). From this perspective, Maheri *et al.* [Maheri *et al.* 2007] presented a method for coupled design of bend-twist adaptive blades in which the aerodynamic and structural designs are treated separately. The evaluation time is reduced by managing coupled-aero-structure (CAS) simulations of finite element analysis (FEA) separately from the aerodynamics. The benefits of this approach are also observed in the proposed study and confirm the numerical convenience of the spinning finite element algorithm developed here. In this line of thinking, other authors [Lee *et al.* 2001] have been studied in depth

the vibrational characteristics of the Euler-Bernoulli beam theory, and this approach has proven successful. In its core, the presented study embraces this methodology aiming at accounting for complex dynamics, but now with the inclusion of a novel matrix-based tapered-swept variation scheme.

From a local coordinate system (x,y,z) perspective, free yaw is the only assumed active degree of freedom in the inboard element. Certainly, this degree of freedom depends on the instantaneous angle of rotation the specimen has at any specific time. When the blade is in the horizontal position, the yaw mode (6th DOF) is the corresponding to yaw alignment, whereas in a vertical position the roll mode (4th DOF) is the corresponding to yaw alignment. Derivation of the damped-gyroscopic matrix controlled by the spinning coordinate system (x_s,y_s,z_s) clarifies this apparently physical discrepancy without explicitly declare which are the active degrees of freedom in the inboard end. In reality, and from a local coordinate stand point of view, all the modes in the inboard end are fixed. In contrast, the nacelle/gearbox base joint is where the actual yaw phenomenon occurs (see Figure 5.1). For this numerical example, only one finite element was employed to reach convergence. This is one of the powerful aspects of the theory presented in this paper and one of the main motivations for developing spinning finite elements. In this line of thinking, a single finite element is able to collect, summarize and perform what several simpler finite elements, concatenated with each other, are required to characterize the rotational mechanistic environment the blade is embedded in. To this end, the incorporation of inertial/geometrical tapered-swept variations can reduce the size of the model greatly, save substantial computational effort which translates into an easy, lighter and more efficient scheduling algorithm, suitable for embedded programming, all without loose of accuracy and convergence. Generally speaking, the convergence occurs very rapidly compared to other methods. In fact, numerical convergence is produced almost immediately once the mass, damped-gyroscopic, centrifugal stiffness, spinning stiffness and elastic stiffness matrices have been properly established and evaluated. The complex-numbers modal analysis can perform rapidly for one, two or even dozens of concatenated finite elements. The numerical bottle neck is not due to the number of finite

elements accounted for, but rather the construction and implementation of the respective equations of motion at each node.

In general terms, the aerodynamic and structural design practice of rotors for horizontal axis wind turbines (HAWT) involves many conflicting requirements that have to be met during the design process. For example, maximum performance (power generation), minimum loads (structural response) and minimum noise (serviceability conditions) must be properly orchestrated to reach a design optimum. Wind turbines operate in very different conditions from other rotor systems, ranging from normal variation in wind speed to extreme wind occurrences. Optimum efficiency is not obtainable in the entire wind speed range, since power regulation is needed to prevent generator burnout at high wind speeds. Optimum efficiency is typically limited to a single-design wind speed for stall regulated HAWTs with fixed rotating speed. Under this perspective, is possible to establish optimization rules for tapered-swept cross section variations with axial-flexural-torsional coupling. Most of the optimization methods rule maximum energy production as the main objective, incorporating off-design performance with none or very few constraints on load combinations. These design methods tend to increase the swept area of the blade specimen for the same generator size, resulting in larger load patterns on tower and rotor-blade systems that exceed the increase in energy yield. For such cases, the refinement in the geometric/inertial design as well as the mathematical framework adopted for characterization, don't pay off the effort invested. Therefore, optimum design should not be restricted to aerodynamic performance. In most cases, the key factor is the minimum cost of energy, defined as the ratio between the total costs from manufacture and erection of the wind turbine system and the annual energy production of the specimen. Proper cost estimates involve calculation of fatigue loads as well as extreme loads on all major components, regardless of the geometric/inertial complexity of the blade specimen. Under such arguments, it is possible to establish optimization rules where the main objective is to restrict the displacements and rotations (six DOFs) at the tip of the blade (outboard end) under certain maximum boundaries, while applying imposed constraints (i.e. extreme loads, material Young's modulus and/or material

density). For this scenario only, shape and mass optimization of rotor-blade systems reduce the cost of energy ratio compared to otherwise not optimized rotor systems of the same size.

Under these considerations, some design recommendations can be drawn suggesting that the tapered ratio is an important parameter, whereas the sweep angle is of less importance. Blades generate lift and capture overturning moment from moving air that is then dispensed to the rotor as the blades spin in the so-called “rotor plane”. In principle, the front or “leading edge” connects the forward-most points of the blade that first hit the air stream. The rear or “trailing edge” is where airflow that has been separated by the leading edge rejoins after passing over the pressure and suction surfaces of the blade. The thickness varies across the platform and the most efficient way to address this variation is by tapering. This thickness is the end result of the maximum distance between the low pressure suction surface and the high pressure surface on the opposite side of the blade. For design purposes, the tapered thickness should account for this differential pressure distance.

Since the speed of the blades relative to air increases radiating out the rotor radius, the shape of the blades is typically twisted in order to maintain a generally consistent angle of attack at most points. In this sense, the normalized distance outward from the center of rotation of the blade, that is occurring along the hub, and blade rotor radius – or percent of rotor radius – may be both approximated as the normalized distance radiating out from the root of the blade rather than from the center of rotation of the blade. This geometrical particularity is properly addressed in the theory presented (see Figure 5.1). For example, negative values indicate that the blade is twisted toward stall, whereas positive values of twist angle indicate that the blade is twisted towards feather. As a rule of thumb, and for design purposes, the twist angle may start with a high positive value inboard and then rotate towards stall conditions outboard. This twist variation might be also tapered-swept in nature and can be handled correctly by the vibration equations proposed in this paper. Vibration noise on the tapered-swept wind turbine depends, in part, upon vortex

development at the tip of the blade. Vortex development can be mitigated by minimizing the aerodynamic load at the tip of the blade – or tip unloading – typically this is the region where the advantage of reducing the exposed area makes its contribution. Drawbacks and advantages of such tip unloading can also be achieved by decreasing the chord near the tip by means of controlling excessive vibrations, minimizing load bearing and maximizing overturning moment. In this line of thinking, adequate projections of tapered-swept design variations are always beneficial.

5.10 Conclusions

This study introduces a spinning finite element model for tridimensional tapered-swept blades in rotational motion with modal axial-flexural-torsional coupling. Stress and strain fields were based on the Saint-Venant's and Timoshenko's theories resigning warping effects, shear deformations and large displacements. Numerical algorithms are applied according to Newtonian principles to solve for the resultant non-steady *dynamics equation* of motion. It was observed that nonlinear manifestations such as base shear, base overturning moment, strain displacements, torsional coupling, and swept effects are adequately captured by this methodology, and suitable for flexible rotor blades. It was concluded also that divergences are more accentuated for uncoupled systems that tend to overestimate the mechanical loads and structural response at higher modes. Centrifugal forces have destabilizing effects on the rotor blades, whereas the projected tapered-swept gradient variation tends to alleviate the amplitude of the frequencies and inertial forces. The amplitude of vibration may vary significantly with respect to the spinning velocity. Resonance and harmonic motion can occur with repeated frequently when spinning velocities change over time. The gyroscopic effect was revealed by analyzing the connection between flap-wise and edge-wise modes under the action of loads applied in one direction. Axial coupling is found to be of much less importance when centrifugal forces are diminished. The theory proposed here has proven to reduce the size of the FE model, with no loss of accuracy and generality, by minimizing the computational effort which ultimately translates into an easier, lighter and more practical computer algorithm

for model updating and design purposes. Next, Chapter 6 will establish the basis and foundations of a probabilistic-based identification model, supported solely by experimental random signals collected *in situ* that will serve to identify the dynamic properties of rotor blades. Results obtained from the identification may be concatenated along with the formerly established damped-gyroscopic Spinning Finite Element (SFE) and, thus, lay the foundations of a model updating numerical machine.

Chapter 6. Output-Only Cyclo-Stationary Linear-Parameter Time-Varying Stochastic Subspace Identification Method

Economical maintenance and operation are critical issues for rotating machinery and spinning structures containing blade elements, especially large slender dynamic beams (*e.g.*, wind turbines). Structural health monitoring systems represent promising instruments to assure reliability and good performance from the dynamics of the mechanical systems. However, such devices have not been completely perfected for spinning structures. These sensing technologies are typically informed by both mechanistic models coupled with data-driven identification techniques in the time and/or frequency domain. Frequency response functions are popular but are difficult to realize autonomously for structures of higher order, especially when overlapping frequency content is present. Instead, time-domain techniques have shown to possess powerful advantages from a practical point of view (*i.e.* low-order computational effort suitable for real-time or embedded algorithms) and also are more suitable to differentiate closely-related modes. Customarily, time-varying effects are often neglected or dismissed to simplify this analysis, but such can not be the case for sinusoidally loaded structures containing spinning multi-bodies. A more complex scenario is constituted when dealing with both periodic mechanisms responsible for the vibration shaft of the rotor-blade system and the interaction of the supporting substructure. Transformations of the cyclic effects on the vibrational data can be applied to isolate inertial quantities that are different from rotation-generated forces that are typically non-stationary in nature. After applying these transformations, structural identification can be carried out by stationary techniques via data-correlated Eigensystem realizations. In this paper, an exploration of a periodic stationary or cyclo-stationary subspace identification technique is presented here for spinning multi-blade systems by means of a modified Eigensystem Realization Algorithm (ERA) via Stochastic Subspace Identification (SSI) and Linear Parameter Time-Varying (LPTV) techniques. Structural response is assumed to be stationary ambient excitation produced by a Gaussian (white) noise within the operative range bandwidth of the machinery or structure in study. ERA-OKID analysis is driven by correlation-function

matrices from the stationary ambient response aiming to reduce noise effects. Singular value decomposition (SVD) and eigenvalue analysis are computed in a last stage to identify frequencies and complex-valued mode shapes. Proposed assumptions are carefully weighted to account for the uncertainty of the environment. A numerical example is carried out based a Spinning Finite Element (SFE) model, and verified using ANSYS® Ver. 12. Finally, comments and observations are provided on how this subspace realization technique can be extended to the problem of modal-parameter identification using only ambient vibration data.

6.1 Introduction

Rotating machinery and spinning structures have been positioned in the past two decades as emerging technologies for energy mass production. An illustrative example for this tendency is the emergence of wind energy-harvesting technologies as a major component of the clean energy production mix worldwide over the past years. In order to maximize power productivity and minimize operation costs, engineering design tendencies are trending toward larger and more slender spinning structures [DLR & EREC 2010]. For this reason, spinning-induced response analyses for structural health monitoring (SHM) techniques have attracted intensive attention in the structural engineering and engineering mechanics communities, specifically in the subspecialties of reliability and risk assessment focused on rotor blades and associated mechanisms. Great flexibility and slenderness ratio are trademarks of these types of aerodynamic structures that are typically treated as flexible dynamic multi-body systems [Lanzafame and Messina 2007]. In order to increase efficiency in energy generation and reduce the high cost of delivered energy production, it is imperative to incorporate technological innovations, such as SHM schemes, that could help to mitigate the risk of failure associated with flexible and slender blade/beam elements. Current system identification techniques (an integral part of the SHM approach) are partially able to integrate some of the peculiarities of the cyclic motion of rotor blade/beam systems in a stationary fashion [Bertha *et al.* 2012]. Most numerical methods and recursive least-squares algorithms

[Franklin *et al.* 2002] [Kuo 1995] are thought to be – and interpreted as – grey boxes AR-structure type, generally aimed for control applications of gearboxes, break systems, and pitch control.

The task for finding actual modes from induced vibrations generated by the along- and across- rotor-dynamic forces exciting the rotor blades is usually not a straightforward procedure and has not been tackled effectively in recent times. Some authors have proposed to perform transient simulations for further analysis of the dominant modes [Svend *et al.* 2002]. Linear parameter varying (LPV) systems have gained popularity over the past years [Verdult and Verhaegen 2002] in topics related to control applications based on Kernel methods and separable least squares. Some authors [Lopes dos Santos *et al.* 2007] have treated a bilinear association between the time-varying periodic parameter and the state vector as a white Gaussian noise, in order to identify the system using multi-input/multi-output (MIMO) recursive subspace system identification algorithms. This algorithm is based on the Picard method [Hsu *et al.* 1985] and employs general inputs and finite linear Kalman filter to assess the augmented input over multiple iterations. Muller [Muller *et al.* 2000] has demonstrated the need of a linear control algorithm able to adapt a schedule scheme to handle in the changes in rotor dynamics throughout time, switching from time-periodic model (constant spinning velocity) to linear parameter-varying (LPV) (changing spinning velocity). Verdult [Verdult 2004] proposed a linear parameter-varying state-space model from a set of local linearizations of input/output data to studying the out-of-plane bending dynamics of a helicopter rotor blade. That study presents a general approach of LPV state-space models capable of dealing with time periodic, parametrically varying and nonlinear systems. The author proposes an extended identification technique competent for periodic systems, but presents some drawbacks due to its high sensibility to the selection of the model structure. For their part, Lee and Poolla [Lee and Poolla 1996] developed an identification LPV system using nonlinear programming that focuses on the output-error identification, by means of a geometrical approach that minimizes the prediction error-based cost function. Some important efforts have been made to formulate stochastic subspace identification (SSI) methods using

linear periodically time-varying (LPTV) systems. Jhinaoui [Jhinaoui *et al.* 2012] derived a solution using Lyapunov-Floquet transformations to replace the state transition matrix by a monodromy matrix, opening thus the possibility of using classical time-invariant identification algorithms to solve the linear sequences. A first group of time-varying identification methods is based on previous information of the variation patterns of the turbine blades [Liu 1997], and employs recursively adaptive algorithms efficient for small variations of the rotational dynamics. On the contrary, a second group of time-varying identification methods utilizes a selected pack of output signals with the same time-varying behavior upon which a classical time-invariant algorithm (*i.e.* ERA-OKID) can be applied.

This paper proposes a LPTV method formulated now for cyclo-stationary systems of arbitrary order. A stochastic subspace identification scheme based on linear parameter time-varying and covariance-based methods is presented in this study. It uses selected combinations of output signals (*i.e.* absolute accelerations, velocities or displacements in three orthogonal directions) to reduce the numerical calculations and achieve numerical stability. The methodology presented here is preferably competent for data collection of output signals in the in-plane spinning direction, given the sinusoidal frequency content dominant in such orientation. A cyclo-stationary Fourier phasor function of finite partial sinusoidal content of order s is then introduced to account for the periodic nature of the output signals, embedding time-varying linear-parameter system matrices to properly characterize the sinusoidal dynamic nature of these mechanical systems within an acceptable approximation range. The theory presented is general and suitable enough for deterministic and non-deterministic external loads. It is also adequate for smooth transitions of the time variations of the spinning velocity, and convenient for the identification of both constant and tapered-swept variations of the beam cross section. Deviations and insights from the initial assumptions prevailed for random independency of noise, among output signals, are also discussed. Difficulties to ensure randomness on the loading combination acting along the beams, especially when dealing with specimens of short length spinning at high frequencies, always prevail. However, for large

prototypes rotating in slow motion and under turbulent flow streams, this approximation is acceptable. As a final note, the system identification technique developed in this study is majorly inspired by the actual challenges existing in the field of Structural Health Monitoring (SHM) applied to rotating machinery and spinning structures. The proposed method is also convenient as a numerical tool for applications in the field of sustainable energy-harvesting technologies; such is the case of the so-called Horizontal Axis Wind Turbines (HAWTs).

6.2 Numerical Model

6.2.1 Subspace Realization

Consider a discrete-time state-space model of the form:

$$\begin{aligned}\mathbf{x}_{k+1} &= \mathbf{A}\mathbf{x}_k + \mathbf{B}\mathbf{u}_k + \mathbf{w}_k \\ \mathbf{y}_k &= \mathbf{C}\mathbf{x}_k + \mathbf{D}\mathbf{u}_k + \mathbf{v}_k\end{aligned}\tag{6.1}$$

where $\mathbf{x}_{k+1} \in \mathcal{R}^{n \times 1}$ is the state vector, $\mathbf{u}_k \in \mathcal{R}^{r \times 1}$ the input vector, $\mathbf{y}_k \in \mathcal{R}^{m \times 1}$ the output vector, $\mathbf{A} \in \mathcal{R}^{n \times n}$ the state transition system matrix, $\mathbf{B} \in \mathcal{R}^{n \times r}$ the state transition controllability matrix, $\mathbf{C} \in \mathcal{R}^{m \times n}$ the state transition observability matrix, $\mathbf{D} \in \mathcal{R}^{m \times r}$ the state transition output amplification matrix, $\mathbf{w}_k \in \mathcal{R}^{n \times 1}$ the input noise approximated as white Gaussian zero-mean random variable, and $\mathbf{v}_k \in \mathcal{R}^{m \times 1}$ is the output noise assumed equally white Gaussian zero-mean as well. Here, n is the number of realization states, r is the number of inputs, and m is the number of outputs. It is assumed that the stochastic process is stationary and the transition state system matrix \mathbf{A} is uncorrelated with both input and output noises. For the case of rotating machinery and spinning structures, the assumption of white Gaussian distribution being as independent of the measured excitation tends to be imprecise or vague [Kailath 1980]. In a more critical scenario, external power forces that provoke rotational motion should be treated as non-stationary

and correlated with input/output noises. For the case of free-gyre based rotational structures subjected to, for example, wind blasts, buffeting and gusts, it is important to consider the coupling turbulent – therefore non-stationary – environment these structures are immersed in. Characterization errors are often crucial for a proper assignation of noise, *e.g.* external turbulent coupled forces are sometimes approximated as constant parameters within the sampling time interval from which the data is collected. Moreover, the interaction between rotor elements, its supporting structure, and the differences in the circulatory pressure violates the assumption of white Gaussian noise stated before [Chen 1984], consequence of coupling phenomenon and shadowing interaction. Under the assumption that these inaccuracies are small, consider an impulse response excitation of the form $\mathbf{u}_0 = \mathbf{1}$ and $\mathbf{u}_k = \mathbf{0}$ for $k = 1, 2, \dots$, and assume a clean signal where $\mathbf{w}_k = \mathbf{0}$, $\mathbf{v}_k = \mathbf{0}$. Expanding the state-space system of Equation (6.1) for k states $\mathbf{x}_0 = \mathbf{0}$, $\mathbf{y}_0 = \mathbf{D}\mathbf{u}_0$, $\mathbf{x}_1 = \mathbf{B}\mathbf{u}_0$, $\mathbf{y}_1 = \mathbf{C}\mathbf{B}\mathbf{u}_0 + \mathbf{D}\mathbf{u}_1$, *etc.* It can be seen that, in general, $\mathbf{Y}_0 = \mathbf{D}$, $\mathbf{Y}_1 = \mathbf{C}\mathbf{B}$, $\mathbf{Y}_2 = \mathbf{C}\mathbf{A}\mathbf{B}$, ..., $\mathbf{Y}_k = \mathbf{C}\mathbf{A}^{k-1}\mathbf{B}$, commonly known as the Markov parameters [*ibid.* Kailath 1980]. Consequently, the Hankel matrix \mathbf{H}_{k-1} is given by [Van Overschee and De Moor 1996]:

$$\mathbf{H}_{k-1} = \begin{bmatrix} \mathbf{Y}_k & \mathbf{Y}_{k+1} & \cdots & \mathbf{Y}_{k+\beta-1} \\ \mathbf{Y}_{k+1} & \mathbf{Y}_{k+2} & \cdots & \mathbf{Y}_{k+\beta} \\ \vdots & \vdots & \ddots & \vdots \\ \mathbf{Y}_{k+\alpha-1} & \mathbf{Y}_{k+\alpha} & \cdots & \mathbf{Y}_{k+\alpha+\beta-2} \end{bmatrix}_{\alpha m \times \beta r} \quad (6.2)$$

valid for dimensions $\alpha \geq n$ and $\beta \geq n$ both acting as control/threshold parameters to determine the order of the system, whereas the Hankel matrix is of rank n . Similarly, Equation (6.2) for the case of state shift $k = 1$:

$$\mathbf{H}_0 = \begin{bmatrix} \mathbf{Y}_1 & \mathbf{Y}_2 & \cdots & \mathbf{Y}_{\beta-1} \\ \mathbf{Y}_2 & \mathbf{Y}_3 & \cdots & \mathbf{Y}_{\beta} \\ \vdots & \vdots & \ddots & \vdots \\ \mathbf{Y}_{\alpha} & \mathbf{Y}_{1+\alpha} & \cdots & \mathbf{Y}_{\alpha+\beta-2} \end{bmatrix}_{cm \times \beta r} \quad (6.3)$$

Note that $\mathbf{Y}_0 = \mathbf{D}$ is not included in \mathbf{H}_0 . Substituting now the identified Markov parameters in Equation (6.3) and decomposing the block Hankel system in a triad of matrices using a similarity transformation, then the $k-1$ order matrix will take the form $\mathbf{H}_{k-1} = \hat{\mathbf{O}}\mathbf{A}\hat{\mathbf{C}}$, where $\hat{\mathbf{O}}$ is expanded as $\hat{\mathbf{O}} = [\mathbf{C} \ \mathbf{CA} \ \mathbf{CA}^2 \ \dots \ \mathbf{CA}^{\alpha-1}]_{cm \times n}^T$ and $\mathbf{C} = [\mathbf{B} \ \mathbf{AB} \ \mathbf{A}^2\mathbf{B} \ \dots \ \mathbf{A}^{\beta-1}\mathbf{B}]_{n \times \beta r}$. Here, $\hat{\mathbf{O}}$ is called the observability matrix of rank n and $\hat{\mathbf{C}}$ is known as the controllability matrix of the same rank n [Juang 1994]. From this point on, and given the uncertainty nature of the data entries referred as inputs \mathbf{u}_k , the stochastic models are conducted through the so-called stochastic subspace using only output signals \mathbf{y}_k characterized with random noise content as stated in [*ibid.* Van Overschee and De Moor 1996].

6.2.2 Stochastic Subspace

For the case of a realization with noisy discrete-time output-only data, the state space model is a reduced version of Equation (6.1) [*ibid.* Van Overschee and De Moor 1996]:

$$\begin{aligned} \mathbf{x}_{k+1} &= \mathbf{Ax}_k + \mathbf{w}_k \\ \mathbf{y}_k &= \mathbf{Cx}_k + \mathbf{v}_k \end{aligned} \quad (6.4)$$

assuming again a perfect zero white noise scenario $\mathbf{w}_k = \mathbf{0}$, $\mathbf{v}_k = \mathbf{0}$. The covariance-driven block Hankel matrix is constructed by several finite dimensional sub-matrices representing the product of shifted Hankel matrices built from correlations of output-only system Markov parameters. Assuming that noise intensities are small but not zero, having $\mathbf{w}_k \neq \mathbf{0}$ and $\mathbf{v}_k \neq \mathbf{0}$, let's reframe an impulse response excitation of the form $\mathbf{u}_0 = \mathbf{0}$ and $\mathbf{u}_k =$

$\mathbf{0}$ for $k = 1, 2, \dots$. Expanding the state-space system of Equation (6.1) for k states $\mathbf{x}_0 = \mathbf{0}, \mathbf{y}_0 = \mathbf{v}_0, \mathbf{x}_1 = \mathbf{w}_0, \mathbf{y}_1 = \mathbf{C}\mathbf{w}_0 + \mathbf{v}_1, \mathbf{x}_2 = \mathbf{A}\mathbf{w}_0 + \mathbf{w}_1, \mathbf{y}_2 = \mathbf{C}\mathbf{A}\mathbf{w}_0 + \mathbf{C}\mathbf{w}_1 + \mathbf{v}_2$, etc. In general, the l number of system Markov parameters of size $m \times m$ are derived as $\mathbf{Y}_0 = \mathbf{I}_{m \times m}$, $\mathbf{Y}_1 = \mathbf{C}\mathbf{I}_{n \times m}$, $\mathbf{Y}_2 = \mathbf{C}\mathbf{A}\mathbf{I}_{n \times m}$, ..., $\mathbf{Y}_k = \mathbf{C}\mathbf{A}^{k-1}\mathbf{I}_{n \times m}$, being \mathbf{I} the identity matrix in order to derive the block Hankel matrix is given by [Di Ruscio 2009]:

$$\mathbf{H}_k^c = \begin{bmatrix} \sum_{i=1}^{\beta} \mathbf{Y}_{k+i} \mathbf{Y}_i^T & \sum_{i=1}^{\beta} \mathbf{Y}_{k+i} \mathbf{Y}_{i+1}^T & \cdots & \sum_{i=1}^{\beta} \mathbf{Y}_{k+i} \mathbf{Y}_{\alpha+i-1}^T \\ \sum_{i=1}^{\beta} \mathbf{Y}_{k+i+1} \mathbf{Y}_i^T & \sum_{i=1}^{\beta} \mathbf{Y}_{k+i+1} \mathbf{Y}_{i+1}^T & \cdots & \sum_{i=1}^{\beta} \mathbf{Y}_{k+i+1} \mathbf{Y}_{\alpha+i-1}^T \\ \vdots & \vdots & \ddots & \vdots \\ \sum_{i=1}^{\beta} \mathbf{Y}_{k+\alpha+i-1} \mathbf{Y}_i^T & \sum_{i=1}^{\beta} \mathbf{Y}_{k+\alpha+i-1} \mathbf{Y}_{i+1}^T & \cdots & \sum_{i=1}^{\beta} \mathbf{Y}_{k+\alpha+i-1} \mathbf{Y}_{\alpha+i-1}^T \end{bmatrix}_{\alpha m \times \alpha m} \quad (6.5)$$

By definition, and recalling Equation (6.2) and Equation (6.3), $\mathbf{H}_k^c = \mathbf{H}_k \mathbf{H}_0^T$, where $\mathbf{H}_0^c = \mathbf{H}_0 \mathbf{H}_0^T$ is the zero-block covariance Hankel matrix with no shift nor lag in time, defined as:

$$\mathbf{H}_0^c = \begin{bmatrix} \sum_{i=1}^{\beta} \mathbf{Y}_i \mathbf{Y}_i^T & \sum_{i=1}^{\beta} \mathbf{Y}_i \mathbf{Y}_{i+1}^T & \cdots & \sum_{i=1}^{\beta} \mathbf{Y}_i \mathbf{Y}_{\alpha+i-1}^T \\ \sum_{i=1}^{\beta} \mathbf{Y}_{i+1} \mathbf{Y}_i^T & \sum_{i=1}^{\beta} \mathbf{Y}_{i+1} \mathbf{Y}_{i+1}^T & \cdots & \sum_{i=1}^{\beta} \mathbf{Y}_{i+1} \mathbf{Y}_{\alpha+i-1}^T \\ \vdots & \vdots & \ddots & \vdots \\ \sum_{i=1}^{\beta} \mathbf{Y}_{\alpha+i-1} \mathbf{Y}_i^T & \sum_{i=1}^{\beta} \mathbf{Y}_{\alpha+i-1} \mathbf{Y}_{i+1}^T & \cdots & \sum_{i=1}^{\beta} \mathbf{Y}_{\alpha+i-1} \mathbf{Y}_{\alpha+i-1}^T \end{bmatrix}_{\alpha m \times \alpha m} \quad (6.6)$$

Block correlation matrices \mathbf{H}_k^c and \mathbf{H}_0^c , both of size $\alpha m \times \alpha m$, consist of autocorrelations and cross-correlations of the output-only Markov parameters \mathbf{Y}_k , and contain less noise artifacts than the Hankel matrices of Equation (6.2) and Equation (6.3). It can be seen that canonical correlation analysis is performed by the product of two double infinite matrices that would validate the state sequence of the stochastic model.

Simultaneously, parameters α and β are the row and column size of the Hankel matrix that depend on the size of the signal (sampling length). Those values must be adjusted arbitrarily having in mind that higher α 's and β 's mean bigger correlation matrices, which in turn mean more accuracy but greater computational effort. For its part, the correlation matrix \mathbf{H}_0^c must contain less noise compared to \mathbf{H}_0 at every transition state and throughout the data sampling. Therefore, correlation matrix \mathbf{H}_k^c can be easily re-expressed as $\mathbf{H}_k^c = \mathbf{H}_k \mathbf{H}_0^T = \hat{\mathbf{O}} \mathbf{A}^k \hat{\mathbf{C}} \hat{\mathbf{C}}^T \hat{\mathbf{O}}^T$, $\mathbf{H}_k^c = \hat{\mathbf{O}} \mathbf{A}^k \hat{\mathbf{C}}^c$ where $\mathbf{C}^c = \hat{\mathbf{C}} \hat{\mathbf{C}}^T \hat{\mathbf{O}}^T$ of size $n \times \alpha m$, and $\hat{\mathbf{O}}$ is of dimensions $\alpha m \times n$. It is important to underline the similarities between the k -th Markov parameter $\mathbf{Y}_k = \mathbf{C} \mathbf{A}^{k-1} \mathbf{B}$ associated with Equation (6.1) and the block Hankel matrix \mathbf{H}_k^c of Equation (6.5). In both cases there is a product of three matrices with the discrete-time transition state matrix of k -th order in between. Thus, the reason why a block correlation Hankel matrix must be implemented in to eventually compute the $\hat{\mathbf{O}}$, \mathbf{A}^k , $\hat{\mathbf{C}}^c$ triad, then solve the stochastic identification problem with standard SI methods (i.e. Eigensystem Realization Algorithm (ERA)) by means of employing output signals only. A direct solution of this probabilistic based identification framework can be achieved by comparing Equation (6.5) and Equation (6.6) with traditional numerical schemes for the deterministic case (i.e. ERA/OKID or ERA/DC). For this approach, the output covariance matrix, defined as $\mathbf{\Lambda}_i = \mathbb{E}[\mathbf{y}_{k+i} \mathbf{y}_k^T]$ of size $m \times m$, can be adopted as a good stochastic approximation and may be treated as a block correlation matrix of system Markov parameters, similar to the covariance Hankel matrices defined in Equation (6.5) and Equation (6.6). A linear array of the output covariance terms $\mathbf{\Lambda}_i = \mathbb{E}[\mathbf{y}_{k+i} \mathbf{y}_k^T]$ will produce the desired block correlation Hankel matrices as follows:

$$\mathbf{H}_k^c = \begin{bmatrix} \Lambda_{k+1} & \Lambda_{k+2} & \cdots & \Lambda_{k+\beta} \\ \Lambda_{k+2} & \Lambda_{k+3} & \cdots & \Lambda_{k+\beta+1} \\ \vdots & \vdots & \ddots & \vdots \\ \Lambda_{k+\alpha} & \Lambda_{k+\alpha+1} & \cdots & \Lambda_{k+\alpha+\beta-1} \end{bmatrix}_{\alpha m \times \alpha m} \quad (6.7)$$

$$\mathbf{H}_0^c = \begin{bmatrix} \Lambda_1 & \Lambda_2 & \cdots & \Lambda_\beta \\ \Lambda_2 & \Lambda_3 & \cdots & \Lambda_{\beta+1} \\ \vdots & \vdots & \ddots & \vdots \\ \Lambda_\alpha & \Lambda_{\alpha+1} & \cdots & \Lambda_{\alpha+\beta-1} \end{bmatrix}_{\alpha m \times \alpha m} \quad (6.8)$$

Here, $\alpha = \beta$ due to the fact that correlations are assumed real-positive square matrices, whereas in order to obtain a full rank Hankel matrix \mathbf{H}_k^c the number of shifts applied to must be at least the estimated order of the system divided by the number of output signals ($\alpha > n/m$) [Ljung 1987]. Both \mathbf{H}_k^c and \mathbf{H}_0^c are of size $\alpha m \times \alpha m$, and must satisfy $2\alpha m - 1 = 2\beta m - 1 \leq l$ and $\alpha m = \beta m > n$. As mentioned before, Equation (6.7) and Equation (6.8) are composed by positive real sequences that are obtained directly from the output data, with no need of information coming from the state space model. In principle, a stochastic stationary process can be ruled by expectation identities among the state \mathbf{x}_k , the output \mathbf{y}_k , the input noise \mathbf{w}_k and the output noise \mathbf{v}_k vectors. Assuming the latter two \mathbf{w}_k and \mathbf{v}_k as zero-mean white gaussian signals as stated in a previous section, it can be proved that [*ibid.* Van Overschee and De Moor 1996]:

$$\begin{aligned} \mathbb{E}[\mathbf{x}_k \mathbf{v}_k^T]_{n \times m} &= \mathbf{0}; & \mathbb{E}[\mathbf{x}_k \mathbf{w}_k^T]_{n \times n} &= \mathbf{0} \\ \mathbb{E}[\mathbf{y}_k \mathbf{v}_k^T]_{m \times m} &= \mathbf{0}; & \mathbb{E}[\mathbf{y}_k \mathbf{w}_k^T]_{m \times n} &= \mathbf{0} \\ \mathbb{E}[\mathbf{w}_{k+i} \mathbf{w}_k^T]_{n \times n} &= \mathbf{0}; & \mathbb{E}[\mathbf{v}_{k+i} \mathbf{v}_k^T]_{m \times m} &= \mathbf{0} \end{aligned} \quad (6.9)$$

$$\begin{aligned} \mathbb{E}[\mathbf{w}_k \mathbf{w}_k^T]_{n \times n} &= \mathbf{Q} \\ \mathbb{E}[\mathbf{v}_k \mathbf{v}_k^T]_{m \times m} &= \mathbf{R} \\ \mathbb{E}[\mathbf{w}_k \mathbf{v}_k^T]_{n \times m} &= \mathbf{S} \end{aligned} \quad (6.10)$$

Expected values of the state \mathbf{x}_k pairs are temporarily assumed constant [Katayama 2005], where the identity $E[\mathbf{x}_k \mathbf{x}_k^T] = E[\mathbf{x}_{k+i} \mathbf{x}_{k+i}^T] = \mathbf{\Sigma}$ of size $n \times n$ stands for stationary conditions. It is easily reproducible from Equation (6.1) that $\mathbf{x}_{k+i} = \mathbf{A}^i \mathbf{x}_k + \mathbf{A}^{i-1} \mathbf{w}_k + \mathbf{A}^{i-2} \mathbf{w}_{k-1} + \dots + \mathbf{w}_{k+i-1}$ for initial conditions $\mathbf{x}_0 = \mathbf{0}$. The shifted expectation of the state vector can be obtained by post-multiplying the latter series expansion by \mathbf{x}_k^T and taking expectations in both left and right hand sides of the state vector \mathbf{x}_{k+i} , then retrieving the first identity of Equation (6.4), in other words $E[\mathbf{x}_{k+i} \mathbf{x}_k^T] = \mathbf{A}^i \mathbf{\Sigma}$ of size $n \times n$ holds as an identity of the transition state in stationary conditions. In parallel, identity terms of the output expectations are defined from shifted expectations $E[\mathbf{y}_{k+i} \mathbf{y}_k^T] = \mathbf{\Lambda}_i$, size $m \times m$, of the outputs where $E[\mathbf{y}_k \mathbf{y}_k^T] = E[\mathbf{y}_{k+i} \mathbf{y}_{k+i}^T] = \mathbf{\Lambda}_0$ is a particular case of the solution at no shift when $i = 0$. In principle, Equation (6.4) is governed by noise vectors $\{w_k\}$ and $\{v_k\}$ that obey expectation sequences of covariance matrices defined as follows:

$$E \left[\begin{Bmatrix} \mathbf{w}_k \\ \mathbf{v}_k \end{Bmatrix} \begin{Bmatrix} \mathbf{w}_k^T & \mathbf{v}_k^T \end{Bmatrix} \right] = \begin{bmatrix} \mathbf{Q} & \mathbf{S} \\ \mathbf{S}^T & \mathbf{R} \end{bmatrix} \delta_{kk} \quad (6.11)$$

where the term δ_{kl} is the delta of Dirac. The state covariance matrix is assumed constant at every state k because the transition state is treated as a stationary process. \mathbf{Q} is the auto-covariance matrix of the input noise of size $n \times n$, \mathbf{R} the auto-covariance matrix of the output noise of size $m \times m$, and \mathbf{S} the cross-covariance matrix of the input and output noises of size $n \times m$. The end goal of this stochastic state-space model is to compute the order n of the unknown system by means of a similarity transformation that equates the second-order statistics of the output of the model with the second-order statistics of the measured output. To accomplish this goal, examination of the controllability and observability matrices is made through a factorization decomposition of the block Hankel matrix \mathbf{H}_0^c defined in Equation (6.8) [Kameyama and Ohsumi 2007]. Recalling $\mathbf{H}_k^c = \hat{\mathbf{O}} \mathbf{A}^k \hat{\mathbf{C}}^c$, where the observability and controllability expansions for the case of the stochastic system

identification problem are modified to the block series $\hat{\mathbf{O}} = [\mathbf{C} \quad \mathbf{CA} \quad \mathbf{CA}^2 \dots \mathbf{CA}^{\alpha-1}]_{cam \times n}^T$ and $\hat{\mathbf{C}}^c = [\mathbf{I} \quad \mathbf{AI} \quad \mathbf{A}^2\mathbf{I} \dots \mathbf{A}^{\alpha-1}\mathbf{I}]_{n \times cam}$. Applying singular value decomposition (SVD) to the non-shifted block Hankel matrix $\mathbf{H}_0^c = \hat{\mathbf{O}}\hat{\mathbf{C}}^c$:

$$[\mathbf{H}_0^c]_{cam \times cam} = [\mathbf{R}_n]_{cam \times n} [\mathbf{R}_s]_{cam \times (cam-n)} \begin{bmatrix} [\Sigma_n]_{n \times n} & [\mathbf{0}]_{n \times n} \\ [\mathbf{0}]_{n \times n} & [\Sigma_s]_{n \times n} \end{bmatrix} \begin{bmatrix} [\mathbf{S}_n]_{n \times cam}^T \\ [\mathbf{S}_s]_{(cam-n) \times cam}^T \end{bmatrix} \quad (6.12)$$

$$[\mathbf{H}_0^c]_{cam \times cam} \approx [\mathbf{R}_n]_{cam \times n} [\Sigma_n]_{n \times n} [\mathbf{S}_n]_{n \times cam}^T$$

where Σ_n groups the largest non-zero n singular values (user defined order of the system) from \mathbf{H}_0^c , whereas Σ_s is the complementary matrix containing the dismissed information. The same rule applies for the left-singular vectors \mathbf{R}_n and \mathbf{R}_s as the eigenvectors of the notable product $\mathbf{H}_0^c \mathbf{H}_0^{cT}$, whereas \mathbf{S}_n^T and \mathbf{S}_s^T operate as the counterpart eigenvectors of the $\mathbf{H}_0^{cT} \mathbf{H}_0^c$ product. Both \mathbf{R}_n and \mathbf{S}_n^T are shaped by the primary n dominant columns and it can be observed that the observability matrix $\hat{\mathbf{O}}$ is related to \mathbf{R}_n , while the controllability matrix $\hat{\mathbf{C}}$ is associated with \mathbf{S}_n^T . A balanced choice of the SVD product of Equation (6.12) would be $\hat{\mathbf{O}} = \mathbf{R}_n \Sigma_n^{1/2}$ and $\hat{\mathbf{C}} = \Sigma_n^{1/2} \mathbf{S}_n^T$. Consequently, \mathbf{H}_k^c can be expanded for $k = 1$ as $\mathbf{H}_1^c = \mathbf{R}_n \Sigma_n^{1/2} \mathbf{A} \Sigma_n^{1/2} \mathbf{S}_n^T$, and solution of the triad $\hat{\mathbf{O}} \mathbf{A}^k \hat{\mathbf{C}}^c$ is:

$$\begin{aligned} \hat{\mathbf{O}} &= \mathbf{R}_n \Sigma_n^{1/2} \\ \mathbf{A} &= \Sigma_n^{-1/2} \mathbf{R}_n^T \mathbf{H}_1^c \mathbf{S}_n \Sigma_n^{-1/2} \\ \hat{\mathbf{C}} &= \Sigma_n^{1/2} \mathbf{S}_n^T \end{aligned} \quad (6.13)$$

Up to this point, no cyclo-stationary effects have been induced yet, and the question raises on how a cyclic induced motion could be filtered out from contaminated – noisy –

output-only random signals, then ensure a description of the output signal content associated exclusively to the structural performance of the spinning structure.

6.2.3 Cyclo-Stationary Stochastic Subspace

Consider an unknown cyclic noisy stochastic system represented by the state-space realization using outputs only, as a special case of Equation (6.1) (see Figure 6.1), rewritten as follows [Lopes dos Santos *et al.* 2005]:

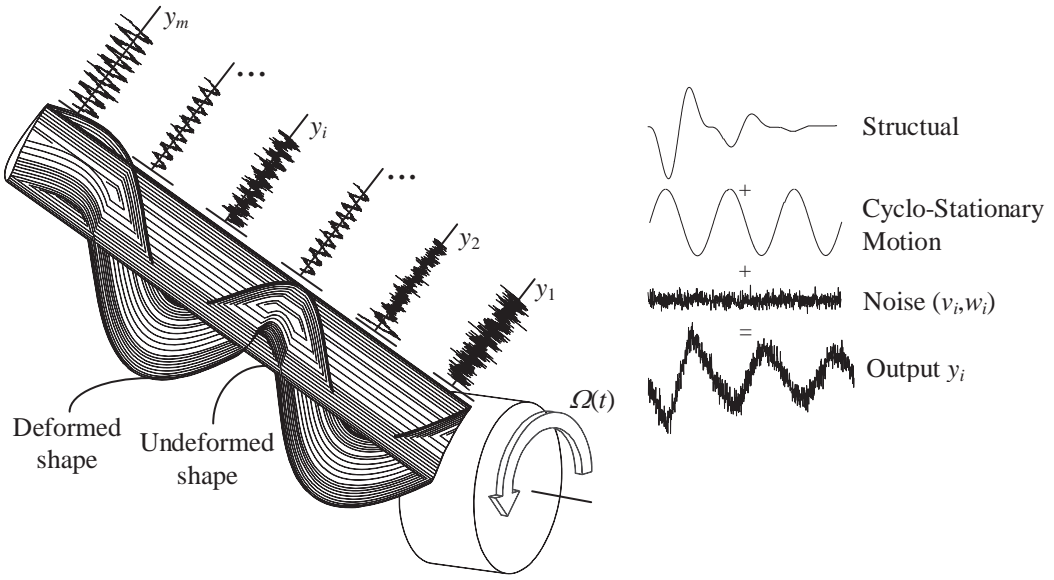


Figure 6.1. Rotating beam element under stochastic subspace identification using output signals only, and governed by a cyclo-stationary time-varying motion $\Omega(t)$.

$$\begin{aligned} \mathbf{x}_{k+1} &= [\mathbf{A}_0 + \bar{\mathbf{A}}] \mathbf{x}_k + \mathbf{w}_k \\ \mathbf{y}_k &= [\mathbf{C}_0 + \bar{\mathbf{C}}] \mathbf{x}_k + \mathbf{v}_k \end{aligned} \quad (6.14)$$

where $\bar{\mathbf{A}}$ and $\bar{\mathbf{C}}$, of order nxn and mxn , respectively, are unknown stationary state and observation matrices variable in time and of periodic nature, whereas \mathbf{A}_0 and \mathbf{C}_0 of sizes nxn and mxn as well, represent the non-cyclo-stationary dependent state and observation matrices. To obtain the unknown cyclo-stationary dependent system matrices $\bar{\mathbf{A}}$ and $\bar{\mathbf{C}}$

, it is convenient to establish first a linear parameter time-varying system (LPTV) [Tóth 2008], which can be induced as a linear system sinusoidal series containing system matrices, as a function of a known time-varying parameter vector. For the case of rotational structures and spinning machinery, a so-called cyclo-stationary operator $p(\Omega(k))$ is proposed to appraise the incidence of the spinning contribution to the rotor-structure modal dynamics, according to a stochastic stationary identification model. In this way, the stochastic state-space will be a function of the time-varying spinning velocity $\Omega(k)$ for $k = 0, 1, 2, \dots$ states of the rotary system. For this study, an expansion of the state-space representation of Equation (6.14) takes the form [*ibid.* Lopes dos Santos *et al.* 2005]:

$$\begin{aligned} \mathbf{x}_{k+1} &= \left[\mathbf{A}_0 + \sum_{i=1}^s [\mathbf{A}_{ci} p_{cki} + \mathbf{A}_{si} p_{ski}] \right] \mathbf{x}_k + \mathbf{w}_k \\ \mathbf{y}_k &= \left[\mathbf{C}_0 + \sum_{i=1}^s [\mathbf{C}_{ci} p_{cki} + \mathbf{C}_{si} p_{ski}] \right] \mathbf{x}_k + \mathbf{v}_k \end{aligned} \quad (6.15)$$

where $\bar{\mathbf{A}} = \sum_{i=1}^s [\mathbf{A}_{ci} p_{cki} + \mathbf{A}_{si} p_{ski}]$ and $\bar{\mathbf{C}} = \sum_{i=1}^s [\mathbf{C}_{ci} p_{cki} + \mathbf{C}_{si} p_{ski}]$, $p_{cki} = \cos(i\Omega(k)k)$ and $p_{ski} = \sin(i\Omega(k)k)$. Therefore, $\mathbf{A} = \mathbf{A}_0 + \sum_{i=1}^s [\mathbf{A}_{ci} p_{cki} + \mathbf{A}_{si} p_{ski}]$ is the combined cyclo-stationary and linear parameter time-varying state-transition matrix; whereas $\mathbf{C} = \mathbf{C}_0 + \sum_{i=1}^s [\mathbf{C}_{ci} p_{cki} + \mathbf{C}_{si} p_{ski}]$ is the combined cyclo-stationary and linear parameter time-varying observation matrix. Matrices \mathbf{A}_{ci} and \mathbf{A}_{si} of order $n \times n$ each can be interpreted as cyclo-stationary cosine and sine transition matrices for the linear parameter $i = 1, 2, \dots, s$. In equal circumstances, \mathbf{C}_{ci} and \mathbf{C}_{si} of order $m \times n$ each are the corresponding cyclo-stationary cosine and sine observation matrices. The series dimension s is an arbitrary number that depends on the complexity and the order of the rotational system. Is a user defined value and the selection of the model structure is critical in terms of computational effort. A trade-off must be analyzed to balance complexity and accuracy according to the state size n [*ibid.* Kailath 1980]. For rotor elements with constant cross-

section as illustrated in Figure 6.1, the state dimensionality s can take small values (*i.e.* $12m$ DOF's), whereas for higher order tapered-swept variations of geometry and inertia s becomes larger. The state-space relations of Equation (6.15) may also be expanded in the form:

$$\begin{aligned}\mathbf{x}_{k+1} &= \mathbf{A}_0 \mathbf{x}_k + \mathbf{A}_{pc} \{\mathbf{p}_{ck} \otimes \mathbf{x}_k\} + \mathbf{A}_{ps} \{\mathbf{p}_{sk} \otimes \mathbf{x}_k\} + \mathbf{w}_k \\ \mathbf{y}_k &= \mathbf{C}_0 \mathbf{x}_k + \mathbf{C}_{pc} \{\mathbf{p}_{ck} \otimes \mathbf{x}_k\} + \mathbf{C}_{ps} \{\mathbf{p}_{sk} \otimes \mathbf{x}_k\} + \mathbf{v}_k\end{aligned}\quad (6.16)$$

where $\mathbf{A}_{pc} = [\mathbf{A}_{c1} \ \mathbf{A}_{c2} \ \dots \ \mathbf{A}_{cs}]$ of size $n \times sn$, and $\mathbf{A}_{ps} = [\mathbf{A}_{s1} \ \mathbf{A}_{s2} \ \dots \ \mathbf{A}_{ss}]$ of size $n \times sn$, are the cosine and sine blocks of the linear parameter time-varying state matrix, respectively. The same illustration can be made for $\mathbf{C}_{pc} = [\mathbf{C}_{c1} \ \mathbf{C}_{c2} \ \dots \ \mathbf{C}_{cs}]$ dimension $m \times sn$, and $\mathbf{C}_{ps} = [\mathbf{C}_{s1} \ \mathbf{C}_{s2} \ \dots \ \mathbf{C}_{ss}]$ size $m \times sn$, as the cosine and sine blocks of the linear parameter time-varying observation matrix. The cyclo-stationary cosine-driven vector is described by $\mathbf{p}_{ck} = \{p_{ck1} \ p_{ck2} \ \dots \ p_{cks}\}^T$ size $s \times 1$, whereas the associated cyclo-stationary sine-driven vector is defined as $\mathbf{p}_{sk} = \{p_{sk1} \ p_{sk2} \ \dots \ p_{sks}\}^T$ with size $s \times 1$. System matrices \mathbf{A}_0 and \mathbf{C}_0 are non-cyclo-stationary in nature, and are presumed constant throughout the analysis. The operator \otimes is known as the Kronecker product formulated as $\mathbf{p}_{ck} \otimes \mathbf{x}_k = \{p_{ck1}\mathbf{x}_k \ p_{ck2}\mathbf{x}_k \ \dots \ p_{cks}\mathbf{x}_k\}^T$ or $\mathbf{p}_{sk} \otimes \mathbf{x}_k = \{p_{sk1}\mathbf{x}_k \ p_{sk2}\mathbf{x}_k \ \dots \ p_{sks}\mathbf{x}_k\}^T$, both of size $sn \times 1$. A block diagram of the Markov model is depicted in Figure 6.2. Given \mathbf{p}_{ck} and \mathbf{p}_{sk} as periodic functions – and therefore stationary – with covariance matrices $[\mathbf{R}_{pck}]_{s \times s}$ and $[\mathbf{R}_{psk}]_{s \times s}$, and cross-covariance matrix $[\mathbf{R}_{pcsk}]_{s \times s}$, being \mathbf{p}_{ck} and \mathbf{p}_{sk} independent of \mathbf{x}_k (*i.e.*, $E[\mathbf{p}_{ck}] = 0$; $E[\mathbf{p}_{sk}] = 0$); two cyclo-stationary products of size $sn \times 1$ can be written as $\mathbf{z}_{ck} = \mathbf{p}_{ck} \otimes \mathbf{x}_k$ and $\mathbf{z}_{sk} = \mathbf{p}_{sk} \otimes \mathbf{x}_k$. The expectation of such products is the expectation of either \mathbf{p}_{ck} and \mathbf{p}_{sk} . In other words, $E[\mathbf{z}_{ck}] = E[\mathbf{p}_{ck} \otimes \mathbf{x}_k] = E[\mathbf{p}_{ck}] \otimes E[\mathbf{x}_k] = \mathbf{0}$ and $E[\mathbf{z}_{sk}] = E[\mathbf{p}_{sk} \otimes \mathbf{x}_k] = E[\mathbf{p}_{sk}] \otimes E[\mathbf{x}_k] = \mathbf{0}$. The covariance matrices for the cyclo-stationary products \mathbf{z}_{ck} and \mathbf{z}_{sk} can be expanded as a lag expectation that takes the form $[\mathbf{R}_{zck}]_{sn \times sn} = E[\mathbf{z}_{ck} \mathbf{z}_{ck+1}^T] = E[\{\mathbf{p}_{ck} \otimes \mathbf{x}_k\} \{\mathbf{p}_{ck+1}^T \otimes \mathbf{x}_{k+1}^T\}]$

$= E[\mathbf{p}_{ck} \mathbf{p}_{ck+1}^T] \otimes E[\mathbf{x}_k \mathbf{x}_{k+1}^T]$. Then $\mathbf{R}_{zcck} = \mathbf{R}_{pcck} \otimes \mathbf{\Sigma}$ for (k, k) pairs and $\mathbf{R}_{zcck} = \mathbf{0}$ for $(k, k+i)$ pairs. Here, $\mathbf{R}_{pcck} = E[\mathbf{p}_{ck} \mathbf{p}_{ck+i}^T]$ is interpreted as the cyclo-stationary cosine covariance matrix, \mathbf{R}_{zcck} is the cyclo-stationary state covariance matrix of the cosine block, and $\mathbf{\Sigma}$ is the state covariance matrix as defined previously. Proceeding similarly for $[\mathbf{R}_{zssk}]_{sn \times sn}$, the cyclo-stationary sine covariance matrix is operated as $\mathbf{R}_{pssk} = E[\mathbf{p}_{sk} \mathbf{p}_{sk+i}^T]$ and follows the same rule as for \mathbf{R}_{pcck} . Therefore, it is said that \mathbf{z}_{ck} and \mathbf{z}_{sk} are cyclo-stationary processes of the state \mathbf{x}_k with variance $\mathbf{R}_{pcck} \otimes \mathbf{\Sigma}$ and $\mathbf{R}_{pssk} \otimes \mathbf{\Sigma}$, respectively. Furthermore, it can be shown [*ibid.* Lopes dos Santos *et al.* 2005] that the noise expectation of \mathbf{z}_{ck} is $E[\mathbf{z}_{ck} \mathbf{w}_k^T] = E[(\mathbf{p}_{ck} \otimes \mathbf{x}_k) \mathbf{w}_k^T] = E[(\mathbf{p}_{ck} \otimes \mathbf{w}_k) \mathbf{x}_k^T] = E[\mathbf{p}_{ck}] \otimes E[\mathbf{x}_k \mathbf{w}_k^T] = \mathbf{0}$. In the same fashion, $E[\mathbf{z}_{sk} \mathbf{w}_k^T] = \mathbf{0}$, $E[\mathbf{z}_{ck} \mathbf{v}_k^T] = \mathbf{0}$ and $E[\mathbf{z}_{sk} \mathbf{v}_k^T] = \mathbf{0}$. Taking now the expected value of the product $\mathbf{x}_{k+1} \mathbf{x}_{k+1}^T$ from the first relation of Equation (6.16), and applying general properties of the Kronecker products and expectation outcomes subscribed in Equation (6.9) and Equation (6.11), combined:

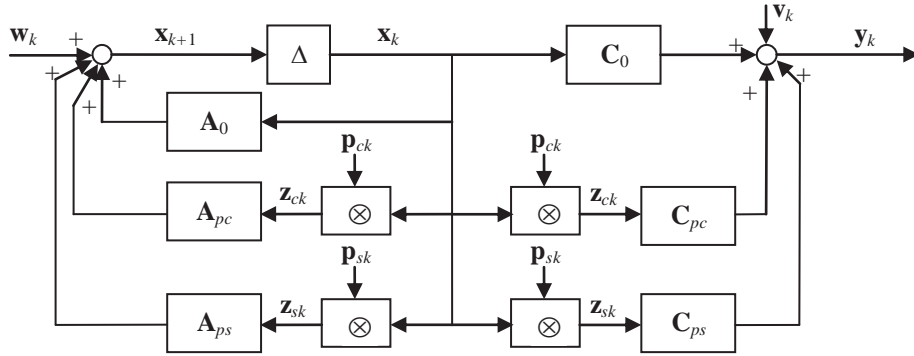


Figure 6.2. Block diagram of a cyclo-stationary stochastic subspace system with time-varying linear parameters \mathbf{A}_{pc} , \mathbf{A}_{ps} , \mathbf{C}_{pc} , \mathbf{C}_{ps} . Symbol Δ stands for delay.

$$\begin{aligned}
E[\mathbf{x}_{k+1}\mathbf{x}_{k+1}^T]_{n \times n} &= \mathbf{A}_0 E[\mathbf{x}_k \mathbf{x}_k^T] \mathbf{A}_0^T \\
&\quad + \mathbf{A}_{pc} E[\mathbf{p}_{ck} \otimes \mathbf{x}_k] E[\mathbf{p}_{ck}^T \otimes \mathbf{x}_k^T] \mathbf{A}_{pc}^T \\
&\quad + \mathbf{A}_{ps} E[\mathbf{p}_{sk} \otimes \mathbf{x}_k] E[\mathbf{p}_{sk}^T \otimes \mathbf{x}_k^T] \mathbf{A}_{ps}^T \\
&\quad + E[\mathbf{w}_k \mathbf{w}_k^T] \\
E[\mathbf{x}_{k+1}\mathbf{x}_{k+1}^T]_{n \times n} &= \mathbf{\Sigma} = \mathbf{A}_0 \mathbf{\Sigma} \mathbf{A}_0^T + \mathbf{A}_{pc} [\mathbf{R}_{pcck} \otimes \mathbf{\Sigma}] \mathbf{A}_{pc}^T \\
&\quad + \mathbf{A}_{ps} [\mathbf{R}_{pssk} \otimes \mathbf{\Sigma}] \mathbf{A}_{ps}^T + \mathbf{Q}
\end{aligned} \tag{6.17}$$

Proceeding now in a similar fashion as Equation (6.17), now for the auto-covariance of the outputs:

$$\begin{aligned}
E[\mathbf{y}_{k+1}\mathbf{y}_{k+1}^T]_{m \times m} &= \mathbf{C}_0 E[\mathbf{x}_k \mathbf{x}_k^T] \mathbf{C}_0^T \\
&\quad + \mathbf{C}_{pc} E[\mathbf{p}_{ck} \otimes \mathbf{x}_k] E[\mathbf{p}_{ck}^T \otimes \mathbf{x}_k^T] \mathbf{C}_{pc}^T \\
&\quad + \mathbf{C}_{ps} E[\mathbf{p}_{sk} \otimes \mathbf{x}_k] E[\mathbf{p}_{sk}^T \otimes \mathbf{x}_k^T] \mathbf{C}_{ps}^T \\
&\quad + E[\mathbf{v}_k \mathbf{v}_k^T] \\
E[\mathbf{y}_{k+1}\mathbf{y}_{k+1}^T]_{m \times m} &= \mathbf{\Lambda}_0 = \mathbf{C}_0 \mathbf{\Sigma} \mathbf{C}_0^T + \mathbf{C}_{pc} [\mathbf{R}_{pcck} \otimes \mathbf{\Sigma}] \mathbf{C}_{pc}^T \\
&\quad + \mathbf{C}_{ps} [\mathbf{R}_{pssk} \otimes \mathbf{\Sigma}] \mathbf{C}_{ps}^T + \mathbf{R}
\end{aligned} \tag{6.18}$$

Defining the one-shifted cyclo-stationary gain from Equation (6.16) as:

$$\begin{aligned}
E[\mathbf{x}_{k+1}\mathbf{y}_k^T]_{n \times m} &= \mathbf{A}_0 E[\mathbf{x}_k \mathbf{x}_k^T] \mathbf{C}_0^T \\
&\quad + \mathbf{A}_{pc} E[\mathbf{p}_{ck} \otimes \mathbf{x}_k] E[\mathbf{p}_{ck}^T \otimes \mathbf{x}_k^T] \mathbf{C}_{pc}^T \\
&\quad + \mathbf{A}_{ps} E[\mathbf{p}_{sk} \otimes \mathbf{x}_k] E[\mathbf{p}_{sk}^T \otimes \mathbf{x}_k^T] \mathbf{C}_{ps}^T \\
&\quad + E[\mathbf{w}_k \mathbf{v}_k^T] \\
E[\mathbf{x}_{k+1}\mathbf{y}_k^T]_{n \times m} &= \mathbf{G}_0 = \mathbf{A}_0 \mathbf{\Sigma} \mathbf{C}_0^T + \mathbf{A}_{pc} [\mathbf{R}_{pcck} \otimes \mathbf{\Sigma}] \mathbf{C}_{pc}^T \\
&\quad + \mathbf{A}_{ps} [\mathbf{R}_{pssk} \otimes \mathbf{\Sigma}] \mathbf{C}_{ps}^T + \mathbf{S}
\end{aligned} \tag{6.19}$$

whereas the i -shifted cyclo-stationary gain version of Equation (6.19) is computed as follows:

$$\begin{aligned}
E[\mathbf{x}_{k+i}\mathbf{y}_k^T]_{n \times m} &= \mathbf{A}_0 E[\mathbf{x}_{k+i-1}\mathbf{x}_k^T] \mathbf{C}_0^T \\
&\quad + \mathbf{A}_{pc} E[\mathbf{p}_{ck+i-1} \otimes \mathbf{x}_{k+i-1}] E[\mathbf{p}_{ck}^T \otimes \mathbf{x}_k^T] \mathbf{C}_{pc}^T \\
&\quad + \mathbf{A}_{ps} E[\mathbf{p}_{sk+i-1} \otimes \mathbf{x}_{k+i-1}] E[\mathbf{p}_{sk}^T \otimes \mathbf{x}_k^T] \mathbf{C}_{ps}^T \\
&\quad + E[\mathbf{w}_{k+i-1} \mathbf{v}_k^T] \\
E[\mathbf{x}_{k+i}\mathbf{y}_k^T]_{n \times m} &= \mathbf{G} = \mathbf{A}_0^i \mathbf{\Sigma} \mathbf{C}_0^T
\end{aligned} \tag{6.20}$$

Retaking the output covariance matrix definition of Equation (6.18), now shifted by i states.

$$\begin{aligned}
E[\mathbf{y}_{k+i}\mathbf{y}_k^T]_{m \times m} &= \mathbf{C}_0 E[\mathbf{x}_{k+i}\mathbf{x}_k^T] \mathbf{C}_0^T \\
&\quad + \mathbf{C}_{pc} E[\mathbf{p}_{ck+i} \otimes \mathbf{x}_{k+i}] E[\mathbf{p}_{ck}^T \otimes \mathbf{x}_k^T] \mathbf{C}_{pc}^T \\
&\quad + \mathbf{C}_{ps} E[\mathbf{p}_{sk+i} \otimes \mathbf{x}_{k+i}] E[\mathbf{p}_{sk}^T \otimes \mathbf{x}_k^T] \mathbf{C}_{ps}^T \\
&\quad + E[\mathbf{v}_{k+i} \mathbf{v}_k^T] \\
E[\mathbf{y}_{k+i}\mathbf{y}_k^T]_{m \times m} &= \mathbf{\Lambda}_i = \mathbf{C}_0 \mathbf{A}_0^i \mathbf{\Sigma} \mathbf{C}_0^T \\
E[\mathbf{y}_{k+i}\mathbf{y}_k^T]_{m \times m} &= \mathbf{\Lambda}_i = \mathbf{C}_0 \mathbf{A}_0^{i-1} \mathbf{G}
\end{aligned} \tag{6.21}$$

The next logical step would be to apply any output-only stochastic method to solve for the triad $[\mathbf{C}_0]_{m \times n}$, $[\mathbf{A}_0]_{n \times n}^{i-1}$, and $[\mathbf{G}]_{n \times m}$ from Equation (6.21) (*i.e.*, forward innovation stochastic identification algorithm [Van Overschee *et al.* 1991]). A direct solution of the stochastic cyclo-stationary linear parameter time-varying identification framework can be achieved by comparing Equation (6.21) with the stochastic subspace skim presented in Section 6.2.2. Solution of the triad $\mathbf{C}_0 \mathbf{A}_0^{i-1} \mathbf{G}$ will follow a similar scheme as that of Equation (6.13), but now removing α shifted lags in the form $\mathbf{C}_0 = \hat{\mathbf{O}}(1:m,:)$ and $\mathbf{G} = \hat{\mathbf{C}}(:,1:m)$. In other words:

$$\begin{aligned}
\mathbf{C}_0 &= [\mathbf{I}]_{m \times cm} \mathbf{R}_n \mathbf{\Sigma}_n^{1/2} \\
\mathbf{A} &= \mathbf{\Sigma}_n^{-1/2} \mathbf{R}_n^T \mathbf{H}_1^c \mathbf{S}_n \mathbf{\Sigma}_n^{-1/2} \\
\mathbf{G} &= \mathbf{\Sigma}_n^{1/2} \mathbf{S}_n^T [\mathbf{I}]_{cm \times m}
\end{aligned} \tag{6.22}$$

Once the subspace realization has been consolidated, the cyclo-stationary effects of the system can be disassembled by first, picking either the velocity profile from the output channels in the frequency domain (*i.e.* Fast Fourier Transformation: FFT), or supplying information by the user, then assigning $\Omega(k)$ as a time-varying local parameter. It is important to note that the spinning velocity $\Omega(k)$ time history does not necessary has to be constant over time, but it should be able to be represented by a smooth transition curve from one velocity to another. This limit is a requirement for keeping consistency and validation of the mathematical framework presented in this study. For instance, the calculation of the total transition system matrix \mathbf{A} and total observability matrix \mathbf{C} , from the forward innovation stochastic identification solver, will serve to draw conclusions of the actual order of the system. Further down in the analysis, the computation of the sinusoidal correlation matrices \mathbf{R}_{pcck} and \mathbf{R}_{pssk} will occur based on the actual value of $\Omega(k)$ at step $k = 1, 2, \dots$. The final procedure would be computing \mathbf{A}_{pc} , \mathbf{A}_{ps} , \mathbf{C}_{pc} and \mathbf{C}_{ps} provided that these are the cyclo-stationary state and observation matrices to be filtered out from the inherent structural loading dynamics. Simultaneously, selection of the magnitude of the control parameter s will be in accordance to the complexity of the model as explained before (*i.e.* $s := 12m$ for constant cross sections (less accuracy), $s := 24m$ for linear variation (middle accuracy), $s := 36m$ for parabolic tapered-swept gradient variation (higher accuracy)). Quantification of external noises \mathbf{w}_k and \mathbf{v}_k , as may well be based on the difference between real and predicted states of the system (real + noise = predicted), as described in the following section.

6.2.4 Prediction and Residual States

Knowing that the bilinear terms \mathbf{z}_{ck} and \mathbf{z}_{sk} are cyclo-stationary white noise processes, uncorrelated with \mathbf{w}_k and \mathbf{v}_k , the cyclo-stationary stochastic model of Equation (6.16) can be rewritten in the form:

$$\begin{aligned}\mathbf{x}_{k+1} &= \mathbf{A}_0 \mathbf{x}_k + \mathbf{A}_{pc} \mathbf{z}_{ck} + \mathbf{A}_{ps} \mathbf{z}_{sk} + \mathbf{w}_k \\ \mathbf{y}_k &= \mathbf{C}_0 \mathbf{x}_k + \mathbf{C}_{pc} \mathbf{z}_{ck} + \mathbf{C}_{ps} \mathbf{z}_{sk} + \mathbf{v}_k\end{aligned}\quad (6.23)$$

For the sake of the stability and convergence of the numerical algorithm, consider a cyclo-stationary Kalman filter with predicted state $\hat{\mathbf{x}}_k$ of the linear form [Grewal and Andrews 1993] (see Figure 6.3):

$$\hat{\mathbf{x}}_{k+1} = \mathbf{A}_0 \hat{\mathbf{x}}_k + \mathbf{A}_{pc} \hat{\mathbf{z}}_{ck} + \mathbf{A}_{ps} \hat{\mathbf{z}}_{sk} + \mathbf{K}_k [\mathbf{y}_k - \mathbf{C}_0 \hat{\mathbf{x}}_k - \mathbf{C}_{pc} \hat{\mathbf{z}}_{ck} - \mathbf{C}_{ps} \hat{\mathbf{z}}_{sk}] \quad (6.24)$$

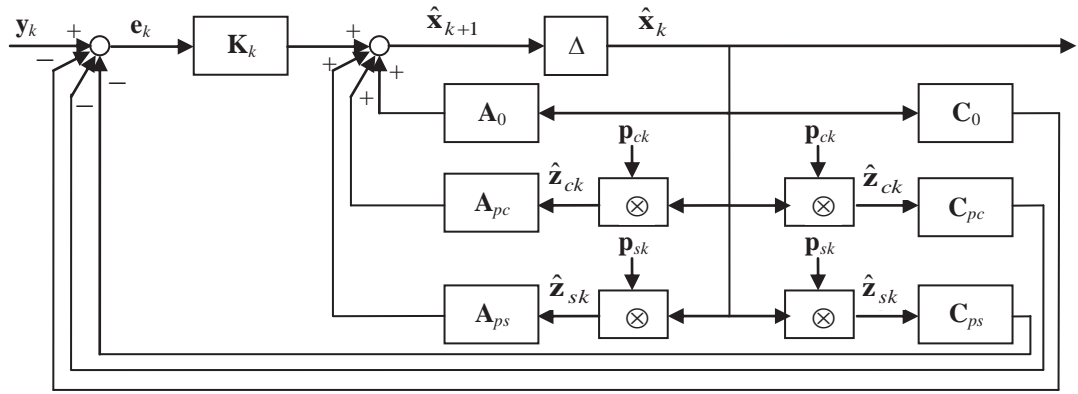


Figure 6.3. Kalman filter block diagram of a cyclo-stationary stochastic subspace system with time-varying linear parameters \mathbf{A}_{pc} , \mathbf{A}_{ps} , \mathbf{C}_{pc} , \mathbf{C}_{ps} . Symbol Δ stands for delay.

where expected noises are zero all and $[\mathbf{K}_k]_{n \times m}$ is the Kalman gain, valid when the noise is canceled out as a result of the filtering action of the feedback quantity, known as the innovation term. Similarly, as stated for the cyclo-stationary products \mathbf{z}_{ck} and \mathbf{z}_{sk} , the corresponding predicted states are also cyclo-stationary and are computed as $\hat{\mathbf{z}}_{ck} = [\mathbf{p}_{ck} \otimes \hat{\mathbf{x}}_k]$ and $\hat{\mathbf{z}}_{sk} = [\mathbf{p}_{sk} \otimes \hat{\mathbf{x}}_k]$ with both dimensions $sn \times 1$. Now, from Kalman filter theory [Kalman 1960], the innovation term should be uncorrelated with $\hat{\mathbf{x}}_k$, $\hat{\mathbf{z}}_{ck}$ and $\hat{\mathbf{z}}_{sk}$. Residual white noise processes can be described as $\{\tilde{\mathbf{w}}_k\}_{n \times 1} = \mathbf{A}_{pc} \tilde{\mathbf{z}}_{ck} + \mathbf{A}_{ps} \tilde{\mathbf{z}}_{sk} + \mathbf{w}_k$ and $\{\tilde{\mathbf{v}}_k\}_{m \times 1} = \mathbf{C}_{pc} \tilde{\mathbf{z}}_{ck} + \mathbf{C}_{ps} \tilde{\mathbf{z}}_{sk} + \mathbf{v}_k$. They can be interpreted as a cyclo-stationary process and

measurement residual noises, respectively, of the linear time-varying model of the LPTV system. Residual cyclo-stationary states are given by the difference between real and predicted quantities $\tilde{\mathbf{z}}_{ck} = \mathbf{z}_{ck} - \hat{\mathbf{z}}_{ck} = \{\mathbf{p}_{ck} \otimes \mathbf{x}_k\} - \{\mathbf{p}_{ck} \otimes \hat{\mathbf{x}}_k\}$ and $\tilde{\mathbf{z}}_{sk} = \mathbf{z}_{sk} - \hat{\mathbf{z}}_{sk} = \{\mathbf{p}_{sk} \otimes \mathbf{x}_k\} - \{\mathbf{p}_{sk} \otimes \hat{\mathbf{x}}_k\}$, both size $sn \times 1$ where the residual state is computed $\tilde{\mathbf{x}}_k = \mathbf{x}_k - \hat{\mathbf{x}}_k$, known as the sinusoidal state estimation error. Both $\tilde{\mathbf{x}}_k$ and $\hat{\mathbf{x}}_k$ have to comply with orthogonality \perp principle by assuming elimination or reduction of noises \mathbf{w}_k and \mathbf{v}_k . Redefine now $\bar{\mathbf{A}} = [\mathbf{A}_{pc} \ \mathbf{A}_{ps}]_{n \times 2sn}$, $\bar{\mathbf{C}} = [\mathbf{C}_{pc} \ \mathbf{C}_{ps}]_{m \times 2sn}$ and $\{\hat{\mathbf{z}}_k\}_{2sn \times 1} = \{\hat{\mathbf{z}}_{ck} \ \hat{\mathbf{z}}_{sk}\}^T$. Under stationary conditions, the cyclo-stationary residual state $\{\tilde{\mathbf{z}}_k\}_{2sn \times 1} = \{\tilde{\mathbf{z}}_{ck} \ \tilde{\mathbf{z}}_{sk}\}^T$ is a white noise process due to the fact that \mathbf{p}_{ck} is also white noise, and the same rule of orthogonality \perp applies for the $\tilde{\mathbf{z}}_k, \hat{\mathbf{z}}_k$ duo. If the cross-covariance matrix is rank deficient, then $\tilde{\mathbf{x}}_k$ and $\hat{\mathbf{x}}_k$ have to be dependent vectors, and consequently $E[\tilde{\mathbf{x}}_k \hat{\mathbf{x}}_k^T] \neq \mathbf{0}$. In reality this occurrence is not credible, therefore $\tilde{\mathbf{x}}_k$ and $\hat{\mathbf{x}}_k$ are assured orthogonal. The same projection applies for $\tilde{\mathbf{z}}_k$ and $\hat{\mathbf{z}}_k$ pairs, where $E[\tilde{\mathbf{z}}_k \hat{\mathbf{z}}_k^T] = \mathbf{0}$. On the other hand:

$$\begin{aligned}
E[\mathbf{x}_k \tilde{\mathbf{x}}_k^T]_{n \times n} &= E[\{\tilde{\mathbf{x}}_k + \hat{\mathbf{x}}_k\} \tilde{\mathbf{x}}_k^T] = E[\tilde{\mathbf{x}}_k \tilde{\mathbf{x}}_k^T + \hat{\mathbf{x}}_k \tilde{\mathbf{x}}_k^T] \\
&= E[\tilde{\mathbf{x}}_k \tilde{\mathbf{x}}_k^T] + E[\hat{\mathbf{x}}_k \tilde{\mathbf{x}}_k^T] = \tilde{\Sigma} + \mathbf{0} = \tilde{\Sigma} \\
E[\mathbf{z}_k \tilde{\mathbf{z}}_k^T]_{2sn \times 2sn} &= E[\{\tilde{\mathbf{z}}_k + \hat{\mathbf{z}}_k\} \tilde{\mathbf{z}}_k^T] = E[\tilde{\mathbf{z}}_k \tilde{\mathbf{z}}_k^T + \hat{\mathbf{z}}_k \tilde{\mathbf{z}}_k^T] \\
&= E[\tilde{\mathbf{z}}_k \tilde{\mathbf{z}}_k^T] + E[\hat{\mathbf{z}}_k \tilde{\mathbf{z}}_k^T] = \tilde{\mathbf{R}}_{zk} + \mathbf{0} = \tilde{\mathbf{R}}_{zk} \\
E[\mathbf{x}_k \tilde{\mathbf{z}}_k^T]_{n \times 2sn} &= E[\mathbf{x}_k \{\mathbf{p}_{ck} \otimes \tilde{\mathbf{x}}_k \ \mathbf{p}_{sk} \otimes \tilde{\mathbf{x}}_k\}^T] \\
&= E[[[\mathbf{x}_k \ \mathbf{p}_{ck}]^T \otimes \{\tilde{\mathbf{x}}_k\}^T] [[\mathbf{x}_k \ \mathbf{p}_{sk}]^T \otimes \{\tilde{\mathbf{x}}_k\}^T]] \\
&= \{ [E[\mathbf{x}_k \mathbf{p}_{ck}^T] \otimes E[\tilde{\mathbf{x}}_k^T]] [E[\mathbf{x}_k \mathbf{p}_{sk}^T] \otimes E[\tilde{\mathbf{x}}_k^T]] \} \\
&= \{ [\mathbf{0} \otimes E[\tilde{\mathbf{x}}_k^T]] [\mathbf{0} \otimes E[\tilde{\mathbf{x}}_k^T]] \} = \mathbf{0}
\end{aligned} \tag{6.25}$$

In order to demonstrate the cyclo-stationary LPTV system, the modified state-space relations in Equation (6.23) can be expanded as follows:

$$\begin{aligned}\mathbf{x}_{k+1} &= \mathbf{A}_0 \mathbf{x}_k + \bar{\mathbf{A}} \mathbf{z}_k + \bar{\mathbf{A}} \hat{\mathbf{z}}_k - \bar{\mathbf{A}} \hat{\mathbf{z}}_k + \mathbf{w}_k \\ \mathbf{y}_k &= \mathbf{C}_0 \mathbf{x}_k + \bar{\mathbf{C}} \mathbf{z}_k + \bar{\mathbf{C}} \hat{\mathbf{z}}_k - \bar{\mathbf{C}} \hat{\mathbf{z}}_k + \mathbf{v}_k\end{aligned}\quad (6.26)$$

Reducing terms of Equation (6.26) and applying previous identity definitions:

$$\begin{aligned}\mathbf{x}_{k+1} &= \mathbf{A}_0 \mathbf{x}_k + \bar{\mathbf{A}} \hat{\mathbf{z}}_k + \tilde{\mathbf{w}}_k \\ \mathbf{y}_k &= \mathbf{C}_0 \mathbf{x}_k + \bar{\mathbf{C}} \hat{\mathbf{z}}_k + \tilde{\mathbf{v}}_k\end{aligned}\quad (6.27)$$

The LPTV system identification problem of Equation (6.27) is equivalent to the white noise driven bilinear system identification problem presented in Equation (6.14), now articulated by a feedback Kalman gain. The estimates for the LPTV case $\bar{\mathbf{A}}$ and $\bar{\mathbf{C}}$ may be obtained by the Picard type Kalman filter chain [Hsu *et al.* 1985]. At each k -state of the chain, and resuming Equation (6.24), the Kalman filter is typed from a predicted state as:

$$\hat{\mathbf{x}}_{k+1} = \mathbf{A}_0 \hat{\mathbf{x}}_k + \bar{\mathbf{A}} \hat{\mathbf{z}}_k + \mathbf{K}_k [\mathbf{y}_k - \mathbf{C}_0 \hat{\mathbf{x}}_k - \bar{\mathbf{C}} \hat{\mathbf{z}}_k] \quad (6.28)$$

where the Kalman gain \mathbf{K}_k now changes over time and is presumed cyclo-stationary in nature. The idea to ensure numerical stability and integrity of both states \mathbf{x}_k and \mathbf{z}_k , based on their predicted counterparts $\hat{\mathbf{x}}_k$ and $\hat{\mathbf{z}}_k$, depends on the ability to compute a feedback quantity that could take into account the induced noise at every step, then reduce to its minimum. Such quantization is known as the innovation process.

6.2.5 Innovation Model

In order for the process to converge to $\hat{\mathbf{x}}_{k+1} - \hat{\mathbf{x}}_k \rightarrow \mathbf{0}$ as $k \rightarrow \infty$, the quantity $\mathbf{y}_k - \mathbf{C}_0 \hat{\mathbf{x}}_k - \bar{\mathbf{C}} \hat{\mathbf{z}}_k$ is called the innovation process, $\{\mathbf{e}_k\}_{mx1}$. Define the innovation process as $\mathbf{e}_k = \mathbf{y}_k - \mathbf{E}[\mathbf{y}_k]$ where $\{\mathbf{e}_0\}_{mx1} = \mathbf{y}_0 - \mathbf{E}[\mathbf{y}_0] = \mathbf{y}_0 - \mu_{y0}$, being $\{\mu_{y0}\}_{mx1}$ the initial mean values of the outputs. Also, define $\hat{\mathbf{x}}_0 = \{\mu_{x0}\}_{nx1}$ as the one step predicted estimate

– initial mean value – at launching state $k = 0$, noting also that by definition $\hat{\mathbf{x}}_k = E[\mathbf{x}_k]$ and $\hat{\mathbf{z}}_k = E[\mathbf{z}_k]$. It can be easily demonstrated that $E[\mathbf{e}_k] = \mathbf{0}$ and $E[\mathbf{e}_{k+1}\mathbf{e}_k^T] = \mathbf{0}$. Hence:

$$\begin{aligned}
\mathbf{e}_0 &= \mathbf{y}_0 - E[\mathbf{C}_0\mathbf{x}_k + \bar{\mathbf{C}}\mathbf{z}_k + \mathbf{v}_k] \\
\mathbf{e}_0 &= \mathbf{y}_0 - \mathbf{C}_0E[\mathbf{x}_k] - \bar{\mathbf{C}}E[\mathbf{z}_k] - E[\mathbf{v}_k] \\
\mathbf{e}_0 &= \mathbf{y}_0 - \mathbf{C}_0\hat{\mathbf{x}}_k - \bar{\mathbf{C}}\hat{\mathbf{z}}_k - \mathbf{0} \\
\mathbf{e}_0 &= \mathbf{y}_0 - \mathbf{C}_0\{\mathbf{x}_k - \tilde{\mathbf{x}}_k\} - \bar{\mathbf{C}}\{\mathbf{z}_k - \tilde{\mathbf{z}}_k\} \\
\mathbf{e}_0 &= \mathbf{C}_0\tilde{\mathbf{x}}_k + \bar{\mathbf{C}}\tilde{\mathbf{z}}_k + \mathbf{v}_k
\end{aligned} \tag{6.29}$$

where $\mathbf{y}_0 - \mathbf{C}_0\mathbf{x}_k - \bar{\mathbf{C}}\mathbf{z}_k = \mathbf{v}_k$. This is how, from Equation (6.29), the auto-covariance of the innovation process is given by:

$$\begin{aligned}
E[\mathbf{e}_k\mathbf{e}_k^T]_{mxm} &= E[(\mathbf{C}_0\tilde{\mathbf{x}}_k + \bar{\mathbf{C}}\tilde{\mathbf{z}}_k + \mathbf{v}_k)(\mathbf{C}_0\tilde{\mathbf{x}}_k + \bar{\mathbf{C}}\tilde{\mathbf{z}}_k + \mathbf{v}_k)^T] \\
E[\mathbf{e}_k\mathbf{e}_k^T]_{mxm} &= E[\mathbf{C}_0\tilde{\mathbf{x}}_k\tilde{\mathbf{x}}_k^T\mathbf{C}_0^T] + E[\bar{\mathbf{C}}\tilde{\mathbf{z}}_k\tilde{\mathbf{z}}_k^T\mathbf{C}_0^T] + E[\mathbf{v}_k\tilde{\mathbf{x}}_k^T\mathbf{C}_0^T] \\
&\quad + E[\mathbf{C}_0\tilde{\mathbf{x}}_k\tilde{\mathbf{z}}_k^T\bar{\mathbf{C}}^T] + E[\bar{\mathbf{C}}\tilde{\mathbf{z}}_k\tilde{\mathbf{z}}_k^T\bar{\mathbf{C}}^T] + E[\mathbf{v}_k\tilde{\mathbf{z}}_k^T\bar{\mathbf{C}}^T] \\
&\quad + E[\mathbf{C}_0\tilde{\mathbf{x}}_k\mathbf{v}_k^T] + E[\bar{\mathbf{C}}\tilde{\mathbf{z}}_k\mathbf{v}_k^T] + E[\mathbf{v}_k\mathbf{v}_k^T]
\end{aligned} \tag{6.30}$$

$$\begin{aligned}
E[\mathbf{e}_k\mathbf{e}_k^T]_{mxm} &= \mathbf{C}_0E[\tilde{\mathbf{x}}_k\tilde{\mathbf{x}}_k^T]\mathbf{C}_0^T + \bar{\mathbf{C}}E[\tilde{\mathbf{z}}_k\tilde{\mathbf{z}}_k^T]\mathbf{C}_0^T + E[\mathbf{v}_k\tilde{\mathbf{x}}_k^T]\mathbf{C}_0^T \\
&\quad + \mathbf{C}_0E[\tilde{\mathbf{x}}_k\tilde{\mathbf{z}}_k^T]\bar{\mathbf{C}}^T + \bar{\mathbf{C}}E[\tilde{\mathbf{z}}_k\tilde{\mathbf{z}}_k^T]\bar{\mathbf{C}}^T + E[\mathbf{v}_k\tilde{\mathbf{z}}_k^T]\bar{\mathbf{C}}^T \\
&\quad + \mathbf{C}_0E[\tilde{\mathbf{x}}_k\mathbf{v}_k^T] + \bar{\mathbf{C}}E[\tilde{\mathbf{z}}_k\mathbf{v}_k^T] + E[\mathbf{v}_k\mathbf{v}_k^T] \\
E[\mathbf{e}_k\mathbf{e}_k^T]_{mxm} &= \mathbf{C}_0\tilde{\Sigma}\mathbf{C}_0^T + \bar{\mathbf{C}}\tilde{\mathbf{R}}_{zk}\bar{\mathbf{C}}^T + \mathbf{R}
\end{aligned} \tag{6.31}$$

validated whenever the expectation of the cyclo-stationary state error estimation is presumed as:

$$\begin{aligned}
E[\tilde{\mathbf{z}}_k \tilde{\mathbf{z}}_k^T]_{2sn \times 2sn} &= E[\{\tilde{\mathbf{z}}_{ck} \tilde{\mathbf{z}}_{sk}\}^T \{\tilde{\mathbf{z}}_{ck}^T \tilde{\mathbf{z}}_{sk}^T\}] \\
E[\tilde{\mathbf{z}}_k \tilde{\mathbf{z}}_k^T]_{2sn \times 2sn} &= E \begin{bmatrix} [\tilde{\mathbf{z}}_{ck} \tilde{\mathbf{z}}_{ck}^T] & [\tilde{\mathbf{z}}_{ck} \tilde{\mathbf{z}}_{sk}^T] \\ [\tilde{\mathbf{z}}_{sk} \tilde{\mathbf{z}}_{ck}^T] & [\tilde{\mathbf{z}}_{sk} \tilde{\mathbf{z}}_{sk}^T] \end{bmatrix} = \begin{bmatrix} E[\tilde{\mathbf{z}}_{ck} \tilde{\mathbf{z}}_{ck}^T] & E[\tilde{\mathbf{z}}_{ck} \tilde{\mathbf{z}}_{sk}^T] \\ E[\tilde{\mathbf{z}}_{sk} \tilde{\mathbf{z}}_{ck}^T] & E[\tilde{\mathbf{z}}_{sk} \tilde{\mathbf{z}}_{sk}^T] \end{bmatrix} \\
E[\tilde{\mathbf{z}}_k \tilde{\mathbf{z}}_k^T]_{2sn \times 2sn} &= \begin{bmatrix} \tilde{\mathbf{R}}_{zcck} & \tilde{\mathbf{R}}_{zcsk} \\ \tilde{\mathbf{R}}_{zcsk}^T & \tilde{\mathbf{R}}_{zssk} \end{bmatrix} = \begin{bmatrix} \mathbf{R}_{pcck} & \mathbf{R}_{pcsk} \\ \mathbf{R}_{pcsk}^T & \mathbf{R}_{pssk} \end{bmatrix} \otimes \tilde{\Sigma} = \mathbf{R}_{pk} \otimes \tilde{\Sigma} = \tilde{\mathbf{R}}_{zk}
\end{aligned} \tag{6.32}$$

where $[\mathbf{R}_{pk}]_{2sn \times 2sn}$ is the total covariance matrix of the periodic functions \mathbf{p}_{ck} and \mathbf{p}_{sk} , whereas $[\tilde{\mathbf{R}}_{zk}]_{2sn \times 2sn}$ is the auto-covariance of the residual cyclo-stationary state $\tilde{\mathbf{z}}_k$. Under the understanding that \mathbf{p}_{ck} and \mathbf{p}_{sk} are white noise zero mean sinusoidal sequences, and being $[\tilde{\Sigma}]_{n \times n} = E[\tilde{\mathbf{x}}_k \tilde{\mathbf{x}}_k^T]$, $[\tilde{\mathbf{R}}_{zcck}]_{sn \times sn} = \mathbf{R}_{pcck} \otimes \tilde{\Sigma}$, $[\tilde{\mathbf{R}}_{zssk}]_{sn \times sn} = \mathbf{R}_{pssk} \otimes \tilde{\Sigma}$, $[\tilde{\mathbf{R}}_{zcsk}]_{sn \times sn} = \mathbf{R}_{pcsk} \otimes \tilde{\Sigma} = \mathbf{0}$, $\mathbf{R}_{pcck} = E[\mathbf{p}_{ck} \mathbf{p}_{ck+1}^T]$ and $\mathbf{R}_{pssk} = E[\mathbf{p}_{sk} \mathbf{p}_{sk+1}^T]$. Similar to the previously stated expectations, the identities $E[\tilde{\mathbf{x}}_k \mathbf{v}_k^T] = E[\tilde{\mathbf{z}}_k \mathbf{v}_k^T] = \mathbf{0}$ provided that \mathbf{v}_k is uncorrelated with \mathbf{p}_{ck} and \mathbf{p}_{sk} . It can be easily demonstrated by following similar derivations obtained for Equation (6.25), that the expectation $E[\tilde{\mathbf{z}}_k \tilde{\mathbf{x}}_k^T]_{2sn \times n} = \mathbf{0}$. Moreover, the expected value between the state and the innovation process using Equation (6.29), the first equality of Equation (6.27), and identities from Equation (6.25):

$$\begin{aligned}
E[\{\mathbf{x}_{k+1}\} \{\mathbf{e}_k\}^T]_{n \times m} &= E[[\mathbf{A}_0 \mathbf{x}_k + \bar{\mathbf{A}} \mathbf{z}_k + \mathbf{w}_k] [\mathbf{C}_0 \tilde{\mathbf{x}}_k + \bar{\mathbf{C}} \tilde{\mathbf{z}}_k + \mathbf{v}_k]^T] \\
E[\mathbf{x}_{k+1} \mathbf{e}_k^T]_{n \times m} &= E[\mathbf{A}_0 \mathbf{x}_k \tilde{\mathbf{x}}_k^T \mathbf{C}_0^T + \bar{\mathbf{A}} \mathbf{z}_k \tilde{\mathbf{x}}_k^T \mathbf{C}_0^T \\
&\quad + \mathbf{A}_0 \mathbf{x}_k \tilde{\mathbf{z}}_k^T \bar{\mathbf{C}}^T + \bar{\mathbf{A}} \mathbf{z}_k \tilde{\mathbf{z}}_k^T \bar{\mathbf{C}}^T \\
&\quad + \mathbf{A}_0 \mathbf{x}_k \mathbf{v}_k^T + \bar{\mathbf{A}} \mathbf{z}_k \mathbf{v}_k^T \\
&\quad + \mathbf{w}_k \tilde{\mathbf{x}}_k^T \mathbf{C}_0^T + \mathbf{w}_k \tilde{\mathbf{z}}_k^T \bar{\mathbf{C}}^T + \mathbf{w}_k \mathbf{v}_k^T]
\end{aligned} \tag{6.33}$$

$$\begin{aligned}
E[\mathbf{x}_{k+1} \mathbf{e}_k^T]_{n \times m} &= \mathbf{A}_0 E[\mathbf{x}_k \tilde{\mathbf{x}}_k^T] \mathbf{C}_0^T + \bar{\mathbf{A}} E[\mathbf{z}_k \tilde{\mathbf{x}}_k^T] \mathbf{C}_0^T \\
&\quad + \mathbf{A}_0 E[\mathbf{x}_k \tilde{\mathbf{z}}_k^T] \bar{\mathbf{C}}^T + \bar{\mathbf{A}} E[\mathbf{z}_k \tilde{\mathbf{z}}_k^T] \bar{\mathbf{C}}^T \\
&\quad + \mathbf{A}_0 E[\mathbf{x}_k \mathbf{v}_k^T] + \bar{\mathbf{A}} E[\mathbf{z}_k \mathbf{v}_k^T] \\
&\quad + E[\mathbf{w}_k \tilde{\mathbf{x}}_k^T] \mathbf{C}_0^T + E[\mathbf{w}_k \tilde{\mathbf{z}}_k^T] \bar{\mathbf{C}}^T + E[\mathbf{w}_k \mathbf{v}_k^T] \\
E[\mathbf{x}_{k+1} \mathbf{e}_k^T]_{n \times m} &= \mathbf{A}_0 \tilde{\Sigma} \mathbf{C}_0^T + \bar{\mathbf{A}} \tilde{\mathbf{R}}_{zk} \bar{\mathbf{C}}^T + \mathbf{S}
\end{aligned} \tag{6.34}$$

In order to construct an algorithm that could solve for the unknown quadruple \mathbf{A}_{pc} , \mathbf{A}_{ps} , \mathbf{C}_{pc} and \mathbf{C}_{ps} of Equation (6.23), a Kalman filtering scheme must be introduced to generate one-step predictions of the state. This piece of information would become valuable enough to predict the system in steady-state conditions one step ahead, given an input/output noise level, complying with a modified state-space version of Equation (6,17) in the form of Equation (6.28) called the innovation model:

$$\begin{aligned}\hat{\mathbf{x}}_{k+1} &= \mathbf{A}_0 \hat{\mathbf{x}}_k + \bar{\mathbf{A}} \hat{\mathbf{z}}_k + \mathbf{K}_k \mathbf{e}_k \\ \mathbf{y}_k &= \mathbf{C}_0 \hat{\mathbf{x}}_k + \bar{\mathbf{C}} \hat{\mathbf{z}}_k + \mathbf{e}_k\end{aligned}\quad (6.35)$$

where $\text{cov}(\mathbf{e}_k) = \mathbf{\Lambda}_0 - \mathbf{C}_0 \tilde{\mathbf{\Sigma}} \mathbf{C}_0^T - \bar{\mathbf{C}} \tilde{\mathbf{R}}_{zk} \bar{\mathbf{C}}^T$.

6.2.6 Kalman Filter

Under the premises described by Equation (6.34) and Equation (6.31), the Kalman gain matrix can be inscribed as the product $[\mathbf{K}_k]_{n \times m} = \mathbf{E}[\mathbf{x}_{k+1} \mathbf{e}_k^T] \mathbf{E}[\mathbf{e}_k \mathbf{e}_k^T]^{-1}$; in other words:

$$\mathbf{K}_k = [\mathbf{A}_0 \tilde{\mathbf{\Sigma}} \mathbf{C}_0^T + \bar{\mathbf{A}} \tilde{\mathbf{R}}_{zk} \bar{\mathbf{C}}^T + \mathbf{S}] \cdot [\mathbf{C}_0 \tilde{\mathbf{\Sigma}} \mathbf{C}_0^T + \bar{\mathbf{C}} \tilde{\mathbf{R}}_{zk} \bar{\mathbf{C}}^T + \mathbf{R}]^{-1} \quad (6.36)$$

Retrieving Equation (6.28) and taking into account that the residual state is given by $\tilde{\mathbf{x}}_k = \mathbf{x}_k - \hat{\mathbf{x}}_k$:

$$\begin{aligned}\tilde{\mathbf{x}}_{k+1} &= \mathbf{A}_0 \mathbf{x}_k + \bar{\mathbf{A}} \mathbf{z}_k + \mathbf{w}_k - \mathbf{A}_0 \hat{\mathbf{x}}_k - \bar{\mathbf{A}} \hat{\mathbf{z}}_k \\ &\quad - \mathbf{K}_k [\mathbf{C}_0 \mathbf{x}_k + \bar{\mathbf{C}} \mathbf{z}_k + \mathbf{v}_k - \mathbf{C}_0 \hat{\mathbf{x}}_k - \bar{\mathbf{C}} \hat{\mathbf{z}}_k] \\ \tilde{\mathbf{x}}_{k+1} &= [\mathbf{A}_0 - \mathbf{K}_k \mathbf{C}_0] \tilde{\mathbf{x}}_k + [\bar{\mathbf{A}} - \mathbf{K}_k \bar{\mathbf{C}}] \tilde{\mathbf{z}}_k + \mathbf{w}_k - \mathbf{K}_k \mathbf{v}_k\end{aligned}\quad (6.37)$$

The expectation of both sides of the previous Equation (6.37) yields $\mathbf{E}[\tilde{\mathbf{x}}_{k+1}]_{n \times 1} = [\mathbf{A}_0 - \mathbf{K}_k \mathbf{C}_0] \mathbf{E}[\tilde{\mathbf{x}}_k] + [\bar{\mathbf{A}} - \mathbf{K}_k \bar{\mathbf{C}}] \mathbf{E}[\tilde{\mathbf{z}}_k]$, where $\mathbf{E}[\tilde{\mathbf{x}}_k]$ and $\mathbf{E}[\tilde{\mathbf{z}}_k]$ are of dimensions $n \times 1$ and $2sn \times 1$, respectively. If \mathbf{w}_k and \mathbf{v}_k are independent of $\tilde{\mathbf{x}}_k$, then:

$$\begin{aligned}
E[\tilde{\mathbf{x}}_{k+1}\tilde{\mathbf{x}}_{k+1}^T]_{n \times n} &= [\mathbf{A}_0 - \mathbf{K}_k \mathbf{C}_0] E[\tilde{\mathbf{x}}_k \tilde{\mathbf{x}}_k^T] [\mathbf{A}_0 - \mathbf{K}_k \mathbf{C}_0]^T \\
&+ [\bar{\mathbf{A}} - \mathbf{K}_k \bar{\mathbf{C}}] E[\tilde{\mathbf{z}}_k \tilde{\mathbf{z}}_k^T] [\bar{\mathbf{A}} - \mathbf{K}_k \bar{\mathbf{C}}]^T \\
&+ [\mathbf{I} \quad -\mathbf{K}_k] \begin{bmatrix} \mathbf{Q} & \mathbf{S} \\ \mathbf{S} & \mathbf{R} \end{bmatrix} \begin{bmatrix} \mathbf{I} \\ -\mathbf{K}_k \end{bmatrix}
\end{aligned} \tag{6.38}$$

Therefore, the state error covariance matrix boils down to the following expression by means of Equation (6.17), Equation (6.32) and Equation (6.38):

$$\begin{aligned}
\tilde{\Sigma} &= [\mathbf{A}_0 - \mathbf{K}_k \mathbf{C}_0] \tilde{\Sigma} [\mathbf{A}_0 - \mathbf{K}_k \mathbf{C}_0]^T \\
&+ [\bar{\mathbf{A}} - \mathbf{K}_k \bar{\mathbf{C}}] \tilde{\mathbf{R}}_{zk} [\bar{\mathbf{A}} - \mathbf{K}_k \bar{\mathbf{C}}]^T \\
&+ \mathbf{Q} + \mathbf{K}_k \mathbf{R} \mathbf{K}_k^T - \mathbf{S} \mathbf{K}_k^T - \mathbf{K}_k \mathbf{S}^T
\end{aligned} \tag{6.39}$$

valid for initial conditions $\hat{\mathbf{x}}_0 = \mu_{x0}$ and $\tilde{\Sigma}_0 = \Sigma_0$. Now, factorizing Equation (6.39) and reducing terms:

$$\begin{aligned}
\tilde{\Sigma} &= \mathbf{A}_0 \tilde{\Sigma} \mathbf{A}_0^T - \mathbf{K}_k [\mathbf{C}_0 \tilde{\Sigma} \mathbf{C}_0^T] \mathbf{K}_k^T \\
&+ \bar{\mathbf{A}} \tilde{\mathbf{R}}_{zk} \bar{\mathbf{A}}^T - \mathbf{K}_k [\bar{\mathbf{C}} \tilde{\mathbf{R}}_{zk} \bar{\mathbf{C}}^T] \mathbf{K}_k^T \\
&+ \mathbf{K}_k \mathbf{R} \mathbf{K}_k^T + \mathbf{Q} - \mathbf{S} \mathbf{K}_k^T - \mathbf{K}_k \mathbf{S}^T \\
\tilde{\Sigma} &= \mathbf{A}_0 \tilde{\Sigma} \mathbf{A}_0^T + \bar{\mathbf{A}} \tilde{\mathbf{R}}_{zk} \bar{\mathbf{A}}^T \\
&- \mathbf{K}_k [\mathbf{C}_0 \tilde{\Sigma} \mathbf{C}_0^T + \bar{\mathbf{C}} \tilde{\mathbf{R}}_{zk} \bar{\mathbf{C}}^T - \mathbf{R}] \mathbf{K}_k^T \\
&+ \mathbf{Q} - \mathbf{S} \mathbf{K}_k^T - \mathbf{K}_k \mathbf{S}^T
\end{aligned} \tag{6.40}$$

Remembering covariance definitions $\Sigma = E[\mathbf{x}_k \mathbf{x}_k^T]$ and $\Lambda_0 = E[\mathbf{y}_k \mathbf{y}_k^T]$ from Section 6.2.2, the solution of Equation (6.40) can be treated as an Algebraic Riccati-like Equation (ARE) [Faure 1976]. This relation can be thought of as the covariance matrix of the predicted estimate \mathbf{x}_k and the residual of the state covariance in the form $\tilde{\Sigma} = \hat{\Sigma} - \Sigma$. It is said:

$$\begin{aligned}
\hat{\Sigma} - \Sigma &= \mathbf{A}_0[\tilde{\Sigma} - \Sigma]\mathbf{A}_0^T + \bar{\mathbf{A}}[\tilde{\mathbf{R}}_{zk} - \mathbf{R}_{zk}]\bar{\mathbf{A}}^T \\
&\quad - \mathbf{K}_k[\mathbf{C}_0[\tilde{\Sigma} - \Sigma]\mathbf{C}_0^T + \bar{\mathbf{C}}[\tilde{\mathbf{R}}_{zk} - \mathbf{R}_{zk}]\bar{\mathbf{C}}^T - \mathbf{R}] \mathbf{K}_k^T \\
&\quad + \mathbf{Q} - \mathbf{S}\mathbf{K}_k^T - \mathbf{K}_k\mathbf{S}^T \\
\hat{\Sigma} - \Sigma &= \mathbf{A}_0\hat{\Sigma}\mathbf{A}_0^T + \bar{\mathbf{A}}\hat{\mathbf{R}}_{zk}\bar{\mathbf{A}}^T \\
&\quad - \mathbf{K}_k[\mathbf{C}_0\hat{\Sigma}\mathbf{C}_0^T + \bar{\mathbf{C}}\hat{\mathbf{R}}_{zk}\bar{\mathbf{C}}^T]\mathbf{K}_k^T + \mathbf{Q} - \mathbf{S}\mathbf{K}_k^T - \mathbf{K}_k\mathbf{S}^T \\
&\quad - \mathbf{A}_0\hat{\Sigma}\mathbf{A}_0^T - \bar{\mathbf{A}}\hat{\mathbf{R}}_{zk}\bar{\mathbf{A}}^T \\
&\quad + \mathbf{K}_k[\mathbf{C}_0\hat{\Sigma}\mathbf{C}_0^T + \bar{\mathbf{C}}\hat{\mathbf{R}}_{zk}\bar{\mathbf{C}}^T + \mathbf{R}]\mathbf{K}_k^T
\end{aligned} \tag{6.41}$$

Assuming both $[\mathbf{G}]_{n \times m} = \mathbf{A}_0\hat{\Sigma}\mathbf{C}_0^T + \bar{\mathbf{A}}\hat{\mathbf{R}}_{zk}\bar{\mathbf{C}}^T + \mathbf{S}$ and $[\mathbf{\Lambda}_0]_{n \times n} = \mathbf{C}_0\hat{\Sigma}\mathbf{C}_0^T + \bar{\mathbf{C}}\hat{\mathbf{R}}_{zk}\bar{\mathbf{C}}^T + \mathbf{R}$ are co-variance matrices computed as predictions product of the prediction state covariance $\hat{\Sigma}$, then the Kalman gain of Equation (6.36) and its transpose can be reintroduced as:

$$\begin{aligned}
[\mathbf{K}_k]_{n \times m} &= \mathbf{S}\mathbf{R}^{-1} = [\mathbf{G} - \mathbf{A}_0\hat{\Sigma}\mathbf{C}_0^T - \bar{\mathbf{A}}\hat{\mathbf{R}}_{zk}\bar{\mathbf{C}}^T] \cdot \\
&\quad [\mathbf{\Lambda}_0 - \mathbf{C}_0\hat{\Sigma}\mathbf{C}_0^T - \bar{\mathbf{C}}\hat{\mathbf{R}}_{zk}\bar{\mathbf{C}}^T]^{-1} \\
[\mathbf{K}_k]_{m \times n}^T &= \mathbf{R}^{-1}\mathbf{S}^T = [\mathbf{\Lambda}_0^T - \mathbf{C}_0\hat{\Sigma}\mathbf{C}_0^T - \bar{\mathbf{C}}\hat{\mathbf{R}}_{zk}\bar{\mathbf{C}}^T]^{-1} \cdot \\
&\quad [\mathbf{G}^T - \mathbf{C}_0\hat{\Sigma}\mathbf{A}_0^T - \bar{\mathbf{C}}\hat{\mathbf{R}}_{zk}\bar{\mathbf{A}}^T]
\end{aligned} \tag{6.42}$$

It can be seen that the Riccati-like equation converges to a constant covariance matrix as $k \rightarrow \infty$ as $\tilde{\Sigma} \rightarrow \Sigma$. Thus, the stationary Kalman gain of Equation (6.36) reaches steadiness when:

$$\begin{aligned}
\mathbf{K}_k &= [\mathbf{A}_0\hat{\Sigma}\mathbf{C}_0^T + \bar{\mathbf{A}}\hat{\mathbf{R}}_{zk}\bar{\mathbf{C}}^T + \mathbf{S}] \cdot \\
&\quad [\mathbf{C}_0\hat{\Sigma}\mathbf{C}_0^T + \bar{\mathbf{C}}\hat{\mathbf{R}}_{zk}\bar{\mathbf{C}}^T + \mathbf{R}]^{-1} \\
\mathbf{K}_k^T &= [\mathbf{C}_0\hat{\Sigma}\mathbf{C}_0^T + \bar{\mathbf{C}}\hat{\mathbf{R}}_{zk}\bar{\mathbf{C}}^T + \mathbf{R}]^{-1} \cdot \\
&\quad [\mathbf{C}_0\hat{\Sigma}\mathbf{A}_0^T + \bar{\mathbf{C}}\hat{\mathbf{R}}_{zk}\bar{\mathbf{A}}^T + \mathbf{S}]
\end{aligned} \tag{6.43}$$

In order to derive steadiness of the original infinite dimensional problem that Equation (6.41) imposes, a recursive optimization solution $[\bar{\mathbf{\Omega}}]_{n \times n} = [\Sigma]_{n \times n}^{-1}$ may employed to

guarantee convergence by finding a stable maximum Σ associated with the covariance matrices of the system [Bittanti *et al.* 1991].

6.2.7 Stationary State Covariance

Taking the terms associated with Σ from Equation (6.41), in particular $\Sigma = \mathbf{A}_0 \Sigma \mathbf{A}_0^T + \bar{\mathbf{A}} \mathbf{R}_{zk} \bar{\mathbf{A}}^T - \mathbf{K}_k [\mathbf{C}_0 \Sigma \mathbf{C}_0^T + \bar{\mathbf{C}} \mathbf{R}_{zk} \bar{\mathbf{C}}^T + \mathbf{R}] \mathbf{K}_k^T$, then applying Kalman filter identities of Equation (6.43), as well as noise covariances presented in both Equation (6.18) and Equation (6.19), expressly noise matrices $\mathbf{S} = \mathbf{G} - \mathbf{A}_0 \Sigma \mathbf{C}_0^T - \bar{\mathbf{A}} \mathbf{R}_{zk} \bar{\mathbf{C}}^T$, or $\mathbf{S}^T = \mathbf{G}^T - \mathbf{C}_0 \Sigma \mathbf{A}_0^T - \bar{\mathbf{C}} \mathbf{R}_{zk} \bar{\mathbf{A}}^T$ and $\mathbf{R} = \Lambda_0 - \mathbf{C}_0 \Sigma \mathbf{C}_0^T - \bar{\mathbf{C}} \mathbf{R}_{zk} \bar{\mathbf{C}}^T$. In sum:

$$\begin{aligned} \Sigma &= \mathbf{A}_0 \Sigma \mathbf{A}_0^T + \bar{\mathbf{A}} \mathbf{R}_{zk} \bar{\mathbf{A}}^T \\ &\quad - [\mathbf{A}_0 \Sigma \mathbf{C}_0^T + \bar{\mathbf{A}} \mathbf{R}_{zk} \bar{\mathbf{C}}^T + \mathbf{S}] \cdot \\ &\quad [\mathbf{C}_0 \Sigma \mathbf{C}_0^T + \bar{\mathbf{C}} \mathbf{R}_{zk} \bar{\mathbf{C}}^T + \mathbf{R}]^{-1} \cdot \\ &\quad [\mathbf{C}_0 \Sigma \mathbf{A}_0^T + \bar{\mathbf{C}} \mathbf{R}_{zk} \bar{\mathbf{A}}^T + \mathbf{S}^T] \end{aligned} \quad (6.44)$$

$$\begin{aligned} \Sigma &= \mathbf{A}_0 \Sigma \mathbf{A}_0^T + \bar{\mathbf{A}} \mathbf{R}_{zk} \bar{\mathbf{A}}^T \\ &\quad + [\mathbf{G} - \mathbf{A}_0 \Sigma \mathbf{C}_0^T - \bar{\mathbf{A}} \mathbf{R}_{zk} \bar{\mathbf{C}}^T] \cdot \\ &\quad [\Lambda_0 - \mathbf{C}_0 \Sigma \mathbf{C}_0^T - \bar{\mathbf{C}} \mathbf{R}_{zk} \bar{\mathbf{C}}^T]^{-1} \cdot \\ &\quad [\mathbf{G}^T - \mathbf{C}_0 \Sigma \mathbf{A}_0^T - \bar{\mathbf{C}} \mathbf{R}_{zk} \bar{\mathbf{A}}^T] \end{aligned} \quad (6.45)$$

Stable solution of the discrete-time Riccati form of Equation (6.45) involves finding the maximum and minimum of an optimal marker $[\bar{\mathbf{\Omega}}]_{n \times n} = [\Sigma]_{n \times n}^{-1}$ – therefore $[\bar{\mathbf{P}}_{zk}]_{2sn \times 2sn} = [\mathbf{R}_{zk}]_{2sn \times 2sn}^{-1}$ – with initial conditions $\bar{\mathbf{\Omega}}_0 = \mathbf{0}$ and $\bar{\mathbf{P}}_{z0} = \mathbf{0}$, that evolves over time to get $\bar{\mathbf{\Omega}}_\infty = \lim_{k \rightarrow \infty} \bar{\mathbf{\Omega}}_k$ and $\bar{\mathbf{P}}_{z\infty} = \lim_{k \rightarrow \infty} \bar{\mathbf{P}}_{zk} = \mathbf{0}$ when $k \rightarrow \infty$, for cyclo-stationary zero-mean terms. Expressly, this limit (boundary) pair $\bar{\mathbf{\Omega}}_\infty, \bar{\mathbf{P}}_{z\infty}$ of the optimization matrix $\bar{\mathbf{\Omega}}$ is supposed to be positive definite and is obtained as a modified inverse-recursive version of the cyclo-stationary LPTV state covariance matrix of Equation

(6.45). In other words:

$$\begin{aligned}
\bar{\mathbf{\Omega}}_{k+1} &= \mathbf{A}_0 \bar{\mathbf{\Omega}}_k \mathbf{A}_0^T + \bar{\mathbf{A}} \bar{\mathbf{P}}_{zk} \bar{\mathbf{A}}^T \\
&\quad + [\mathbf{G} - \mathbf{A}_0 \bar{\mathbf{\Omega}}_k \mathbf{C}_0^T - \bar{\mathbf{A}} \bar{\mathbf{P}}_{zk} \bar{\mathbf{C}}^T] \cdot \\
&\quad [\mathbf{\Lambda}_0 - \mathbf{C}_0 \bar{\mathbf{\Omega}}_k \mathbf{C}_0^T - \bar{\mathbf{C}} \bar{\mathbf{P}}_{zk} \bar{\mathbf{C}}^T]^{-1} \cdot \\
&\quad [\mathbf{G}^T - \mathbf{C}_0 \bar{\mathbf{\Omega}}_k \mathbf{A}_0^T - \bar{\mathbf{C}} \bar{\mathbf{P}}_{zk} \bar{\mathbf{A}}^T] \\
\bar{\mathbf{\Omega}}_{k+1} &= \mathbf{A}_0 \bar{\mathbf{\Omega}}_k \mathbf{A}_0^T \\
&\quad + [\mathbf{G} - \mathbf{A}_0 \bar{\mathbf{\Omega}}_k \mathbf{C}_0^T] \cdot \\
&\quad [\mathbf{\Lambda}_0 - \mathbf{C}_0 \bar{\mathbf{\Omega}}_k \mathbf{C}_0^T]^{-1} \cdot \\
&\quad [\mathbf{G}^T - \mathbf{C}_0 \bar{\mathbf{\Omega}}_k \mathbf{A}_0^T]
\end{aligned} \tag{6.46}$$

At this point, and once the cyclo-stationary stochastic model has been identified, a reconstruction of the output signals $\{\mathbf{y}\}_{mxl} = \{\mathbf{y}_1 \mathbf{y}_2 \dots \mathbf{y}_k \dots \mathbf{y}_l\}$ can be achieved by means of the predicted system Markov parameters as explained in the next section.

6.2.8 Stochastic Cyclo-Stationary System Markovs

Expanding the innovation model state-space series of Equation (6.35), and recalling from Equation (6.15) the linear – now time-varying – parameter definitions $\bar{\mathbf{A}}_k = \sum_{i=1}^s [\mathbf{A}_{ci} p_{cki} + \mathbf{A}_{si} p_{ski}]$ and $\bar{\mathbf{C}}_k = \sum_{i=1}^s [\mathbf{C}_{ci} p_{cki} + \mathbf{C}_{si} p_{ski}]$, it can be seen that:

$$\begin{aligned}
\hat{\mathbf{x}}_{k+1} &= [\mathbf{A}_0 + \bar{\mathbf{A}}] \hat{\mathbf{x}}_k + \mathbf{K}_k \mathbf{e}_k \\
\mathbf{y}_k &= [\mathbf{C}_0 + \bar{\mathbf{C}}] \hat{\mathbf{x}}_k + \mathbf{e}_k
\end{aligned} \tag{6.47}$$

A set of trotting states for initial conditions $\mathbf{x}_0 = \mathbf{0}$ will derive as $\mathbf{y}_0 = \mathbf{e}_0$, $\hat{\mathbf{x}}_1 = \mathbf{K}_k \mathbf{e}_0$, $\mathbf{y}_1 = [\mathbf{C}_0 + \bar{\mathbf{C}}_1] \mathbf{K}_0 \mathbf{e}_0 + \mathbf{e}_1$, $\hat{\mathbf{x}}_2 = [\mathbf{A}_0 + \bar{\mathbf{A}}_1] \hat{\mathbf{x}}_1 + \mathbf{K}_k \mathbf{e}_1$, $\mathbf{y}_2 = [\mathbf{C}_0 + \bar{\mathbf{C}}_2] [[\mathbf{A}_0 + \bar{\mathbf{A}}_1] \mathbf{K}_0 \mathbf{e}_0 + \mathbf{K}_1 \mathbf{e}_1] + \mathbf{e}_2$. In general:

$$\begin{aligned}
[\mathbf{Y}]_{mxml} = & [\mathbf{I}]_{mxm} \cdots \\
& [\mathbf{C}_0 + \bar{\mathbf{C}}_{l-1}] \mathbf{K}_{l-2} \cdots \\
& [\mathbf{C}_0 + \bar{\mathbf{C}}_{l-1}] [\mathbf{A}_0 + \bar{\mathbf{A}}_{l-2}] \mathbf{K}_{l-3} \cdots \\
& [\mathbf{C}_0 + \bar{\mathbf{C}}_{l-1}] [\mathbf{A}_0 + \bar{\mathbf{A}}_{l-2}] [\mathbf{A}_0 + \bar{\mathbf{A}}_{l-3}] \mathbf{K}_{l-4} \cdots \\
& [\mathbf{C}_0 + \bar{\mathbf{C}}_{l-1}] [\mathbf{A}_0 + \bar{\mathbf{A}}_{l-2}] [\mathbf{A}_0 + \bar{\mathbf{A}}_{l-3}] \cdots [\mathbf{A}_0 + \bar{\mathbf{A}}_1] \mathbf{K}_0]
\end{aligned} \tag{6.48}$$

where the Toeplitz (noise) matrix, associated with Equation (6.48), is described by an arrangement of innovation processes:

$$[\mathbf{U}]_{mlxl} = \begin{bmatrix} \{\mathbf{e}_0\} & \{\mathbf{e}_1\} & \{\mathbf{e}_2\} & \cdots & \{\mathbf{e}_{l-1}\} \\ & \{\mathbf{e}_0\} & \{\mathbf{e}_1\} & \cdots & \{\mathbf{e}_{l-2}\} \\ & & \{\mathbf{e}_0\} & \cdots & \{\mathbf{e}_{l-3}\} \\ & & & \ddots & \vdots \\ & & & & \{\mathbf{e}_0\} \end{bmatrix} \tag{6.49}$$

that solve for the predicted output signals $\{\mathbf{y}_{prd}\}_{mxl} = [\mathbf{Y}]_{mxml} [\mathbf{U}]_{mlxl}$. Equation (6.48) and Equation (6.49) can be truncated to block series of size $q < l$ by just by changing sub-indexes accordingly. As of now, the only pending task is to determine is the reconstruction and identification of noise signals \mathbf{w}_k and \mathbf{v}_k , as well as the innovation process \mathbf{e}_k from the covariance and cross-covariance matrices defined in Equation (6.10).

6.2.9 Noise Identification

Under the assumption of white noise Gaussian distribution, a generation of random realizations of a noise vector, take $\{\mathbf{v}\}_{mxl} = \{\mathbf{v}_1 \ \mathbf{v}_2 \ \dots \ \mathbf{v}_k \ \dots \ \mathbf{v}_l\}$ as an example, can be achieved by means of diagonalizing the covariance matrix that governs the process, in this case \mathbf{R} (see Equation (6.10)) [Rybicki and Press 1992]. The objective is to uncouple modes that are statistically independent, then select m random Gaussian independent variations, of zero mean and unit variance, by finding eigenvalues and eigenvectors of the ruling symmetric and positive definite correlation matrix $[\mathbf{R}_c]_{mxm}$. This result can be computed from covariance matrix \mathbf{R} as follows:

$$[\mathbf{R}_c]_{m \times m} = \frac{\mathbf{R}(i, j)}{\sqrt{\mathbf{R}(i, i) \mathbf{R}(j, j)}} \quad i = 1, 2, \dots, m; \quad j = 1, 2, \dots, m \quad (6.50)$$

where $\mathbf{R}(i, j)$ is the $(i\text{th}, j\text{th})$ element of the covariance matrix \mathbf{R} . Therefore, the signal decomposition will be carried out by uncoupling \mathbf{R}_c in the form $[\mathbf{R}_c] = \boldsymbol{\Phi} [\text{diag}(\lambda_1, \lambda_2, \dots, \lambda_m)] \boldsymbol{\Phi}^T$, where $\boldsymbol{\Phi}$ is an orthogonal matrix acquiesced by the resulting eigenvector columns $[\boldsymbol{\Phi}]_{m \times m} = [\boldsymbol{\Phi}_1 \ \boldsymbol{\Phi}_2 \ \dots \boldsymbol{\Phi}_m]$, and $\lambda_1, \lambda_2, \dots, \lambda_m$ are the corresponding eigenvalues. Let $[\boldsymbol{\Phi}]_{m \times m} = [\boldsymbol{\Phi}_1 \ \boldsymbol{\Phi}_2 \ \dots \boldsymbol{\Phi}_m]$ be a vector of l independent Gaussian random deviates of zero mean and unit variance. A realization of \mathbf{v} will be constituted as:

$$\mathbf{v} = \boldsymbol{\Phi} [\text{diag}(\lambda_1^{1/2}, \lambda_2^{1/2}, \dots, \lambda_m^{1/2})] \boldsymbol{\Phi}^T + \bar{\mathbf{v}} \quad (6.51)$$

where $\bar{\mathbf{v}}$ is any wished baseline mean value, typically $\bar{\mathbf{v}} = \mathbf{0}$. The same procedure can be reproduced for input noise vector \mathbf{w} and/or innovation process \mathbf{e} by engaging eigenrealization of \mathbf{Q} and \mathbf{R} matrices, respectively. Having established a mathematical scheme for stochastic cyclo-stationary systems, it is now feasible to propose a recursive algorithm for the solution of the cyclo-stationary based system matrices, in specific the quadruple \mathbf{A}_{pc} , \mathbf{A}_{ps} , \mathbf{C}_{pc} and \mathbf{C}_{ps} , previously established in Equation (6.16).

6.2.10 Iterative System Identification Algorithm

The proposed output-only cyclo-stationary linear-parameter time-varying stochastic subspace identification algorithm is synthetized in Figure 6.4 and outlined as follows:

Step 0. Set the outputs vector $\{\mathbf{y}\}_{m \times l} = \{\{\mathbf{y}_1\}_{m \times 1} \ \{\mathbf{y}_2\}_{m \times 1} \ \dots \ \{\mathbf{y}_k\}_{m \times 1} \ \dots \ \{\mathbf{y}_l\}_{m \times 1}\}$ of dimension $m \times l$ from experimental data, as well as the spinning velocity time-history vector $\{\boldsymbol{\Omega}\}_{1 \times l} = \{\boldsymbol{\Omega}_1 \ \boldsymbol{\Omega}_2 \ \dots \boldsymbol{\Omega}_k \ \dots \boldsymbol{\Omega}_l\}$ from experimental work including sampling time Δt ,

where m is the number of output channels (sensors) and l is the total sampling size. Predefine the positive integer parameter s of Equation (6.12) as the LPTV dimensionality of the system, remembering that this is a trade-off between model accuracy and computational effort.

Step 1. Compute the non-shifted output covariance matrix $[\Lambda_0]_{m \times m} = E[\mathbf{y}_k \mathbf{y}_k^T] = E[\mathbf{y}_{k+1} \mathbf{y}_{k+1}^T]$ and as many as $2\alpha+1$ of i -shifted output covariance matrices $[\Lambda_i]_{m \times m} = E[\mathbf{y}_{k+i} \mathbf{y}_k^T]$, in order to construct block Hankel matrices \mathbf{H}_k^c and \mathbf{H}_0^c articulated in Equation (6.7) and Equation (6.8), respectively.

Step 2. Compute the SVD of \mathbf{H}_0^c as stated in Equation (6.12), then solve for the triad $\mathbf{C}_0 \mathbf{A}_0 \mathbf{G}$ in accordance to Equation (6.22).

Step 3. Compute the state-space covariance matrix Σ , delineated in Equation (6.45), by means of iterative repetitions of the convergent Algebraic Riccati-like Equation (ARE) presented in Equation (6.46), in order to ensure a symmetric positive-definite matrix $[\Sigma]_{n \times n} = [\bar{\Omega}]_{n \times n}^{-1}$.

Step 4. Compute the initial Kalman gain \mathbf{K}_0 assuming no cyclo-stationary effects have been established yet. Employ a reduced version of Equation (6.42), namely $[\mathbf{K}_0]_{n \times m} = [\mathbf{G} - \mathbf{A}_0 \Sigma \mathbf{C}_0^T][\Lambda_0 - \mathbf{C}_0 \Sigma \mathbf{C}_0^T]^{-1}$.

Step 5. Generate the initial non cyclo-stationary noise covariance matrices \mathbf{Q}_0 , \mathbf{R}_0 and \mathbf{S}_0 established in Equation (6.11), by trimming out Equation (6.17), Equation (6.18) and Equation (6.19) in reduced forms $\mathbf{Q}_0 = \Sigma - \mathbf{A}_0 \Sigma \mathbf{A}_0^T$, $\mathbf{R}_0 = \Lambda_0 - \mathbf{C}_0 \Sigma \mathbf{C}_0^T$, and $\mathbf{S}_0 = \mathbf{G} - \mathbf{A}_0 \Sigma \mathbf{C}_0^T$, respectively.

Step 6. Reconstruct noises and innovation process time histories \mathbf{v} , \mathbf{w} and \mathbf{e} by applying the scheme presented in Section 6.2.9, based on the definitions induced in Equation (10), for \mathbf{R}_0 , \mathbf{Q}_0 , \mathbf{R}_0 , respectively.

Step 7. Setup initial conditions $\mathbf{x}_0 = \mathbf{0}$, $\bar{\mathbf{A}}_0 = \mathbf{0}$ and $\bar{\mathbf{C}}_0 = \mathbf{0}$ at initial state $k = 0$.

Step 8. Compute cyclo-stationary functions $\mathbf{p}_{ck} = \{p_{ck1} \ p_{ck2} \ \dots p_{cks}\}^T$ and complementary $\mathbf{p}_{sk} = \{p_{sk1} \ p_{sk2} \ \dots p_{sks}\}^T$ given $p_{cki} = \cos(i\Omega(k)k)$ and $p_{ski} = \sin(i\Omega(k)k)$. Obtain current $\mathbf{z}_{ck} = \mathbf{p}_{ck} \otimes \mathbf{x}_k$ and $\mathbf{z}_{sk} = \mathbf{p}_{sk} \otimes \mathbf{x}_k$ declared in Section 6.2.3. Then derive the integrated cyclo-stationary state $\{\mathbf{z}_k\}_{2sn \times 1} = \{\mathbf{z}_{ck} \ \mathbf{z}_{sk}\}^T$.

Step 9. Assess \mathbf{R}_{zk} similar to the residual cyclo-stationary state covariance matrix set out in Equation (6.32), through the calculation of the expected values of the cyclo-stationary operators $\{p_{ck}\}$ and $\{p_{sk}\}$, as follows:

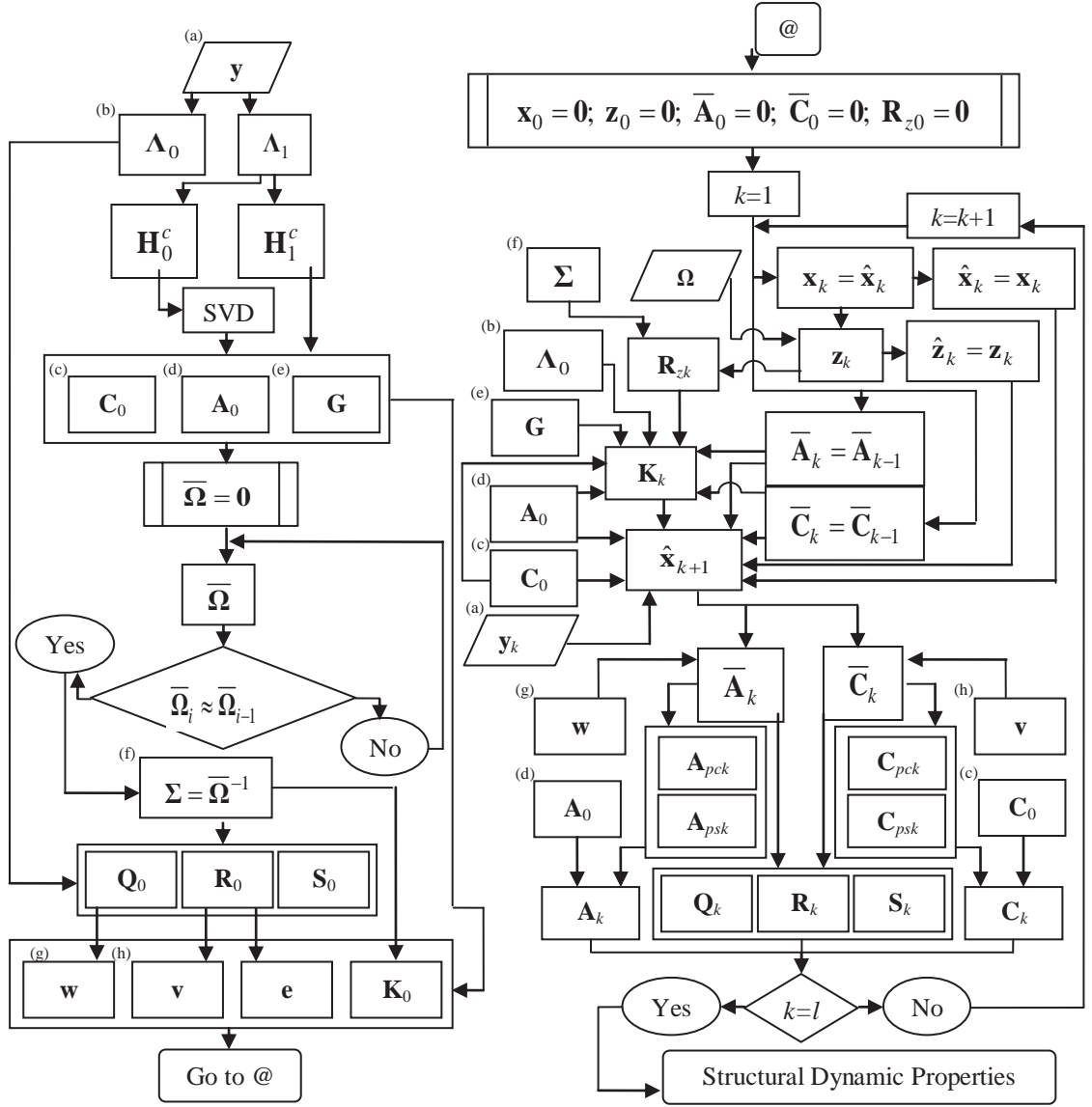


Figure 6.4. Output-Only Cyclo-Stationary Linear-Parameter Time-Varying Stochastic Subspace Identification (CS-SSI-LPTV) algorithm.

$$\begin{aligned}
 \mathbf{R}_{zk} &= E[\mathbf{z}_k \mathbf{z}_k^T] \\
 \mathbf{R}_{zk} &= \mathbf{R}_{pk} \otimes \Sigma = \begin{bmatrix} \mathbf{R}_{zcck} & \mathbf{R}_{zcsk} \\ \mathbf{R}_{zcsk}^T & \mathbf{R}_{zssk} \end{bmatrix} \\
 \mathbf{R}_{zk} &= \begin{bmatrix} \mathbf{R}_{pcck} & \mathbf{R}_{pcsk} \\ \mathbf{R}_{pcsk}^T & \mathbf{R}_{psk} \end{bmatrix} \otimes \Sigma = \begin{bmatrix} E[\mathbf{p}_{ck} \mathbf{p}_{ck}^T] & \mathbf{0} \\ \mathbf{0} & E[\mathbf{p}_{sk} \mathbf{p}_{sk}^T] \end{bmatrix} \otimes \Sigma
 \end{aligned} \tag{6.52}$$

Step 10. Compute the new Kalman gain \mathbf{K}_k using the first expression of Equation (6.42).

Step 11. Compute the one-step forward state prediction by means of the innovation model of Equation (6.28), where $\hat{\mathbf{z}}_k$ is approximated to \mathbf{z}_k and $\hat{\mathbf{x}}_k$ to \mathbf{x}_k to get $\hat{\mathbf{x}}_{k+1}$ as $k \rightarrow \infty$.

Step 12. Solve for $\bar{\mathbf{A}}_k$ and $\bar{\mathbf{C}}_k$ by means of Equation (6.14) extended to Equation (6.27), holding the approximations mentioned in *Step 11*:

$$\begin{aligned}\bar{\mathbf{A}}_k &= \mathbf{x}_{k+1} \mathbf{z}_k^t - \mathbf{A}_0 \mathbf{x}_k \mathbf{z}_k^t - \mathbf{w}_k \mathbf{z}_k^t \\ \bar{\mathbf{C}}_k &= \mathbf{y}_k \mathbf{z}_k^t - \mathbf{C}_0 \mathbf{x}_k \mathbf{z}_k^t - \mathbf{v}_k \mathbf{z}_k^t\end{aligned}\tag{6.53}$$

where the operator t stands for the pseudo-inverse. Disassemble directly $\bar{\mathbf{A}}_k$ and $\bar{\mathbf{C}}_k$ to obtain linear-parameter system matrices \mathbf{A}_{pck} , \mathbf{A}_{psk} , \mathbf{C}_{pck} and \mathbf{C}_{psk} at each step k as augmented in Equation (6.16). The latter LPTV matrices can be expanded for the s sinusoidal pair contributions in the form $\mathbf{A}_{pck} = [\mathbf{A}_{c1k} \ \mathbf{A}_{c2k} \ \dots \ \mathbf{A}_{csk}]$ and $\mathbf{A}_{psk} = [\mathbf{A}_{s1k} \ \mathbf{A}_{s2k} \ \dots \ \mathbf{A}_{ssk}]$ (see Equation (6.16)).

Step 13. Compute the total state matrix $\mathbf{A}_k = \mathbf{A}_0 + \bar{\mathbf{A}}_k$ and the total observation matrix $\mathbf{C}_k = \mathbf{C}_0 + \bar{\mathbf{C}}_k$ as originally defined in Equation (6.14).

Step 14. Re-evaluate noise covariance matrices \mathbf{Q}_k , \mathbf{R}_k , \mathbf{S}_k from to the extent of Equation (6.17), Equation (6.18) and Equation (6.19) as $\mathbf{Q}_k = \Sigma - \mathbf{A}_0 \Sigma \mathbf{A}_0^T - \bar{\mathbf{A}}_k \mathbf{R}_{zk} \bar{\mathbf{A}}_k^T$, $\mathbf{R}_k = \Lambda_0 - \mathbf{C}_0 \Sigma \mathbf{C}_0^T - \bar{\mathbf{C}}_k \mathbf{R}_{zk} \bar{\mathbf{C}}_k^T$, and $\mathbf{S}_k = \mathbf{G} - \mathbf{A}_0 \Sigma \mathbf{C}_0^T - \bar{\mathbf{A}}_k \mathbf{R}_{zk} \bar{\mathbf{A}}_k^T$.

Step 15. Assign $k = k + 1$.

Step 16. Go to *Step 8* and repeat recursively until $k = l$.

Step 17. Reconstruct the model predicted output signal \mathbf{y} according to the guidelines of the Section 6.2.8, where $\{\mathbf{y}_{prd}\}_{m \times l} = [\mathbf{Y}]_{m \times m} [\mathbf{U}]_{m \times l}$ and both \mathbf{Y} and \mathbf{U} are defined in Equation (6.48) and Equation (6.49), respectively.

Step 18. Compare structural properties such as damping ratios, frequencies, mode shapes, and participation factors as a function of the resultant noisy-cyclo-stationary system matrices \mathbf{A}_0 and \mathbf{C}_0 from *Step 2*, with the corresponding filtered and integrated system matrices \mathbf{A}_k and \mathbf{C}_k , recognized in *Step 13*. Employ standard derivations from discrete to continuous time expressions of the System Realization Theory (SRA) [*ibid.* Kuo 1995] in order to generate spectral decompositions of the system matrices \mathbf{A}_0 or \mathbf{A}_k , and compute dynamic properties accordingly (see Table 6.1).

Step 19. If desired, and following the same directive of *Step 18*, compute the weighted Modal Phase Collinearity (MPC) and Modal Amplitude Coherence (MAC) indexes to distinguish true modes from noise modes [Vold *et al.* 1982]. The MAC can be thought as the dot product between (1) the vector composed of a chosen number of time steps of the unit pulse response history associated with a mode of the identified model, and (2) the corresponding vector from the pulse response data – experimental – used in the identification. In other words, MAC index is the theoretical unit pulse response versus its experimental counterpart.

6.3 Numerical Example

6.3.1 Prototype

A numerical model consisting of six degrees of freedom (DOF's) is presented in this section to illustrate the capabilities, strengths and limitations of the proposed cyclo-stationary linear-parameter time-varying stochastic subspace identification model (CS-SSI-LPTV). It is composed of an arrangement of six lumped masses with corresponding stiffness intensities and damping coefficients, as illustrated in Figure 6.5. Dynamic outputs y_i , $i = 1, 2, \dots, 6$ from the spinning finite element (SFE) numerical solver [Yunus *et al.* 1991][ANSYS 2011], acceleration, velocity or displacement channels, were treated as an output signals – data time histories – for the CS-SSI-LPTV algorithm (see Figure 6.6). The model is composed of masses $m_1 = 2 \text{ N}\cdot\text{sec}^2/\text{m}$, $m_2 = m_3 = m_4 = m_5 = 1.5 \text{ N}\cdot\text{sec}^2/\text{m}$ and $m_6 = 1 \text{ N}\cdot\text{sec}^2/\text{m}$; with stiffnesses $k_1 = 1,800 \text{ N/m}$, $k_2 = k_3 = k_4 = k_5 = 1200 \text{ N/m}$ and $k_6 = 600 \text{ N/m}$. Damping coefficients c_1, c_2, c_3, c_4, c_5 and c_6 were subjected to the current values of the damping ratio $0.001 \leq \zeta \leq 0.5$ and the dominant static eigen-frequencies ω_i , $i = 1, 2, \dots, 6$ of the system. A set of six random concentrated loads at each node are applied to exercise the harmonics of the system in spinning motion.

Table 6.1. Structural Dynamic Properties from Eigensystem Realization Theory.

Filter	Cyclo-Stationary	Cyclo-Stationary Filtered
Continuous State Matrix	$[\mathbf{A}_c]_{n \times n} = \frac{\log(\mathbf{A}_0)}{\Delta t}$	$[\mathbf{A}_{kc}]_{n \times n} = \frac{\log(\mathbf{A}_k)}{\Delta t}$
Continuous Observation Matrix	$[\mathbf{C}_c]_{n \times n} = \mathbf{C}_0$	$[\mathbf{C}_{kc}]_{n \times n} = \mathbf{C}_k$
Continuous State Eigenrealization	$\mathbf{A}_c = [\Phi]_{n \times n} [\lambda]_{n \times n} [\Phi]_{n \times n}^{-1}$	$\mathbf{A}_{kc} = [\Phi]_{n \times n} [\lambda]_{n \times n} [\Phi]_{n \times n}^{-1}$
Complex Conjugates	$[\mathbf{a}]_{n \times n} = \text{real}(\lambda)$ $[\mathbf{b}]_{n \times n} = \text{imag}(\lambda)$	$[\mathbf{a}]_{n \times n} = \text{real}(\lambda)$ $[\mathbf{b}]_{n \times n} = \text{imag}(\lambda)$
Damping	$\zeta_i = \frac{1}{\sqrt{1 + (\mathbf{b}_i / \mathbf{a}_i)^2}}; \quad i = 1, 2, \dots, n$	$\zeta_{ik} = \frac{1}{\sqrt{1 + (\mathbf{b}_i / \mathbf{a}_i)^2}}; \quad i = 1, 2, \dots, n$
Circular Frequency	$\omega_i = \mathbf{a}_i \sqrt{1 + (\mathbf{b}_i / \mathbf{a}_i)^2}; \quad i = 1, 2, \dots, n$	$\omega_{ik} = \mathbf{a}_i \sqrt{1 + (\mathbf{b}_i / \mathbf{a}_i)^2}; \quad i = 1, 2, \dots, n$
Natural Frequency	$f_i = \frac{\omega_i}{2\pi}; \quad i = 1, 2, \dots, n$	$f_{ik} = \frac{\omega_i}{2\pi}; \quad i = 1, 2, \dots, n$
Mode Shapes	$[\phi]_{n \times n} = \mathbf{C}_c \Phi$	$[\phi_k]_{n \times n} = \mathbf{C}_{kc} \Phi$
Participation Factors (from SVD)	$[\Gamma]_{n \times n} = [\phi]_{n \times n}^{-1} [\Sigma_n]_{n \times n}^{1/2} [\mathbf{S}_n(1:n,:)]_{n \times n}$	$[\Gamma_k]_{n \times n} = [\phi]_{n \times n}^{-1} [\Sigma_n]_{n \times n}^{1/2} [\mathbf{S}_n(1:n,:)]_{n \times n}$

6.3.2 Results

Table 6.2 summarizes twelve cases of the multivariable fourth order and Kalman filtered stochastic innovation systems for different damping ratios ζ and for four spinning-velocity $\Omega(t)$ time histories, including null spinning, constant, linear increasing and smooth random variations. Hankel dimension-based parameters were set to $q = 500$, $\alpha = 5, 10, 20$ and 30 . Recognition of the non-zero singular values are typically self-evident for low damping ratios and smaller $\Omega(t)$ magnitudes. Extra pairs of non-zero singular values, not associated with the structure, are evident when spinning motion overlaps the natural frequencies of the system. Boundaries between clusters of zero and

non-zero singular values become less distinct for linear and non-linear variations of the spinning intensity, as illustrated in the last two rows of Table 6.2. A better identification of computational modes and system modes, for the case of variable spinning motion, can be achieved by increasing the size of the Hankel matrix by four times (at minimum) with respect to the static and constant speed cases. Table 6.3 illustrates several configurations of the so-called stability curves for different structural damping ratios and different spinning time histories, for Hankel dimensionality $q = 500$ and $\alpha = 200$. Plots are presented for 100 different orders n of the system with their corresponding cyclo-stationary eigen-frequencies. Again, simulations with low damping ratios ($\zeta \leq 0.05$) are better identified compared to highly damped rotating blade systems ($\zeta \geq 0.1$). The differences between the static and the constant spinning cases are minor in terms of frequency identification and frequency variation. This fact means the proposed CS-SSI-LPTV algorithm performs best under controlled cyclo-stationary conditions, when constant spinning speed is guaranteed. It is important to underline the relevance that the high sampling rate and sufficiently long sampling duration have both on the accuracy of the identification when CS-SSI-LPTV is employed. These considerations are imperative for non-linear and random – spline like – variations of the rotational speed, as clearly stated in the last two rows of Table 6.3, where the spinning-frequency $\Omega(t)$ wobbles and threads around minimum and maximum rotating speeds. This chart tries to emulate the behavior of different identification systems under rotational lows and highs, and exhibits how the frequency associated with the spinning motion is filtered out from the solely structural system. A numerical effort is highlighted when the CS-SSI-LPTV algorithm tries to detach structural high frequency content from the spinning action, producing characteristic wave forms that follow the path of motion. Table 6.4 summarizes the correlation distribution of a several cases for the auto-covariance matrix \mathbf{Q} of the input noise \mathbf{w}_k for the four different structural damping ratios and three different spinning time histories, $q = 500$ and $\alpha = 200$, $n = 12$. It can be seen that correlation is good for low damping ratios and decreases regularly among modes for higher energy absorption cases. Spinning velocity profile plays a role by inducing noise when the slope of the time history descriptor is steeper. In other words, sudden changes in speed contaminate the

impulse response (Markov chains) of the output signals. A similar pattern can be observed for the case of the state covariance matrix Σ as presented in Table 6.5, $q = 500$, $\alpha = 200$, and $n = 12$.

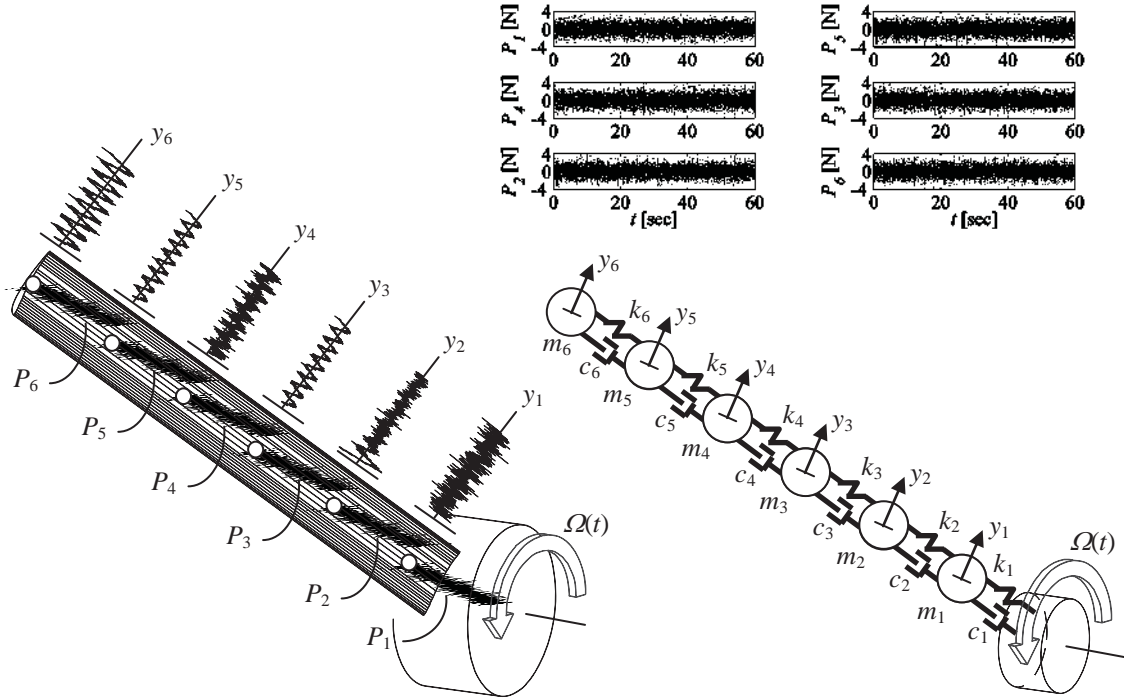


Figure 6.5. Chain-like spinning finite element model governed by a cyclo-stationary time-varying spinning velocity $\Omega(t)$. A preliminary set of six random out-of-plane loads (inputs) were imprinted on each node to excite the modal harmonics of the structure.

Correlation among the DOF's is highlighted for high energy absorption ($\zeta = 0.5$) in static conditions $\Omega(t) = 0$. Therefore, additional data points are needed in order to get good estimates of Σ , which in turn is critical to prevent ill-conditioned models by achieving positive real matrices of the quadruple $\mathbf{C}_0, \mathbf{A}_0, \mathbf{G}, \mathbf{\Lambda}_0$. There is a possibility to encounter numerical issues since the estimated finite covariance sequence may not be positive real. Table 6.6 depicts similar cases for the distribution of the auto-covariance matrix \mathbf{R} of the output noise \mathbf{v}_k , again, $q = 500$, $\alpha = 200$, and $n = 12$. Clearly, the covariance distributions denote a pattern due to the fact that \mathbf{v}_k is closely related to the

controlled outputs \mathbf{y}_k . Similar to the general distribution of \mathbf{Q} (see Table 6.4), the output covariance noise, is more controlled for less damped systems and low spinning velocities $\Omega(t)$; whereas for either high intensities or/and high variations of $\Omega(t)$, the noise covariance distribution generates shifted correlation waveforms towards the tip of the blade. Similar patterns can be observed for the input-output cross-covariance matrix \mathbf{S} , as seen in Table 6.7. In order to achieve numerical stability in the solution of the state covariance matrix Σ , a set of $n_{it} = 100$ recursive iterations of the inverse matrix $\bar{\Omega} = \Sigma^{-1}$ were made for distinct spinning velocity profiles and damping ratios, using the same values for q , α , and n as before (see Table 6.8). Plots are generated on the convergence of the 12 states associated with the 12th computational DOF (last row) of $\bar{\Omega}$. Stability in the covariance coefficients can be induced at higher states of the system as illustrated. A symmetric positive-definite state covariance Σ is critical for the identification success. It can be observed that, for a particular cluster of states x_i , as a function of the actual order of the system n , the projected values in the associated cells of $\bar{\Omega} = \Sigma^{-1}$ tend to oscillate around a baseline average that, for well conditioned systems, produce the desired symmetric positive-definite matrix. The last row of Table 6.8 exemplifies how nonlinear changes in the spinning velocity complicate the extraction of a stable state covariance matrix, not the case for static systems (first row) or systems with constant spinning velocity (second row). Given the cyclo-stationary nature of the state matrix \mathbf{A}_0 and observation matrix \mathbf{C}_0 , numerical convergence is captured more rapidly when the spinning velocity changes over time, as observed in the last row of Table 6.8. The cyclo-stationary phenomenon tends to create more coherence in the computed states, thus promoting a faster convergence. Complementary to the covariance matrices analysis, Table 6.9 incorporates spectral density functions $\Phi(z) = \sum_{i=-\infty}^{\infty} \Lambda_i z^{-i}$ in the z -domain of the six output signals \mathbf{y}_k in order to illustrate their contribution to the stochastic identification of the rotational system. The contribution of the sixth output channel (tip of the blade) is relevant for low damping ratios and decreases as the energy absorption becomes stronger. For the cases of variable rotational speed, there is a loss of information in the frequency content, due to the alignment of modes, that can be associated to the effects that the centrifugal force and gyroscopic motion have on the system [Velazquez

and Swartz 2012]. This phenomenon impacts directly on the quality of the identification of higher modes (high frequencies and damping ratios, as illustrated in Table 6.10, Table 6.11, and Table 6.12, respectively). For those cases, a comparison of the identified dominant modes, frequencies and damping ratios of the system, is achieved versus the contended exact solution of the SFE system. In all cases, the spinning velocity contribution is filtered out from the structural dynamics. By comparing the last two rows of Table 6.11 and Table 6.12, it is seen that systems with both high damping and high variable rotational speeds tend to be more difficult to identify. To demonstrate the accuracy of the CS-SSI-LPTV algorithm, Figure 6.7 draws four cases of the prediction of the output signal at the sixth node y_6 versus the corresponding measured channel, for different spinning velocity profiles and different damping ratios. Here, $q = 500$, $\alpha = 200$, $n = 12$, and each cluster contains five cases that match up, from top to bottom: $\zeta = 0.0001$, $\zeta = 0.001$, $\zeta = 0.01$, $\zeta = 0.1$ and $\zeta = 0.5$. Finally, Figure 6.8 outlines computational-time trending curves of CS-SSI-LPTV versus the cyclo-stationary transition-matrix coefficient s , for different orders of the system n , and performed for three different orders of the Hankel matrix $\alpha = 10$, $\alpha = 30$ and $\alpha = 50$. In all cases $q = 300$ and 6000 sample points at $\Delta t = 0.01$ sec were carried out. Comparing numerical results from those of the deterministic system identification techniques group, some numerical issues related to unstable poles were encountered. The data analysis indicates that the identification method presented in this study using cyclo-stationary stochastic system identification is sensitive to the application of a transition state dimensionality criterion s (*i.e.*, $s = 12m, 24m, 36m$, *etc.*). This effect is especially true for the goodness-of-fit ratio, prediction error, and output noise intensities. Analysis of different combined output data pairs showed some numerical inconsistencies and prediction errors at times. It is important to note that predicted outputs of sensor devices located in the proximity of the outboard end were difficult to characterize for highly damped structures with high spinning velocity variability, whereas the ones located in the inboard end were much easier to handle presumably due to the larger signal to noise ratios for flexural vibrations. Similarly, singular values were pin-pointed with acceptable accuracy whereas unstable poles manifested themselves when the block Hankel matrix size was increased. Similarly,

the goodness-of-fit ratio of a model depends greatly on properties of the data set used for validation such as sampling size, distance from sensor to sensor, independency among signals, noise content, smoothness of $\Omega(t)$, and energy absorption ratios. Despite the integrity of the mathematical framework presented here, numerical stability issues have emerged as a result of the high sensitivity of the periodic linear time-varying parametrization and sinusoidal cyclo-stationary functions. It is also important to comment that the application of coherent external forces to the rotating system produce more correlation in the data sets, which translates into a deterioration of the signal content for CS-SSI-LPTV identification purposes. As observed in Figure 6.6, cyclo-stationary motion is coherent in nature, and coherence becomes stronger as $\Omega(t)$ increases.

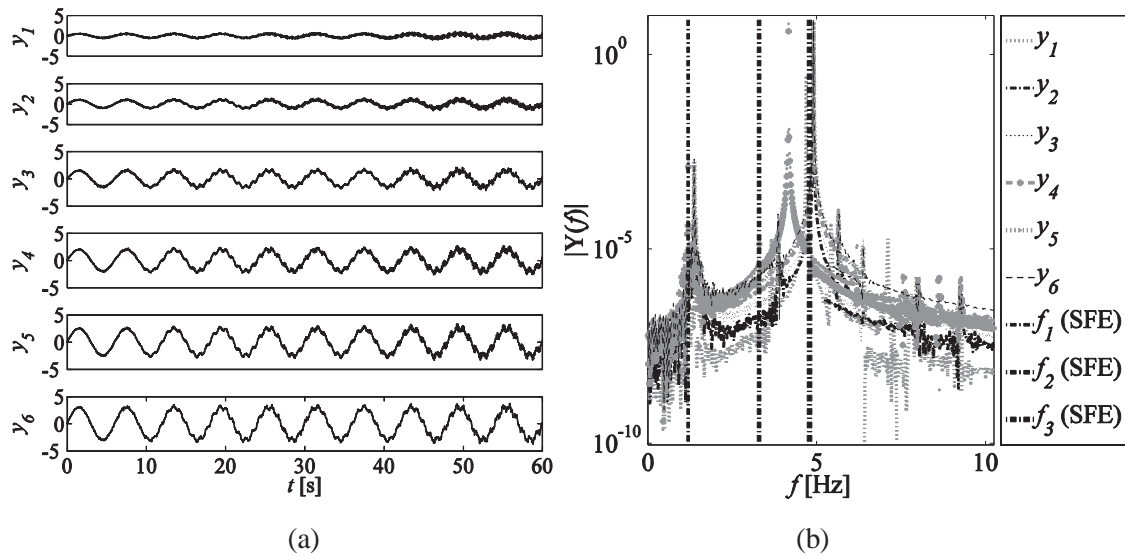


Figure 6.6. (a) Typical set of outputs $y_i(t)$ (input data time histories for CS-SSI-LPTV model) adopting velocity signals (m/sec) of the spinning finite element (SFE) model running at constant spinning velocity $\Omega = 10$ RPM. (b) Corresponding spectral density functions.

Consequently, parameter identification turns out to be difficult in some particular cases, and when output signals are picked up in the rotating plane only. Although this research has produced some acceptable results, it has also produced several inquiries. A more in-depth analysis of nonlinear identification techniques may be worthwhile to apply, considering now rotational in-plane and rotational out-of-plane combined signals.

Table 6.2. Distribution of the Hankel matrix Singular-Value-Decomposition (SVD) values employed to define the order of the system n via CS-SSI-LPTV identification method.

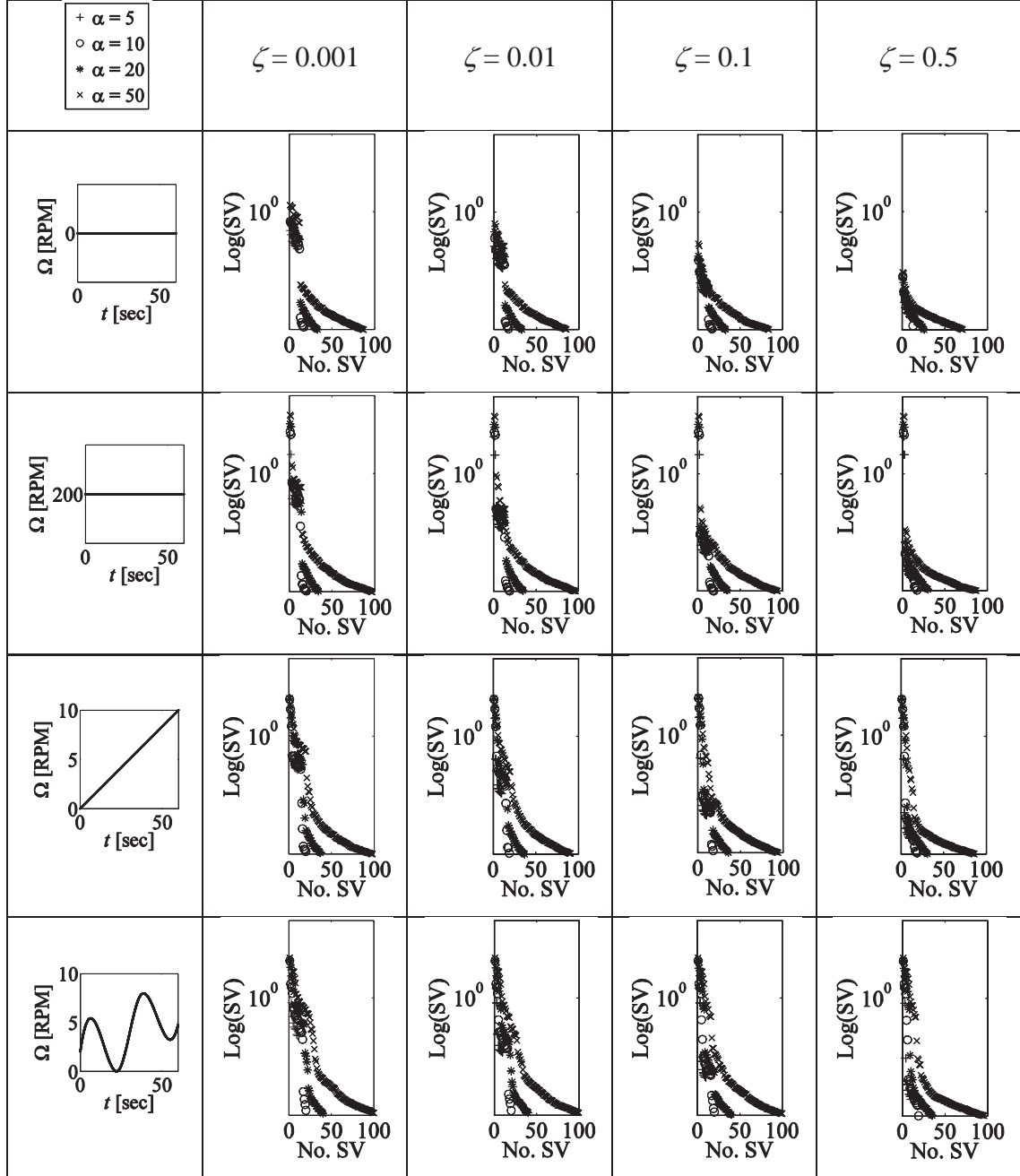


Table 6.3(a). Stability curves for distinct orders of the system n and for different structural damping ratios and three distinct spinning-velocity profiles, by means of the CS-SSI-LPTV identification algorithm.

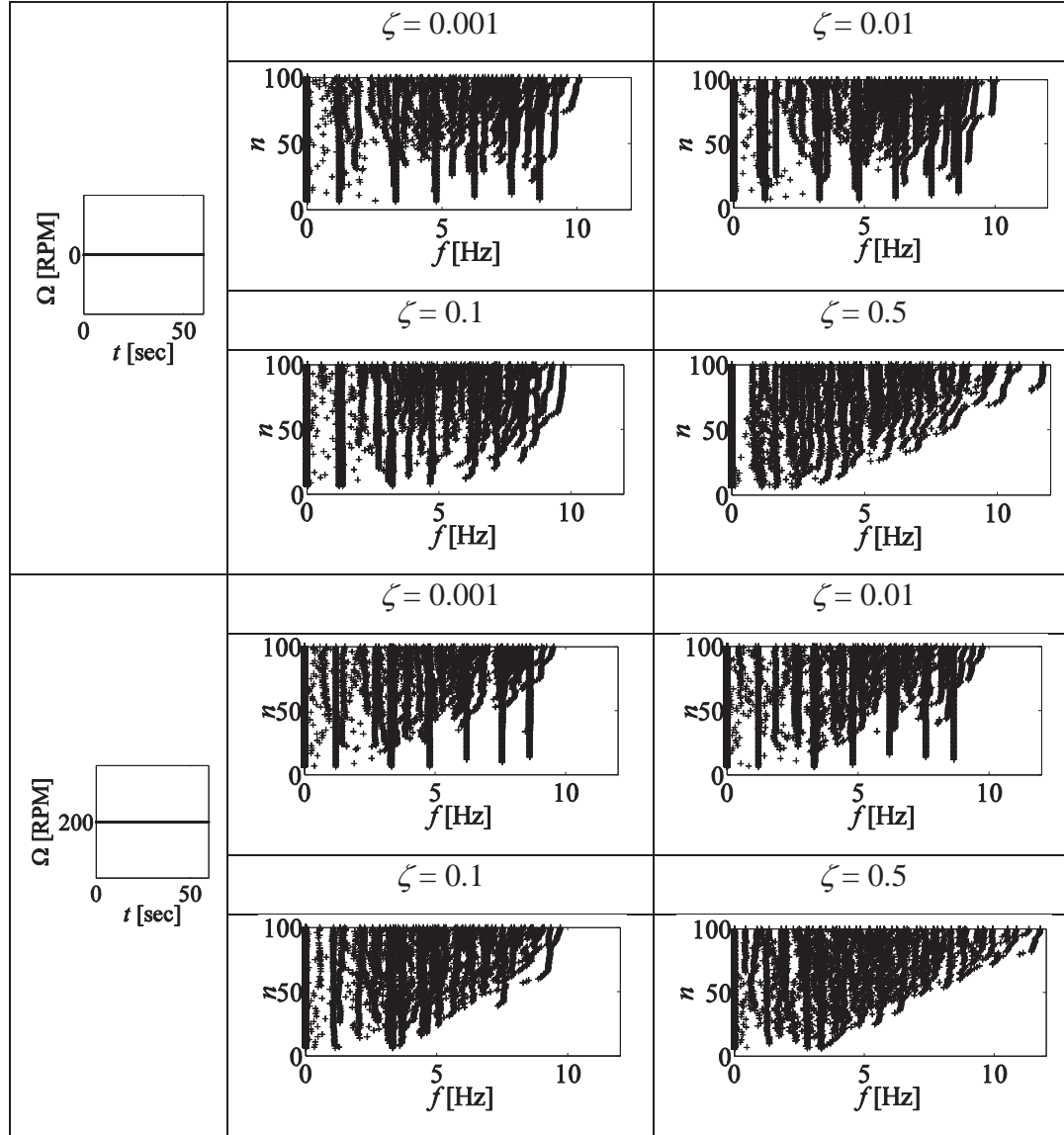


Table 6.3(b). Stability curves for distinct orders of the system n and for different structural damping ratios and three distinct spinning-velocity profiles, by means of the CS-SSI-LPTV identification algorithm.

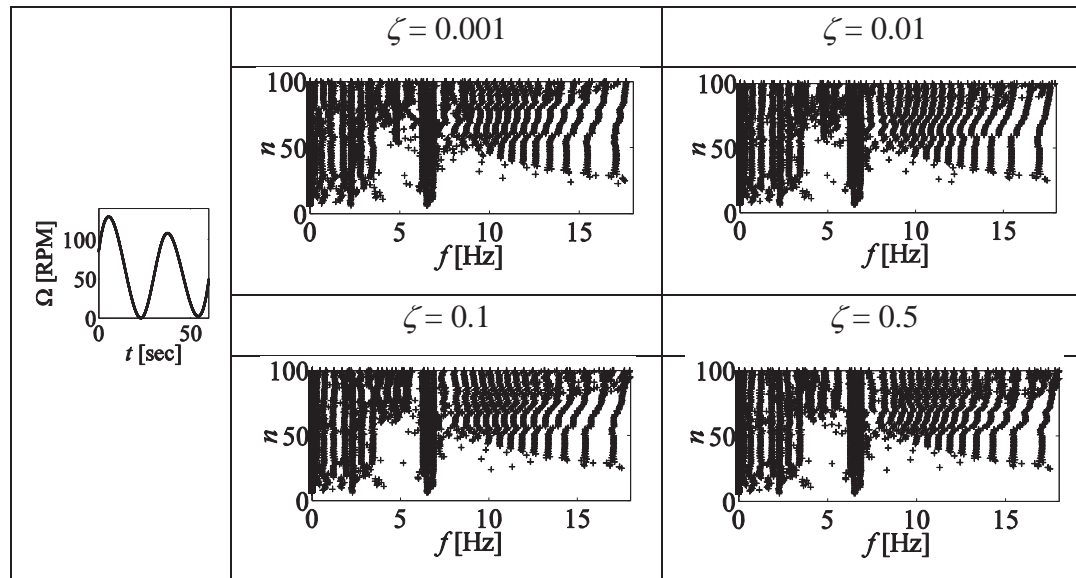


Table 6.4. Distributions of the auto-covariance matrix \mathbf{Q} of the input noise \mathbf{w}_k , for different structural damping ratios ζ and for three different spinning velocity time histories $\Omega(t)$.

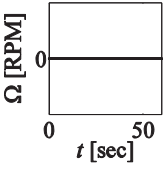
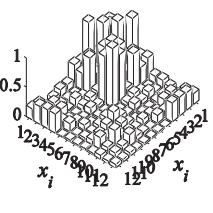
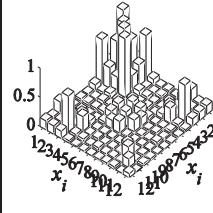
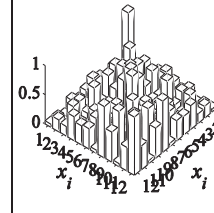
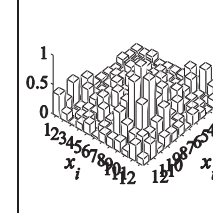
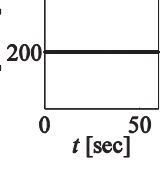
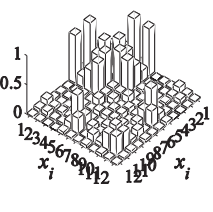
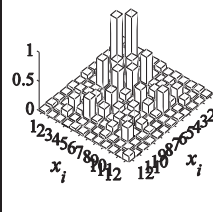
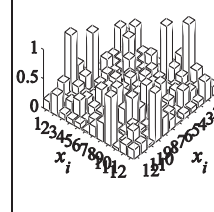
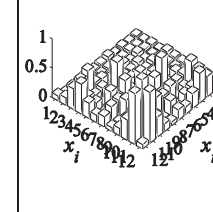
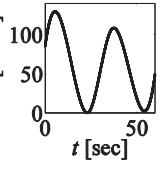
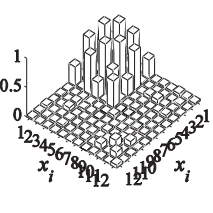
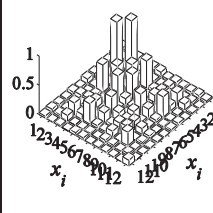
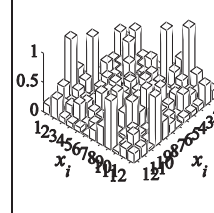
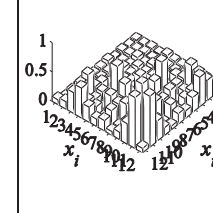
\mathbf{Q}	$\zeta = 0.001$	$\zeta = 0.01$	$\zeta = 0.1$	$\zeta = 0.5$
				
				
				

Table 6.5. Correlation distributions of the state covariance matrix Σ for different structural damping ratios ζ and for three different spinning velocity time histories $\Omega(t)$.

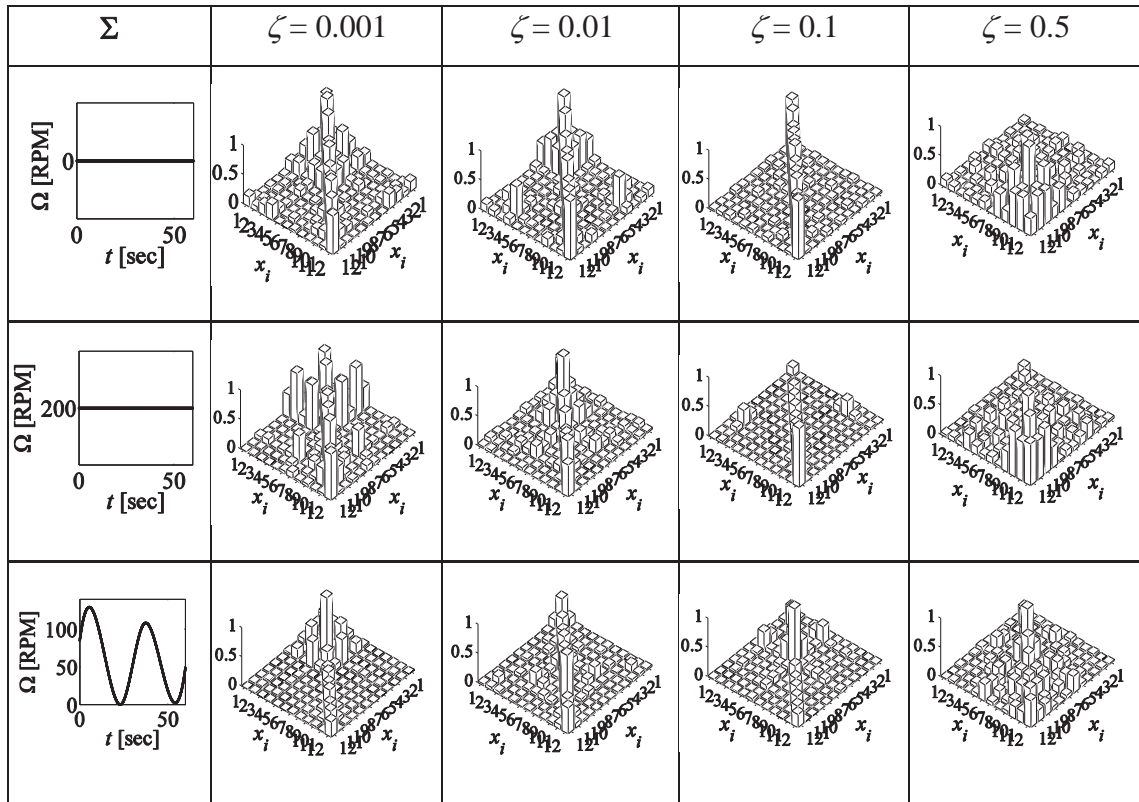


Table 6.6. Distributions of the auto-covariance matrix \mathbf{R} of the output noise \mathbf{v}_k , for different structural damping ratios ζ and for three different spinning velocity time histories $\Omega(t)$.

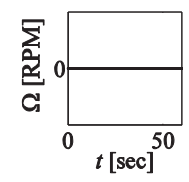
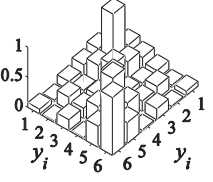
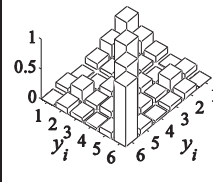
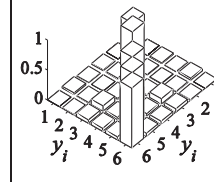
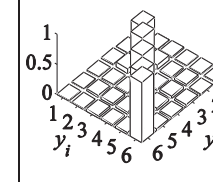
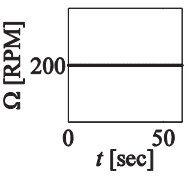
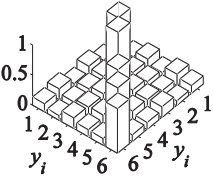
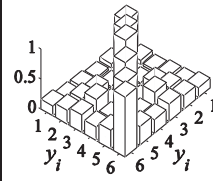
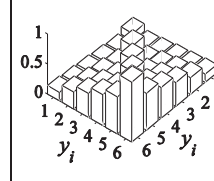
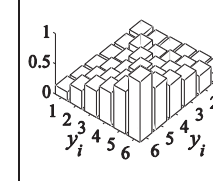
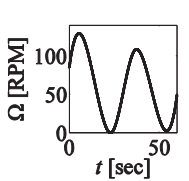
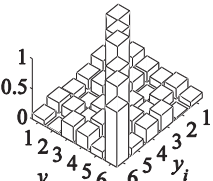
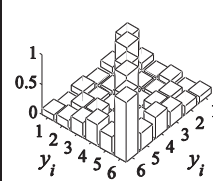
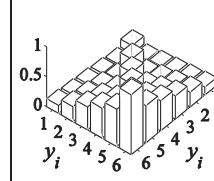
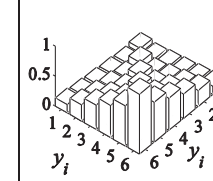
\mathbf{R}	$\zeta = 0.001$	$\zeta = 0.01$	$\zeta = 0.1$	$\zeta = 0.5$
				
				
				

Table 6.7. Distributions of the cross-covariance matrix \mathbf{S} of the input/output noise pair \mathbf{w}_k and \mathbf{v}_k , for different structural damping ratios ζ and for three different spinning velocity time histories

$$\Omega(t).$$

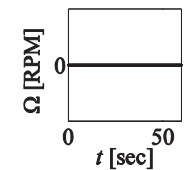
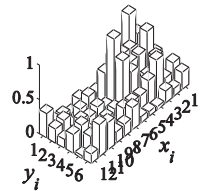
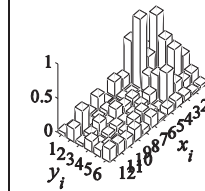
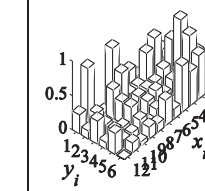
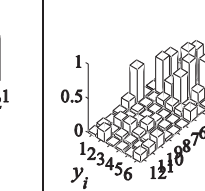
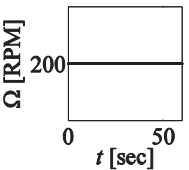
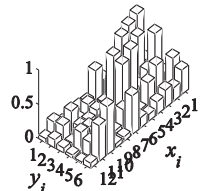
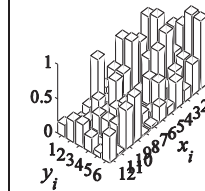
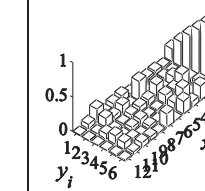
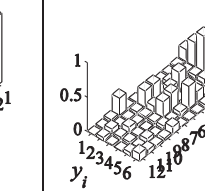
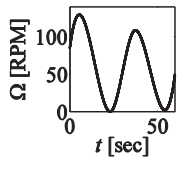
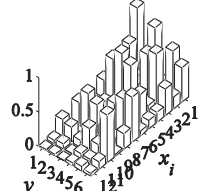
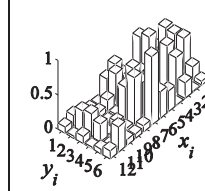
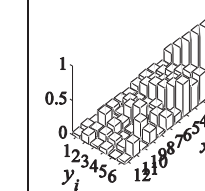
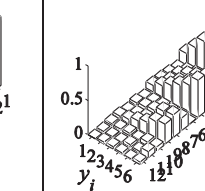
\mathbf{S}	$\zeta = 0.001$	$\zeta = 0.01$	$\zeta = 0.1$	$\zeta = 0.5$
				
				
				

Table 6.8. Recursive $n_{it} = 100$ iterations of the state-covariance inverse matrix $\bar{\Omega} = \Sigma^{-1}$ aimed to reach stationary conditions of the covariance matrices, for different structural damping ratios ζ and for four different spinning velocity time histories $\Omega(t)$.

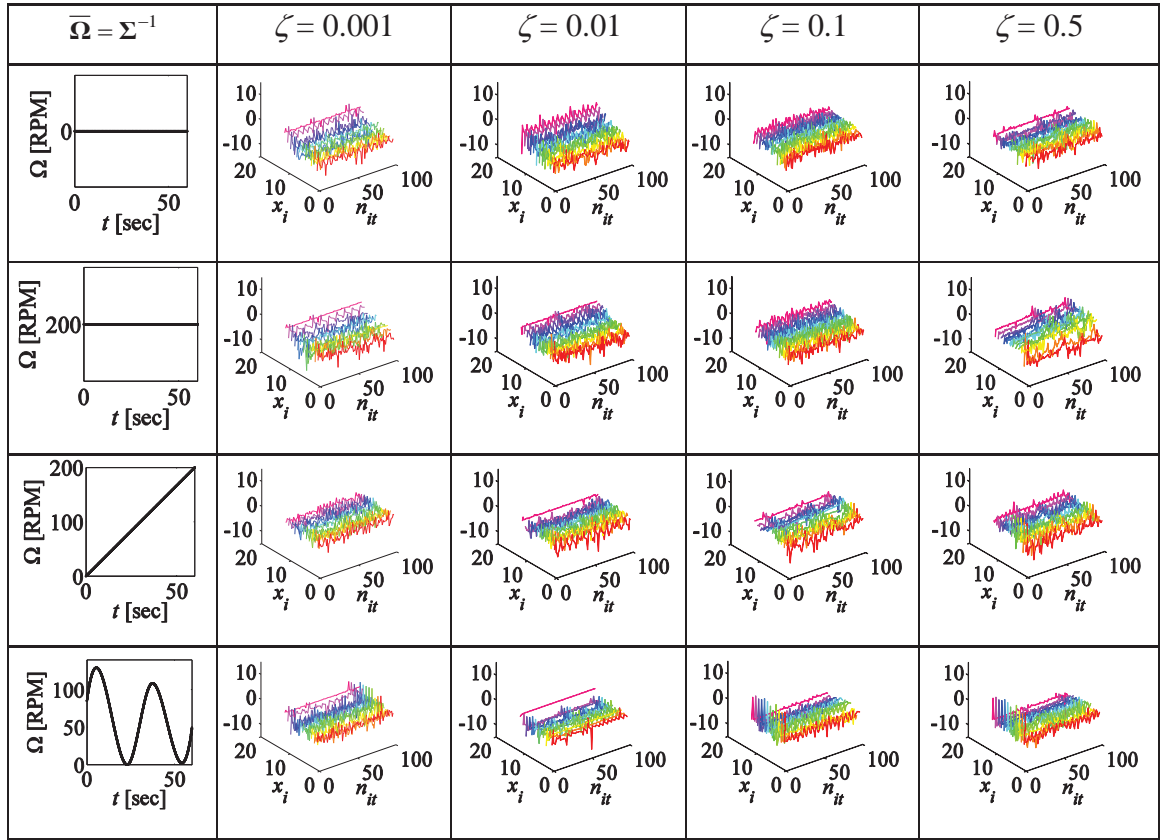


Table 6.9. Spectral density functions $\Phi(z)$ of output signals y_k for different structural damping ratios ζ and for four different spinning velocity time histories $\Omega(t)$.

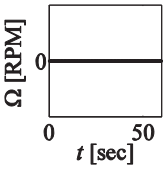
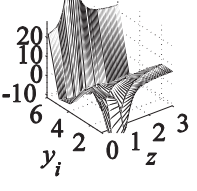
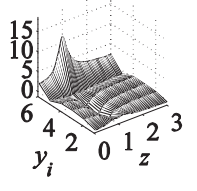
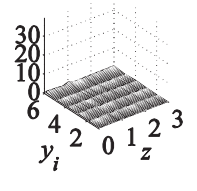
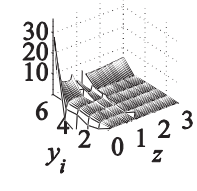
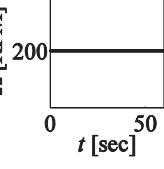
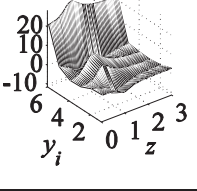
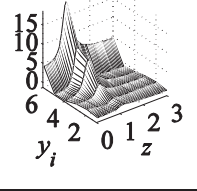
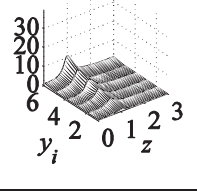
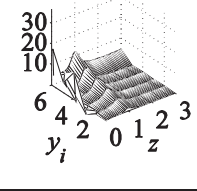
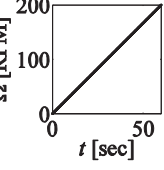
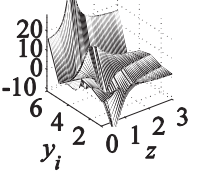
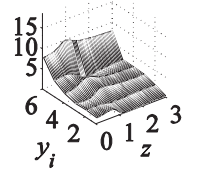
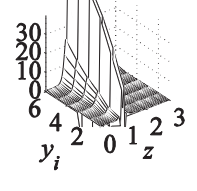
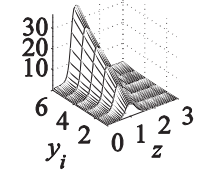
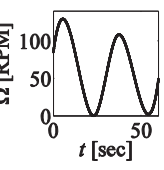
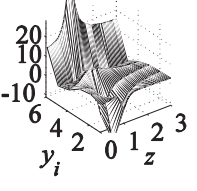
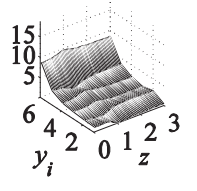
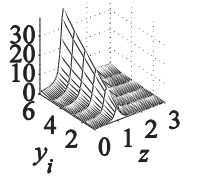
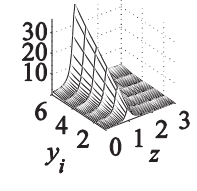
$\Phi(z)$	$\zeta = 0.001$	$\zeta = 0.01$	$\zeta = 0.1$	$\zeta = 0.5$
				
				
				
				

Table 6.10(a). Comparison of the identified first three dominant modes of the system computed for different structural damping ratios ζ and different spinning-velocity time histories $\Omega(t)$. CS-SSI-LPTV identification algorithm is benchmarked with the exact solutions from SFE.

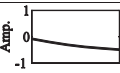
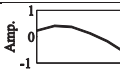
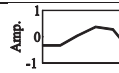
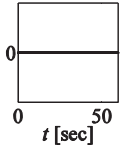
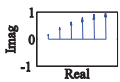
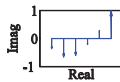
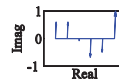
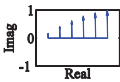
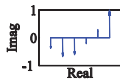
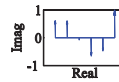
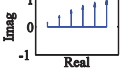
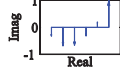
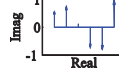
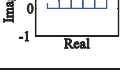
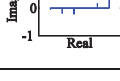
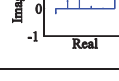
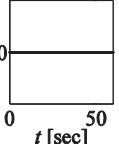
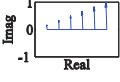
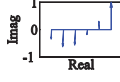
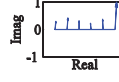
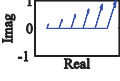
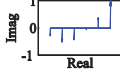
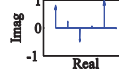
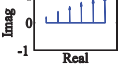
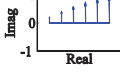
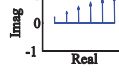
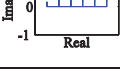

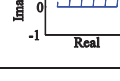
		1 st Mode	2 nd Mode	3 rd Mode
SFE				
 Ω [RPM]	$\zeta = 0.001$			
	$\zeta = 0.01$			
	$\zeta = 0.1$			
	$\zeta = 0.5$			
 Ω [RPM]	$\zeta = 0.001$			
	$\zeta = 0.01$			
	$\zeta = 0.1$			
	$\zeta = 0.5$			

Table 6.10(b). Comparison of the identified first three dominant modes of the system computed for different structural damping ratios ζ and different spinning-velocity time histories $\Omega(t)$. CS-SSI-LPTV identification algorithm is benchmarked with the exact solutions from SFE.

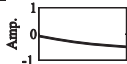
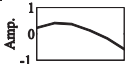
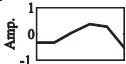
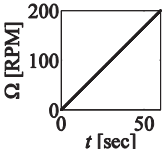
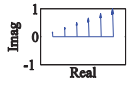
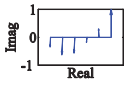
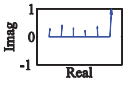
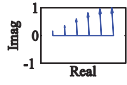
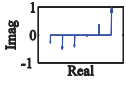
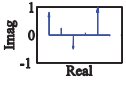
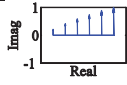
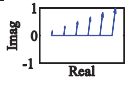
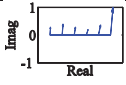
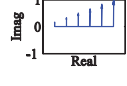
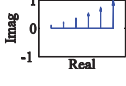
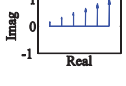
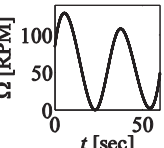
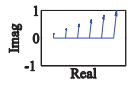
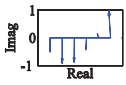
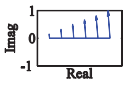
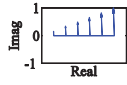
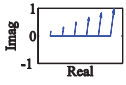
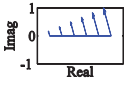
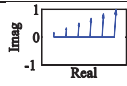
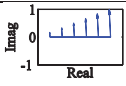
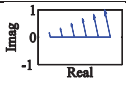
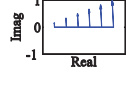
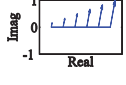
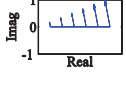
		1 st Mode	2 nd Mode	3 rd Mode
SFE				
	$\zeta = 0.001$			
	$\zeta = 0.01$			
	$\zeta = 0.1$			
	$\zeta = 0.5$			
	$\zeta = 0.001$			
	$\zeta = 0.01$			
	$\zeta = 0.1$			
	$\zeta = 0.5$			

Table 6.11. Comparison of the identified dominant frequencies of the system computed for different structural damping ratios ζ and different spinning-velocity time histories $\Omega(t)$. CS-SSI-LPTV identification algorithm is benchmarked with a standard procedure (non cyclo-stationary) of Stochastic ID, and with the exact solutions from SFE.

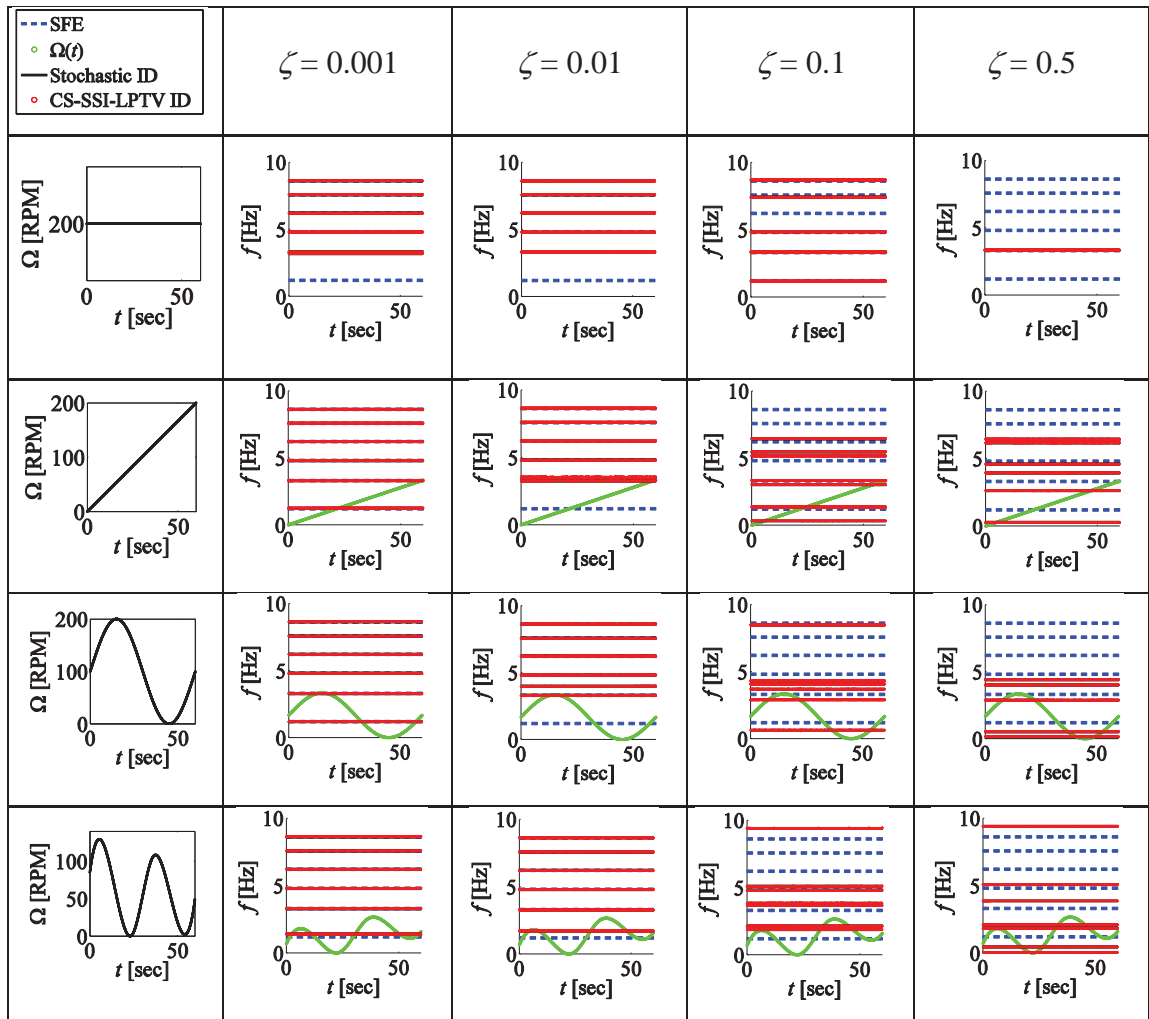
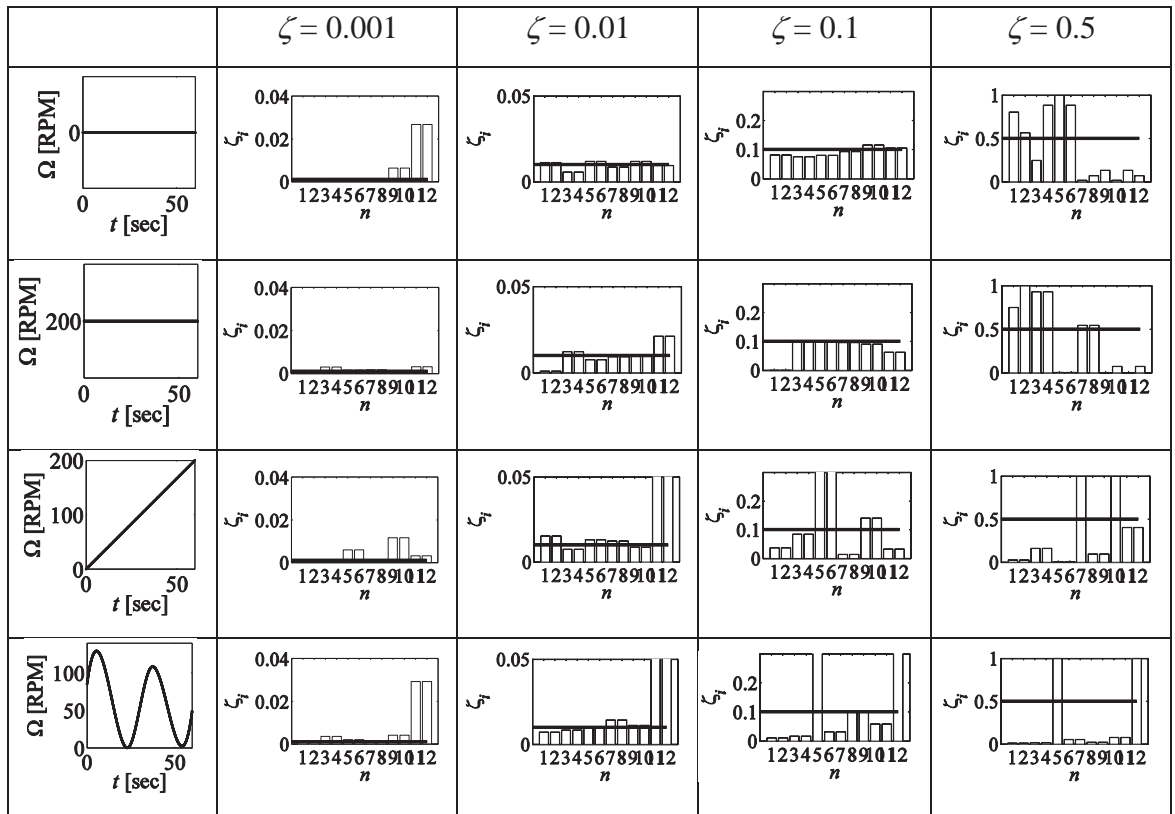


Table 6.12. Comparison of the identified CS-SSI-LPTV damping ratios versus SFE structural damping ratios ζ at different spinning-velocity time histories $\Omega(t)$.



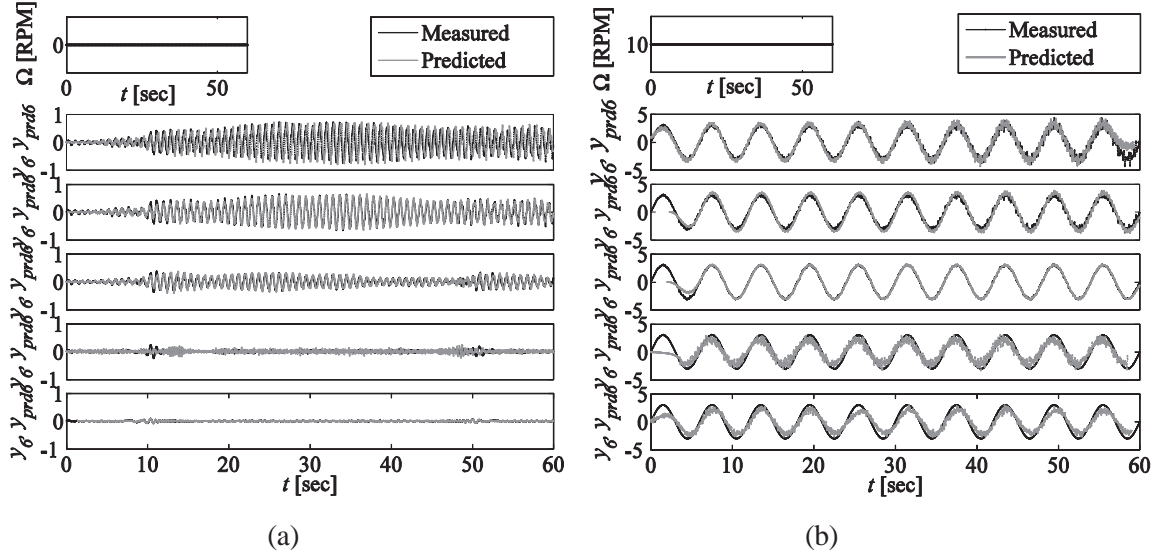


Figure 6.7(a)(b). Measured vs prediction of the output signal of the sixth node y_6 for different spinning velocity profiles $\Omega(t)$. For each cluster (a) null or (b) constant spinning velocity, simulations with five damping ratios are computed, from top to bottom, $\zeta = 0.0001$, $\zeta = 0.001$, $\zeta = 0.01$, $\zeta = 0.1$ and $\zeta = 0.5$.

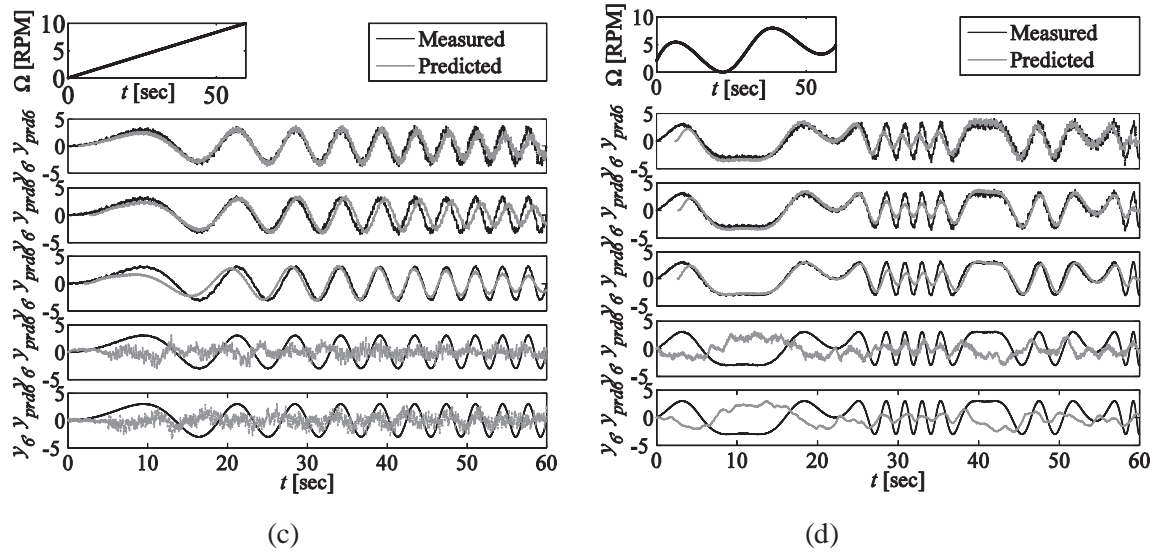


Figure 6.7(c)(d). Measured vs prediction of the output signal of the sixth node y_6 for different spinning velocity profiles $\Omega(t)$. For each cluster (c) linear or (d) smooth random spinning velocity, simulations with five damping ratios are computed, from top to bottom, $\zeta = 0.0001$, $\zeta = 0.001$, $\zeta = 0.01$, $\zeta = 0.1$ and $\zeta = 0.5$.

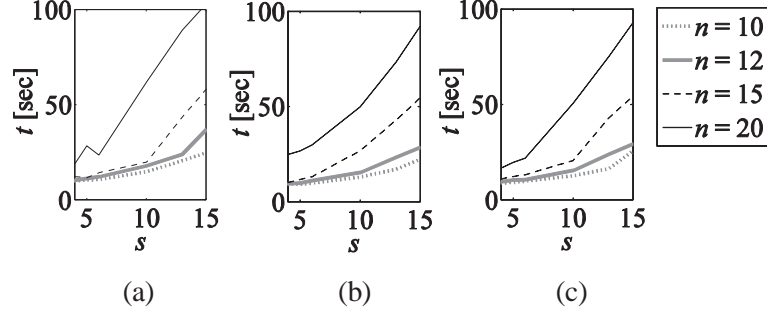


Figure 6.8. Computational time versus cyclo-stationary transition-matrix coefficient s , for four distinct orders of the system n , via CS-SSI-LPTV algorithm. (a) $\alpha = 10$, (b) $\alpha = 30$ and (c) $\alpha = 50$.

6.4 Conclusions

This paper presented a proposed approach for identifying modal properties of spinning beam structures with varying spinning velocities for rotating machinery and spinning structures models. In general terms, identification of the cyclo-stationary effects was successful with some reservations and constraints on the numerical precision and numerical stability for both prediction of input/output noise distributions and innovation processes, and the assurance of a symmetric positive-definite state covariance matrix. The proposed stochastic subspace identification with time-varying linear parameters method was implemented using numerical verification data sets to explore its dependencies on features such as spinning velocity variation, noise level, damping, and input frequency content. The analytical framework has proven numerically feasible when there is consistency and smoothness of the time-varying non-stationary spinning velocities. Further analysis must be performed to better characterize the effects of zero-mean white Gaussian input/output noise approximations, and discussion must be contended for an optimized algorithm architecture suitable in practical applications such as automated, embedded system or in wireless sensor networks. Following, Chapter 7 establishes the basis of an iterative numerical method for updating the rotor-blades structural model, based on both canonical Adaptive Simulated Annealing (ASA) and complex-conjugate Modal Assurance Criterion (MAC). This numerical machinery will link the principles of Spinning Finite Element, previously established in Chapter 4 and Chapter 5, with the experimental probabilistic identification skim presented in here, in

such a way that the objectives of the Thesis document can be fully crowned.

Chapter 7. Model Updating via Adaptive Simulated Annealing

Rotational machinery such as Horizontal Axis Wind Turbines (HAWTs) exhibit complex and nonlinear dynamics (*e.g.*, precession and Coriolis effects, torsional coupling); and are subjected to nonlinear constrained conditions (*i.e.*, aeroelastic interaction). For those reasons, aeroelastic and computer-aided models reproduced under controlled conditions may fail to predict the correct non-stationary loading and resistance patterns of wind turbines in actual operation. Operational techniques for extracting modal properties under actual non-stationary loadings are needed in order to: improve computer-aided elasto-aerodynamic models to better characterize the actual behavior of HAWTs in operational scenarios, monitor and diagnose the system for integrity and damage through time, and optimize control systems. For structural health monitoring (SHM) applications, model updating of stochastic aerodynamic problems has gained interest over the past decades. A probability theory framework is employed in this study to update a HAWT model using such a stochastic global optimization approach. Structural identification is addressed under regular wind turbine operation conditions for non-stationary, unmeasured, and uncontrolled excitations by means of Stochastic Subspace Identification (SSI) techniques. This numerical framework is then coupled with an adaptive simulated annealing (ASA) numerical engine for solving the problem of model updating. Numerical results are presented for an experimental deployment of a small HAWT structure.

7.1 Introduction

The aim of structural health monitoring (SHM) is to identify and characterize damage in structures from operational data [Farrar and Worden 2012]. In many SHM applications, the presence and characterization of damage is informed by comparing measured behavior to models of expected behavior. To rectify these two sources of information, combinatorial optimization is an important tool and consists of a set of problems that are necessary in many engineering disciplines, not just SHM [Imregun and Visser 1991]. Research in this area aims to develop efficient techniques for finding minimum or maximum values of some function of independent variables [Mottershead

and Friswell 1993], usually called the cost function or objective function, that represents a quantitative measure of the “goodness” of a complex system realization. The cost function depends on the detailed configuration of the many parts of the system. A major goal of this approach is to identify an optimal model that represents the system by minimizing this cost function. All exact methods known for determining an optimal route require a computational effort that increases exponentially with the number of independent (target) variables n . Model updating using Simulated Annealing belongs to a large class of NP-complete (nondeterministic polynomial time complete) problems, which has received extensive attention in the past years [Davis 1987] due to its ability to discriminate between a global minimum from many local minima in a stable and relatively efficient manner and its demonstrated capacity for parallelization in wireless sensor networks [Zimmerman and Lynch 2009], which is a useful technology for monitoring the so-called Horizontal Axis Wind Turbines (HAWT) systems [Swartz *et al.* 2010][Song *et al.* 2013].

In this study, a model updating approach for use with a dynamic vibrational model of operational wind turbine blades, suitable for SHM, and based on simulated annealing is proposed. Analytical models of wind turbines are usually managed by standard Finite Element Methods (FEM) and often neglect spinning dynamics [Mares and Surace 1996] which creates problems for model updating algorithms. In addition, nearly all commonly-used modal identification methods are based on the assumption of viscous (linear) damping. Damped-gyroscopic systems such as wind turbines are an exception and must be modeled to account for both gyroscopic damping and complex mode shapes. Typical outputs of modal identification algorithms of this kind of system are eigenfrequencies, complex-mode pairs, and modal damping. This study will details the steps required to extract these parameters from operational wind turbine vibrational data via cyclostationary stochastic subspace identification and use them to update novel spinning finite elements that can form the basis of an SHM model. A new variant of Adaptive Simulated Annealing (ASA) is implemented to optimize for rotation speed of the rotor blades. This numerical engine is tested using several objective functions via eigensystem Realization

Algorithm (ERA) first, then Stochastic Subspace Identification (SSI) as the prime modal analysis technique.

The ERA algorithm allows to identify a state-space model of the structural system under some uncertainty of measurement noise based on the Least Squares (LS) approach [Juang 1994]. In contrast, Stochastic Subspace Identification (SSI) employs Markov models to simulate stationary stochastic process, associated with a covariance matrix, to identify the state-space system [Katayama 2010]. ERA is based on rendering a minimum model order realization in the absence of noise and can be very suitable for complex structures such as HAWT wind turbines. SSI renders a minimum stochastic realization by using the deterministic realization theory and linear matrix inequality (LMI), contended by the state covariance matrix. ERA state-space realizations are relevant to modal testing because the first-order form descriptor enhances linear system behavior with, either classical, or non-classical damped structural dynamics. Conversely, SSI derives a first-order form descriptor of valid stochastic state sequences with a finite number of output measurements as inputs, treating either classical or non-classical damping by assuring a positive definite covariance matrix. The next section of this paper discusses relevant considerations of the ERA and SSI methods to compute eigenfrequencies and eigenvectors and realize relevant real modes from extracted complex modes. The following section describes the general approach of a novel Spinning Finite Element (SFE), reframed for high order tapered-swept variations of the blades cross section. Some guidelines that are required to compute the eigenrealization of damped-gyroscopic systems are discussed and the alternative solutions are proposed to handle complex frequencies and complex modes that result from the low-order state-space representation. These results should be consistently equiparable with the values driven by both ERA and SSI.

Having identified the basic elements to conform the SFE model updating, the complex-domain modal assurance criterion (MAC) is presented as a means of quantitatively comparing the mode shapes realized from the mechanics-driven and the data-driven

models, and weight coefficients, required to ensure convergence of the numerical optimization algorithm via Adaptive Simulated Annealing (ASA), are defined. In addition, the thermodynamic equilibrium basis of the ASA is delineated for adapting the general methodology to rotor blade systems with variable speed. A search algorithm is presented for low-temperature stages by fixing the value of the spinning velocity previously identified on the input-output data sets. Finally, a numerical experiment using data generated from a numerical model of a small wind turbine (BWC XL.1) is included to demonstrate some features of the ASA numerical method proposed here.

7.2 Eigensystem Realization Algorithm (ERA)

The ERA is a group of subspace identification algorithms designed to estimate the sequences directly from a given data, either explicitly or implicitly, through an orthogonal or oblique projection of the row spaces of block Hankel matrices of data into the row spaces of shifted block Hankel matrices, followed by a singular value decomposition (SVD) and QR decomposition that sets the order, the state sequence, and the observability matrix of the system [*ibid.* Juang 1994]. In a final stage, the extraction of the state space model is achieved using a least-squares approach. Modal parameter identification applied to rotator machines, such is the case of wind turbines, is based on a transfer function matrix that generates Markov parameters from an impulse response point of view. Hankel matrices are built upon Markov parameters and form the basis of the realization of a discrete-time state-space model.

Much research effort in automated model realization (*e.g.*, for autonomous SHM systems) has been made on linear time-invariant (LTI) systems, whereas the literature on time-varying (TV) cases is limited [Ljung 1999]. Time-varying methods are suited for a set of output sequences that have the same time-varying (cycling) behavior [Verhaegen and Yu 1995] under steady-state conditions making possible the application of the classical data-correlated ERA identification algorithm, leading to the need to consider the Stochastic Subspace Identification (SSI) family of algorithms. However, as the name implies, this approach is stochastic in nature, which makes the construction of the

physical properties of the system from an eigenrealization algorithm cumbersome. Meanwhile, mode shapes are solved in the stochastic complex-number domain, and arise from a non-deterministic source and therefore cannot be computed easily. This limitation presents computational challenges that are difficult to overcome requiring the computation of envelopes and phase shifts as a function of position coordinates [Hoen 2005]. However, for low spinning velocities and steady-state rotational motion, it is possible to classify and filter out the spinning frequency embedded in a cyclic system. This observation goes hand in hand with the explicit derivation of the damped-gyroscopic dynamic system derived for the SFE model (see the following section). Under this assumption, and given the scope of the present study, a classical ERA scheme is implemented with the inclusion of eigen-properties in the identified bandwidth that can be extracted from the continuous time realization results [Bernal 2006]. By limiting the realization to modes conforming to the SFE model it is possible to discern between computational modes and system modes. The goal is to demonstrate a numerically-stable platform for Simulated Annealing where the dominant modes, typically flap and chord bending for the case of wind turbine rotor blades, are matched with the same dominant modes that the eigensolution produces from the SFE model.

In structural dynamics, it is customary to refer the concept of shape modes as the eigenvectors associated with the undamped problem $\mathbf{M}_B \ddot{\mathbf{x}} + \mathbf{K}_B \mathbf{x} = \mathbf{0}$ or equivalent array $\mathbf{M}_B^{-1} \mathbf{K}_B$ eigenvectors. Given the assumption that the modes have a clearance or gap between the closest eigenvalue, the latent – physical – vectors can be normalized to the real component and provide a good approximation of the undamped modes when the damping is treated as classical [Lancaster 1966]. However, for the case of wind turbine blades, damping is by default presumed as non-classical, and this characteristic carries out a series of impediments to compute latent vectors in a straightforward way. When the associated response of a system is complex, it cannot vibrate freely in a single complex mode but rather the resulting shape is a superposition of the latent vector and its associated complex conjugate. Extracting undamped modes from system identification analysis works well when the stiffness and mass matrices are estimated from known

physics reflected within the mechanistic (in this case, finite element) models. Decoupling the damping mechanism (and also the gyroscopic effect when blades are in yaw motion) gives the best chance to adjust the model parameters as close as possible to those supported by the measured data. It is important to determine the quality of the prediction of ERA by discarding computational modes from system modes [Papa and Elliot 1993]. Newland [Newland 1989] has interpreted the complex eigenvectors as counter rotating phasors, but does not show how they are translated into a real valued response. A solution can be found by investigating the inverse problem and computing flexibility matrices from the eigenrealization in the complex domain. Once the flexibility matrices \mathbf{M}_B^{-1} and \mathbf{K}_B^{-1} are determined, they can be linearized to a certain level, at least for the first dominant frequencies associated with flap bending and chord bending modes, which dominated the blade response observed during the experimental portion of this study [Velazquez and Swartz 2013]. However, a more direct solution is to work directly with complex modes, characterizing their similarity using a complex MAC [Vacher *et al.* 2010] taking advantage of the phasor information to aid in the model updating process. This result provides the basis used in this study to establish comparisons between ERA and SFE models, but also serves to benchmark mass and stiffness matrices from both sources, and subsequently verify the quality of the convergence algorithm from the Simulated Annealing engine. Again, the problem of modal truncation needs to be clarified with the goal to establish a platform numerically stable and theoretically valid for Simulated Annealing calculations.

7.3 Stochastic Subspace Identification (SSI)

To deal with the problem of truncation of modes, Stochastic Subspace Identification (SSI) is a set of subspace identification algorithms designed to compute stochastic state-space models from a given output data set. Compared to ERA, the main idea of SSI is to introduce canonical correlations of two matrices that are assumed semi-infinite [Akaike 1975]. A finite-dimensional vector series defined by sequential covariances of output signals to form a block Hankel matrix would be a valid state sequence of the stochastic model. Similar to the provisions for ERA introduced above, a singular value

decomposition (SVD) of the block Hankel matrix will help to set the order and state sequence, according to positive definite state-covariance matrix rule, in order to extract the model from the identified low-order eigenrealization [van Overschee and De Moor 1996]. From there, extraction of the state space model can be executed traditionally following the ERA guidelines presented in a previous section. For this aim, and compared to the ERA outline composed by minimum Markov realizations, SSI employs block Hankel matrices upon minimum covariances of output signals to form the basis of the realization. As was mentioned above for ERA, the question arises on how to filter out the spinning velocity contribution from the real dynamics of the system. In other words, how a cyclic induced motion could be removed or dismissed from contaminated – noisy – output-only random signals. A cyclo-stationary stochastic subspace identification algorithm using linear-time-varying parameters CS-SSI-LPTV is used here to tackle this problem [Verdult and Verhaegen 2002][Lopes dos Santos *et al.* 2007]. The goal is to introduce a linear parameter varying (LPV) scheme variable in time that would follow a sinusoidal – therefore cyclic – stationary function to rule out the spinning effect from the identification [Verdult 2002][Kameyama and Ohsumi 2007]. The goal is to perform a numerically-stable solution for ASA where the identified dominant modes of the blade, expressed in the complex-numbers domain, matches the dominant modes of the SFE model, expressed also in the same complex-numbers domain. Given this parity in the nature of the modes, it is possible to establish an indexed criteria containing both amplitudes and phases of the resulting latent vectors in a complex-conjugate duality, namely MAC under complex vectorizations. Consequently, it is not necessary to convert complex-number modes to their physical counterparts during the iterative annealing process while updating the model. CS-SSI-LPTV provides a viable solution to face both SSI and SFE models towards a proper identification, adequate characterization and efficient update of numerical HAWT models (Figure 7.1).

7.4 Spinning Finite Element (SFE)

The general damped-gyroscopic dynamic equation that governs the response of a spinning tapered-swept wind turbine blade element is given by [Leung and Fung

1988][Christensen and Lee 1986][Baumgart 2002][Larwood 2009][Nelson 1985]:

$$\mathbf{M}_B \ddot{\mathbf{q}}(t) + [2\mathbf{G}_B + \mathbf{C}_B] \dot{\mathbf{q}}(t) + [\mathbf{K}_{eB} + \mathbf{K}_{cB} - \mathbf{K}_{\Omega B}] \mathbf{q}(t) = \mathbf{0} \quad (7.1)$$

where \mathbf{M}_B and \mathbf{K}_{eB} are the mass and elastic stiffness matrices for non-rotating beam elements, \mathbf{G}_B is the skew-symmetric gyroscopic matrix, \mathbf{C}_B is a classical damping matrix, assumed proportional to the mass and stiffness matrices.

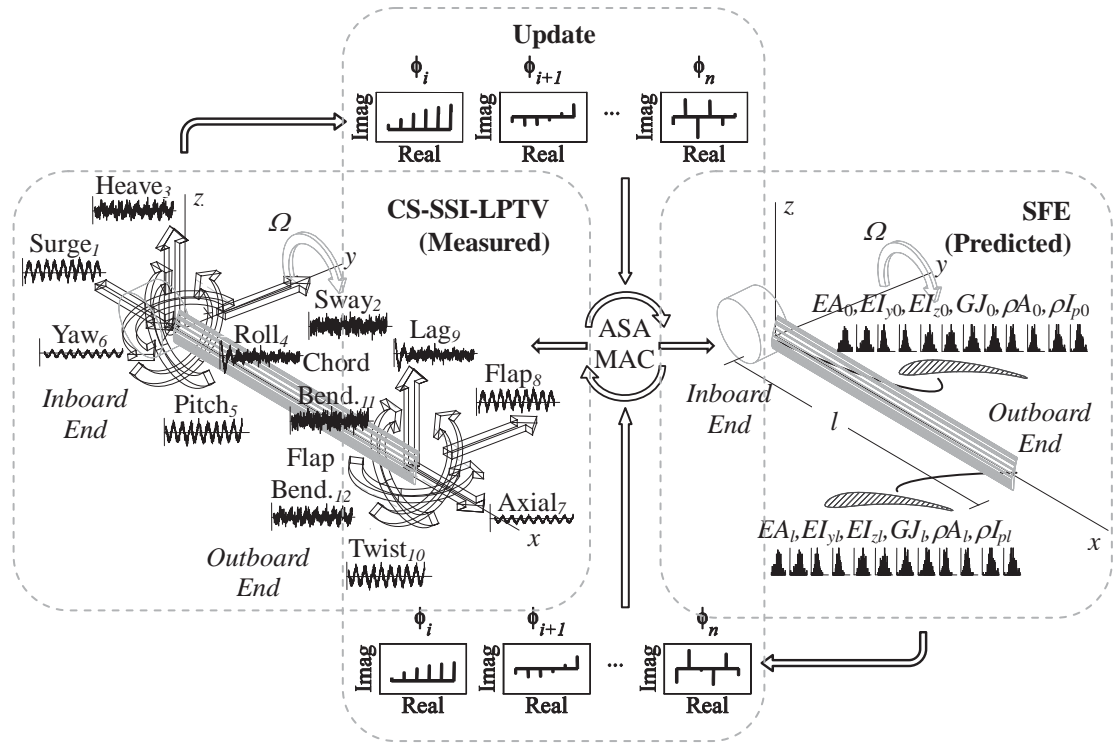


Figure 7.1. Scope of the Adaptive Simulated Annealing engine for SFE model updating via CS-SSI-LPTV.

Matrix $\mathbf{K}_{\Omega B}$ is the stabilizing stiffness spinning matrix and \mathbf{K}_{cB} is the destabilizing centrifugal stiffness matrix, $\mathbf{q}(t)$ is the global nodal displacement vector (inboard and outboard ends) when the oscillation occurs about the steady state as a function of time. Prime notation means differentiation with respect to time t . In principle:

$$\begin{aligned}
\mathbf{M}_B &= \int_0^l \rho A(s) \mathbf{m} ds; \quad \mathbf{G}_B = \int_0^l \rho A(s) \mathbf{g} ds \\
\mathbf{C}_B &= [c_u \mathbf{C}_u + c_v \mathbf{C}_v + c_w \mathbf{C}_w + c_\theta \mathbf{C}_\theta + c_\phi \mathbf{C}_\phi + c_\psi \mathbf{C}_\psi] \\
\mathbf{K}_{eB} &= [\mathbf{k}_{e1} + \mathbf{k}_{e2} + \mathbf{k}_{e3} + \mathbf{k}_{e4}] \\
\mathbf{K}_{cB} &= [\mathbf{k}_{c1} + \mathbf{k}_{c2}]; \quad \mathbf{K}_{\Omega B} = \int_0^l \rho A(s) \mathbf{k}_\Omega ds
\end{aligned} \tag{7.2}$$

$$\begin{aligned}
\mathbf{m} &= \mathbf{N}^T \mathbf{N}; \quad \mathbf{g} = \mathbf{N}^T \mathbf{R} \boldsymbol{\Omega} \boldsymbol{\Omega}^T \mathbf{N} \\
\mathbf{C}_u &= \int_0^l \mathbf{N}^{uT} \mathbf{N}^u ds; \quad \mathbf{C}_v = \int_0^l \mathbf{N}^{vT} \mathbf{N}^v ds; \quad \mathbf{C}_w = \int_0^l \mathbf{N}^{wT} \mathbf{N}^w ds \\
\mathbf{C}_\theta &= \int_0^l \mathbf{N}^{\theta T} \mathbf{N}^\theta ds; \quad \mathbf{C}_\phi = \int_0^l \mathbf{N}^{\phi T} \mathbf{N}^\phi ds; \quad \mathbf{C}_\psi = \int_0^l \mathbf{N}^{\psi T} \mathbf{N}^\psi ds \\
\mathbf{k}_{e1} &= \int_0^l EA(s) \mathbf{N}^{u,T} \mathbf{N}^u ds \\
\mathbf{k}_{e2} &= \int_0^l EI_z(s) \mathbf{N}^{v,T} \mathbf{N}^v ds \\
\mathbf{k}_{e3} &= \int_0^l EI_y(s) \mathbf{N}^{w,T} \mathbf{N}^w ds \\
\mathbf{k}_{e4} &= \int_0^l GJ(s) \mathbf{N}^{\theta,T} \mathbf{N}^\theta ds \\
\mathbf{k}_{c1} &= \int_0^l F(s) \mathbf{N}^{v,T} \mathbf{N}^v ds \\
\mathbf{k}_{c2} &= \int_0^l F(s) \mathbf{N}^{w,T} \mathbf{N}^w ds \\
\mathbf{k}_\Omega &= \mathbf{N}^T \mathbf{R} \boldsymbol{\Omega}^T \boldsymbol{\Omega} \mathbf{R}^T \mathbf{N}
\end{aligned} \tag{7.3}$$

where $\rho A(s)$, $EA(s)$, $A(s)$, $EI_y(s)$, $EI_z(s)$, $GJ(s)$ and $F_c(s)$ are the tapered-swept variations of mass density, elastic modulus, cross-section area, moments of inertia around y, moment of inertia around z, polar moment of inertia around x, and generalized axial (centrifugal) force, respectively. The matrix \mathbf{R} is the transformation matrix of size 3x3 composed by the direction cosines tensor, \mathbf{N} is the Hermite cubic shape functions matrix of size 12x12 contemplating twelve degrees of freedom (six for inboard and six for outboard ends). Spinning matrix is defined as $\boldsymbol{\Omega} = \boldsymbol{\Omega}(t)$ [0,0,1; 0, 0, 0; -1, 0, 0]. Similarly, \mathbf{N}^u , \mathbf{N}^v , \mathbf{N}^w , \mathbf{N}^θ , \mathbf{N}^ϕ and \mathbf{N}^ψ are the shape function vectors for longitudinal along x, transverse across y, transverse across z, torsion around x, rotation around y, and rotation around z, respectively. With the same token, c_u , c_v , c_w , c_θ , c_ϕ and c_ψ are damping coefficients for u_x , v_x , w_x , θ_x , ϕ_x , ψ_x directions, respectively. The gyroscopic system as Equation (7.1) is composed by two real nonsingular, one symmetric, and one skew symmetric matrices. For such systems, Meirovitch [Meirovitch 1974] developed a numerical solution where the eigenvalue problem is transformed and expanded into one

composed by real symmetric matrices by means of state-vector principles and orthogonality relations. Due to the non-classical damping nature of Equation (7.1), but most importantly, the incidence of yaw (gyroscope) motion of the turbine that affects the spinning finite element a calculation of complex-mode-shape pairs is inevitable. The eigensolution of the state-space system of the form:

$$\mathbf{A} = \begin{bmatrix} \mathbf{G}_B + \mathbf{C}_B & \mathbf{M}_B \\ -\mathbf{M}_B & \mathbf{0} \end{bmatrix} \quad \mathbf{B} = \begin{bmatrix} \mathbf{K}_B & \mathbf{0} \\ \mathbf{0} & \mathbf{M}_B \end{bmatrix} \quad (7.4)$$

where \mathbf{A} is skew-symmetric and \mathbf{B} is symmetric, leads to reduce the eigenvalue problem to a standard form in terms of two real symmetric matrices for both the real and imaginary parts of the eigenvectors. Still, the problem of modal truncation of the eigensolution of Equation (7.4) prevents a direct computation of real modes from complex eigenvectors. It is imperative to compare and calibrate the SFE through an experimental data set in order to gain, with a level of acceptance, the correct characterization of the dynamic loads on the wind turbine model. This updating is also necessary to reveal the presence of changes in the blade over time that might be indicative of damage. Hence, the complex form of the modal assurance criterion (MAC) is used in the objective function for the model updating step of this study.

7.5 Complex-Conjugate Modal Assurance Criterion (MAC)

The aim of the SFE model updating is to correctly identify the geometric/inertial properties that would feasibly reproduce the measured data, interpreted the latter as the correct layout from where comparisons will be driven by several SFE models. An objective function or energy absorption $E(s)$ is computed to calculate the distance between measured ERA natural frequencies and mode shapes, from one side, and predicted SFE natural frequencies and mode shapes, from the other. Namely [Marwala 2010]:

$$E(s) = \sum_{i=1}^{n_m} \gamma_i \left(\frac{\omega_i^{ERA} - \omega_i^{SFE}}{\omega_i^{ERA}} \right)^2 + \beta \sum_{i=1}^{n_m} \left(1 - \text{diag}(\text{MAC}(\boldsymbol{\varphi}_i^{ERA}, \boldsymbol{\varphi}_i^{SFE})) \right) \quad (7.5)$$

where ω_i is the i th natural frequency, $\boldsymbol{\varphi}_i$ is the i th mode shape vector, n_m is the number of modes, γ_i is a weighting factor that measures the relative distance between the measured ERA frequency for the i th mode, and the estimated SFE frequency for the same mode. Parameter β is the weighting function that pairs ERA and SFE modes. MAC is the Modal Assurance Criterion acting is a measure of the least-squares deviation of the computed mode shapes from the measured mode shapes in a straight-line correlation. The MAC between two complex-conjugate mode shapes is defined as:

$$\text{MAC}(\boldsymbol{\varphi}_i^{ERA}, \boldsymbol{\varphi}_j^{SFE}) = \frac{|\boldsymbol{\varphi}_i^{ERA*T} \boldsymbol{\varphi}_j^{SFE}|^2}{|\boldsymbol{\varphi}_i^{ERA*T} \boldsymbol{\varphi}_i^{ERA}| |\boldsymbol{\varphi}_j^{SFE*T} \boldsymbol{\varphi}_j^{SFE}|} \quad (7.6)$$

where the superscript $*$ stands for complex-conjugate mode shape [*ibid.* Vacher *et al.*, 2010]. Parameter β , closely associated with MAC ratio, is a correction coefficient that compensates for the maximum distortion between the measured ERA modes and the worst conditional SFE modes accepted by the cooling schedule of the SA algorithm employed. In other words, β measures the range of possible mode shape predictions and scales down accordingly to ensure the energy absorption at iteration stage s is consistently lower than an acceptable probability of occurrence. Both γ_i and β are critical to ensure “thermodynamic” stability, numerical convergence, and iteration speed within the selected optimization solver. The weighting factor γ_i accounts for the vague estimates and numerical impairments that the ERA algorithm tends to produce for high frequencies and their related shape modes. Thus, γ_i penalizes for high frequencies and versus low frequencies. When the spinning velocity Ω is fixed for any SFE realization, a narrow set of predictions can be subscribed to reach the maximum target peak. This means γ_i and β can become less penalizing, resulting in an alleviation of the convergence process. A

similar treatment of the MAC index value can done for the case of CS-SSI-LPTV simply by exchanging the ERA superscripts of Equation (7.5) and Equation (7.6) with the CS-SSI-LPTV ones. Once the MAC metric has been established to conjure both SFE and ERA – or CS-SSI-LPTV – data inflows, it is convenient now to introduce the principles of adaptive simulated annealing for wind turbine blades.

7.6 Adaptive Simulated Annealing (ASA)

A new adaptive numerical technique is proposed in the present paper aiming to withstand an efficient SA (potentially parallel) implementation dedicated to HAWT blade models with tapered-swept variation of order n_t . The algorithm is designed with two parts: (1) an adaptive version of the traditional SA scheme validated for high cooling temperature stages ($T_s > 0.1$); and (2) a speculative solution for low cooling temperatures ($T_s < 0.1$), where independent random assignments to different geometric/inertial conditions are established resulting in a more efficient convergence as the spinning constraints are imposed to the model (*i.e.*, constant spinning velocity). This is how a number of previously accepted models, for a given temperature intensity, offer a reference point to fix the upcoming predictions in normal distribution, by generating a previous knowledge of the spinning modulation of the SFE model. This numerical optimization is typically called Adaptive Simulated Annealing (ASA) and previous efforts have been made to adapt suitable algorithms for rotating structures [Ziaei-Rad 2005]. Also, hybrid Monte-Carlo algorithms have been proposed to speed up convergence for multivariate target functions [Salazar and Toral 2008], such is the case of the present study.

The temperature and the step size is adjusted such a way that the sampling happens in a coarse – initial – search space resolution for the early stages, validated against defective, ill-conditioned, or corrupted rotor blade model characterization. Here, the spinning velocity of the model, Ω , is treated as variable and a uniform distribution within the valid range for this parameter is considered in order to catch a first round of achievable realizations set. This accommodation will define the subsequent optimized paths at $T_s <$

0.1. Once this temperature is reached, a refined model is adopted, reducing the operating window for the n -dimensional normal distribution once the spinning velocity is fixed. Simultaneously, the search path progresses towards the maximum peak. The approach also makes use of thermodynamic principles by adjusting and reducing the temperature trot according to a minimum energy absorption rule between two consecutive stages [Metropolis *et al.* 1953]. The objective here is to find a method or rule to get the lowest energy state from all possible, stable, and well conditioned SFE models. The temperature is then lowered little by little until freeze conditions appear and no new solutions are generated. The annealing process, properly implemented, assures to pick the global minimum from a large number of possible SFE models constrained, to a spinning velocity Ω that should match the one identified from the experiments. This assurance is obtained only if the maximum temperature is sufficiently high and the cooling schedule is done sufficiently low. Otherwise, the solver will freeze into a meta-stable state rather than into a minimum energy state. Hence, if the lowering of the temperature is decreased slowly enough, the solid can reach thermal equilibrium at each temperature.

To simulate annealing it is necessary to consider the underlying thermodynamics behind the process. The ASA engine implemented here for wind turbine blades with complex geometry utilizes the Boltzmann equation principle to describe thermal equilibrium between one modal realization and another [Levin *et al.* 1998]. The state is described as a modal solution from a set of all possible SFE model outcomes. Each acceptable model must be well conditioned by assuring a minimal (observable) gap among frequencies, numerical stability on damped-gyroscopic system eigenrealizations, and modal property feasibility considerations.

Each cooling temperature state T_s absorbs an energy $E(T_s) = E(s)$ associated with it according to an objective function that computes the distance or state s between measured natural frequencies and mode shapes resolved from either ERA or CS-SSI-LPTV experimental data, from one side, and frequencies and mode shapes obtained from the SFE model, on the other. The probability of the system being in a state $s \in S$ is computed

as [Levin and Lieven 1998] $p(s) = e^{-E(s)/kT_s} / \sum_{w \in S} e^{-E(w)/kT_w}$ where S is the space of all possible cooling energy outcomes and k is the Boltzmann constant. To account for the way in which the model reaches a thermal equilibrium, a nearby randomly chosen state s_{new} with a corresponding energy $E(s_{new})$ is perturbed. If the energy emitted decreases, the new stage is accepted otherwise an acceptance probability is computed to match Boltzmann distribution [Kirkpatrick *et al.* 1983] and reach thermal equilibrium:

$$p(s) = e^{-\{E(s_{new}) - E(s_{old})\}/kT_s} = e^{-\Delta E(s)/kT_s} \quad (7.7)$$

Here, the state of the system is established as the input parameters, temperature T_s operates as a convergence control, and the energy $E(s)$ function is managed as the objective function. The lowest energy state at stable freezing temperature translates to a global minimum and the input parameters associated with it represent the update set of tapered-swept geometric/inertial properties of the studied rotor blade. Transition from an old state to a new one depends on either the uniform ($T_s > 0.1$) or normal ($T_s < 0.1$, $\Omega = \text{cst}$) random neighbor functions and a cooling schedule (Figure 7.2).

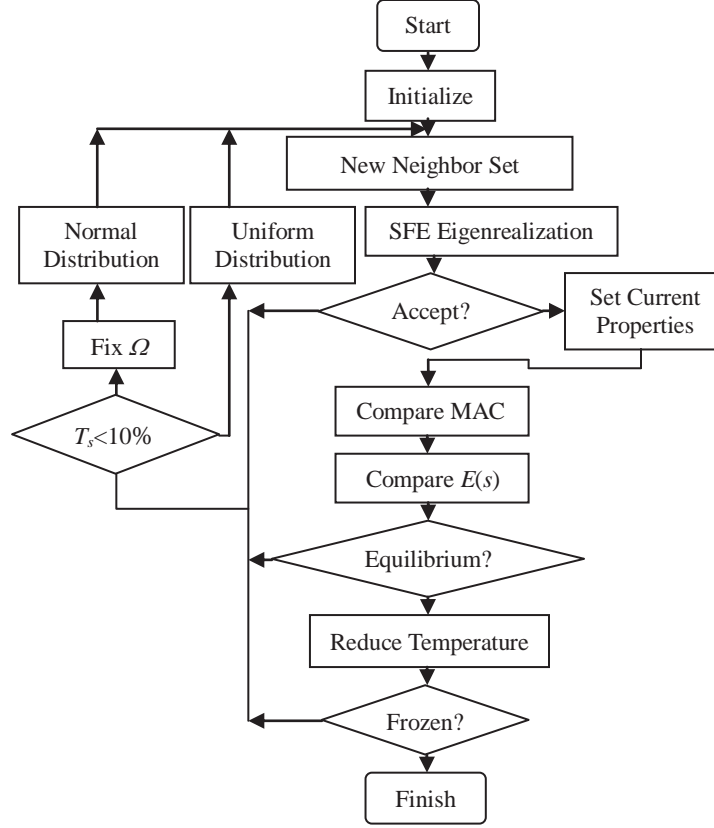


Figure 7.2. Adaptive Simulated Annealing (ASA) flowchart.

This cooling schedule consists of starting at an initial temperature $T_0 = 1$ and letting the minimum energy absorption algorithm run for n_s successful steps. The minimum energy depends on the progressing computed state values for MAC and the ratio between either ERA and SFE, or CS-SSI-LPTV and SFE frequencies, as described in Equation (7.7). A thermal equilibrium is established at passing n_s steps and the new equilibrium temperature is reduced by a schedule $T_{s+1} = T_s/(1+\sigma)$ where σ is the cooling rate. The algorithm terminates when very few moves are accepted at a stabilized freezing temperature. For this study n_s is computed as $n_s = 100*n_d$ where $n_d = 13$ is the total dimension of the geometric/inertial set, namely: ρA_0 , ρA_l , ρI_{p0} , ρI_{pl} , EA_0 , EA_l , EI_{y0} , EI_{yl} , EI_{z0} , EI_{zl} , GJ_0 , GJ_l , and Ω geometric/inertial properties. Here ρ is material density, A the area of the cross section, I_p the mass polar moment of inertia, I_y and I_z moments of inertia in two orthogonal planes, J the area polar moment of inertia, E Young modulus and G shear modulus. Subscripts 0 and l stand for inboard end and outboard

end, respectively. It is discussed briefly an example of the ASA engine proposed in this paper, now applied to a small wind turbine system instrumented for CS-SSI-LPTV analysis and modeled via SFE method.

7.7 Numerical Simulation

A representative numerical wind turbine model composed of 12 DOF's is implemented in this study (see Figure 7.3) and employed for both reconstruction of cyclo-stationary based output data and model updating. It has a starting wind speed of 3 RPM and cut-in wind speed 300 RPM. The blade material is modeled as a homogeneous composite and pultruded fiber glass E-Glass with standard traits $E = 1,9305.3196$ MPa, $\rho = 1826.873$ kg/m³, and $\nu = 0.33$. For simplicity, blade is projected with constant cross section all along with geometric properties $A_0=A_l = 6.392 \times 10^{-4}$ m², $I_{y0} = I_{yl} = 5.453 \times 10^{-9}$ m⁴, $I_{z0} = I_{zl} = 3.637 \times 10^{-7}$ m⁴, $J_0 = J_l = 3.691 \times 10^{-7}$ m⁴, and $I_{p0} = I_{pl} = 1.865 \times 10^{-5}$ m². Maximum design wind speed is 54 m/s and rotor blade specimen consist of a 1.25 m. diameter. Cross-section profile is a recreation of a SH3045 type airfoil with no pitch nor is yaw (free) control available for the system.

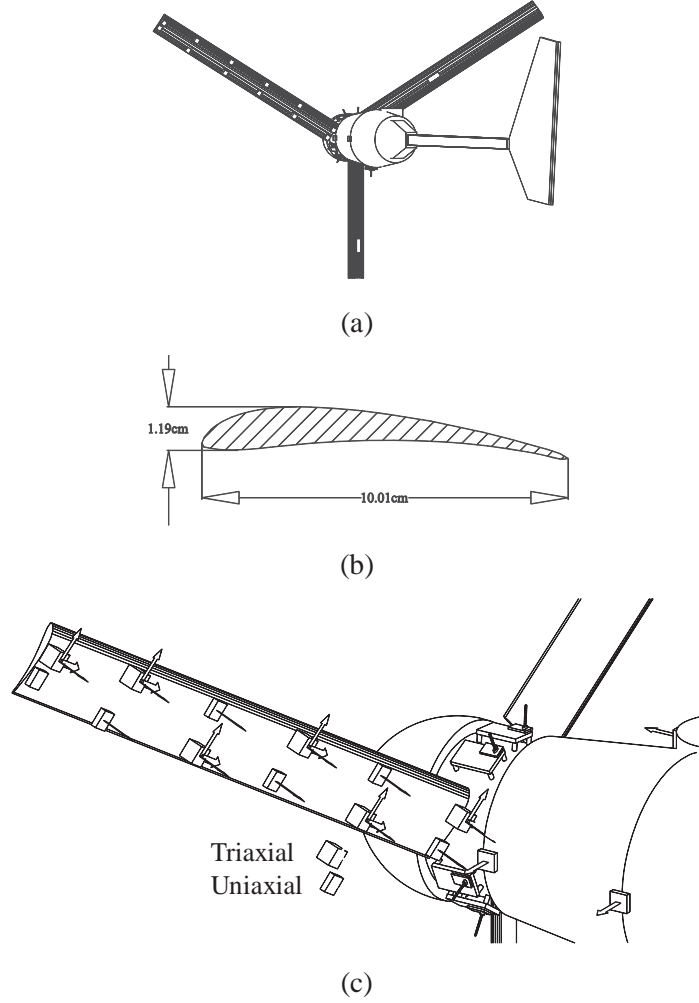


Figure 7.3. Overview of wind turbine BWC XL.1 (a) power generator, (b) blade airfoil cross section SH3045 profile type, (c) sensors deployment and instrumentation.

7.8 Results

Results of the model updating process applied to the numerically generated blade vibrational data under a range of spinning velocities (*i.e.*, $\Omega = 0, 50, 150$, and 300 RPM) are presented in this section. Figure 7.4 illustrates an example of the Modal Assurance Criterion (MAC) principle applied to compare complex-conjugate modes between the measured CS-SSI-LPTV algorithm and the predicted SFE model scheduled for updating. In Figure 7.4 MAC values for 6 identified modes from the CS-SSI-LPTV and 6 SFE modes are compared (left-to-right) as the adaptive simulated annealing algorithm progresses to its freezing temperature. It can be seen that MAC matrix tends towards a

unitary-diagonal correlation representative of the updated real modes at the end of the cooling schedule. This trend can be seen to be true for the investigated range of spinning velocities presented in Figure 7.4(a-d). It is observed that the MAC coefficient tends to converge more rapidly for data sets with higher values of Ω , with the disadvantage being that the accuracy of time-history prediction made with the identified model seems to decrease as Ω increases. The reason likely being that modes tend to stiffen together in a similar wave form towards a common shape alignment as the rotational speed increases, producing shadowing and overlapping of modes. Alternatively, convergence is reached more slowly as the system tends to be less rotating (pseudo-static). In these cases the energy absorption tends to become more diffuse as the neighborhood-phase space solution is broader (Figure 7.5). Figure 7.5(b) depicts the stiffening phenomenon occurring at high speed rotations. One of the axes is related to a new update of the model whereas the complementary axis is in relation to an old version. The distance between the two of them defines the relative energy absorption at the decremented cooling step, according to Equation (7.5). One of the axes tests one updated model – first state – at a spinning velocity Ω_i , while the other axis is a subsequent model case – second state – with spinning velocity Ω_j . Here, the computation of a new update of the model from an old version, according to a randomized generator rule (*i.e.*, uniform distribution), takes the previous solution as input and gives a valid consecutive solution (*i.e.*, some point in the solution space) as output with a consistent lower energy rule because of the alignment of modes, as exemplified in Figure 7.6. Therefore, Boltzman differential energy tends to be more stable for higher Ω during the cooling-schedule. Dominant frequencies depicted in Figure 7.6(d) do not reach a fixed value because of the speed of the numerical convergence at high spinning velocities. In this case, the number of iterations is reduced to less than ten, so the algorithm has limited time to stabilize the trend of the frequencies, as energy dissipation decreases very fast because of the alignment of modes at high spinning rates.

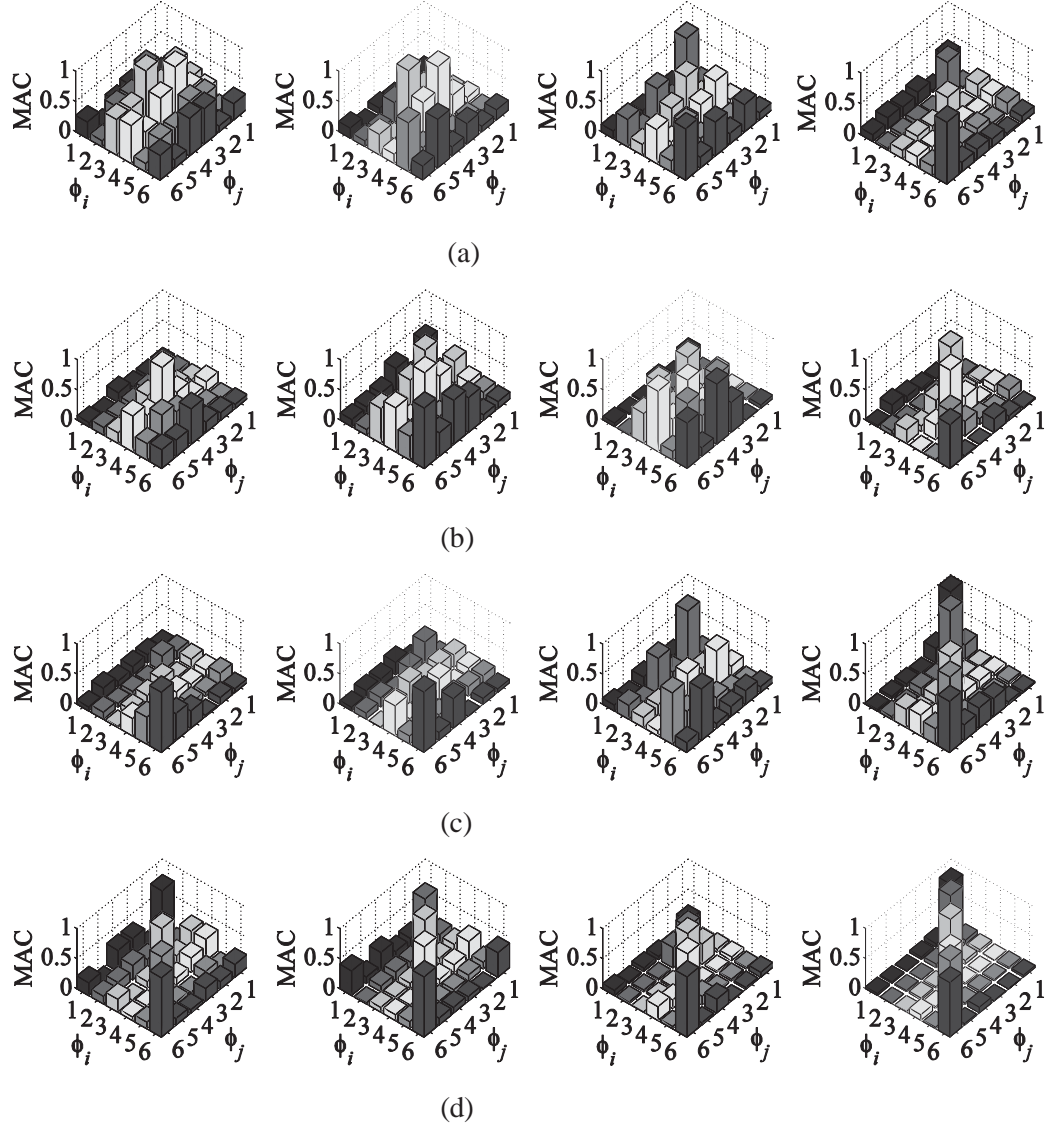


Figure 7.4. Progression of Modal Assurance Criterion (MAC) for (left to right) initial $T_s = 1$, $1/3T_s$, $2/3T_s$, and T_s obtained through the ASA engine using CS-SSI-LPTV algorithm and SFE model, applied to four different cases: (a) $\Omega = 0$ RPM (final $T_s = 0.0015$), (b) $\Omega = 50$ RPM (final $T_s = 0.0181$), (c) $\Omega = 150$ RPM (final $T_s = 0.0037$), (d) $\Omega = 300$ RPM (final $T_s = 0.0196$).

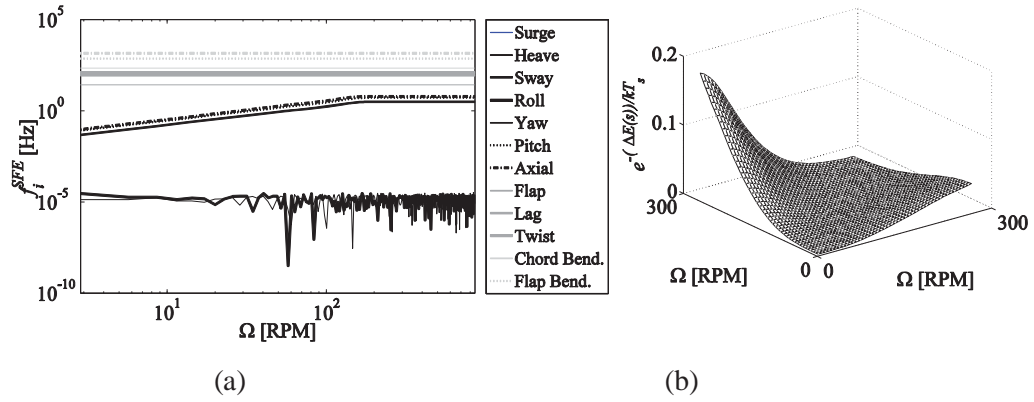


Figure 7.5. (a) Spinning velocity Ω vs frequencies f_i^{SFE} of the updated model. (b) Energy absorption probability for different spinning velocities Ω produced by neighborhood-phase realizations of the updating model. The energy absorption is smaller - therefore convergence faster - for higher speeds.

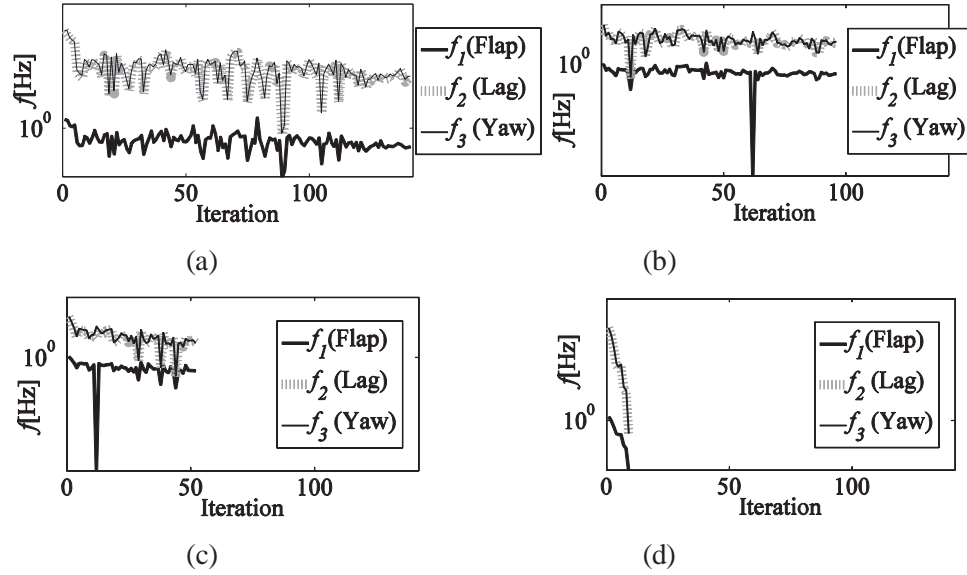


Figure 7.6. Update progression of three dominant SFE model frequencies obtained with the ASA engine using CS-SSI-LPTV algorithm, applied to four different cases: (a) $\Omega = 0$ RPM (final $T_s = 0.0015$), (b) $\Omega = 50$ RPM (final $T_s = 0.0181$), (c) $\Omega = 150$ RPM (final $T_s = 0.0037$), (d) $\Omega = 300$ RPM (final $T_s = 0.0196$).

Table 7.1 summarizes a comparison between the exact and final updated values of the target geometric/inertial parameters for the same model running at four different spinning velocities. In general, the identification of model parameters is better at low frequencies. Similarly, Figure 7.7 illustrates the statistical distribution of the identified parametrization values for the same models through many realizations of the ASA algorithm. The default random parametrization function generates a new set of geometric/inertial values which slightly differs from the input vector in one adjacent neighborhood-phase space. The sparsity norm (*i.e.*, uniform distribution) generates a neighbor random integer that is dejected in order to smooth the step transition, then added to the old assigned set of target parameters aiming to obtain the new neighbor set.

Table 7.1. Comparison of exact and final predictions of target geometric/inertial parameters obtained with the ASA engine using CS-SSI-LPTV algorithm and SFE model, by means of MAC complex-conjugate mode shapes applied to four different cases: (a) $\Omega = 0$ RPM (final $T_s = 0.0015$), (b) $\Omega = 50$ RPM (final $T_s = 0.0181$), (c) $\Omega = 150$ RPM (final $T_s = 0.0037$), (d) $\Omega = 300$ RPM (final $T_s = 0.0196$).

Target	Exact	$\Omega = 0$ RPM	$\Omega = 50$ RPM	$\Omega = 150$ RPM	$\Omega = 300$ RPM
Ω [RPM]		0.08	48.322	145.226	290.846
ρA_0 [kg/m]	1.167	1.147	1.080	1.261	1.585
ρA_l [kg/m]	1.167	1.150	1.019	1.281	1.619
ρI_{p0} [kg ² /m]	0.034	0.031	0.029	0.029	0.025
ρI_{pl} [kg ² /m]	0.034	0.032	0.029	0.024	0.019
EA_0 [N]	1.234e+007	1.255e+007	1.270e+006	1.497e+007	1.203e+007
EA_l [N]	1.234e+007	1.261e+007	1.304e+007	1.403e+007	1.195e+007
EI_{y0} [N*m ²]	105.271	100.707	99.144	120.492	148.484
EI_{yl} [N*m ²]	105.271	101.074	100.529	118.916	153.2504
EI_{z0} [N*m ²]	7.021e+003	6.638e+003	6.624e+003	6.558e+003	7.669e+003
EI_{zl} [N*m ²]	7.021e+003	6.896e+003	6.650e+003	6.534e+003	7.780e+003
GJ_0 [N*m ²]	2.678e+003	2.519e+003	2.263e+003	2.764e+003	2.801e+003
GJ_l [N*m ²]	2.678e+003	2.409e+003	2.236e+003	2.707e+003	2.786e+003

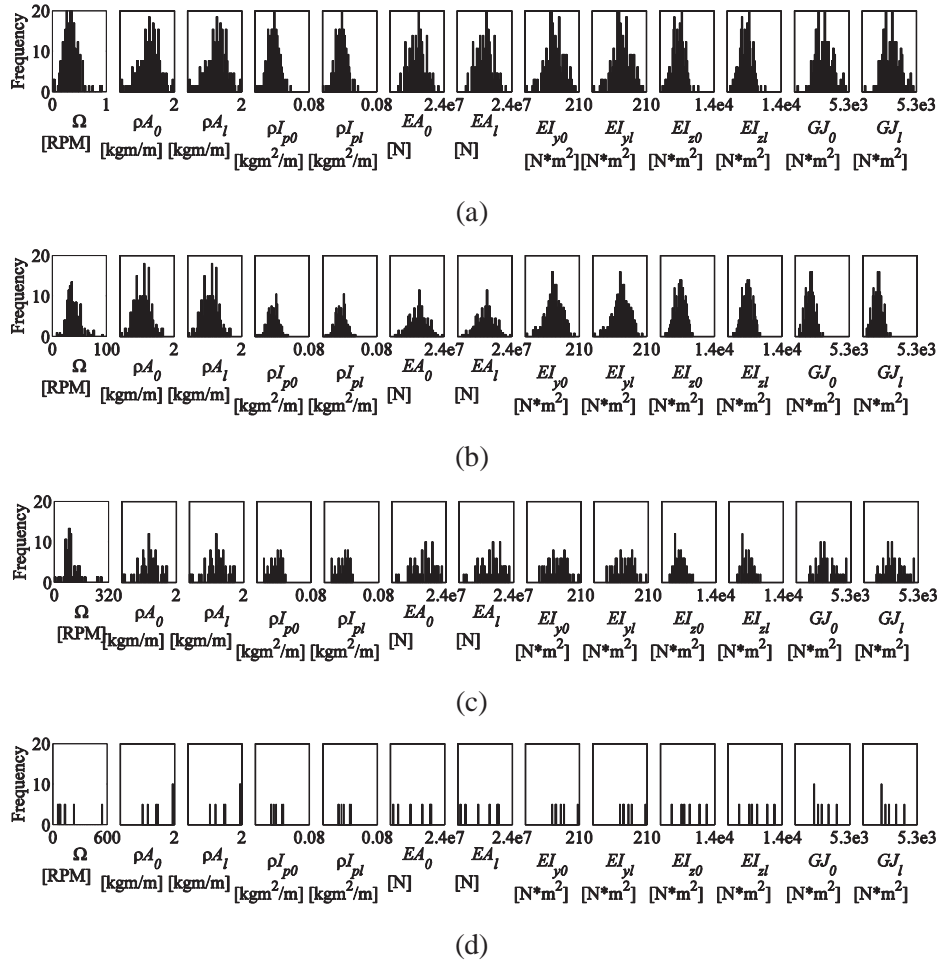


Figure 7.7. Statistical distribution of target geometric/inertial parameters obtained with the ASA engine using CS-SSI-LPTV algorithm and SFE model, by means of MAC complex-conjugate mode shapes applied to four different cases: (a) $\Omega = 0$ RPM (final $T_s = 0.0015$), (b) $\Omega = 50$ RPM (final $T_s = 0.0181$), (c) $\Omega = 150$ RPM (final $T_s = 0.0037$), (d) $\Omega = 300$ RPM (final $T_s = 0.0196$).

As previously commented, the probability distribution of the target parametrization tends to be wider as Ω increases. This implies that while the updating convergence is fast, the accuracy is denigrated in the same proportion. The orthogonality condition of the mode shapes fits best when dealing with complex-conjugate eigenvectors rather than physical mode shapes. Conversion to physical shapes is not necessary during the ASA model-updating process, because the MAC indicator can operate in the complex-numbers vectors domain. Disturbances identified among the experimental (CS-SSI-LPTV) and

theoretical (SFE) complex-conjugate mode shapes are the result of errors produced by – or as consequence of – the CS-SSI-LPTV identification algorithm and measurement data, as depicted in Figure 7.8. Examples of sources of error are noise in the output signals, dependent – ill conditioned – output channels, low frequency content, waveform, sampling size, and close proximity among frequencies. For comparison purposes, Figure 7.9 depicts a set of transformed physical modes from dominant modes shapes at $\Omega = 0$ RPM (final $T_s = 0.0015$), comparing source, CS-SSI-LPTV – Figure 7.9(a), and target, SFE – Figure 7.9(b), transformed real-modes at the end of the ASA cycle where T_s is reached. Figure 7.9(c) depicts the evolution of the mode shapes over one realization of the ASA algorithm in order to verify its random nature.

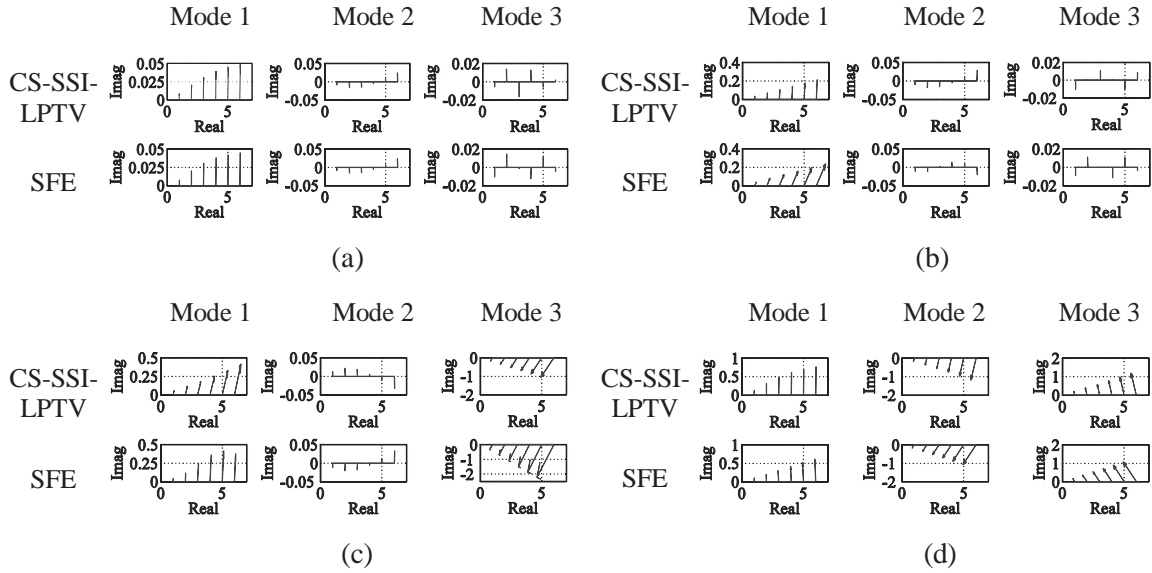


Figure 7.8. Measured (CS-SSI-LPTV) vs predicted (SFE) complex mode shapes at minimum energy absorption obtained with the ASA engine by means of MAC complex-conjugate mode shapes applied to four different cases: (a) $\Omega = 0$ RPM (final $T_s = 0.0015$), (b) $\Omega = 50$ RPM (final $T_s = 0.0181$), (c) $\Omega = 150$ RPM (final $T_s = 0.0037$), (d) $\Omega = 300$ RPM (final $T_s = 0.0196$).

It was found that the ASA algorithm, optimized for constant spinning velocity, accelerated the numerical convergence by up to 40% ($T_s < 0.1$, $\Omega = \text{cst}$), compared to the uniform distribution randomization for ($T_s > 0.1$, $\Omega = \text{variable}$). Random and bias-based errors can be carried out by both CS-SSI-LPTV and SFE in terms of numerical

truncation, non-linearity produced by the damped gyroscopic-effects, theoretical approximations of the SFE model, floating point errors due to the concatenated – reverse operation – iterations of the system (typically expressed as the pseudo-inversion of a $2n \times 2n$ state-space matrix, where n is the order of the system), the existence of unstable poles, no positive definite covariance matrices and ill-conditioned finite models, are all possible source of numerical errors in the algorithm. Increasing the number of observer Markov chains employed for the identification of measured output channels, reducing signal noise and minimizing damping (energy absorption), all may produce more accurate CS-SSI-LPTV. This effort will impact the efficiency of the ASA engine in terms of convergence speed, a faster cooling schedule, a smaller margin in the energy acceptance probability, minimum energy dissipation, and subsequently, higher marks on the MAC coefficient. Figure 7.10 depicts the progression of energy prediction error and acceptance probability for the same cases studied above.

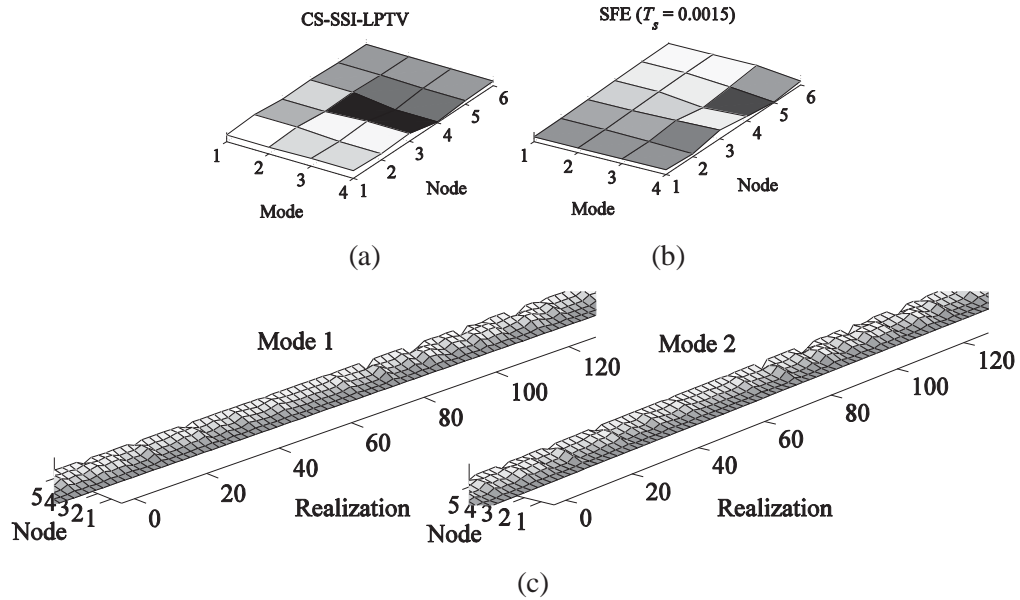


Figure 7.9. Transformation from complex-numbers to physical counterparts of the first four dominant modes shapes for (a) CS-SSI-LPTV and (b) SFE. (c) Update progression of two dominant SFE physical modes. $\Omega = 0$ RPM (final $T_s = 0.0015$).

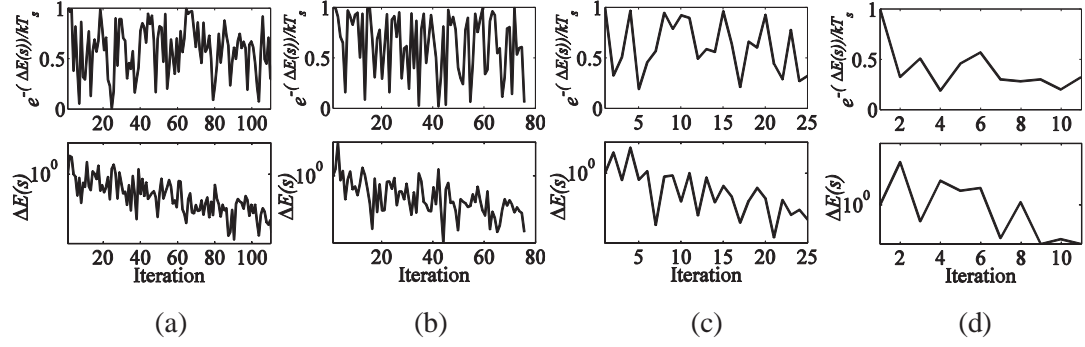


Figure 7.10. Progression of energy acceptance probability and its corresponding energy error obtained with the ASA engine using CS-SSI-LPTV algorithm and SFE, applied to four different cases: (a) $\Omega = 0$ RPM (final $T_s = 0.0015$), (b) $\Omega = 50$ RPM (final $T_s = 0.0181$), (c) $\Omega = 150$ RPM (final $T_s = 0.0037$), (d) $\Omega = 300$ RPM (final $T_s = 0.0196$).

7.9 Discussion

If numerical truncation occurs, numerical overflow exists, or out-of-memory errors occur, one possibility is to switch output types using either acceleration, velocity, or displacement channels (an admittedly difficult tactic in experimental studies). A good identification can be achieved with a cyclo-stationary noise content lower than 1% of the maximum modal amplitude. Another possibility is to escalate or filter down/up signals to increase the CS-SSI-LPTV identification observability. In general terms, and given the stochastic nature of the CS-SSI-LPTV method, randomized outputs are more proclive to improve outcomes in the updated model. Simultaneously, SFE models with uncoupled modes (axial, flexural, and torsional) are more likely to correlate with their CS-SSI-LPTV counterparts because of their orthogonality composure against the coupled models (axial-flexural-torsional coupling). The complex-conjugate adjustment process using parity modes is less tedious for independent (uncoupled) mechanical elements given that coupled damped-gyroscopic SFE models are more absorbent energy, therefore the energy acceptance probability has to exceed during the ASA cooling schedule algorithm. Another source of perturbation comes from the phase angle of the complex-conjugate modes while comparing MAC coefficients, an indicator of the computational effort invested to achieve an acceptable confidence ratio while controlling the Boltzman temperature-cooling schedule variation. A drawback in the damped-gyroscopic SFE

implemented in this study is that the eigenvalue problem consists of two real nonsingular matrices, one symmetric (mass and stiffness matrices) and the other skew symmetric (damped-gyroscopic matrix), which can present computational issues. Reducing this eigenvalue problem to a standard form (*i.e.*, two real symmetric matrices) by reassembling the eigenvalue problem of a non-rotating structure at each ASA iteration reduces the risk of falling into indeterminacy for ill-conditioned cases while testing adjacent geometric/inertial sets. For example, high damping ratios matching high spinning velocities will produce shadowing effects on the complex eigenvalues and eigenvectors. For this case, the ASA engine is programmed to dispose of such indeterminate and ill-conditioned cases. In practical terms, variations of the rotation speed are unpredictable, but must be held as steady as possible in order to reduce potential numerical issues. For this project, only constant rotational speed was considered. To work in the current framework, spinning velocity changes should be smooth and gradual during identification and within the SFE model. Any abrupt jumps in the spinning velocity time-history will lead to errors. There will be some extra poles during the identification process due to the spinning rotation (no structural) action, self-evident when dismantling the stochastic output signals via Singular Value Decomposition. Similarly, rotational frequencies alien to the structure may be computed during the inverse method of the complex-conjugate eigen-realization procedure. The MAC index coefficient comparison algorithm should discard this contribution as a thermodynamic energy argument. The ASA numerical engine presented here removes this information by establishing Ω as an online random variable. For stochastic output signals it may be feasible to repeat the simulation with the exact conditions (*i.e.*, order of the system) and expect similar outcomes, but not exactly as obtained previously.

7.10 Conclusions

The Adapted Simulated Annealing (ASA) proposed in the present study was applied to update a Spinning Finite Element (SFE) model via numerical data by means of the Cyclo-Stationary Stochastic Subspace ID via Linear Parameter Time-Varying Method (CS-SSI-LPTV) for Horizontal-Axis Wind Turbines (HAWT) model updating. Different updating

geometric/inertial parameter sets were selected for the analysis of a wind turbine blade with constant cross-section variations. The numerical example presented suggested that the objective function treated as non-classical damped- gyroscopic system has many local minima and tends to be sensitive to the assigned value of spinning velocity especially high rotating speeds. The choice of parameter sets for model updating, assurance of a clean and independent set of outputs for system identification, sustained spinning velocity, and assignation of proper damping ratios– structural energy absorption – are of extreme importance for an efficient ASA model update. Numerical instability was recognized for a segment of both potential eigen-solutions of the gyroscopic system and stochastic identification. SFE model was acceptably updated and final solution showed improved correlation for dominant frequencies and mode shapes, suggesting that the calibrated SFE actually represents the physical structural used in the numerical algorithm. Having successfully reached the goals of the Thesis project, it is time now to draw some observations on future work, as well as final remarks and conclusions in the next Chapter 8.

Chapter 8. Final Remarks

8.1 Future Work

Some of the topics that are pending for future work are the design, analysis, and optimization of special and complex multi-body dynamic structures, near-collapse characterization, and development of dependable/disposable long-range wireless sensors for long-lasting deployments. In the long run, it is advisable to venture into the analysis and design of expert systems for near-collapse scenarios of overall wind-harvesting structures, human decision making and automated control; all applied in growing research areas, that is the case of Structural Health Monitoring (SHM). Similarly, to explore new energy-harvesting avenues, that is the case of wind-pyroelectric and wind-piezoelectric technologies.

8.2 Summary

Great technological expectation and outstanding commercial penetration has shown the so-called Horizontal-Axis Wind Turbines (HAWT) technologies. Given its great acceptance, size evolution of wind turbines over time has increased exponentially. However, safety and economical concerns have emerged because of the newly design tendencies for massive scale wind-turbine structures presenting high slenderness ratios and complex shapes, typically located in remote areas (e.g. offshore wind farms). In this regard, the Thesis project was focused to tackle down some aspects of the safety operation that requires not only having first-hand information regarding actual structural dynamic conditions under aerodynamic loading, but also a deep understanding of the environmental factors in which these multi-body rotating structures operate. Given the cyclo-stochastic patterns of the wind loading exerting pressure on a HAWT, a probabilistic framework seemed to be appropriate to characterize the risk of failure in terms of resistance and serviceability conditions, at any given time. Furthermore, sources of uncertainty such as material imperfections, buffeting, flutter, aeroelastic damping, turbulence, and most importantly, gyroscopic effects, have pleaded for the use of a more

sophisticated mathematical framework that could properly handle all these sources of indetermination. The attainable modeling complexity that emerged because of these characterizations demanded a data-driven experimental validation methodology to calibrate and corroborate the mathematical model.

For this aim, System Identification (SI) techniques were implemented to establish numerical methods appropriated for stationary, deterministic, and data-driven numerical schemes, capable of predicting actual dynamic states (eigen-realizations) of traditional time-invariant dynamic systems. Consequently, it was proposed a modified data-driven SI metric based on the so-called Subspace Realization Theory, an approach now adapted for stochastic non-stationary and time-varying systems, as is the case of HAWT's complex aerodynamics. Simultaneously, it was explored the characterization of the turbine loading and response envelopes for critical failure modes of the structural components the wind turbine is made of. In the end, both aerodynamic framework (theoretical model) and system identification (experimental model) merged in a numerical engine formulated as a search algorithm for model updating, also known as Simulated Annealing (SA) process. This iterative engine is founded on a set of function minimizations computed by a metric called Modal Assurance Criterion (MAC) in order to optimize the model in study. To date, little progress has been done in this direction, and as a result, some questions have emerged that should be clarified. As an example, the dismantling or uncoupling of the cyclo-stationary frequencies coming from the wind-turbine gearbox disturbing the resistance of the rotor blades in terms of structural fatigue and exhaustion. Another example is the optimization of the ratio between maximum power generation and maximum wind loading (serviceability and fatigue), in both the along- and across-wind directions. A novel contribution of this investigation advances in these issues is the development of a Spinning Finite Element (SFE) capable of characterize combined gyroscopic effects, torsion coupling, and non-classical damping in a comprehensive theoretical framework sufficiently low order to operate in an autonomous Structural Health Monitoring (SHM) system.

8.3 Conclusions

The present Thesis project delivers a simulation of the structural response of a spinning system composed by three rotor blades with tapered-swept cross-section, under stochastic along-wind distributed load. Results reveal the influence of the gyroscopic action on the structural response above bedplate level (hub elevation). Simulation of the along wind field has been achieved by adopting a rotational sampled spectral density function via spectral analysis in the frequency domain. The generation of an analytical wind turbine model by spinning finite elements has been carried out with the objective of both accuracy and simplicity, compared against alternative methods such as standard finite element models, or time-domain model-updated techniques. It is demonstrated that careful attention should be paid to the eccentricity of rotor components and to the location of the nacelle center of mass. The stress state on the tower bedplate changes considerably due to the moment caused by the equivalent eccentric mass of the rotor blades arrangement, at any moment in time. Gyroscopic torque is generated throughout \mathbf{G}_B influencing the vibration of the upper structure of the wind turbine. It also shown that gyroscopic torque is very small compared to the bending moment caused by the along-wind force, given a low spinning velocity Ω and constant cross-section (less than 5%). On the other hand, higher spinning rates proportionally increment the free-yaw motion. Eigen-frequencies tend to be more unstable for this latter scenario. Similarly, the gyroscopic effects tend to alter the fundamental frequencies and reduce critical speeds of the rotating machinery. Damping has a major role in the amplification otherwise reduction of the gyroscopic effects, specially evaluated in the surroundings of the hub component. Therefore, a proper definition of \mathbf{C}_B is imperative to have a good prediction of the model. For individual, rather combined, tapered-swept blades analysis it has been shown the importance of embracing gyroscopic effects. A combined system composed by rotor blades, shaft, nacelle and tower substructures is less propitious to represent the overall gyroscopic action. Gyroscopic effects are characterized with a non-symmetric equivalent damping matrix and require a non-symmetric numerical eigen-solution to solve for natural frequencies and mode shapes, both expressed in complex-numbers domain. Gyroscopic motion transmits a dynamic torque in the wind turbine tower, not

addressed in the present study. On the other hand, an adverse scenario where coincident turbine yaw rate and rotor speed, large enough to induce high gyroscopic moments, can be placed in one of the following worst scenarios: (a) rapid changes in wind direction related to wind speed increments, (b) presence of turbulent flow, (c) all the above. The maximum base shears and moments are practically unaffected by the gyroscopic moment. Self weight and out-of-plane forces dominate the stress field; so for reliability purposes this effect has no practical consequences, not the case for the risk of having fatigue loads beyond an acceptable level at the bedplate location.

References

1. Chapter 1. Introduction

- Bonger P.M.M. (1991), “*Experimental Validation of a Flexible Wind Turbine Model*”, IEEE Proceedings of the 30th Conference on Decision and Control, England.
- Brownjohn J.M.W., Moyo P., Omenzetter P. and Lu Y. (2003), “*Assessment of Highway Bridge Upgrading by Dynamic Testing and Finite-Element Model Updating*”, Journal of Bridge Engineering, Vol. 8(3), pp. 162-172.
- Chang S.-Y., Brill E.D. and Hopkins L.D. (1982), “*Efficient Random Generation of Feasible Alternatives: A Land Use Example*”, Journal of Regional Science, Vol. 22(3), pp. 303-314.
- Chi-Tsong C. (1998), “*Linear System Theory and Design*”, 3rd Edition, Oxford University Press.
- Imregun M. and Visser W.J. (1991), “*A Review of Model Updating Techniques*”, Shock and Vibration Digest, Vol. 23(1), pp. 9-20.
- Friswell M.I. and Mottershead J.E. (1995), “*Best Practice in Finite Element Model Updating*”, International Forum on Aeroelasticity and Structural Dynamics, Vol. 2, pp. 57-1 – 57-11.
- Juang J. (1994), “*Applied System Identification*”, Prentice Hall PTR, New Jersey.
- Juang J.-N. and Pappa R.S. (1985), “*An Eigensystem Realization Algorithm for Modal Parameter Identification and Model Reduction*”, Journal of Guidance Control and Dynamics, Vol. 8(5), pp. 620-627.
- Levin R.I. and Lieven N.A.J. (1997), “*Dynamic Finite Element Model Updating using Simulated Annealing and Genetic Algorithms*”, SEM-IMAC XV 15th International Modal Analysis Conference, pp. 1195-1201.
- Mares C., Dratz B., Mottershead J.E. and Friswell M.I. (2006), “*Model Updating using Bayesian Estimation*”, Proceedings of the ISMA, pp. 2607-2616.
- Nelder J.A. and Mead R. (1965), “*A Simplex Method for Function Minimization*”, The Computer Journal, Vol. 7, pp. 308-313.

- Novak P. (1994), “*Modeling and Identification of Drive-System Dynamics in a Variable-Speed Wind Turbine*”, IEEE.
- Yang W. (2008), “*Wind Turbine Condition Monitoring and Fault Diagnosis using both Mechanical and Electrical Signatures*”, IEEE International Conference on Advance Intelligent Mechatronics, China.
- Zhang Q.W., Chang T.Y.P. and Chang C.C. (2001), “*Finite Element Model Updating for the Kap Shui Mun Cable-Stayed Bridge*”, Journal of Bridge Engineering, Vol. 6(4), pp. 285-293.

2. Chapter 2. Literature Review

- Ahlström A. (2005), “*Aeroelastic Simulation of Wind Turbine Dynamics*”, Ph.D Thesis in Structural Mechanics, Royal Institute of Technology, KTH, Stockholm, Sweden.
- Anon. (2005), “*Design Codes FAST and ADAMS for Load Calculations of Onshore Wind Turbines*”, Tech. Rep., Germanischer Lloyd Wind Energie GmbH.
- Banerjee J.R. (2000), “*Free Vibration of Centrifugal Stiffened Uniform and Tapered Beams using the Dynamic Stiffness Method*”, Journal of Sound and Vibration, Vol. 233(5), pp. 857–75.
- Baumgart A. (2002), “*A Mathematical Model for Wind Turbine Blades*”, Journal of Sound and Vibration, Vol. 251(1), pp. 1–12.
- Bazoune A., Khulief Y.A. and Stephen N.G. (1999), “*Further Results for Modal Characteristics of Rotating Tapered Timoshenko Beams*”, Journal of Sound and Vibration, Vol. 219, pp. 157–74.
- Bechly M.E., Clausen P.D. (1995), “*Structural Design of a Composite Wind Turbine Blade using Finite Element Analysis*”, Computers & Structures, Vol. 63(3), pp. 639-646.
- Buhl Jr. M.L. (2005), “*The NWTC Design-Codes Suite: An Overview*”, ASME Wind Energy Symposium Technical Papers, 43rd AIAA Aerospace Sciences Meeting and Exhibit, ASME/AIAA, Reno, NV, United States, pp. 156–166.
- Buhl Jr. M. L. (2005), “*NWTC Design Codes (Modes)*”.

- Burton T., Sharpe D., Jenkins N. and Bossanyi E.A. (2001), “*Wind Energy Handbook*”, John Wiley, Chichester, New York.
- Chen X-B., Li J. and Chen J-Y. (2009), “*Wind-Induced Response Analysis of a Wind Turbine Tower including the Blade-Tower Coupling Effect*”, Journal of Zhejiang University, Vol. 10(11), pp. 1573-1580.
- Chung J. and Yoo H.H. (2002), “*Dynamic Analysis of a Rotating Cantilever Beam by using the Finite Element Method*”, Journal of Sound and Vibration, Vol. 249(1), pp. 147–64.
- Craig R.R. Jr. (1981), “*Structural Dynamics*”, John Wiley & Sons, Hoboken, NJ.
- Das D., Sahoo P. and Saha K. (2009), “*Out-of-Plane Free Vibration Analysis of Rotating Tapered Beams in Post-Elastic Regime*”, Materials and Design, Vol. 30, pp. 2875-2894.
- Det Norske Veritas (2001), “*Guidelines for Design of Wind Turbines*”, Copenhagen: Det Norske Veritas.
- Dimitrov N. (2008), “*Methods for Analysing Torsion Stiffness of Wind Turbine Blades*”, Master’s Thesis, Department of Mechanical Engineering, Technical University of Denmark.
- Duque P.N., Van Dam C.P., Huges S.C., “*Navier-Stokes Simulation of the NREL Combined Experiment Rotor*”, ASME Wind Energy Symposium, 1999.
- Fedorov V.A., Dimitrov N., Berggreen C., Krenk S., Branner K. and Berring P. (2010), “*Investigation of Structural Behaviour due to Bend-Twist Couplings in Wind Turbine Blades*”, Dansk Selskab for Vindenergi, Vingstedcentret, Vingsted Skovvej, Bredsten, Denmark.
- Gasch R. and Tvele J. (2002), “*Wind Power Plants*”, Solarpraxis, Berlin.
- Griffin D.A. and Ashwill T.D. (2003), “*Alternative Composite Materials for Megawatt-Scale Wind Turbine Blades: Design Considerations and Recommended Testing*”, Journal of Solar Energy Engineering, Vol. 125 (4), pp. 515.
- Hansen A. (2005), “*ADAMS Overview*” Wind Turbine Design Workshop, National Renewable Energy Laboratory, Boulder, Colorado, pp. 1–10.
- Hansen M.O.L. (2008), “*Aerodynamics of Wind Turbines*”, Earthscan, London; UK.

- Hansen M.O.L., Sørensen J.N., Voutsinas S., Sørensen N. and Madsen H. Aa. (2006), “*State of the Art in Wind Turbine Aerodynamics and Aeroelasticity*”, Progress in Aerospace Sciences, Vol. 42 (4), pp. 285–330.
- Hodges D.H. (2003), “*Geometrically Exact, Intrinsic Theory for Dynamics of Curved and Twisted Anisotropic Beams*”, AIAA Journal, Vol. 41(6), pp. 1131–1137.
- Hodges D.H., Shang X. and Cesnik C.E.S. (1996), “*Finite Element Solution of Nonlinear Intrinsic Equations for Curved Composite Beams*”, Journal of the American Helicopter Society, Vol. 41(4), pp. 313–321.
- Jen C.W., Johnson D.A. and Dubois F. (1995), “*Numerical Modal Analysis of Structures based on a Revised Substructure Synthesis Approach2*”, Journal of Sound and Vibration, Vol. 180(2), pp. 185–203.
- Jonkman J.M. (2003), “*Modeling of the UAE Wind Turbine for Refinement of FAST AD*”, NREL/TP-500-34755, National Renewable Energy Laboratory.
- Jonkman J.M. (2005), “*NWTC Design Codes (FAST)*”, Available at: <http://wind.nrel.gov/designcodes/simulators/FAST/>.
- Kane T.R. and Levinson D.A. (1985), “*Dynamics: Theory and Applications*”, McGraw-Hill, New York.
- Kelley N. and Jonkman B. (2006), “*NWTC Design Codes (TurbSim)*”, Available at: <http://wind.nrel.gov/designcodes/preprocessors/turbsim/>.
- Khulief Y.A., Bazoune A. (1992), “*Frequencies of Rotating Tapered Timoshenko Beams with different Boundary Conditions*”, Computers and Structures, Vol. 42, pp. 781–95.
- Kosmatka J.B. (1986), “*Structural Dynamic Modeling of Advanced Composite Propellers by the Finite Element Method*”, Ph.D. Thesis, University of California Los Angeles.
- Laino D.J. (2005a), “*NWTC Design Codes (AeroDyn)*”, Available at: <http://wind.nrel.gov/designcodes/simulators/aerodyn/>.
- Laino D. J.(2005b), “*NWTC Design Codes (IECWind)*”, Available at: <http://wind.nrel.gov/designcodes/preprocessors/iecwind/>.

- Larwood S. and Zuteck M. (2006), “*Swept Wind Turbine Blade Aeroelastic Modeling for Loads and Dynamic Behavior*”, AWEA Windpower 2006, American Wind Energy Association, Pittsburgh, PA, pp. 1–17.
- Lee S.Y. and Kuo Y.H. (1993), “*Bending Frequency of a Rotating Timoshenko Beam with General Elastically Restrained Root*”, Journal of Sound and Vibration, Vol. 162, pp. 243–50.
- Leung A.Y.T. and Fung T.C. (1988), “*Spinning Finite Elements*”, Journal of Sound and Vibration, Vol. 125(3), pp. 523–537.
- Liebst B.S. (1986), “*Wind Turbine Gust Load Alleviation Utilizing Curved Blades*”, Journal of Propulsion, Vol. 2(4), pp. 371–377.
- Lobitz D.W., Veers P.S. and Migliore P.G. (1996), “*Enhanced Performance of HAWTs Using Adaptive Blades*”, Wind Energy '96, Energy Week Conference and Exhibition, Book VIII Vol. 1, PennWell Conferences and Exhibitions, Houston, TX, pp. 41–45.
- Madsen P.H. and Frandsen S. (1984), “*Wind-Induced Failure of Wind Turbines*”, Engineering Structures, Vol. 6(4), pp. 281–7.
- Manwell J.F., McGowan J.G. and Rogers A.L. (2002), “*Wind Energy Explained: Theory, Design and Application*”, 1st Edition, John Wiley and Sons, Chichester, New York.
- Molenaar D.-P. (2003), “*Cost-Effective Design and Operation of Variable Speed Wind Turbines: Closing the Gap between the Control Engineering and the Wind Engineering Community*”, Ph.D. Thesis, Delft University Press.
- Murtagh P.J., Basu B. and Broderick B.M. (2004), “*Simple Models for the Natural Frequencies and Mode Shapes of Towers Supporting Utilities*”, Computers and Structures; Vol. 82(20–21), pp. 1745–50.
- Murtagh P.J., Basu B. and Broderick B.M. (2004), “*Mode Acceleration Approach for Rotating Wind Turbine Blades*”, Proc. Inst. Mech. Eng. Part K: J Multi-body Dynamics, Vol. 218, pp. 159–67.

- Murtagh P.J., Basu B. and Broderick B.M. (2005), “*Along-Wind Response of a Wind Turbine Tower with Blade Coupling subjected to Rotationally Sampled Wind Loading*”, Engineering Structures, Vol. 27, pp. 1209-1219.
- Naguleswaran S. (1994), “*Lateral Vibration of a Centrifugally Tensioned Uniform Euler–Bernoulli Beam*”, Journal of Sound and Vibration, Vol. 176(5), pp. 613–24.
- Øye S. (1996), “*FLEX4 Simulation of Wind Turbine Dynamics*”, Proceedings of 28th IEA Meeting of Experts Concerning State of the Art of Aeroelastic Codes for Wind Turbine Calculations.
- Pohit G., Mallik A.K. and Venkatesan C. (1999), “*Free Out-of-Plane Vibrations of a Rotating beam with Non-Linear Elastomeric Constraints*”, Journal of Sound and Vibration, Vol. 220, pp. 1–25.
- Rao S.S. (2005), “*The Finite Element Method in Engineering*”, 4th Ed., Elsevier Butterworth-Heinemann, Burlington, MA.
- Rumman W.S. (1970), “*Basic Structural Design of Concrete Chimeneys*”, J. Power Div., ASCE (96), pp. 309-318.
- Scheble M. and Strizzolo C.N. (1998), “*Convergi SC. Rayleigh–Ritz Substructure Synthesis Method in Physical Co-ordinates for Dynamic Analysis of Structures*”, Journal of Sound and Vibration, Vol. 213(1), pp. 193–200.
- Simiu E. and Scanlan R. (1996), “*Wind Effects on Structures*”, 3rd Ed., John Wiley & Sons, New York.
- Sorenson N.N. and Michelsen J.A. (2002), “*Navier-Stokes Prediction of the NREL Phase VI Rotor in the NASA AMES 80-by-120 Wind Tunnel*”, ASME Wind Energy Symposium.
- Swaminathan M. and Rao J.S. (1977), “*Vibrations of Rotating, Pre-twisted and Tapered Blades*”, Mech. Mach. Theory, Vol. 12(331-7).
- Timoshenko S. and Gere J.M. (1972), “*Mechanics of Materials*”, D. Van Nostrand Company.
- Velazquez A. and Swartz R.A. (2011), “*Probabilistic Analysis of Mean-Response Along-Wind Induced Vibrations on Wind Turbine Towers using Wireless Network Data Sensors*”, SPIE Smart Structures Conf., San Diego, CA.

- Vickery B.J. and Clark A.W. (1972), “*Lift or Across-Wind Response of Tapered Stacks*”, J. Struct. Div., ASCE (98), No. ST1, pp. 1 – 20.
- Wilson R.E., Freeman L., Walker S. and Harman C. (1996), “*FAST Advanced Dynamics Code*”, OSU/NREL 96-01, Oregon State University, Department of Mechanical Engineering.
- Wilson R.E. and Lissaman P.B.S. (1974), “*Applied Aerodynamics of Wind Power Machine*”, Oregon State University.
- Wilson R.E., Lissaman P.B.S. and Walker S.N. (1976), “*Aerodynamics Performance of Wind*”, Energy Research and Development Administration. ERDA/NSF/04014-76/1.
- Wilson R.E., Walker S.N. and Heh P.S.N. (1999), “*Technical and User’s Manual for the fast_ad Advanced Dynamics Code*”, Oregon State University. OSU/NREL Report 99-01.
- Wright A.D. and Elliott A.S. (1992), “*Development of a Wind Turbine System Dynamics Model Using the Automatic Dynamic Analysis of Mechanical Systems (ADAMS) Software*”, Windpower ’92, American Wind Energy Association, Seattle, WA, pp. 329–338.
- Yokoyama T. (1988), “*Free Vibration Characteristics of Rotating Timoshenko Beams*”, Int. J. Mech. Sci., Vol. 30, pp.743–55.
- Yoo H.H. and Shin S.H. (1998), “*Vibration Analysis of Rotating Cantilever Beams*”, Journal of Sound and Vibration, Vol. 212, pp. 807–28.
- Zuteck M. (2002), “*Adaptive Blade Concept Assessment: Curved Planform Induced Twist Investigation*”, SAND2002-2996, Sandia National Laboratories.

3. Chapter 3. Aeroelastic Analysis

- Basu R.I. (1983), “*Across-Wind Response of Slender Structures of Circular Cross Section to Atmospheric Turbulence*”, Vol. 1, Report BLWT-2-1983, University of Western Ontario, London, Ontario, Canada.

- Basu R.I. and Vickery B. J. (1983), “*Across-Wind Vibrations of Structures of Circular Cross-Section, Development of a Mathematical Model for Full Scale Application*”, J. Wind Eng. Ind. Aerodyn., Vol. 12, pp. 75-97.
- Berman A. and Fi W.G. (1971), “*Theory of Incomplete Models of Dynamics Structures*”, AL4A J., Vol. 9(8), pp. 1481-1487.
- Braam H. and van Dam J.J.D. (1998), “*Methods for Probabilistic Design of Wind Turbines*”, Riso-R-1082(EN) Report, National Laboratory, Roskilde, Denmark.
- Chen X-B., Li J. and Chen J-Y. (2009), “*Wind-Induced Response Analysis of a Wind Turbine Tower including the Blade-Tower Coupling Effect*”, Journal of Zhejiang University, Vol. 10(11), p.p. 1573-1580.
- Chien C.W. and Jang J.J. (2008), “*A Study of Dynamic Analysis and Wind-resistant Safety Design of Wind Turbines*”, Proc. of 3rd Taiwan Wind Energy Symp, TwnWEA, Taipei, p.p. 225-231.
- Chopra A.K. (2007), “*Dynamics of Structures*”, Prentice Hall, Englewood Cliffs, New Jersey.
- Clough R.W. and Penzien J. (1975), “*Dynamics of Structures*”, Higher Education Press, Beijing, p.p. 135-139.
- Dyrbye C. and Hansen S.O. (1997), “*Wind Loads on Structures*”, John Wiley & Sons, New York, New York.
- Hurty W.C. and Rubinstein M.F. (1996), “*Dynamics of Structures*”, Prentice-Hall, Englewood Cliffs, NJ.
- IEC 61400-12 (1998), “*Wind Turbine Power Performance Testing*”, IEC 61400-12.
- Lanzafame R. and Messina M. (2007), “*Fluid Dynamic Wind Turbine Design: Critical Analysis, Optimization and Application to BEM Theory*”, Renewable Energy, Vol. 32(14), pp. 2291-2305.
- Larsen G.C. (2006), “*Wind Farms Wind field and Turbine Loading, Complex Terrain and Fatigue Loading*”, EWTS Part 1, EUREC-Agency, Leuven, Belgium.
- Lavassas I. and Nikplaidis G. (2003), “*Analysis and Design of the Prototype of a Steel 1-MW Wind Turbine Tower*”, Engineering Structures, Vol. 25(8), pp. 1097-1106.

- Meirovitch L. (1986), "*Elements of Vibration Analysis*", McGraw Hill, New York, NY, 1986.
- Murtagh P.J., Basu B. and Broderick B.M. (2005), "*Along-Wind Response of a Wind Turbine Tower with Blade Coupling subjected to Rotationally Sampled Wind Loading*", Engineering Structures, Vol. 27, p.p. 1209-1219.
- Naguleswaran S. (1994), "*Lateral Vibration of a Centrifugally Tensioned Uniform Euler-Bernoulli Beam*", Journal of Sound and Vibration, Vol. 176(5), pp. 613-624.
- Newland D.E. (1996), "*An Introduction to Random Vibrations, Spectral and Wavelet Analysis*", 3rd Ed., Prentice Hall.
- Prowell I. and Veletzos M. (2010), "*Experimental and Numerical Seismic Response of a 65kW Wind Turbine*", Jrnl. of Earthquake Engineering, Vol. 13(8), p.p. 1172-1190.
- Rumman W.S. (1970), "*Basic Structural Design of Concrete Chimeneys*", J. Power Div., ASCE, Vol. 96, pp. 309-318.
- Shinozuka M. (1998), "*Statistical Analysis of Bridge Fragility Curves*", Proceedings of the US-Italy Workshop on Protective Systems for Bridges, New York, NY, pp. 26-28.
- Simiu E. and Lozier D.W. (1979), "*The Buffeting of Structures by Strong Winds-Windload Program*", NTIS Accession No. PB 294757/AS, Computer Program for Estimating Along-Wind Response, National Technical Information Service, Springfield, VA.
- Simiu E. and Scanlan R. (1996), "*Wind Effects on Structures*", 3rd Ed., John Wiley & Sons, New York, NY.
- Simiu E., Shaver J.R. and Filliben J.J. (1981), "*Wind Speed Distributions and Reliability Estimates*", J. Struct. Div., ASCE, Vol. 107, pp. 1003-1007.
- Stathopoulos T. and Baniotopoulos C.C. (2007), "*Wind Effect on Buildings and Design of Wind-Sensitive Structures*", CISM Lectures, SpringerWien, NewYork, NY.
- Tamura Y., et al. (1996), "*Wind Load and Wind-Induced Response Estimations in RLB-AIJ1993*", Engineering Structures, Vol. 18(6), p.p. 399-411.

- Velazquez A. and Swartz R.A. (2011), “*Probabilistic Analysis of Mean-Response Along-Wind Induced Vibrations on Wind Turbine Towers using Wireless Network Data Sensors*,” SPIE Smart Structures Conf., San Diego, CA.
- Vickery B.J. and Basu R.I. (1983), “*Simplified Approaches to the Evaluation of the Across-Wind Response of Chimeneys*”, Proceedings 6th International Conference on Wind Engineering, Gold Coast, Australia, Jnl. Wind Eng. & Ind. Aerodyn., Vol 14, p.p. 153-166.
- Vickery B.J. and Clark A.W. (1972), “*Lift or Across-Wind Response of Tapered Stacks*”, Jnl. Struct. Div., ASCE, 98, No. ST1, 1 – 20.
- Zimmerman A.T., Shiraishi M., Swartz R.A. and Lynch J.P. (2008), “*Automated Modal Parameter Estimation by Parallel Processing within Wireless Monitoring Systems*”, Jnl. of Infrastructure Systems, Vol. 14(1), pp. 102-113.

4. Chapter 4. Spinning Finite Element

- Ambrosini R.D., Riera J.D. and Danesi R.F. (2002), “*Analysis of Structures Subjected to Random Wind Loading by Simulation in the Frequency Domain*”, Probabilistic Engineering Mechanics, Vol. 17, pp 233-239.
- Basu R.I. (1983), “*Across-Wind Response of Slender Structures of Circular Cross Section to Atmospheric Turbulence*”, Vol. 1., Report BLWT-2-1983, University of Western Ontario, London, Ontario, Canada.
- Bauer H.F. (1980), “*Vibration of a Rotating Uniform beam Orientation in the Axis of Rotation*”, Journal of Sound and Vibration, Vol. 72, pp. 177-189, Part 1.
- Baumgart A. (2002), “*A Mathematical Model for Wind Turbine Blades*”, Journal of Sound and Vibration, Vol. 251(1), pp. 1-12.
- BWEA (2005a), “*Guidelines for Health and Safety in the Wind Energy Industry*”.
- CEN EN 50308 (2004), “*Wind Turbines - Protective Measures - Requirements for Design, Operation and Maintenance*, CSN EN Standard.
- Chen X-b., Li J., Chen J-y. (2009), “*Wind-Induced Response Analysis of a Wind Turbine Tower including the Blade-Tower Coupling Effect*”, J. Zhejiang University Sci.

- A., Vol. 10(11), pp. 1573-1580.
- Christensen E.R. and Lee S.W. (1986), “*Nonlinear Finite Element Modeling of the Dynamics of Unrestrained Flexible Structures*”, Computers and Structures, Vol. 23, pp. 819-829.
- Di Paola M. and Zingales M. (2008), “*Stochastic Differential Calculus for Wind-Exposed Structures with Autoregressive Continuous (ARC) Filters,*”, Journal of Wind Engineering and Industrial Aerodynamics, Vol. 96(12), pp. 2403-2417.
- EWEA (2012), “*Green Growth The Impact of Wind Energy on Jobs and The Economy*”, European Wind Energy Association, Brussels, Belgium.
- Gardner P., Garrad A., Jamieson P, Snodin H., Nicholls G. and Tindal A. (2003), “*Wind Energy – The Facts*”, European Wind Energy Association (EWEA), Vol. 1 Technology.
- Hansen M.O.L. (2008), “*Aerodynamics of Wind Turbines*”, e.d. Earthscan, 2nd edition, Sterling, VA.
- Horn R. A. and Johnson C.R. (1985), “*Matrix Analysis*”, Cambridge University Press, Cambridge, MA.
- Johansen J., Madsen H.A., Gaunaa M., *et al.* (2009), “*Design of a Wind Turbine Rotor for Maximum Aerodynamic Efficiency*”, Wind Energy, Vol 12(3), pp. 261-273.
- Jonkman J.M. (2003), “*Modeling of the UAE Wind Turbine for Refinement of FAST AD*”, NREL/TP-500-34755, National Renewable Energy Laboratory.
- Kaimal J.C., Wyngaard J.C., Izumi Y. and Coté O.R. (1972), “*Spectral Characteristics of Surface-Layer Turbulence*”, Quart. J. R. Met. Soc., Vol. 98, pp. 563-589.
- Lanzafame R. and Messina M. (2007), “*Fluid Dynamic Wind Turbine Design: Critical Analysis, Optimization and Application of BEM Theory*”, Renewable Energy, Vol. 32(14), pp. 2291-2305.
- Larwood S.M. (2009), “*Dynamic Analysis Tool Development for Advanced Geometry Wind Turbine Blades*”, Ph.D Dissertation,”, Mechanical and Aeronautical Engineering, University of California, Davis, Sacramento, CA.
- Lee C.L., Al-Salem M.F. and Woehrle T.G. (2001), “*Natural Frequency Measurements for Rotating Span Wise Uniform Cantilever Beams*”, Journal of Sound Vibration,

- Vol. 240(5), pp. 57-61.
- Leung A.Y.T. and Fung T.C. (1988), “*Spinning Finite Elements*”, Journal of Sound and Vibration, Vol. 125, No. 3, pp. 523-537.
- Meirovitch L. (1986), “*Elements of Vibration Analysis*”, McGrawhill, New York, NY.
- Meirovitch L. (1980), “*Computational Methods in Structural Dynamics*”, The Netherlands: Sitjhoff and Noordhoff.
- Murtagh P.J., Basu B. and Broderick B.M. (2004), “*Mode Acceleration Approach for Rotating Wind Turbine Blades*”, Proceedings of the Institution of Mechanical Engineers. Part K, Jrnl. of Multi-Body Dynamics, Vol 218(3), pp. 159-167.
- Murtagh P. J., Basu B. and Broderick B.M. (2005), “*Along-Wind Response of a Wind Turbine Tower with Blade Coupling Subject to Rotationally Sampled Wind Loading*”, Engineering Structures, Vol. 27(8), pp. 1209-1219.
- Naguleswaran S. (1994), “*Lateral Vibration of a Centrifugally Tensioned Uniform Euler-Bernoulli Beam*”, Journal of Sound and Vibration, Vol. 176(5), pp. 613-624.
- Nelson H.D. (1985), “*Rotor Dynamics Equations in Complex Form*”, American Society of Mechanical Engineers, Journal of Vibration, Acoustics, Stress and Reliability in Design, Vol. 107, 460-461.
- Rao S.S. (2005), “*The Finite Element Method in Engineering*”, Elsevier Butterworth-Heinemann, Burlington, MA, 4th ed.
- Shinozuka M. (1971), “*Simulation of Multivariate and Multidimensional Random Process*”, Journal of the Acoustical Society of America, Vol. 49(1B), pp. 357-367.
- Simiu E. and Scanlan R.H. (2007), “*Wind Effects on Structures: An Introduction to Wind Engineering*”, e.d. Wiley, 2nd edition.
- Soong T.T. and Grigoriu M. (1992), “*Random Vibrations of Mechanical and Structural Systems*”, Prentice Hall, Englewood Cliffs, NJ.
- Wilkinson J.H. (1965), “*The Algebraic Eigenvalue Problem*”, Oxford University Press.
- Wittrick W.H. and Williams F.W. (1982), “*On the Free Vibration Analysis of Spinning Structures by Using Discrete or Distributed Mass Models*”, Journal of Sound and Vibration, Vol. 82, pp.1-15.

Zheng Z., Ren G. and Williams F.W. (1997), “*The Eigenvalue Problem for Damped Gyroscopic Systems*”, Int. J. Mech. Sci., Vol. 39(6), pp. 741-750.

5. Chapter 5. Spinning Finite Element with Damped Gyroscopic Effects and Axial-Flexural-Torsional Coupling

Ashwill T. (2010), “*Sweep-Twist Adaptive Rotor Blade: Final Project Report*”, Technical Report, Sandia Report SAND2009-8037, Sandia National Laboratories, Albuquerque, NM.

Bhadbhade V., Jalili N. and Mahmoodi S.N. (2008), “*A Novel Piezoelectrically Actuated Flexural/Torsional Vibrating Beam Gyroscope*”, Journal of Sound and Vibration, Vol. 311, pp. 1305-1324.

Bottasso C.L., Campagnolo F., Croce A. and Tibaldi C. (2011), “*Optimization-Based Study of Bend-Twist Coupled Rotor Blades for Passive and Integrated Passive/Active Load Alleviation*”, Technical Report, Scientific Report DIA-SR 11-02, Politecnico di Milano, Milano, Italy.

Chhabra P.P.S. and Ganguli R. (2010), “*Superconvergent Finite Element for Coupled Torsional-Flexural-Axial Vibration Analysis of Rotating Blades*”, International Journal for Computational Methods in Engineering Science and Mechanics, Vol. 11, pp. 48-69.

Cox B.N., Andrews M., Massabo R., Rosakis A., Sridhar N. and Yang Q.D. (2004), “*Shear Lag and Beam Theories for Structures*”, Structural Integrity and Fracture International Conference (SIF2004), Brisbane, September, pp. 63-69.

DLR & EREC (2010), “*The global wind energy outlook scenarios*”, Global Wind Energy Council.

Fonseca J.R. and Ribeiro P. (2006), “*Beam p-Version Finite Element for Geometrically Non-Linear Vibrations in Space*”, Computational Methods and Applied Mechanical Engineering, Vol. 195, pp. 905-924.

Hansen M.O.L. (2008), “*Aerodynamics of Wind Turbines*”, Earthscan, 2nd edition, London, UK.

- Horn R.A. and Johnson C.R. (1985), "*Matrix Analysis*", Cambridge University Press, Cambridge, MA.
- Johansen J., Madsen H.A., Gaunaa M., Bak C. and Sorensen N.N. (2009), "*Design of a Wind Turbine Rotor for Maximum Aerodynamic Efficiency*", Journal of Wind Energy, Vol. 12(3), pp. 261-273.
- Ganguli R. and Chopra I. (1997), "*Aeroelastic Tailoring of Composite Couplings and Blade Geometry of a Helicopter Rotor using Optimization Methods*", Journal of the American Helicopter Society, Vol. 42(3), pp. 218-228.
- Griffin D.A. (2002), "*Evaluation of Design Concepts for Adaptive Wind Turbine Blades*", Technical Report, Report SAND2002-2424, Sandia National Laboratories, Albuquerque, NM.
- Hoogedoorn E., Jacobs G.B. and Beyene A. (2010), "*Aero-Elastic Behavior of a Flexible Blade for Wind Turbine Application: A 2D Computational Study*", [J] Energy, Vol. 35(2), pp. 778-785.
- Kooij J.F. (2003), "*One-Dimensional Variations: Blades*", Seminar Report, Task 5, Dutch Offshore Wind Energy Converter Project (DOWEC).
- Lalanne M. and Ferraris G. (1998), "*Rotor Dynamics Prediction in Engineering*", John Wiley & Sons, 2nd edition, London, England.
- Lanzafame R. and Messina M. (2007), "*Fluid Dynamic Wind Turbine Design: Critical Analysis, Optimization and Application of BEM Theory*", Journal of Renewable Energy, Vol. 32(14), pp. 2291-2305.
- Larwood S.M. (2009), "*Dynamic Analysis Tool Development for Advanced Geometry Wind Turbine Blades*", Ph.D Thesis, Mechanical and Aeronautical Engineering Department, University of California, Davis, Sacramento, CA.
- Lazaridis L.P. (2005), "*Economic Comparison of HVAC and HVDC Solutions for Large Offshore Wind Farms under Special Consideration of Reliability*", Master's Thesis, Department of Electrical Engineering, Royal Institute of Technology, Stockholm.
- Lee C.L., Al-Salem M.F. and Woehrle T.G. (2001), "*Natural Frequency Measurements for Rotational Span Wise Uniform Cantilever Beams*", Journal of Sound and

- Vibration, Vol. 240(5), pp. 957-961.
- Leung A.Y.T. and Fung T.C. (1988), “*Spinning Finite Elements*”, Journal of Sound and Vibration, Vol. 125(3), pp.523-537.
- Lewandowski R. (1994), “*Non-linear Free Vibrations of Beams by the Finite Element and Continuation Methods*”, Journal of Sound and Vibration, Vol. 170(5), pp. 577-593.
- Linscott B.S., Dennet J.T. and Gordon L.H. (1981), “*The MOD-2 Wind Turbine Development Project*”, DOE/NASA 20 305-5, NASA TM-82 681.
- Lynette R. (1988), “*California Wind Farms Operational Data Collection and Analysis*”, Solar Energy Research Institute (SERI).
- MacEwen K.W. (2001), “*Non-Local Periodic Motions of Thin Cantilevered Rod*”, Journal of Nonlinear Dynamics, Vol. 26(3), pp. 297-308.
- Maheri A., Noroozi S. and Vinney J. (2007), “*Decoupled Aerodynamic and Structural Design of Wind Turbine Adaptive Blades*”, Journal of Renewable Energy, Vol. 32, pp. 1753-1767.
- Malatkar P. (2003), “*Nonlinear Vibrations of Cantilever Beams and Plates*”, Ph.D Thesis, Virginia Tech, Blacksburg, Virginia.
- Manwell J.F. and McGowan J.G. (2009), “*Wind Energy Explained. Theory, Design and Application*”, Wiley, 2nd edition, West Sussex, UK.
- Meirovitch L. (1974), “*A New Method of Solution of the Eigenvalue Problem for Gyroscopic Systems*”, Journal of The American Institute of Aeronautics and Astronautics, Vol. 12, pp. 1337-1342.
- Oguamanam D.C.D. (2003), “*Free Vibration of Beams with Finite Mass Rigid Tip Load and Flexural-Torsional Coupling*”, International Journal of Mechanical Sciences, Vol. 45, pp. 963-979.
- Ozgumus O.O. and Kaya M.O. (2007), “*Energy Expressions and Free Vibration Analysis of a Rotating Double Tapered Timoshenko Beam Featuring Bending-Torsion Coupling*”, International Journal of Engineering Science, Vol. 45, pp. 562-586.

- Salarieh H. and Ghorashi M. (2006), “*Free Vibration of Timoshenko Beam with Finite Mass Rigid Tip Load and Flexural-Torsional Coupling*”, International Journal of Mechanical Sciences, Vol. 48, pp. 763-779.
- Stoykov S. and Ribeiro P. (2010), “*Nonlinear Forced Vibrations and Static Deformations of 3D Beams with Rectangular Cross Section: the Influence of Warping, Shear Deformation and Longitudinal Displacements*”, International Journal of Mechanical Sciences, Vol. 52, pp. 1505-1521.
- Stoykov S. and Ribeiro P. (2013), “*Vibration Analysis of Rotating 3D Beams by the p-Version Finite Element Method*”, Journal of Finite Elements in Analysis and Design, Vol. 65, pp. 76-88.
- Ribeiro P. and Petyt M. (1999), “*Non-Linear Vibration of Beams with Internal Resonance by the Hierarchical Finite-Element Method*”, Journal of Sound and Vibration, Vol. 224(4), pp. 591-624.
- Walker J.F. (1996), “*Wind Energy Technology*”, John Walker & Sons, West Essex, U.K.
- Wang C., Reddy J. and Lee K. (2000), “*Shear Deformable Beams and Plates*”, Elsevier, Oxford.
- Weaver W., Timoshenko S.P. and Young D.H. (1990), “*Vibration Problems in Engineering*”, Wiley.
- Wempner G. and Talaslidis D. (2003), “*Mechanics of Solids and Shells, Theory and Application*”, CRC Press, Boca Raton, Florida.
- Wilkinson J.H. (1965), “*The Algebraic Eigenvalue Problem*”, Oxford University Press.
- Zheng Z., Ren G. and Williams F.W. (1997), “*The Eigenvalue Problem for Damped Gyroscopic Systems*”, International Journal of Mechanical Sciences, Vol. 39(6), pp. 741-750.

6. Chapter 6. Output-Only Cyclo-Stationary Linear-Parameter Time-Varying Stochastic Subspace Identification Method

ANSYS© (2011) Workbench Release Ver. 11.

Bertha M., Mayorga-Rios J.P. and Golinval J.-C. (2012), “*Modal Identification of Time-*

- Varying Systems using Simulated Response on Wind Turbines*", Proceedings ISMA2012-USD2012, Leuven, Belgium.
- Bittanti S., Laub A.J. and Willems J.C. (1991), "*The Riccati Equation*", Springer, 1991.
- Chen C.T. (1984), "*Linear System Theory and Design*", Holt-Saunders.
- Di Ruscio D. (2009), "*Subspace System Identification*", Telemark University College, 6th ed., Porsgrunn, Norway.
- DLR & EREC (2010), "*The Global Wind Energy Outlook Scenarios*", Global Wind Energy Council.
- Faurre P.L. (1976), "*Stochastic Realization Algorithms, in System Identification: Advances and Case Studies*", R. Mehra and D. Lainiotis, eds., Academic, pp. 1-25.
- Franklin G.F., Powell J.D. and Emami-Naeini A. (2002), "*Feedback Control of Dynamic Systems*", Prentice Hall, 4th ed., New York, NY.
- Grewal M.S. and Andrews A.P. (1993), "*Kalman Filtering – Theory and Practice*", Prentice Hall, New York, NY.
- Hsu C.S., Desai U.B. and Crawley C.A. (1985), "*Realization and Approximation of Discrete Bilinear Systems*", Applications in Digital Control, Elsevier, Science Publishers, North-Holland, pp. 171-187.
- Jhinaoui A., Mevel L. and Morlier J. (2012), "*Extension of Subspace Identification to LPTV Systems: Application to Helicopters*", Proceedings of Society for Experimental Mechanics, Vol. 30, pp. 425-433.
- Juang J.-N. (1994), "*Applied System Identification*", Prentice Hall, Saddle River, NJ.
- Kailath T. (1980), "*Linear Systems*", Prentice-Hall, New Yourk, NY.
- Kalman R.E. (1960), "*A New Approach to Linear Filtering and Prediction Problems*", Transactions ASME, Journal of Basic Engineering 82D(1), pp. 34-45.
- Kameyama K. and Ohsumi A. (2007), "*Subspace-Based Prediction of Linear Time-Varying Stochastic System*", Automatica, Vol. 43, pp. 2009-2021.
- Katayama T. (2005), "*Subspace Methods for System Identification*", Springer, Leipzig, Germany.
- Kuo B.C. (1995), "*Automatic Control Systems*", Prentice Hall, 7th ed., New York,

NY.

- Lanzafame R. and Messina M. (2007), “*Fluid Dynamic Wind Turbine Design: Critical Analysis, Optimization and Application of BEM Theory*”, Renewable Energy, Vol. 32(14), pp. 2291-2305.
- Lee L.H. and Poolla K. (1996), “*Identification of Linear Parameter-Varying Systems using Nonlinear Programming*”, Proceedings of the 35th IEEE Conference on Decision and Control.
- Liu K. (1997), “*Identification of Linear Time-Varying Systems*”, Journal of Sound and Vibration, Vol. 206(4), pp. 487-505.
- Ljung L. (1987), “*System Identification: Theory for the User*”, Prentice Hall, Engelwood Cliffs, NJ.
- Lopes dos Santos P., Ramos J.A and Martins de Carvalho J.L. (2005), “*Identification of Bilinear Systems using an Iterative Deterministic-Stochastic Subspace Approach*”, Proceedings of the 44th IEEE Conference on Decision and Control & European Control Conference, pp. 7120-7126.
- Lopes dos Santos P., Ramos J.A. and Martins de C.J.L. (2007), “*Identification of Linear Parameter Varying Systems using an Iterative Deterministic-Stochastic Subspace Approach*”, Proceedings of European Control Conference, Kos, Greece, pp. 4867-4873.
- Muller M., Arnold U.T.P. and Morbitzer D. (2000), “*On the Importance and Effectiveness of 2/rev IBC for Noise, Vibration and Pitch Link Load Reduction*”, 55th Proceedings of American Helicopter Society Annual Forum, Montreal, Canada.
- Rybicki G.B. and Press W.H. (1992), “*Interpolation, Realization, and Reconstruction of Noisy, Irregularly Sampled Data*”, The Astrophysical Journal, Vol. 298, pp. 169-176.
- Svend G., Moller Nis B., Herlufsen H. and Konstantin-Hansen H. (2002), “*Frequency Domain Techniques for Operational Modal Analysis*”, International Journal SAE Annual Congres, pp. 17-20.
- Tóth R. (2008), “*Modeling and Identification of Linear Parameter-Varying Systems*”,

- Doctoral Thesis, Dutch Institute of Systems and Control (DISC).
- Van Overschee P. and De Moor B. (1996), “*Subspace Identification for Linear Systems. Theory – Implementation – Applications*”, Vol. 2008, Leuven, Belgium.
- Van Overschee P., De Moor B. and Suykens J. (1991), “*Subspace Algorithms for System Identification and Stochastic Realization*”, Proceeding Conference on Mathematical Theory for Networks and Systems, MTNS, Kobe, Japan, pp. 589-595.
- Velazquez A. and Swartz R.A. (2012), “*Gyroscopic Effects of Horizontal Axis Wind Turbines using Stochastic Aeroelasticity via Spinning Finite Elements*”, Proceedings of the ASME 2012 Conference on Smart Materials Adaptive Structures and Intelligent Systems (SMASIS2012).
- Verdult V. (2004), “*Identification of Linear Parameter-Varying State-Space Models with Application to Helicopter Rotor Dynamics*”, International Journal of Control, Vol. 77 (13), pp. 1149-1159.
- Verdult V. and Verhaegen M. (2002), “*Subspace Identification of Multivariable Linear Parameter-Varying Systems*”, Automatica, Vol. 38, pp. 805-814.
- Vold H., Kundrat J., Rocklin G.T. and Russell R. (1982), “*A Multi-Input Modal Estimation Algorithm for Mini-Computers*”, SAE Paper 820194.
- Yunus S.M., Pawlak T.P., Cook R.D. (1991), “*Solid Elements with Rotational Degrees of Freedom Part 1 and Part 2*”, International Journal for Numerical Methods in Engineering 31, pp. 573-610.

7. Chapter 7. Model Updating via Adaptive Simulated Annealing

- Akaike H. (1975), “*Markovian Representation of Stochastic Processes by Canonical Variables*”, Siam J. Control, Vol. 13(1), pp. 162-173.
- Baumgart A. (2002), “*A Mathematical Model for Wind Turbine Blades*”, Journal of Sound and Vibration, Vol. 251, pp. 1-12.
- Bernal D. (2006), “*Flexibility-Based Damage Localization from Stochastic Realization Results*”, Journal of Engineering Mechanics, Vol. 132, pp. 651-658.

- Christensen E.R. and Lee S.W. (1986), “*Nonlinear Finite Element Modeling of the Dynamics of Unrestrained Flexible Structures*”, Computers and Structures, Vol. 23.
- Davis L. (1987), “*Genetic Algorithms and Simulated Annealing*”, London, UK: Pitman.
- Farrar C.R. and Worden K. (2012), “*Structural Health Monitoring: A Machine Learning Perspective*”, New York, NY: Wiley.
- Hoen C. (2005), “*An Engineering Interpretation of the Complex Eigensolution of Linear Dynamic Systems*”, International Modal Analysis Conference XXIII. Orlando, FL.
- Imregun M. and Visser W.J. (1991), “*A Review of Model Updating Techniques*”, Shock and Vibration Digest, Vol. 23, pp. 9-20.
- Juang J-N. (1994), “*Applied System Identification*”, Upper Saddle River, NJ: Prentice Hall.
- Kameyama K. and Ohsumi A. (2007), “*Subspace-Based Prediction of Linear Time-Varying Stochastic Systems*”, Automatica, Vol. 43, pp. 2009-2021.
- Katayama T. (2005), “*Subspace Methods for System Identification*”, Springer. Leipzig, Germany.
- Kirkpatrick S., Gelatt C.D. and Vecchi M.P. (1983), “*Optimization by Simulated Annealing*”, Science (J), Vol. 220(4598), pp. 671-680.
- Lancaster P. (1966), “*Lambda-Matrices and Vibrating Systems*”, Pergamon Press.
- Larwood S.M. (2009), “*Dynamic Analysis Tool Development for Advanced Geometry Wind Turbine Blades*”, Mechanical and Aeronautical Engineering Department. Sacramento, CA., University of California, Davis.
- Leung A.Y.T. and Fung T.C. (1988), “*Spinning Finite Elements*”, Journal of Sound and Vibration, Vol. 125, pp. 523–537.
- Levin R.I. and Lieven A.J. (1998), “*Dynamic Finite Element Model Updating using Simulated Annealing and Genetic Algorithms*”, Mechanical Systems and Signal Processing, Vol. 12, pp. 91-120.
- Levin R.I., Waters T.P. and Lieven N.A.J. (1998), “*Required Precision and Valid Methodologies for Dynamic Finite Element Model Updating*”, ASME Journal of Vibration and Acoustics, Vol. 120, pp. 733-741.

- Ljung L. (1999), *“System Identification, Theory for the User”*, Upper Saddle River, NJ: Prentice Hall.
- Lopes dos Santos P., Ramos J.A. and Martins de C.J.L. (2007), *“Identification of Linear Parameter Varying Systems using an Iterative Deterministic-Stochastic Subspace Approach”*, Proceedings of the European Control Conference, Kos, Greece, pp. 4867-4873.
- Mares C. and Surace C. (1996), *“Finite Element Model Updating using a Genetic Algorithm”*, 2nd Intl. Conf. on Struct. Dyn. Modelling, pp. 41-52.
- Marwala T. (2010), *“Finite-Element-Model Updating using Computational Intelligence Techniques”*, Applications to Structural Dynamics, Springer.
- Meirovitch L. (1974), *“A New Method of Solution of the Eigenvalue Problem for Gyroscopic Systems”*, AIAA Jnl., Vol. 12, pp. 1337-1342.
- Metropolis N., Rosebluth A., Rosebluth M., *et al.* (1953), *“Equation of State Calculations by Fast Computing Machines”*, Journal Chemical Physics, Vol. 21, pp. 1087-1092.
- Mottershead J.E. and Friswell M.I. (1993), *“Model Updating in Structural Dynamics”*, Journal of Sound and Vibration, Vol. 167, pp. 347-375.
- Nelson H.D. (1985), *“Rotor Dynamics Equations in Complex Form”*, American Society of Mechanical Engineers, Journal of Vibration, Acoustics, Stress and Reliability in Design, Vol. 107, pp. 460-461.
- Newland D.E. (1989), *“Mechanical Vibration Analysis and Computation”*, Longman Scientific and Technical, Longman Group UK Limited.
- Papa R.S. and Elliot K.B. (1993), *“Consistent Mode Indicator for the Eigensystem Realization Algorithm”*, Journal of Guidance and Control, Vol. 16, pp. 832-838.
- Salazar R. and Toral R. (2008), *“Simulated Annealing using Hybrid Monte Carlo”*, arXiv:cond-mat/9706051.
- Song G., Li H., Gajic B., *et al.* (2013), *“Wind Turbine Blade Health Monitoring with Piezoceramic-Based Wireless Sensor Network”*, International Journal of Smart and Nano Materials, Vol. 4, pp. 150-166.

- Swartz R.A, Lynch J.P, Sweetman B., *et al.* (2010), “*Structural Monitoring of Wind Turbines using Wireless Sensor Networks*”, Journal of Smart Structures and Systems, Vol. 6, pp. 1-8.
- Vacher P., Jacquier B. and Bucharles A. (2010), “*Extensions of the MAC Criterion to Complex Modes*”, Proceedings of ISMA2010 including USD2010. Leuven, Belgium.
- van Overschee P. and De Moor B. (1996), “*Subspace Identification for Linear Systems. Theory – Implementation – Applications*”, Kluwer Academic. Leuven, Belgium.
- Velazquez A. and Swartz R.A. (2013), “*Model Updating of Aero-Elastic Spinning Finite Elements for SHM of HAWT Blades*”, Proceedings of the 9th International Workshop on Structural Health Monitoring (IWSHM). Stanford, CA.
- Verdult V. (2002), “*Nonlinear System Identification: A State-Space Approach*”, Ph.D Thesis, University of Twente. Twente, Holland.
- Verdult V. and Verhaegen M. (2002), “*Subspace Identification of Multivariable Linear Parameter-Varying Systems*”, Automatica, Vol. 38, pp. 805-814.
- Verhaegen M. and Yu X. (1995), “*A Class of Subspace Model Identification Algorithms to Identify Periodically and Arbitrarily Time-Varying Systems*”, Automatica, Vol. 31, pp. 201-216.
- Ziaei-Rad S. (2005), “*Finite Element Model Updating of Rotating Structures using Different Optimisation Techniques*”, Iranian Jrnl. of Sc. and Tech., Trans B: Eng, Vol. 29, pp. 569-585.
- Zimmerman A.T. and Lynch J.P. (2009), “*A Parallel Simulated Annealing Architecture for Model Updating in Wireless Sensor Networks*”, IEEE Sensors Journal, IEEE 9, pp. 1503-1510.

Appendix A

A.1 General Parameters.

$$\begin{aligned}
 \kappa_{EA} &= EA_0 \sqrt{EA_l / EA_0}; & \kappa_{EI_y} &= EI_{y0} \sqrt{EI_{yl} / EI_{y0}} \\
 \kappa_{EI_z} &= EI_{z0} \sqrt{EI_{zl} / EI_{z0}}; & \kappa_{GJ} &= GJ_0 \sqrt{GJ_l / GJ_0} \\
 \kappa_{\rho A} &= \rho A_0 \sqrt{\rho A_l / \rho A_0}; & \kappa_{\rho I_p} &= \rho I_{p0} \sqrt{\rho I_{pl} / \rho I_{p0}} \\
 a_{11} &= \alpha_{11}^2 + \alpha_{13}^2; & a_{12} &= \alpha_{11}\alpha_{21} + \alpha_{13}\alpha_{23}; & a_{13} &= \alpha_{11}\alpha_{31} + \alpha_{13}\alpha_{33} \\
 a_{22} &= \alpha_{21}^2 + \alpha_{23}^2; & a_{23} &= \alpha_{21}\alpha_{31} + \alpha_{23}\alpha_{33}; & a_{33} &= \alpha_{31}^2 + \alpha_{33}^2 \\
 b_1 &= \alpha_{11}\alpha_{23} - \alpha_{13}\alpha_{21}; & b_2 &= \alpha_{11}\alpha_{33} - \alpha_{13}\alpha_{31}; & b_3 &= \alpha_{21}\alpha_{33} - \alpha_{23}\alpha_{31} \\
 a &= \alpha_{11}x_{s0} + \alpha_{13}z_{s0}; & b &= \alpha_{11}^2 + \alpha_{13}^2; & \{r_g\} &= \{x_{s0}, y_{s0}, z_{s0}\}
 \end{aligned}$$

A.2 Mass Matrix.

$$\begin{aligned}
 M_{B(1,1)} &= \frac{l}{30} (6\rho A_0 + 3\kappa_{\rho A} + \rho A_l) \\
 M_{B(1,7)} &= \frac{l}{60} (3\rho A_0 + 4\kappa_{\rho A} + 3\rho A_l) \\
 M_{B(2,2)} &= \frac{l}{630} (145\rho A_0 + 70\kappa_{\rho A} + 19\rho A_l) \\
 M_{B(2,6)} &= \frac{l^2}{2520} (65\rho A_0 + 50\kappa_{\rho A} + 17\rho A_l) \\
 M_{B(2,8)} &= \frac{l}{630} (23\rho A_0 + 35\kappa_{\rho A} + 23\rho A_l) \\
 M_{B(2,12)} &= -\frac{l^2}{2520} (25\rho A_0 + 34\kappa_{\rho A} + 19\rho A_l) \\
 M_{B(3,3)} &= \frac{l}{630} (145\rho A_0 + 70\kappa_{\rho A} + 19\rho A_l) \\
 M_{B(3,5)} &= -\frac{l^2}{2520} (65\rho A_0 + 50\kappa_{\rho A} + 17\rho A_l) \\
 M_{B(3,9)} &= \frac{l}{630} (23\rho A_0 + 35\kappa_{\rho A} + 23\rho A_l) \\
 M_{B(3,11)} &= \frac{l^2}{2520} (25\rho A_0 + 34\kappa_{\rho A} + 19\rho A_l)
 \end{aligned}$$

$$M_{B(4,4)} = \frac{l}{30} (6\rho I_{\rho 0} + 3\kappa_{\rho I_p} + \rho I_{pl})$$

$$M_{B(4,10)} = \frac{l}{60} (3\rho I_{\rho 0} + 4\kappa_{\rho I_p} + 3\rho I_{pl})$$

$$M_{B(5,5)} = \frac{l^3}{1260} (5\rho A_0 + 5\kappa_{\rho A} + 2\rho A_l)$$

$$M_{B(5,9)} = -\frac{l^2}{2520} (25\rho A_0 + 34\kappa_{\rho A} + 19\rho A_l)$$

$$M_{B(5,11)} = -\frac{l^3}{2520} (5\rho A_0 + 8\kappa_{\rho A} + 5\rho A_l)$$

$$M_{B(6,6)} = \frac{l^3}{1260} (5\rho A_0 + 5\kappa_{\rho A} + 2\rho A_l)$$

$$M_{B(6,8)} = \frac{l^2}{2520} (19\rho A_0 + 34\kappa_{\rho A} + 25\rho A_l)$$

$$M_{B(6,12)} = -\frac{l^3}{2520} (5\rho A_0 + 8\kappa_{\rho A} + 5\rho A_l)$$

$$M_{B(7,7)} = \frac{l}{30} (\rho A_0 + 3\kappa_{\rho A} + 6\rho A_l)$$

$$M_{B(8,8)} = \frac{l}{630} (19\rho A_0 + 70\kappa_{\rho A} + 145\rho A_l)$$

$$M_{B(8,12)} = -\frac{l^2}{2520} (17\rho A_0 + 50\kappa_{\rho A} + 65\rho A_l)$$

$$M_{B(9,9)} = \frac{l}{630} (19\rho A_0 + 70\kappa_{\rho A} + 145\rho A_l)$$

$$M_{B(9,11)} = \frac{l^2}{2520} (17\rho A_0 + 50\kappa_{\rho A} + 65\rho A_l)$$

$$M_{B(10,10)} = \frac{l}{30} (\rho I_{\rho 0} + 3\kappa_{\rho I_p} + 6\rho I_{pl})$$

$$M_{B(11,11)} = \frac{l^3}{1260} (2\rho A_0 + 5\kappa_{\rho A} + 5\rho A_l)$$

$$M_{B(12,12)} = \frac{l^3}{1260} (2\rho A_0 + 5\kappa_{\rho A} + 5\rho A_l)$$

A.3 Gyroscopic Matrix.

$$G_{B(1,2)} = \frac{b_1 l \Omega}{420} (90 \rho A_0 + 44 \kappa_{\rho A} + 13 \rho A_l)$$

$$G_{B(1,3)} = \frac{b_2 l \Omega}{420} (90 \rho A_0 + 44 \kappa_{\rho A} + 13 \rho A_l)$$

$$G_{B(1,5)} = -\frac{b_2 l^2 \Omega}{420} (10 \rho A_0 + 8 \kappa_{\rho A} + 3 \rho A_l)$$

$$G_{B(1,6)} = \frac{b_1 l^2 \Omega}{420} (10 \rho A_0 + 8 \kappa_{\rho A} + 3 \rho A_l)$$

$$G_{B(1,8)} = \frac{b_1 l \Omega}{420} (15 \rho A_0 + 26 \kappa_{\rho A} + 22 \rho A_l)$$

$$G_{B(1,9)} = \frac{b_2 l \Omega}{420} (15 \rho A_0 + 26 \kappa_{\rho A} + 22 \rho A_l)$$

$$G_{B(1,11)} = \frac{b_2 l^2 \Omega}{210} (2 \rho A_0 + 3 \kappa_{\rho A} + 2 \rho A_l)$$

$$G_{B(1,12)} = -\frac{b_1 l^2 \Omega}{210} (2 \rho A_0 + 3 \kappa_{\rho A} + 2 \rho A_l)$$

$$G_{B(2,3)} = \frac{b_3 l \Omega}{630} (145 \rho A_0 + 70 \kappa_{\rho A} + 19 \rho A_l)$$

$$G_{B(2,5)} = -\frac{b_3 l^2 \Omega}{2520} (65 \rho A_0 + 50 \kappa_{\rho A} + 17 \rho A_l)$$

$$G_{B(2,7)} = -\frac{b_1 l \Omega}{420} (15 \rho A_0 + 26 \kappa_{\rho A} + 22 \rho A_l)$$

$$G_{B(2,9)} = \frac{b_3 l \Omega}{630} (23 \rho A_0 + 35 \kappa_{\rho A} + 23 \rho A_l)$$

$$G_{B(2,11)} = \frac{b_3 l^2 \Omega}{2520} (25 \rho A_0 + 34 \kappa_{\rho A} + 19 \rho A_l)$$

$$G_{B(3,6)} = -\frac{b_3 l^2 \Omega}{2520} (65 \rho A_0 + 50 \kappa_{\rho A} + 17 \rho A_l)$$

$$G_{B(3,7)} = -\frac{b_2 l \Omega}{420} (15 \rho A_0 + 26 \kappa_{\rho A} + 22 \rho A_l)$$

$$G_{B(3,8)} = -\frac{b_3 l \Omega}{630} (23 \rho A_0 + 35 \kappa_{\rho A} + 23 \rho A_l)$$

$$G_{B(3,12)} = \frac{b_3 l^2 \Omega}{2520} (25 \rho A_0 + 34 \kappa_{\rho A} + 19 \rho A_l)$$

$$G_{B(5,6)} = \frac{b_3 l^3 \Omega}{1260} (5 \rho A_0 + 5 \kappa_{\rho A} + 2 \rho A_l)$$

$$G_{B(5,7)} = \frac{b_2 l^2 \Omega}{210} (2 \rho A_0 + 3 \kappa_{\rho A} + 2 \rho A_l)$$

$$G_{B(5,8)} = \frac{b_3 l^2 \Omega}{2520} (19 \rho A_0 + 34 \kappa_{\rho A} + 25 \rho A_l)$$

$$G_{B(5,12)} = -\frac{b_3 l^3 \Omega}{2520} (5 \rho A_0 + 8 \kappa_{\rho A} + 5 \rho A_l)$$

$$G_{B(6,7)} = -\frac{b_1 l^2 \Omega}{210} (2 \rho A_0 + 3 \kappa_{\rho A} + 2 \rho A_l)$$

$$G_{B(6,9)} = \frac{b_3 l^2 \Omega}{2520} (19 \rho A_0 + 34 \kappa_{\rho A} + 25 \rho A_l)$$

$$G_{B(6,11)} = \frac{b_3 l^3 \Omega}{2520} (5 \rho A_0 + 8 \kappa_{\rho A} + 5 \rho A_l)$$

$$G_{B(7,8)} = \frac{b_1 l \Omega}{420} (13 \rho A_0 + 44 \kappa_{\rho A} + 90 \rho A_l)$$

$$G_{B(7,9)} = \frac{b_2 l \Omega}{420} (13 \rho A_0 + 44 \kappa_{\rho A} + 90 \rho A_l)$$

$$G_{B(7,11)} = \frac{b_2 l^2 \Omega}{420} (3 \rho A_0 + 8 \kappa_{\rho A} + 10 \rho A_l)$$

$$G_{B(7,12)} = -\frac{b_1 l^2 \Omega}{420} (3 \rho A_0 + 8 \kappa_{\rho A} + 10 \rho A_l)$$

$$G_{B(8,9)} = \frac{b_3 l \Omega}{630} (19 \rho A_0 + 70 \kappa_{\rho A} + 145 \rho A_l)$$

$$G_{B(8,11)} = \frac{b_3 l^2 \Omega}{2520} (17 \rho A_0 + 50 \kappa_{\rho A} + 65 \rho A_l)$$

$$G_{B(9,12)} = \frac{b_3 l^2 \Omega}{2520} (17 \rho A_0 + 50 \kappa_{\rho A} + 65 \rho A_l)$$

$$G_{B(11,12)} = \frac{b_3 l^3 \Omega}{1260} (2 \rho A_0 + 5 \kappa_{\rho A} + 5 \rho A_l)$$

A.4 Stiffness Matrix.

$$K_{eB(1,1)} = \frac{1}{3l}(EA_0 + \kappa_{EA} + EA_l)$$

$$K_{eB(1,7)} = -\frac{1}{3l}(EA_0 + \kappa_{EA} + EA_l)$$

$$K_{eB(2,2)} = \frac{1}{5l^3}(24EI_{y0} + 12\kappa_{EI_y} + 24EI_{yl})$$

$$K_{eB(2,6)} = \frac{1}{5l^2}(17EI_{y0} + 6\kappa_{EI_y} + 7EI_{yl})$$

$$K_{eB(2,8)} = -\frac{1}{5l^3}(24EI_{y0} + 12\kappa_{EI_y} + 24EI_{yl})$$

$$K_{eB(2,12)} = \frac{1}{5l^2}(7EI_{y0} + 6\kappa_{EI_y} + 17EI_{yl})$$

$$K_{eB(3,3)} = \frac{1}{5l^3}(24EI_{z0} + 12\kappa_{EI_z} + 24EI_{zl})$$

$$K_{eB(3,5)} = -\frac{1}{5l^2}(17EI_{z0} + 6\kappa_{EI_z} + 7EI_{zl})$$

$$K_{eB(3,9)} = -\frac{1}{5l^3}(24EI_{z0} + 12\kappa_{EI_z} + 24EI_{zl})$$

$$K_{eB(3,11)} = -\frac{1}{5l^2}(7EI_{z0} + 6\kappa_{EI_z} + 17EI_{zl})$$

$$K_{eB(4,4)} = \frac{1}{3l}(GJ_0 + \kappa_{GJ} + GJ_l)$$

$$K_{eB(4,10)} = -\frac{1}{3l}(GJ_0 + \kappa_{GJ} + GJ_l)$$

$$K_{eB(5,5)} = \frac{1}{15l}(38EI_{z0} + 14\kappa_{EI_z} + 8EI_{zl})$$

$$K_{eB(5,9)} = \frac{1}{5l^2}(17EI_{z0} + 6\kappa_{EI_z} + 7EI_{zl})$$

$$K_{eB(5,11)} = \frac{1}{15l}(13EI_{z0} + 4\kappa_{EI_z} + 13EI_{zl})$$

$$K_{eB(6,6)} = \frac{1}{15l}(38EI_{y0} + 14\kappa_{EI_y} + 8EI_{yl})$$

$$K_{eB(6,8)} = -\frac{1}{5l^2}(17EI_{y0} + 6\kappa_{EI_y} + 7EI_{yl})$$

$$K_{eB(6,12)} = \frac{1}{15l} (13EI_{y0} + 4\kappa_{EI_y} + 13EI_{yl})$$

$$K_{eB(7,7)} = \frac{1}{3l} \{EA_0 + \kappa_{EA} + EA_l\}$$

$$K_{eB(8,8)} = \frac{1}{5l^3} (24EI_{y0} + 12\kappa_{EI_y} + 24EI_{yl})$$

$$K_{eB(8,12)} = -\frac{1}{5l^2} (7EI_{y0} + 6\kappa_{EI_y} + 17EI_{yl})$$

$$K_{eB(9,9)} = \frac{1}{5l^3} (24EI_{z0} + 12\kappa_{EI_z} + 24EI_{zl})$$

$$K_{eB(9,11)} = \frac{1}{5l^2} (7EI_{z0} + 6\kappa_{EI_z} + 17EI_{zl})$$

$$K_{eB(10,10)} = \frac{1}{3l} (GJ_0 + \kappa_{GJ} + GJ_l)$$

$$K_{eB(11,11)} = \frac{1}{15l} (8EI_{z0} + 14\kappa_{EI_z} + 38EI_{zl})$$

$$K_{eB(12,12)} = \frac{1}{15l} (8EI_{y0} + 14\kappa_{EI_y} + 38EI_{yl})$$

A.5 Spinning Stiffness Matrix

$$K_{\Omega B(1,1)} = \frac{a_{11}l\Omega^2}{30} (6\rho A_0 + 3\kappa_{\rho A} + \rho A_l)$$

$$K_{\Omega B(1,2)} = \frac{a_{12}l\Omega^2}{420} (90\rho A_0 + 44\kappa_{\rho A} + 13\rho A_l)$$

$$K_{\Omega B(1,3)} = \frac{a_{13}l\Omega^2}{420} (90\rho A_0 + 44\kappa_{\rho A} + 13\rho A_l)$$

$$K_{\Omega B(1,5)} = -\frac{a_{13}l^2\Omega^2}{420} (10\rho A_0 + 8\kappa_{\rho A} + 3\rho A_l)$$

$$K_{\Omega B(1,6)} = \frac{a_{12}l^2\Omega^2}{420} (10\rho A_0 + 8\kappa_{\rho A} + 3\rho A_l)$$

$$K_{\Omega B(1,7)} = \frac{a_{11}l\Omega^2}{60} (3\rho A_0 + 4\kappa_{\rho A} + 3\rho A_l)$$

$$K_{\Omega B(1,8)} = \frac{a_{12}l\Omega^2}{420} (15\rho A_0 + 26\kappa_{\rho A} + 22\rho A_l)$$

$$\begin{aligned}
K_{\Omega B(1,9)} &= \frac{a_{13} l \Omega^2}{420} (15 \rho A_0 + 26 \kappa_{\rho A} + 22 \rho A_l) \\
K_{\Omega B(1,11)} &= \frac{a_{13} l^2 \Omega^2}{210} (2 \rho A_0 + 3 \kappa_{\rho A} + 2 \rho A_l) \\
K_{\Omega B(1,12)} &= -\frac{a_{12} l^2 \Omega^2}{210} (2 \rho A_0 + 3 \kappa_{\rho A} + 2 \rho A_l) \\
K_{\Omega B(2,2)} &= \frac{a_{22} l \Omega^2}{630} (145 \rho A_0 + 70 \kappa_{\rho A} + 19 \rho A_l) \\
K_{\Omega B(2,3)} &= \frac{a_{23} l \Omega^2}{630} (145 \rho A_0 + 70 \kappa_{\rho A} + 19 \rho A_l) \\
K_{\Omega B(2,5)} &= -\frac{a_{23} l^2 \Omega^2}{2520} (65 \rho A_0 + 50 \kappa_{\rho A} + 17 \rho A_l) \\
K_{\Omega B(2,6)} &= \frac{a_{22} l^2 \Omega^2}{2520} (65 \rho A_0 + 50 \kappa_{\rho A} + 17 \rho A_l) \\
K_{\Omega B(2,7)} &= \frac{a_{12} l \Omega^2}{420} (15 \rho A_0 + 26 \kappa_{\rho A} + 22 \rho A_l) \\
K_{\Omega B(2,8)} &= \frac{a_{22} l \Omega^2}{630} (23 \rho A_0 + 35 \kappa_{\rho A} + 23 \rho A_l) \\
K_{\Omega B(2,9)} &= \frac{a_{23} l \Omega^2}{630} (23 \rho A_0 + 35 \kappa_{\rho A} + 23 \rho A_l) \\
K_{\Omega B(2,11)} &= \frac{a_{23} l^2 \Omega^2}{2520} (25 \rho A_0 + 34 \kappa_{\rho A} + 19 \rho A_l) \\
K_{\Omega B(2,12)} &= -\frac{a_{22} l^2 \Omega^2}{2520} (25 \rho A_0 + 34 \kappa_{\rho A} + 19 \rho A_l) \\
K_{\Omega B(3,3)} &= \frac{a_{33} l \Omega^2}{630} (145 \rho A_0 + 70 \kappa_{\rho A} + 19 \rho A_l) \\
K_{\Omega B(3,5)} &= -\frac{a_{33} l^2 \Omega^2}{2520} (65 \rho A_0 + 50 \kappa_{\rho A} + 17 \rho A_l) \\
K_{\Omega B(3,6)} &= \frac{a_{23} l^2 \Omega^2}{2520} (65 \rho A_0 + 50 \kappa_{\rho A} + 17 \rho A_l) \\
K_{\Omega B(3,7)} &= \frac{a_{13} l \Omega^2}{420} (15 \rho A_0 + 26 \kappa_{\rho A} + 22 \rho A_l) \\
K_{\Omega B(3,8)} &= \frac{a_{23} l \Omega^2}{630} (23 \rho A_0 + 35 \kappa_{\rho A} + 23 \rho A_l)
\end{aligned}$$

$$\begin{aligned}
K_{\Omega B(3,9)} &= \frac{a_{33} l \Omega^2}{630} (23 \rho A_0 + 35 \kappa_{\rho A} + 23 \rho A_l) \\
K_{\Omega B(3,11)} &= \frac{a_{33} l^2 \Omega^2}{2520} (25 \rho A_0 + 34 \kappa_{\rho A} + 19 \rho A_l) \\
K_{\Omega B(3,12)} &= -\frac{a_{23} l^2 \Omega^2}{2520} (25 \rho A_0 + 34 \kappa_{\rho A} + 19 \rho A_l) \\
K_{\Omega B(5,5)} &= \frac{a_{33} l^3 \Omega^2}{1260} (5 \rho A_0 + 5 \kappa_{\rho A} + 2 \rho A_l) \\
K_{\Omega B(5,6)} &= -\frac{a_{23} l^3 \Omega^2}{1260} (5 \rho A_0 + 5 \kappa_{\rho A} + 2 \rho A_l) \\
K_{\Omega B(5,7)} &= -\frac{a_{13} l^2 \Omega^2}{210} (2 \rho A_0 + 3 \kappa_{\rho A} + 2 \rho A_l) \\
K_{\Omega B(5,8)} &= -\frac{a_{23} l^2 \Omega^2}{2520} (19 \rho A_0 + 34 \kappa_{\rho A} + 25 \rho A_l) \\
K_{\Omega B(5,9)} &= -\frac{a_{33} l^2 \Omega^2}{2520} (19 \rho A_0 + 34 \kappa_{\rho A} + 25 \rho A_l) \\
K_{\Omega B(5,11)} &= -\frac{a_{33} l^3 \Omega^2}{2520} (5 \rho A_0 + 8 \kappa_{\rho A} + 5 \rho A_l) \\
K_{\Omega B(5,12)} &= \frac{a_{23} l^3 \Omega^2}{2520} (5 \rho A_0 + 8 \kappa_{\rho A} + 5 \rho A_l) \\
K_{\Omega B(6,6)} &= \frac{a_{22} l^3 \Omega^2}{1260} (5 \rho A_0 + 5 \kappa_{\rho A} + 2 \rho A_l) \\
K_{\Omega B(6,7)} &= \frac{a_{12} l^2 \Omega^2}{210} (2 \rho A_0 + 3 \kappa_{\rho A} + 2 \rho A_l) \\
K_{\Omega B(6,8)} &= \frac{a_{22} l^2 \Omega^2}{2520} (19 \rho A_0 + 34 \kappa_{\rho A} + 25 \rho A_l) \\
K_{\Omega B(6,9)} &= \frac{a_{23} l^2 \Omega^2}{2520} (19 \rho A_0 + 34 \kappa_{\rho A} + 25 \rho A_l) \\
K_{\Omega B(6,11)} &= \frac{a_{23} l^3 \Omega^2}{2520} (5 \rho A_0 + 8 \kappa_{\rho A} + 5 \rho A_l) \\
K_{\Omega B(6,12)} &= -\frac{a_{22} l^3 \Omega^2}{2520} (5 \rho A_0 + 8 \kappa_{\rho A} + 5 \rho A_l) \\
K_{\Omega B(7,7)} &= \frac{a_{11} l \Omega^2}{30} (\rho A_0 + 3 \kappa_{\rho A} + 6 \rho A_l)
\end{aligned}$$

$$K_{\Omega B(7,8)} = \frac{a_{12} l \Omega^2}{420} (13 \rho A_0 + 44 \kappa_{\rho A} + 90 \rho A_l)$$

$$K_{\Omega B(7,9)} = \frac{a_{13} l \Omega^2}{420} (13 \rho A_0 + 44 \kappa_{\rho A} + 90 \rho A_l)$$

$$K_{\Omega B(7,11)} = \frac{a_{13} l^2 \Omega^2}{420} (3 \rho A_0 + 8 \kappa_{\rho A} + 10 \rho A_l)$$

$$K_{\Omega B(7,12)} = -\frac{a_{12} l^2 \Omega^2}{420} (3 \rho A_0 + 8 \kappa_{\rho A} + 10 \rho A_l)$$

$$K_{\Omega B(8,8)} = \frac{a_{22} l \Omega^2}{630} (19 \rho A_0 + 70 \kappa_{\rho A} + 145 \rho A_l)$$

$$K_{\Omega B(8,9)} = \frac{a_{23} l \Omega^2}{630} (19 \rho A_0 + 70 \kappa_{\rho A} + 145 \rho A_l)$$

$$K_{\Omega B(8,11)} = \frac{a_{23} l^2 \Omega^2}{2520} (17 \rho A_0 + 50 \kappa_{\rho A} + 65 \rho A_l)$$

$$K_{\Omega B(8,12)} = -\frac{a_{22} l^2 \Omega^2}{2520} (17 \rho A_0 + 50 \kappa_{\rho A} + 65 \rho A_l)$$

$$K_{\Omega B(9,9)} = \frac{a_{33} l \Omega^2}{630} (19 \rho A_0 + 70 \kappa_{\rho A} + 145 \rho A_l)$$

$$K_{\Omega B(9,11)} = \frac{a_{33} l^2 \Omega^2}{2520} (17 \rho A_0 + 50 \kappa_{\rho A} + 65 \rho A_l)$$

$$K_{\Omega B(9,12)} = -\frac{a_{23} l^2 \Omega^2}{2520} (17 \rho A_0 + 50 \kappa_{\rho A} + 65 \rho A_l)$$

$$K_{\Omega B(11,11)} = \frac{a_{33} l^3 \Omega^2}{1260} (2 \rho A_0 + 5 \kappa_{\rho A} + 5 \rho A_l)$$

$$K_{\Omega B(11,12)} = -\frac{a_{23} l^3 \Omega^2}{1260} (2 \rho A_0 + 5 \kappa_{\rho A} + 5 \rho A_l)$$

$$K_{\Omega B(12,12)} = \frac{a_{22} l^3 \Omega^2}{1260} (2 \rho A_0 + 5 \kappa_{\rho A} + 5 \rho A_l)$$

A.6 Centrifugal Stiffness Matrix

$$K_{cB(2,2)} = \frac{a \Omega^2}{140} (10 \rho A_0 + 28 \kappa_{\rho A} + 46 \rho A_l) + \frac{b l \Omega^2}{140} (5 \rho A_0 + 18 \kappa_{\rho A} + 37 \rho A_l)$$

$$K_{cB(2,6)} = -\frac{a l \Omega^2}{1680} (20 \rho A_0 + 8 \kappa_{\rho A} - 28 \rho A_l) - \frac{b l^2 \Omega^2}{1680} (5 \rho A_0 - 2 \kappa_{\rho A} - 27 \rho A_l)$$

$$\begin{aligned}
K_{cB(2,8)} &= -\frac{a\Omega^2}{140}(10\rho A_0 + 28\kappa_{\rho A} + 46\rho A_l) - \frac{bl\Omega^2}{140}(5\rho A_0 + 18\kappa_{\rho A} + 37\rho A_l) \\
K_{cB(2,12)} &= \frac{al\Omega^2}{1680}(28\rho A_0 + 64\kappa_{\rho A} + 76\rho A_l) + \frac{bl^2\Omega^2}{1680}(13\rho A_0 + 38\kappa_{\rho A} + 57\rho A_l) \\
K_{cB(3,3)} &= \frac{a\Omega^2}{140}(10\rho A_0 + 28\kappa_{\rho A} + 46\rho A_l) + \frac{bl\Omega^2}{140}(5\rho A_0 + 18\kappa_{\rho A} + 37\rho A_l) \\
K_{cB(3,5)} &= \frac{al\Omega^2}{1680}(20\rho A_0 + 8\kappa_{\rho A} - 28\rho A_l) + \frac{bl^2\Omega^2}{1680}(5\rho A_0 - 2\kappa_{\rho A} - 27\rho A_l) \\
K_{cB(3,9)} &= -\frac{a\Omega^2}{140}(10\rho A_0 + 28\kappa_{\rho A} + 46\rho A_l) - \frac{bl\Omega^2}{140}(5\rho A_0 + 18\kappa_{\rho A} + 37\rho A_l) \\
K_{cB(3,11)} &= -\frac{al\Omega^2}{1680}(28\rho A_0 + 64\kappa_{\rho A} + 76\rho A_l) - \frac{bl^2\Omega^2}{1680}(13\rho A_0 + 38\kappa_{\rho A} + 57\rho A_l) \\
K_{cB(5,5)} &= \frac{al^2\Omega^2}{2520}(65\rho A_0 + 86\kappa_{\rho A} + 101\rho A_l) + \frac{bl^3\Omega^2}{2520}(20\rho A_0 + 46\kappa_{\rho A} + 57\rho A_l) \\
K_{cB(5,9)} &= -\frac{al\Omega^2}{1680}(20\rho A_0 + 8\kappa_{\rho A} - 28\rho A_l) - \frac{bl^2\Omega^2}{1680}(5\rho A_0 - 2\kappa_{\rho A} - 27\rho A_l) \\
K_{cB(5,11)} &= -\frac{al^2\Omega^2}{5040}(22\rho A_0 + 28\kappa_{\rho A} + 34\rho A_l) - \frac{bl^3\Omega^2}{5040}(7\rho A_0 + 14\kappa_{\rho A} + 27\rho A_l) \\
K_{cB(6,6)} &= \frac{al^2\Omega^2}{2520}(65\rho A_0 + 86\kappa_{\rho A} + 101\rho A_l) + \frac{bl^3\Omega^2}{2520}(20\rho A_0 + 46\kappa_{\rho A} + 57\rho A_l) \\
K_{cB(6,8)} &= \frac{al\Omega^2}{1680}(20\rho A_0 + 8\kappa_{\rho A} - 28\rho A_l) + \frac{bl^2\Omega^2}{1680}(5\rho A_0 - 2\kappa_{\rho A} - 27\rho A_l) \\
K_{cB(6,12)} &= -\frac{al^2\Omega^2}{5040}(22\rho A_0 + 28\kappa_{\rho A} + 34\rho A_l) - \frac{bl^3\Omega^2}{5040}(7\rho A_0 + 14\kappa_{\rho A} + 27\rho A_l) \\
K_{cB(8,8)} &= \frac{a\Omega^2}{140}(10\rho A_0 + 28\kappa_{\rho A} + 46\rho A_l) + \frac{bl\Omega^2}{140}(5\rho A_0 + 18\kappa_{\rho A} + 37\rho A_l) \\
K_{cB(8,12)} &= -\frac{al\Omega^2}{1680}(28\rho A_0 + 64\kappa_{\rho A} + 76\rho A_l) - \frac{bl^2\Omega^2}{1680}(13\rho A_0 + 38\kappa_{\rho A} + 57\rho A_l) \\
K_{cB(9,9)} &= \frac{a\Omega^2}{140}(10\rho A_0 + 28\kappa_{\rho A} + 46\rho A_l) + \frac{bl\Omega^2}{140}(5\rho A_0 + 18\kappa_{\rho A} + 37\rho A_l) \\
K_{cB(9,11)} &= \frac{al\Omega^2}{1680}(28\rho A_0 + 64\kappa_{\rho A} + 76\rho A_l) + \frac{bl^2\Omega^2}{1680}(13\rho A_0 + 38\kappa_{\rho A} + 57\rho A_l) \\
K_{cB(11,11)} &= \frac{al^2\Omega^2}{2520}(11\rho A_0 + 26\kappa_{\rho A} + 47\rho A_l) + \frac{bl^3\Omega^2}{2520}(5\rho A_0 + 16\kappa_{\rho A} + 39\rho A_l) \\
K_{cB(12,12)} &= \frac{al^2\Omega^2}{2520}(11\rho A_0 + 26\kappa_{\rho A} + 47\rho A_l) + \frac{bl^3\Omega^2}{2520}(5\rho A_0 + 16\kappa_{\rho A} + 39\rho A_l)
\end{aligned}$$